Graphene Integrated Metamaterial Devices for Terahertz Modulation

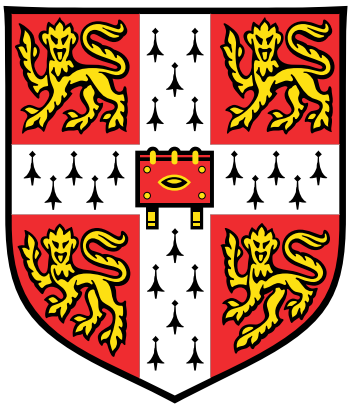

Stephen Kindness

Department of Physics
University of Cambridge

This dissertation is submitted for the degree of
Doctor of Philosophy

Clare College

September 2019

Declaration

This dissertation is the result of work carried out in the Semiconductor Physics Group at the Cavendish Laboratory from October 2015 to March 2019. This dissertation is the result of my own work and includes nothing which is the outcome of work done in collaboration except where specifically stated in the text. This work is not the same as any I have already submitted, or I am in the process of submitting, for any degree at this, or any other university. This dissertation contains fewer than 60,000 words including appendices, bibliography, footnotes, tables and equations.

Stephen Kindness
September 2019

Abstract - Graphene Integrated Metamaterial Devices for Terahertz Modulation - Stephen Kindness

Terahertz (THz) research has experienced impressive progress in recent decades, with unique applications emerging in fields such as spectroscopy, communications, and imaging, all of which require fast and accurate control of the THz radiation properties. To unlock the full potential of THz radiation, it is essential to develop a catalogue of high speed, electrically controllable modular THz devices, which can be implemented with standardised sources to build versatile THz systems. Due to THz frequencies lying outside of the typical operation range for the mature microwave and photonic technologies, alternative approaches are required to solve the unique engineering problems associated with operating in this frequency regime. This thesis will look to design and develop novel device architectures using metamaterial arrays to strongly couple with THz radiation, whilst implementing electrically tunable graphene to modify the strength and nature of this interaction, leading to active control of the amplitude, phase, polarisation and frequency of THz radiation.

Chapter 1 discusses two THz sources: THz time-domain spectroscopy (THz-TDS) and THz quantum cascade lasers (THz-QCLs). A range of THz modulator architectures will then be discussed, focusing on the methods which involve converting passive metamaterial arrays into actively tunable devices, including the implementation of microelectromechanical systems (MEMS), photoactive semiconductors, and electrostatically tunable graphene.

Chapter 2 outlines the basic device design principles for the graphene integrated metamaterial devices shown in this thesis. The steps to build a basic split ring resonator (SRR) and graphene amplitude modulator device are discussed, starting with the design process using finite element electromagnetic simulation, before outlining the fabrication steps required to build the device, and finally performing the experimental procedure to test the device performance in a THz-TDS system. The SRR/graphene device discussed in this chapter demonstrates amplitude modulation depths in the region of 12%, achieved by electrostatically tuning the graphene conductivity using a voltage range of 30 V.

Chapter 3 investigates more sophisticated graphene integrated metamaterial devices which involve lithographically selecting targeted areas of the metamaterial structure to be actively tuned by graphene. More interesting modulation effects, such as resonant frequency tuning, are achieved by integrating a coupled resonator metamaterial array with targeted graphene damping. A continuous tuning of the resonant frequency over a 60 GHz range, and binary tuning of over 200 GHz are achieved. Due to the highly dispersive nature of the coupled resonator array, dramatic phase and group delay modulation effects are also demonstrated.

Chapter 4 builds on the work from chapter 3, converting the coupled resonator and graphene devices into polarisation modulators by adding an intrinsic chirality into the metamaterial design. Two different devices are designed and fabricated, both achieving electrical control over the polarisation angle and ellipticity of the transmitted radiation. Polarisation tuning of up to 30 degrees is experimentally confirmed, with linear radiation successfully converted into perfectly circular radiation, achieving an ellipticity tuning range from 0.6 to 1.0.

Chapter 5 discusses the implementation of the active devices described in the previous chapters with quantum cascade lasers, for the conversion of a standard THz source into a highly versatile amplitude, polarisation and frequency controllable modular THz system. MHz modulation speeds of QCLs are achieved by directing a QCL output through the polarisation devices, with the polarisation angle actively tuned by up to 9 degrees. Dramatic modulation effects are achieved by externally coupling radiation back into a QCL using the devices as electrically tunable mirrors in an external cavity configuration. 100 % amplitude modulation of the QCL is achieved using this method, and the frequency of THz output is also successfully manipulated, with 20 GHz binary tuning of the laser output achieved.

Chapter 6 discusses future methods which could be used to enhance the modulation depths of the devices described in this thesis. A modified reflection modulation scheme is proposed and theoretically described which could greatly enhance the tuning range of the modulators. Preliminary TDS experiments are performed showing near 100 % amplitude modulation depths by employing this modulation scheme. Further to this, a continuous $\pi/2$ phase tuning range is achieved, corresponding to a 10 times improvement compared to the standard transmission and reflection modulation schemes. A modified QCL feedback scheme is also described which could utilize this enhanced phase modulation to achieve continuous tuning of the QCL output over 10s of GHz. A similar scheme is simulated to produce greatly enhanced polarization modulation depths with nearly 90 degrees polarization angle tuning, and near linear to perfectly circular polarisation modulation predicted. A potential modular TDS set-up is also proposed which involves implementing the polarisation modulators into the standard set-up, for fast material birefringence characterisation.

Acknowledgements

I would like to thank the Integrated Photonics and Electronic Systems CDT, the Engineering and Physical Sciences Research Council, and the Semiconductor Physics Group for financial support. Thanks goes to my supervisor, Prof. David Ritchie, for his guidance and advice throughout. Thanks also goes to Dr. Harvey Beere for extensive technical support throughout the PhD, and for his help proof reading this thesis.

I would like to acknowledge collaborations with Binbin Wei, Nikita Almond, and Dr. Riccardo Degl'Innocenti, who contributed to the experiments presented in chapter 5, and I would also like to thank Wladislaw Michailow for many in depth discussions which helped shape the theoretical groundwork in this thesis. I would like to acknowledge and thank Philipp Braeuninger-Weimer for growing the CVD graphene which was used for the devices in this thesis. A particular thanks goes to David Jessop, who initially developed the Comsol simulation process and taught me how to use the simulation tool for device design.

A special thanks goes to Dr. Riccardo Degl'Innocenti who contributed massively to the device design principles, as well as teaching me the fabrication processes to make, and experimental methods to test, the devices presented in this thesis. Without his continued technical advice and moral support, these projects would not have been possible.

Thank you to everyone in the THz corner, David Jessop, Robert Wallis, Adam Kilmont, Varun Kamboj, Binbin Wei, Yuqing Wu, Nikita Almond, Wladislaw Michailow, Kaveh Delfanazari, Lukas Jakob, and Peter Spencer, for many stimulating discussions over the years, but most importantly for the emotional support and camaraderie through the dark times.

I cannot thank my parents enough for their loving support over all these years, putting up with me spending the best part of a decade at university. And finally, I will be forever grateful to Megan for being there with me every step of the way.

Publications

S. J. Kindness, N. W. Almond, W. Michailow, B. Wei, L. A.Jakob, K. Delfanazari R. Wallis, P. Braeuninger-Weimer, S. Hofmann, H. E. Beere, D. A. Ritchie, and R. Degl'Innocenti, "Graphene-Integrated Metama-terial Device for All-Electrical Polarization Control of Terahertz Quantum CascadeLasers." *ACS Photonics*, 6(6):1547–1555, 2019.

S. J. Kindness, N. W. Almond, B. Wei, R. Wallis, W. Michailow, V. S. Kamboj, P. Braeuninger-Weimer, S. Hofmann, H. E. Beere, D. A. Ritchie, and R. Degl'Innocenti, "Active Control of Electromagnetically Induced Transparency in a Terahertz Metamaterial Array with Graphene for Continuous Resonance Frequency Tuning." *Advanced Optical Materials*, 6(21):1800570, 2018.

S. J. Kindness, D. S. Jessop, B. Wei, R. Wallis, V. S. Kamboj, L. Xiao, Y. Ren, Braeuninger-Weimer, A. I. Aria, S. Hofmann, H. E. Beere, D. A. Ritchie, and R. Degl'Innocenti, "External amplitude and frequency modulation of a terahertz quantum cascade laser using metamaterial/graphene devices." *Scientific Reports*, 7(1):1–10, 2017.

R. Degl'Innocenti, **S. J. Kindness**, H. E. Beere and D. A. Ritchie, "All-integrated terahertz modulators." *Nanophotonics*, 7(1):127-144, 2018.

B. Wei, **S. J. Kindness**, N.W. Almond, R. Wallis, Y. Wu, Y. Ren, S. C. Shi,P. Braeuninger-Weimer, S. Hofmann, H. E. Beere, and D. A. Ritchie, "Amplitude stabilization and active control of a terahertz quantum cascade laser with a graphene loaded split-ring-resonator array." *Applied Physics Letters*, 112(20):201102, 2018.

D. S. Jessop, **S. J. Kindness**,L. Xiao, P. Braeuninger-Weimer, H. Lin, Y. Ren, C. X. Ren, C, S. Hofmann, J. A. Zeitler, H. E. Beere, and D. A. Ritchie, "Graphene based plasmonic terahertz amplitude modulator operating above 100 MHz." *Applied Physics Letters*, 108(17):171101, 2016.

R. Degl'Innocenti, L. Xiao, **S. J. Kindness**, V. S. Kamboj, B. Wei, P. Braeuninger-Weimer, K. Nakanishi, A. I. Aria, S. Hofmann, H. E. Beere, and D. A. Ritchie, "Bolometric detection of terahertz quantum cascade laser radiation with graphene-plasmonic antenna arrays." *Journal of Physics D: Applied Physics*, 17(50):174001 2017.

R. Degl'Innocenti, L. Xiao, D. S. Jessop, **S. J. Kindness**, Y. Ren, H. Lin, J. A. Zeitler, J. A. Alexander-Webber, H. J. Joyce, P. Braeuninger-Weimer, S. Hofmann, H. E. Beere, and D. A. Ritchie, "Fast room-temperature detection of terahertz quantum cascade lasers with graphene-loaded bow-tie plasmonic antenna arrays." *ACS Photonics*, 3(10):1747-1753, 2016.

R. Degl'Innocenti, R. Wallis, B. Wei, L. Xiao, **S. J. Kindness**, O. Mitrofanov, P. Braeuninger-Weimer, S. Hofmann, H. E. Beere, and D. A. Ritchie, "Terahertz nanoscopy of plasmonic resonances with a quantum cascade laser." *ACS Photonics*, 4(9):2150-2157, 2017.

R. Degl'Innocenti, D. S. Jessop, C. Sol, L. Xiao, **S. J. Kindness**, H. Lin, J. A. Zeitler, P. Braeuninger-Weimer, S. Hofmann, Y. Ren, V. S. Kamboj, J. P. Griffiths, H. E. Beere, and D. A. Ritchie, "Fast modulation of terahertz quantum cascade lasers using graphene loaded plasmonic antennas." *ACS Photonics*, 3(3):464-470, 2016.

Peer Reviewed Conference Proceedings

S. J. Kindness, N. W. Almond, R. Wallis, B. Wei, V. S. Kamboj, P. Braeuninger-Weimer, S. Hofmann, H. E. Beere, D. A. Ritchie, and R. Degl'lnnocenti, "Active frequency modulation of metamaterial/graphene optoelectronic device using coupled resonators", *CLEO*: *QELS Fundamental Science*, 2018.

S. J. Kindness, D. S. Jessop, B. Wei, R. Wallis, V. S. Kamboj, L. Xiao, Y. Ren, P. Braeuninger-Weimer, S. Hofmann, H. E. Beere, D. A. Ritchie, and R. Degl'Innocenti, "100 % amplitude modulation of external cavity terahertz QCL using an optoelectronic chopper based on metamaterial and graphene." *2017 Conference on Lasers and Electro-Optics Europe and European Quantum Electronics Conference*, 2017.

S. J. Kindness, D. S. Jessop, B. Wei, R. Wallis, V. S. Kamboj, L. Xiao, Y.Ren, P. Braeuninger-Weimer, S. Hofmann, H. E. Beere, D. A. Ritchie, and R. Degl'Innocenti, "Optoelectronic control of an external cavity quantum cascade laser using a graphene loaded metamaterial array." *CLEO: Science and Innovations*, 2017.

R. Degl'Innocenti, **S. J. Kindness**, N. W. Almond, W. Michailow, P. Braeuninger-Weimer, S. Hofmann, H. E. Beere, and D. A Ritchie, "Metamaterial/graphene active terahertz modulators", *2019 IEEE MTT-S International Wireless Symposium (IWS)*, 2019.

R. Degl'Innocenti, **S. J. Kindness**, N. W. Almond, W. B. Wei, R. Wallis, V. S. Kamboj, P. Braeuninger-Weimer, S. Hofmann, H. E. Beere, and D. A Ritchie, "Metamaterial/graphene amplitude and frequency modulators for the active control of terahertz quantum cascade lasers", *Terahertz Emitters, Receivers, and Applications IX*, 2018.

B. Wei, **S. J. Kindness**, N. W. Almond, R. Wallis, Y. Wu, Y. Ren, P. Braeuninger-Weimer, S. Hofmann, H. E. Beere, D. A. Ritchie, and R. Degl'lnnocenti "Amplitude Stabilization of a Terahertz Quantum Cascade Laser with an External Metamaterial Amplitude Modulator", *CLEO: Science and Innovations*, 2018.

D. S. Jessop, **S. J. Kindness**, L. Xiao, P. Braeuninger-Weimer, H. Lin, Y. Ren, J. Griffiths, C. X. Ren, S. Hofmann, J. A. Zeitler, H. E. Beere, D. A. Ritchie, and R. Degl'Innocenti, "Fast graphene based plasmonic terahertz amplitude modulators." *CLEO: Science and Innovations*, 2016.

B. Wei, R. Wallis, **S. J. Kindness**, O. Mitrofanov, H. E. Beere, D. A. Ritchie, and R. Degl'Innocenti, "Terahertz s-SNOM with> /1000 resolution based on self-mixing in quantum cascade lasers." *2017 Conference on Lasers and Electro-Optics Europe and European Quantum Electronics Conference*, 2017.

D. S. Jessop, C. Sol, L. Xiao, **S. J. Kindness**, P. Braeuninger-Weimer, H. Lin, J. P. Griffiths, Y. Ren, V. S. Kamboj, S. Hofmann, J. A. Zeitler, H. E. Beere, D. A. Ritchie, and R. Degl'Innocenti, "Fast terahertz optoelectronic amplitude modulator based on plasmonic metamaterial antenna arrays and graphene." *Terahertz, RF, Millimeter, and Submillimeter-Wave Technology and Applications IX*, 2016.

R. Degl'Innocenti, L. Xiao, D. S. Jessop, **S. J. Kindness**, C. Sol, Y. Ren, H. Lin, J. A. Zeitler, P. Braeuninger-Weimer, S. Hofmann, H. E. Beere, and D. A. Ritchie, "Bow-tie plasmonic arrays loaded with graphene for the fast room temperature detection of terahertz quantum cascade lasers." *CLEO: Science and Innovations*, 2016.

Table of contents

List of figures

List of tables

Chapter 1

Introduction

1.1 Terahertz overview

Terahertz (THz) radiation is defined by electromagnetic waves in the frequency band between the microwave and far infrared regions (1-10 THz; 300-30 μm; 4-40 meV). The exact definition of this frequency range has altered over time, depending on the interpretation of the author [1–3], however in this thesis, the frequency range between 1 and 4 THz will be focused on. THz radiation has applications in many different research areas and shows much promise for a range of industrial applications [4]. One of the standout applications for THz radiation is in material characterization, with low energy THz photons suitable for probing electronic excitations and vibrational modes in solids, as well as vibrational and rotational transitions in molecules [5]. Other applications involve the use of THz radiation in gas spectroscopy [6, 7], for the characterization of fundamental semiconductor physics [8, 9], and for the monitoring of industrial processes such as the manufacture of pharmaceuticals [10, 11] or the characterization of thin film paint thicknesses [12]. Due to the non-ionizing nature of THz radiation, there is significant interest in THz medical imaging [13, 14]. Also, due to the frequency being much higher than standard microwave carrier frequencies, there are exciting opportunities to exploit the unused sub-THz [15] and THz frequency bands to shape the future of wireless communication [16–18]. All of these applications require THz sources and detectors, and there has been significant progress in developing such devices in recent years [16, 19, 20]. However, there is still a shortage of modular optoelectronic components to be used as the building blocks for THz systems [21]. This thesis will focus on investigating and demonstrating novel modulator device architectures, capable of electrically controlling the amplitude, polarization, phase and frequency of THz radiation.

1.2 Terahertz instrumentation

One of the main challenges of developing THz instrumentation, is that the frequency range falls between the normal operating limits of typical electrical and optical based components, resulting in the so called THz Gap [22, 23]. Standard electrical microwave sources are limited by the carrier mobility of the oscillating semiconductor charges when increasing operation frequency [24], whereas for standard optical sources, there are significant challenges as the frequency is reduced into the THz region, particularly due to the lack of sufficiently small band-gap materials, as well as thermal considerations [25]. There has, however, been a significant move towards filling this THz gap in recent years with significant breakthroughs in developing THz sources from the low frequency electrical side, as well as from the high frequency optical side [26, 27]. There are a number of solid state voltage controlled diode oscillators, based on microwave technology, which are capable of operating above 1 THz [28], such as the impact ionization avalanche transit-time (IMPATT) diode [29], resonant tunnelling diode [30], and Gunn diode [31]. However, as the frequency of operation increases, there is a sharp drop off in the output power [32], with power levels above the mW level difficult to achieve in the THz region [2].

The most powerful demonstrated THz source is the free electron laser, capable of producing 100s of Watts of output power. However, these lasers are bulky, requiring the use of a linear accelerator as well as strong magnetic fields, and have a high power consumption which makes them impractical for most applications [33]. Another electron beam based source is the backward wave oscillator, achieving mW's of power [34]. A solid state high power source, operating in the high frequency THz region, is the quantum cascade laser (QCL) [2, 35] which utilizes the inter sub-band transition of quantum well heterostructure, demonstrating peak output powers > 1 W [36]. These lasers require cryogenic cooling, however, QCL sources which operate by exploiting difference frequency generation using two infrared (IR) active regions, are a potential way forward for realizing high temperature operation of THz QCLs [37].

Other source designs involve the use of a physical medium to convert optical laser power into emitted THz power. Optical parametric down-conversion can be achieved using a non-linear crystal to produce THz radiation from a single incident source [38]. Alternatively, two far-infrared pump lasers can be used to produced THz radiation via heterodyne mixing [39]. Photoconductive antennas (PCA) which consist of a metal antenna design on a photoconductive substrate, can be used to effectively produce CW THz generation by photo-mixing two frequency offset incident pump lasers [40, 41]. These antennas can also be used for THz pulse generation using a single femtosecond laser [19, 42] as well as for THz detection, forming the building blocks of the important THz time domain spectroscopy (TDS) system.

The following section will document the range of THz components used in this thesis to characterize and test the fabricated devices, which include a THz TDS system and THz QCLs.

1.2.1 Time domain spectroscopy set-up

One of the most versatile and promising THz instruments, particularly for material characterisation in science and industry, is the THz time domain spectroscopy (TDS) system. This set-up uses photoconductive antennas which are excited by a femtosecond pulsed IR laser to produce and detect THz radiation in a fully integrated room temperature system. Pulse bandwidths of up to 20 THz [43, 44], are achievable depending on the emitter and detector used [45], and average emitted power in the 10s of μWs are possible [46]. The highly repeatable nature of the pulse generation enables the averaging of a large number of pulses, allowing for an accurate retrieval of the pulse shape on a sub-picosecond timescale with a signal to noise ratio (SNR) 100 dB despite the low average power. TDS systems are the most widely used THz systems in science and industry, being central to many of the applications already mentioned, including pharmaceutical quality control [47–55, 10, 11], material characterisation [56–64], layer thickness measurements [65–69], and also explosives detection [70–75]. The TDS system is important for the work in this thesis as it is vital for characterising the broadband transmission through fabricated active devices. Crucially, it allows for the complex transmitted electric field to be measured, enabling the characterisation of the phase and polarization of transmitted radiation through devices, as well as the amplitude.

The TDS system used for the measurements in this thesis is a Menlo K15 operated in transmission mode, with the set-up described in figure (1.1). A mode-locked femtosecond pulsed IR laser with a wavelength of 1560 nm, operating with a repetition rate of 100 MHz, is used to excite charge carriers in the photoconductive antennas for THz pulse emission and detection. Each optical pulse has a duration of $\sim$90 fs with an energy of $\sim$2.0 nJ. This pulse is split into two paths using a beam splitter, labelled A and B in figure (1.1). Path B is fibre coupled to the emitter which is an InGaAs/InAlAs strip line antenna. A THz pulse is generated when the electron-hole pairs in the antenna substrate are excited by the impinging optical pulse, before being accelerated in a DC bias applied across the antenna arms. The accelerating charges produce a short pulse of electromagnetic radiation, emitting as a broadband THz pulse which has a bandwidth determined by factors such as the electron-hole lifetime and electron mobility, as well as the antenna geometry [76–78]. The emitted broadband THz pulse is then collimated and focused onto a sample using plastic

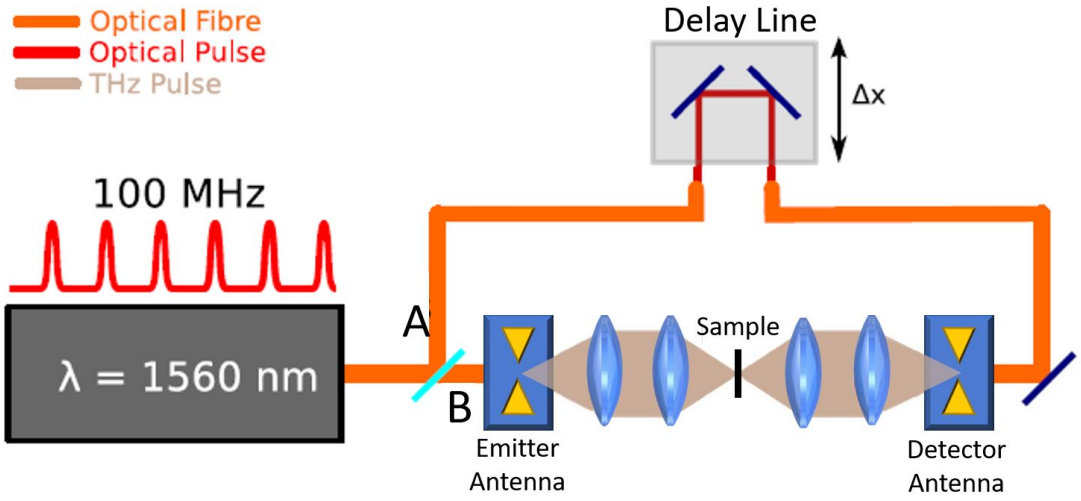

Fig. 1.1 Schematic of the Menlo K15 THz TDS system in transmission

lenses. An identical lens arrangement is used after the sample for collimition and focusing the transmitted THz pulse on to the detector antenna.

Path A passes through an optical delay line before being fibre coupled with the PCA detector which is a low temperature (LT) InGaAs/InAlAs dipole detector antenna. As with the emitter PCA, when the femtosecond laser optical pulse is incident on the detector, electron-hole pairs are optically excited. The incident THz radiation from the emitter accelerates these excited charge carriers across the dipole antenna, producing a photocurrent between the two electrodes. The current is measured after passing through a low noise amplifier, giving a direct indication of the average electric field from the THz pulse accelerating the carriers over their lifetime. The detector is only sensitive to the electric field from the THz pulse when the laser optical pulse is incident, and hence a snapshot of the electric field in the THz pulse is detected. To build up the full time domain pulse, the delay line in path A is varied by up to 100 ps using a sub-picosecond step size, with the THz pulse electric field measured as a function of delay time. There will be a convolution between the sensitivity time of the detector and the incident pulse electric field, and hence short, sub-picosecond, electron-hole recombination times are the primary material requirement for the detector semiconductor [76, 79].

Using the method described, THz pulses are generated by optical excitation with a 100 MHz repetition rate, and with the pulse shape being fully mapped out several times a second. The SNR can be improved dramatically by averaging over many measured pulses, with this process performed in the electrical post processing unit, typically over the course of 5

minutes for a high SNR up to 3 THz. The TDS system is resilient to variation in pump pulse timing caused by random jitter, as this effect is cancelled out due to the delay being identical for path A and B. However, if there is a relative drift in temperature between path A and path B, the measured pulse will be smeared out, adding a drift to the amplitude and phase of the spectral measurement. To mitigate against this, measurements taken in this thesis are typically not averaged for over 5 minutes, unless it is essential to improve the noise floor in the spectral region above 3 THz.

1.2.2 Time domain spectroscopy analysis

One characteristic of this technique which makes it so versatile, is the phase sensitive detection of the electric field due to the detection of the polarity of the induced photocurrent as well as the amplitude. This extra information, which is not available for optical power detection schemes, is crucial for quantifying complex material parameters such as the permittivity, refractive index and conductivity. It does however, make the data analysis more complicated than a CW frequency domain system, as the time domain signal must be converted into the frequency domain using a Fourier transformation.

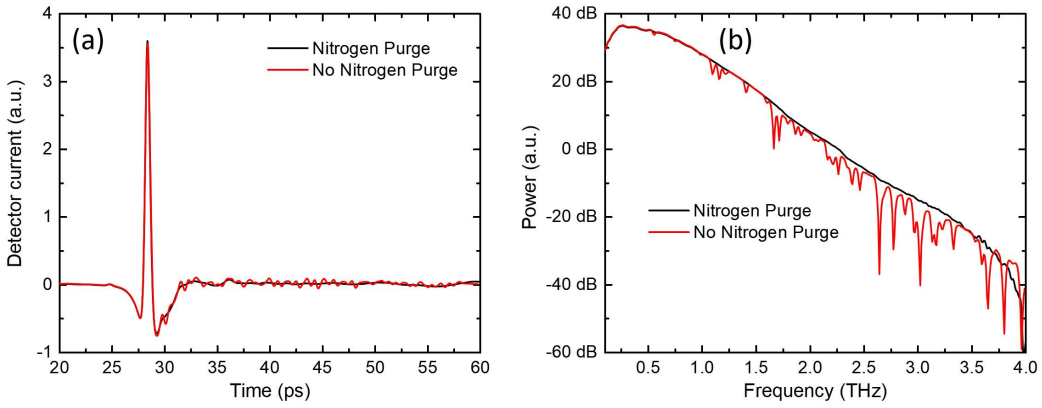

Fig. 1.2 (a) Time domain detector current measurement of THz pulse. (b) Spectral power content of pulse determined by performing a Fourier transform. The black and red lines indicate measurements with and without nitrogen purging respectively.

A standard time domain pulse shape through air is shown in the red curve in figure (1.2 (a)), constructed by moving the delay line over a range of 80 ps, and averaging for 5 minutes. To extract the spectral power content of the pulse from the time domain data, Matlab is used in post processing to perform a fast Fourier transform (FFT) on the measured time domain data before squaring the result to convert from electric field to power. The resultant power

spectrum of the pulse measured by the photodetector is shown by the red curve in figure (1.2 (b)). When inputting the time domain data into the Matlab FFT function, a frequency domain result is produced with equal length as the input time domain signal given, and the absolute value of frequency must be added later. The value for the minimum frequency step is given by the inverse of the time domain window length, t, which is 80 ps, giving a frequency step of 12.5 GHz. This is sufficient to observe strong absorption dips in the transmitted power due to water absorption in the atmosphere. Conversely, the maximum frequency is proportional to the inverse of the minimum time step. To counter these absorption lines, the set-up is enclosed in a plastic bag for nitrogen purging, with the humidity dropping from around 30% for this example to a value of <10 % after 30 minutes of continuous nitrogen flow. The time domain and frequency domain results performed after nitrogen purging are shown by the black curves in figures (1.2 (a) and (b)) respectively. The time domain signal for the nitrogen purged path is very smooth beyond the initial peak, and the sharp transmission dips between 1 and 4 THz are almost completely removed from the frequency domain graph. There is a smooth logarithmic decrease in the measured power as a function of frequency, with the noise floor of the set-up typically washing out the signal at frequencies above 3.75 THz when using an integration time of 5 minutes.

When a sample is placed in the beam path for characterisation, there are complications which arise from multiple reflections of the pulse from the back and front facets of the substrate. These reflections result in secondary peaks being detected in the time domain measurement, resulting in a Fabry Perot interference effect in the power spectrum. The time domain signal through a standard 500 μm p-doped silicon substrate with a 300 nm SiO_2 insulating layer is shown in figure (1.3 (a)), using a nitrogen purged setup, and compared to the TDS signal measured with no sample. For many applications it is desirable to remove the effect that the substrate has on the measurement, as the substrate is only used to hold a material of interest, and the Fabry Perot effect of the substrate can make normalization of the transmitted power highly complex. To counter this, a post processing window function can be multiplied with the raw data to filter the first peak of the time domain data, negating any of the internal reflection peaks, and using this single peak to build the frequency domain data. However, the generated power spectrum will now be a convolution of the Fourier transform of the TDS data with the Fourier transform of the window function, and therefore one must carefully choose the window function shape to minimise perturbations to the end result.

A simple and effective window is the Hann function [80], which is essentially one period of a cosine function oscillating from 0 to 1, as shown in figure (1.3 (a)). The power spectrum generated by using the time domain data passing through the substrate, including all the peaks is shown by the red curve in figure (1.3 (b)). The Fabry Perot effect can be clearly

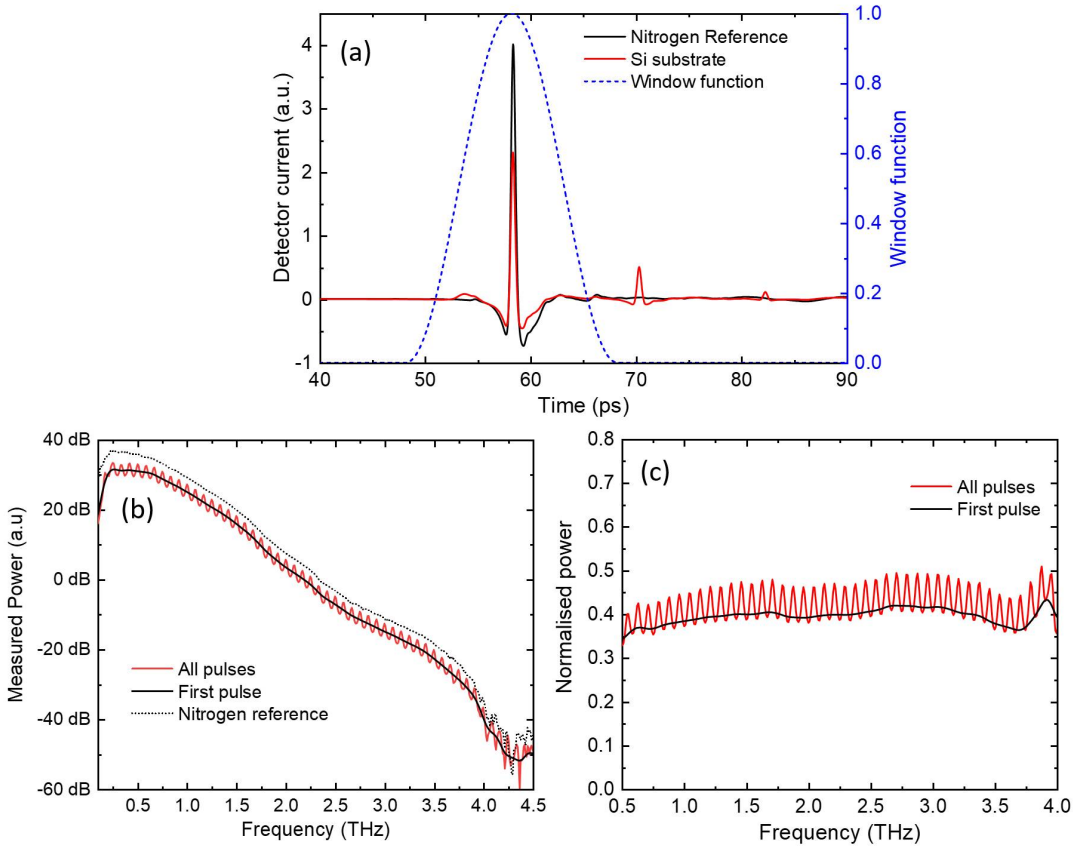

Fig. 1.3 (a) Time domain data from nitrogen reference and through silicon substrate with Hann window function shown to isolate the first peak. (b) Power spectrum for the nitrogen reference (dotted black line), full silicon substrate signal containing all reflected pulses (red line), and from the silicon substrate data multiplied by the window function (black line). (c) Power spectrum normalised to transmission through air using full data through substrate (All pulses) and data through substrate multiplied by Hann window (First pulse).

observed due to the regular interference fringes as a function of frequency, however, if the time domain data is first filtered, isolating only the first pulse, the regular interference fringes disappear leading to a smooth line illustrated by the black curve in figure (1.3 (b)). To characterize the percentage of transmitted power through the substrate, the power is divided by the power through nitrogen, with the resultant normalized transmission shown in figure (1.3 (c)), with a broadband transmission of around 40 percent through the substrate when windowing the first pulse. The windowing function is effective at removing the Fabry Perot perturbations, however, it is important to note that sharp features in the spectrum may no longer be resolvable as our time domain data length has reduced from 80 ps to 20 ps, reducing the theoretical frequency resolution of the spectral measurement from 12.5 GHz to 50 GHz.

Zero padding of the time domain signal can be used to smooth the spectral measurement, however, no extra resolution can be achieved using this method as there is no additional data being added.

1.2.3 Quantum cascade laser principles

The THz-TDS system is a powerful tool for the characterisation of the devices fabricated in this thesis, however, for applications such as THz communications, high power, coherent, single frequency sources are required. To demonstrate the applicability of the devices designed and fabricated in this thesis, THz-QCLs are used in proof of principle experiments. QCLs are high power solid state lasers which utilise quantum well confinement in semiconductor heterostructures, enabling energy transitions in the conduction band, sidestepping the requirement for a semiconductor with a direct narrow THz bandgap. Electrons are injected into the carefully designed quantum well superlattice structure, emitting radiation through stimulated emission as the electron cascades through repeated active region periods. The conduction band energy levels are tuned by the spatial quantum confinement of the heterostructure layers, rather than the bandgap of the semiconductor itself, allowing for the emission frequency to be chosen via the growth thicknesses. The curvature of the band diagram for the different energy levels are similar as they are all in the conduction band, and therefore the energy gap remains more consistent with changes in the electron momentum. This leads to QCLs being more resilient to thermal noise than standard interband transition semiconductor lasers, solving one of the fundamental challenges with realizing a THz semiconductor laser. Maximum THz-QCL outputs of >1 W [36] in pulsed mode, and 0.23 W [81] in CW mode have been demonstrated in current state of the art devices. These lasers are typically operated with cryogenic cooling, however, operation is proven to be possible up to 200 K [82].

The standard operating principle of a QCL is diagrammatically described in figure (1.4), showing an electron cascading through different active regions when a bias is applied across the structure. QCL active regions can typically be characterised as 3 level laser systems with the electrons tunnelling from the injector region into the top energy level 3. The electron then decays to energy level 2 due to stimulated emission, emitting a further THz photon before rapidly decaying into energy level 1. This electron can now tunnel into the relaxation/injection region with a lifetime determined by the barrier height and thickness, and if the bands are correctly aligned from the external electric field, the electron can then subsequently tunnel into level 3 of the next period. This defines a single active region period. This process is repeated through 100 to 200 repeat active region periods until the electron reaches the electrode attached to the final active region period. To achieve population inversion in the active region the scattering times are configured such that $\tau_{32} > \tau_2$ by controlling the

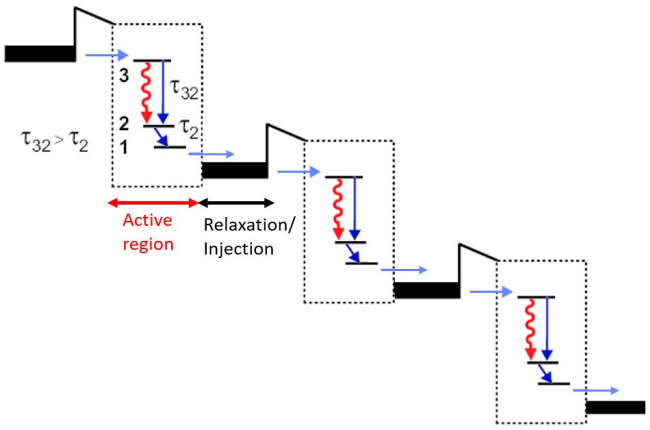

Fig. 1.4 Quantum Cascade Laser illustrated quantum well structure showing three repeated periods.

thicknesses of the quantum wells in the heterostructure [83]. The laser cavity can then be completed by providing optical feedback due to the Fresnel reflection from the cleaved ends of the waveguide, leading to lasing when the active region gain is sufficient to compensate for round trip losses. To support the laser mode, a single plasmon (SP) waveguide design can be used which supports an optical mode bound between the top metallic contact, and a highly doped layer on the substrate. An alternative waveguide method is the double metal design which involves sandwiching the mode between a top and bottom metal contact on either side of the QCL ridge. The SP design has some advantages over the double metal design including ease of processing, and the improved quality and higher power of the quasi-Gaussian output beam profile. These waveguide designs are also easier to couple back into using external cavity configurations, which will be relevant for the external cavity modulation experiments discussed in chapter 5.

There are different active region designs, most notably the resonant phonon [84, 85] and bound to continuum (BTC) designs [86, 87], employed to generate the required active region energy levels whilst providing efficient relaxation of the electrons from level 2 to enable population inversion. The lasers discussed in this thesis use various (BTC) active region designs. The working principle of this design is to bring active regions which employ a large number of quantum wells (>10) in close proximity, causing the lower energy states to couple together, forming a miniband of energy levels separated by small energy gaps. After an electron radiatively decays from state 3 to state 2, there is a fast non-radiative decay due to electron-electron scattering between the many states in this miniband, with the electron thermalising quickly to the bottom energy state before tunnelling into the next injector region.

A standard BTC design, taken from Ref. [86] is shown in figure (1.5 (a)), with one of the periods shown.

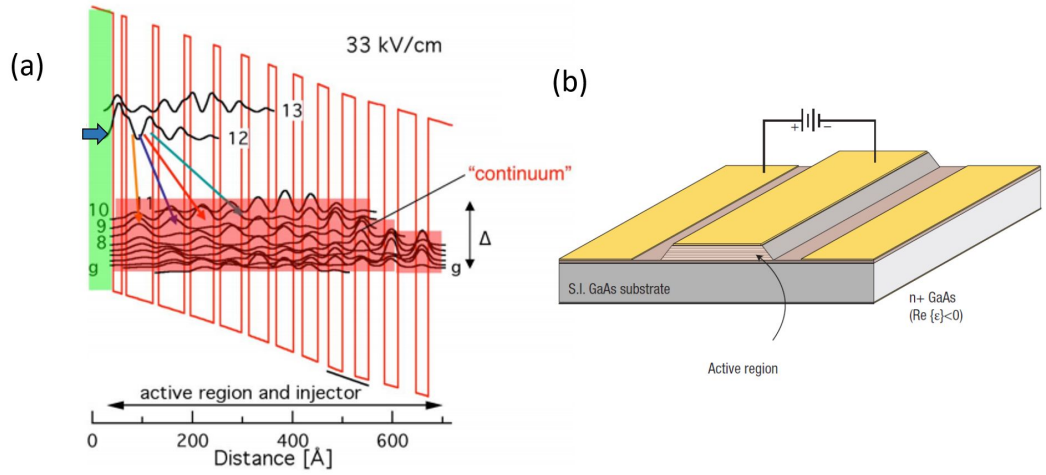

Fig. 1.5 (a) Band diagram of one period of BTC QCL taken from Ref. [86]. (b) QCL single plasmon waveguide structure illustration taken from Ref. [2].

The THz-QCLs used in this thesis have been fabricated in the semiconductor physics group, using the molecular beam epitaxy (MBE) facility and standard clean room methods, following a process which is outlined in detail in Ref. [88]. MBE is required to produce precise alternating semiconductor layers [89], typically GaAs/AlGaAs. The different band gap energies of these layers provides the quantum well confinement, with heavily doped regions to provide enough carriers to avoid depletion and space-charge formation. The QCL active region is grown onto a host substrate, GaAs(100), and can be etched into various waveguide designs. The lasers in this thesis all have a single plasmon (SP) [35] waveguide design, which is illustrated in figure (1.5 (b)). This design supports an optical mode bound between the top metallic contact, which is created by the deposition of gold on the active region ridge with a length of 2-3 mm and width of 250 μm, and a highly doped layer on the substrate between the active region and the semi-insulating GaAs substrate. This doped layer is optically thin in the THz, hence the optical mode penetrates >100 μm into the substrate, with minimum ohmic losses in the doped layer.

1.2.4 Quantum cascade laser operation

The QCLs used in this thesis have optimal <50 K operating temperatures, therefore cryogenic cooling with liquid helium is used. Also, to maximise output power a pulsed QCL arrangement, illustrated in figure (1.6) is applied. A 10 kHz rectangular voltage pulse is

applied to the QCL, with the duty cycle (DC) set between 2% and 10% depending on the desired average output power. Typically a 14 Hz gating signal is multiplied to the original 10 kHz modulation, and this frequency is used for Lock-in detection along with a Golay cell to detect the output power. The Golay cell has a time constant in the order of milliseconds and therefore the 14 Hz gated signal is detected, and the 10 kHz modulation is averaged as a DC power.

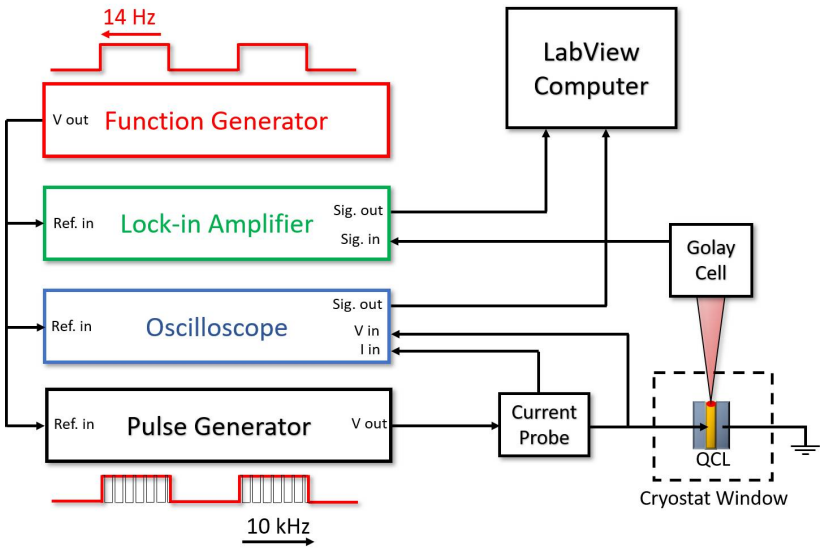

Fig. 1.6 Typical QCL biasing set-up and detection scheme to characterise the output power using a Golay cell.

To characterise the output power and electrical properties of the QCL, a light-output, current, voltage (LIV) measurement is performed which involves sweeping the voltage across the device, and measuring the current drawn from the voltage source, as well as the optical output power. A standard LIV of one of the lasers used is shown in figure (1.7 (a)). As the current is increased from zero the laser remains off until it reaches a current value of 0.6 A, which is referred to as the threshold current, I_{Th}. At this current, the gain from the injected electrons is great enough due to band alignment to match the round trip loss, and the laser begins lasing. As the current is increased further, the output power increases relatively linearly, which is expected due to the greater population inversion achievable. The power reaches a maximum value with a peak power output at 0.9 A, and beyond this current the power starts to drop again. This is due to the bands becoming increasingly misaligned with a sharp drop off in laser power at 1.0 A with lasing ceasing. The voltage current relationship is non linear near 0 V due to the Schottky barrier created between the metal electrodes and doped semiconductor. The voltage current ratio drops slightly as the laser starts to lase, due

to the artificial increase in charge carriers, and there is a sharp increase in voltage when the bands become misaligned at 1 A, due to the destruction of the electron cascade process.

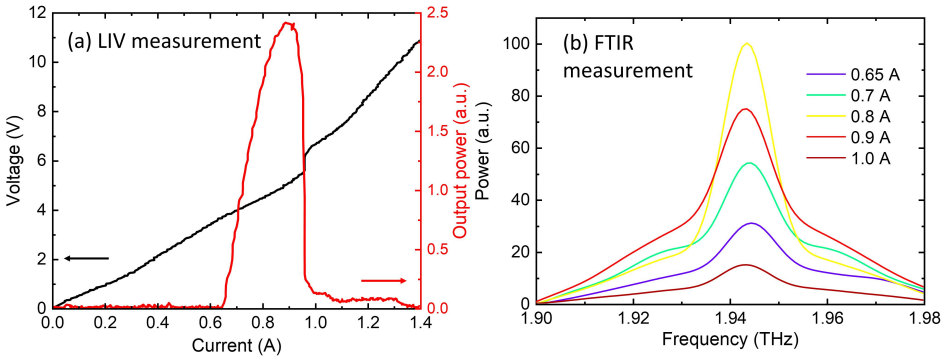

Fig. 1.7 (a) Example LIV of BTC laser. (b) Example FTIR spectrum measurement of the laser output for different operating currents. FTIR resolution 0.25 cm^{-1}. 10 kHz pulsed QCL operation with 5% duty cycle 14 Hz gating for Golay detection.

To characterise the spectral output of the laser, the Golay cell in figure (1.6 is replaces with a Fourier transform infrared interferometer (FTIR), which uses a SiGe 4K bolometer as a detector. This operates using a standard Michelson interferometer architecture to determine the spectrum from the laser. A standard spectral measurement of the laser at different operating currents is shown in figure (1.7 (b)). This laser is operating in one mode throughout the dynamic range, however, due to the Fabry Perot cavity created by the SP waveguide, with a ridge length of between 1 and 4 mm, there are typically many possible laser modes for QCLs spaced by the free spectral range (FSR) of the cavity. QCL mode selection mechanism will be discussed in more detail in chapter 5.

1.3 Comsol simulation

For the purposes of designing the electromagnetic response of active modulator devices presented in this thesis, the RF module of Comsol Multiphysics® v 5.3a is used, which is a commercial finite element method (FEM) based multiphysics software. This simulation tool was used to model the THz optical response of different metamaterial device architectures as a function of incoming plane wave frequency, for the purpose of designing novel metamaterial/graphene devices. This section will look to describe the theoretical framework of the FEM simulation, while also going through the basic method for building a Comsol simulation model.

The Comsol simulation frequency domain model assumes that the fields vary sinusoidally in time at a known angular frequency, and that all material properties respond linearly with respect to field strength. The time varying electric field and magnetic field vectors can be expressed as a function of space and time as follows.

$$\mathbf{E}(x,y,z,t) = \mathbf{E}(x,y,z)e^{j\omega t} \tag{1.1}$$

$$\mathbf{H}(x,y,z,t) = \mathbf{H}(x,y,z)e^{j\omega t} \tag{1.2}$$

To derive the wave equation which is used to determine the electromagnetic response in the simulation, Maxwell-Ampère's and Faraday's laws can be combined, shown in equations (1.3) and (1.4) respectively.

$$\nabla \times \mathbf{H} = \mathbf{J} + \frac{\partial \mathbf{D}}{\partial t} \tag{1.3}$$

$$\nabla \times \mathbf{E} = -\frac{\partial \mathbf{B}}{\partial t} \tag{1.4}$$

The constituent relations for linear materials, $\mathbf{D} = \varepsilon_0 \varepsilon_r \mathbf{E}$ and $\mathbf{B} = \mu_0 \mu_r \mathbf{H}$ as well as the Drude model for electrical conductivity $\mathbf{J} = \sigma \mathbf{E}$, are used to express these equations as a function of $\mathbf{E}$ and $\mathbf{H}$. As the electric field is oscillating sinusoidally, the time varying electric field can be described as, $\frac{\partial \mathbf{E}}{\partial t} = j\omega \mathbf{E}$. Using this relations, equations (1.3) and (1.4) can now be combined to create the governing wave equation for the Comsol simulation, shown in equation (1.5).

$$\nabla \times (\mu_r^{-1} \nabla \times \mathbf{E}) - \frac{\omega^2}{c_0^2}(\varepsilon_r - \frac{j\sigma}{\omega \varepsilon_0})\,\mathbf{E} = 0 \tag{1.5}$$

This equation is used to determine the electric field, $\mathbf{E}$, throughout the structure for different excitation angular frequencies ω. c_0 and ε_0 are the speed of light in a vacuum and the vacuum permittivity, respectively. To describe the electromagnetic response of materials in the simulation, the permeability μ_r, permittivity ε_r, and conductivity σ, are determined throughout the 3D structure. These are all complex values, and the imaginary part of the permittivity and real part of the conductivity have qualitatively equivalent effects in equation (1.5) for a given ω. Conductivity typically refers to current induced by free charges in a material, and imaginary permittivity refers to bound current caused by exciting bound charges with an AC electric field. These two types of current are essentially equivalent to each other in the simulation and therefore it is important not to double count the induced current in the material by defining both an imaginary permittivity and real conductivity when describing a

material. Therefore in this thesis, the permittivity is set to be completely real, and induced currents are fully contained in the value chosen for the conductivity.

To describe the spatial configuration of the materials in a simulated device, three dimensional material regions are determined, with an example unit cell for the standard silicon/SiO_2 substrate used throughout this thesis shown in figure (1.8 (a)). For this simulation, the permittivity and permeability for air are set to 1, with the conductivity set to 0. The SiO_2 layer is assumed to be a perfect dielectric, and therefore the material parameters are the same as air, apart from the permittivity which is set to 3.76. The silicon substrate has a standard permittivity of 11.56, however it is p-doped, resulting in a non-zero conductivity which can be described via the frequency dependent Drude model as follows.

$$\sigma_{AC}(f) = \frac{\sigma_{DC}}{1 + j2\pi f\tau} \tag{1.6}$$

σ_{DC} is taken from the resistivity of the substrate which is 100 Ωcm, and the Drude scattering time, τ, is 10 ps. In this simulation, the electric field at port 1, as illustrated in figure (1.8), is configured to transmit incident radiation with a given angular frequency, ω, and a nominal power of 1 W, with the electric field polarized in the y direction. The measured electric field amplitude in the y direction at port 2 is used to determine the transmitted power through the sample. The area above port 1 and below port 2 are defined as perfectly matched layers (PML), which are used to minimise any reflections from this surface. Floquet, periodic boundary conditions are defined in the x and y directions, simulating an infinite repeating structure in these dimensions. This method is suitable for the simulation of the metamaterial arrays used in this thesis which have 100s of repeating unit cells, allowing for the optical response of these relatively large structures to be simulated efficiently and accurately from a single unit cell.

To determine the electric field throughout the structure, equation (1.5) is solved via the finite element method (FEM) [90]. For this purpose, the continuous structure is split up into discrete domains containing the material parameters, as shown in figure (1.8 (b)). The partial differential equation (1.5) is then discretised to solve the electric field value for the nodes, at the corners of every domain, in relation to the surrounding nodes. The denser the domains, the more accurate the finite approximation of the electric field is. The domains should be roughly no larger than 1/10th of the wavelength, and can be designed to be finer where the electric field gradient is expected to be largest. All other quantities, such as magnetic fields, currents, and power flow, can be derived from the complex electric field, including the S-parameters for the two port configuration. The ratio of transmitted power between port 1 and port 2, $|S_{21}|^2$, and the ratio of reflected power back into port 1, $|S_{11}|^2$, are determined for different incident frequencies, with the results shown in figure (1.8 (c)). The transmission and

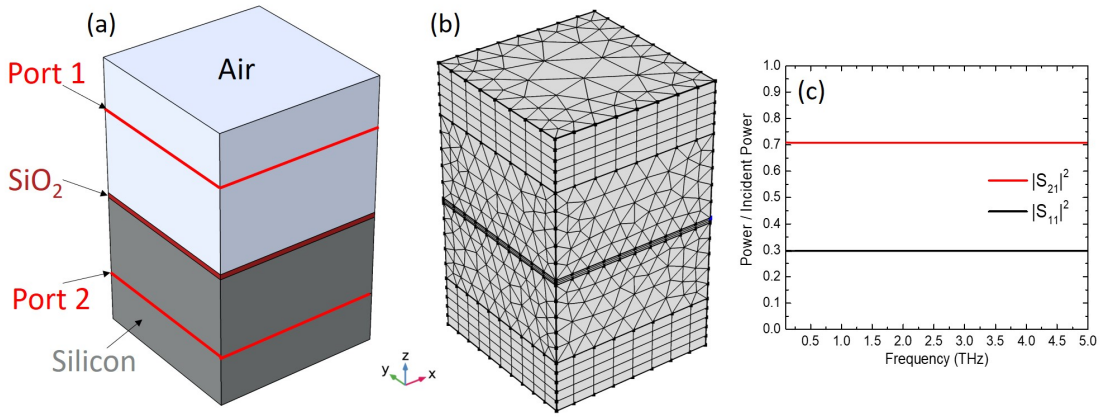

Fig. 1.8 (a) Illustration of 3D simulation model, showing Air, silicon, and SiO_2 regions, and the position of Port 1 and Port 2. (b) Picture of typical meshing of the 3D structure, discretised into separate domain elements. (c) Transmitted power measured by Port 1 and reflected power measured by Port 2 normalised to incident power as a function of frequency.

reflection ratios are flat at around 0.7 and 0.3 respectively, and the loss ratio $1-|S_{11}|^2-|S_{21}|^2$ is negligible due to the low carrier concentration in the substrate. It will be relevant however, to consider the loss when metal resonators and graphene are introduced, due to high ohmic losses.

1.4 External terahertz modulators

Thus far, different THz sources have been discussed which have played a significant role in filling the THz gap, opening many potential research and industrial THz applications. However, it is also essential to have a wide range of THz modular components, capable of electrically controlling the amplitude, frequency, polarization and phase of THz radiation. One can directly modulate the amplitude of a QCL for example [91–93], however, this can lead to frequency chirping, and modulation speeds are ultimately limited by the RC constant of the laser. It is therefore advantageous to use external optoelectronic modular components to modulate the THz radiation externally to the source. Also, due to the complexity involved in building tunable THz sources, it would be ideal to integrate standard sources with a range of external THz modulators to build a tunable THz system. External modulators suffer from a similar THz gap as sources with the radiation frequency being too high for standard microwave modulation devices such as Schottky diodes, and field effect transistors (FET), due to the RC time constant falling off well below the THz region. The photon energy is also too low for the semiconductor bandgap of photonic modulation devices such as band edge absorbers [94]. Novel techniques are therefore required to realise a broad scope of

THz components, and this section will look to describe a range of different fundamental techniques for building such devices.

1.4.1 Photoconductive semiconductor

An effective technique for realizing a THz modulation system is to focus the output radiation from a standard source onto a material which can have its THz transmission and reflection properties varied. Photo-active semiconductors such as silicon can have electron and holes photo-induced to various densities depending on the power of an external incident pump beam, causing a modulation of the THz optical properties of the material [95]. If optically pumped above the bandgap of the material, a dielectric semiconductor material can be converted into a semi-metallic, highly doped semiconductor, drastically altering its optical properties in the THz frequency region. The frequency dependant permittivity of the semiconductor in the THz region, $\varepsilon_r(f)$, can now be expressed as a function of the frequency dependant conductivity caused by the photo-excited charge carriers, $\sigma(f)$, which itself can be estimated to follow a Drude like response as already shown in equation (1.6).

$$\varepsilon_r(f) = \varepsilon_r(\infty) - \frac{j\sigma(f)}{\omega\varepsilon_0} \tag{1.7}$$

$\varepsilon_r(\infty)$ is the high frequency relative permittivity, with ω and ε_0 being the angular frequency of the incident radiation and the permittivity of free space, respectively. The conductivity is typically proportional to the charge carrier density, which for intrinsic semiconductors is very low, resulting in a purely real permittivity, leading to a dielectric response. When optical excitation above the bandgap is applied, the number of free charge carriers can be increased by many orders of magnitude, leading to the permittivity changing to a highly negative and imaginary value. This results in a metallic response for incident frequencies up to the bandgap of the material [95]. This process is illustrated in figure (1.9).

This metallic nature of the material can be controlled by varying the excitation pump power impinging on the substrate, leading to transmission modulation depths of up 100 % [95–97]. A powerful additional tool is the integration of a spatial light modulator (SLM) with the pump beam to selectively switch the material into a metallic form in determined shapes, adding spatially dependent metallic resonant components which can be actively defined [98–101]. The modulation speed of such devices is fundamentally limited by the semiconductor recombination time, which varies drastically between different semiconductors, however, recombination times <400 fs [102] are observed for low temperature GaAs (LT-GaAs) which corresponds to maximum modulation speeds in the THz region. A drawback of this technique

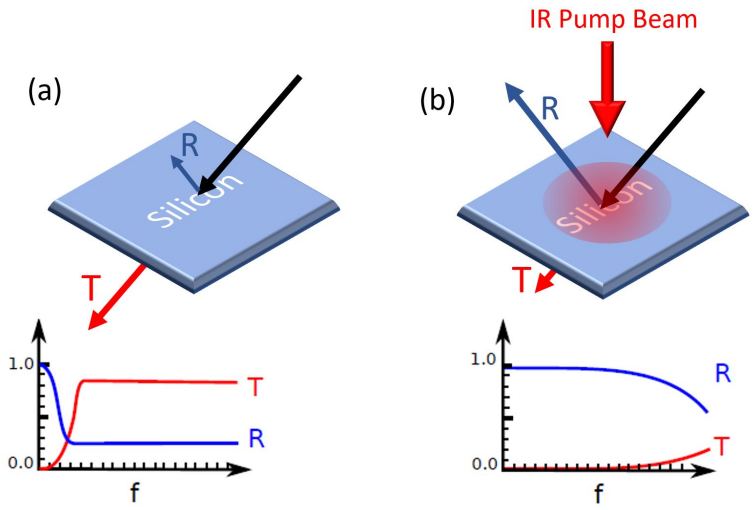

Fig. 1.9 (a) Illustration of typical frequency dependant transmission and reflection parameters in the THz region of standard doped silicon with no photo-induced carriers. (b) Illustration of transmission and reflection parameters of doped silicon with IR optical pump beam exciting electron and hole charge carriers.

is the requirement for an extra optical set-up and ideally a device working purely by electrical modulation with no optical components would be desirable.

1.4.2 Graphene modulators

Graphene is a material which has attracted a large degree of interest for the realization of electrically modulated THz devices [103] due to its unique, tunable electrical properties. Charge carriers in graphene can be optically excited in a similar way as discussed for photo-active silicon [104–109], however, the material characteristics can also be electrically modulated [110] with the concentration of charge carriers in graphene modulated over a large tuning range, with concentrations $> 1 \times 10^{12}\ cm^{-2}$ achievable [111, 112]. To achieve this electrical modulation, electrostatic gating between a doped substrate and the graphene layer, separated with a dielectric, is used to vary the charge carrier concentration in the graphene layer. For devices operating in the THz region, a Drude model, similar to the one used in equation (1.6) can be used to estimate the frequency dependence of the graphene conductivity [113, 110, 114–118]. The transmission and reflection parameters of the graphene layer can be modulated using this technique, giving broadband modulation [110, 119–124, 109] with an example device architecture shown in figure (1.10).

The optical modulation depth of the graphene layer itself is limited as it is optically thin for incoming THz radiation. Typical modulation depths are therefore in the order of a few %

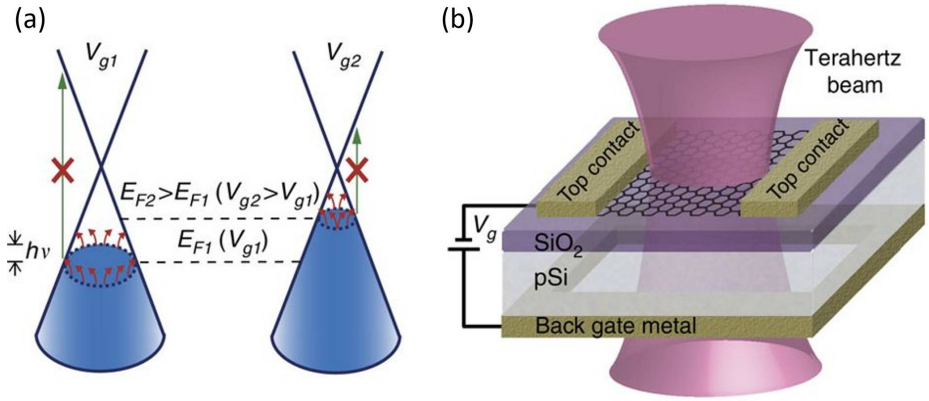

Fig. 1.10 (a) Illustration of intraband absorption of incident THz radiation in a graphene layer for different Fermi levels, with interband absorption prohibited for THz radiation due to the photon energy being too low. (b) Illustration of THz modulator device using graphene backgate electrical conductivity tuning. Figure modified from Ref. [110].

unless the graphene layer is integrated with some other feature. The absorption in graphene can be significantly enhanced by carefully selecting the substrate thickness to include an interference effect [125, 126], and this effect can be employed to enhance the modulation depth of graphene modulator devices [127–129]. Electrically tunable graphene can also be implemented with standard metamaterial structures, to provide versatile, frequency selective modulation effects, greatly enhancing the modulation potential of graphene.

1.4.3 Metamaterial modulators

The term metamaterial refers to a class of artificially produced structures which have electrical and magnetic properties which are not found in naturally occurring bulk materials [130]. Exotic properties such as negative refractive index can be engineered by manipulating the effective permittivity and permeability of the material [131]. This is typically achieved by building sub-wavelength metal arrays of resonator elements, which can be thought of as typical Lorentzian oscillators enabled by the spatial confinement of electrons in the metal array producing an artificial restoring force. This results in the metamaterial layer exhibiting dramatic, highly frequency dependant, optical properties not typically observed in the bulk material. One of the strengths of metamaterials, is that the frequency dependency of the optical response is entirely controllable by lithographically scaling the structure size. Countless metamaterial resonant structures have been demonstrated in the microwave, through to the IR and optical frequencies [132–134].

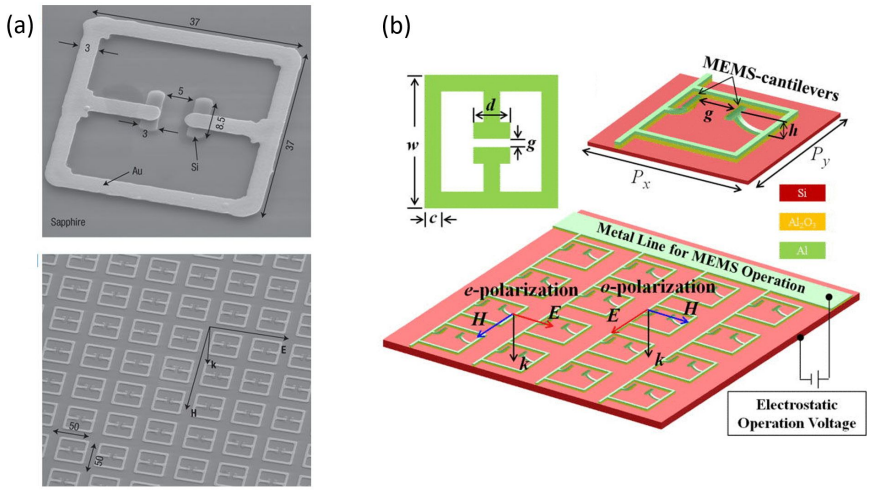

Fig. 1.11 (a) Image of metamaterial device using photoactive silicon forming the capacitor for modulation, taken from Ref. [135] (b) Design of tunable Mems metamaterial device, taken from Ref. [136]

To build a modulator device out of these metamaterial structures, an active component must be built into the metamaterial design to modulate the resonance effect, and hence alter the optical response of the material. One method involves the integration of a photoactive material, such as silicon, discussed in the previous section. The silicon acts as an optically activated switch for current paths in the structure by the variable excitation of a pump beam. Such a device structure is shown in figure (1.11 (a)) which involves a capacitor region in the centre of the unit cell which becomes conductive when the silicon is photo activated, causing a dramatic shift in the resonance frequency of the resonator array. This figure is adapted from Ref. [135], and there are many other examples of similar active metamaterial designs which use photoactive semiconductor materials [137–141]. This is a powerful modulation technique with large modulation depths achievable, but as discussed before, an additional optical set-up is required to use photoactive silicon.

Another effective method for metamaterial modulation is to physically manipulate the shape of the metal structure, using micro mechanical electrical systems (MEMS). An example device is shown in figure (1.11 (b)), which is modified from Ref. [136]. This involves metal cantilevers which change shape when electrostatically charged. When a bias is applied across the backgate of the device in figure (1.11 (b)), the metal cantilever arms are electrostatically attracted to the substrate, and hence move downwards. This dramatically alters the capacitive gap in the center of the metamaterial structure, once again producing a dramatic modification of the metamaterial resonance, resulting in a modulation of the THz optical response of the

device. There are many similar device structures [142–146], however these devices have limitations due to fabrication constraints, and the limited modulation speeds around the kHz region which arise from physically moving components.

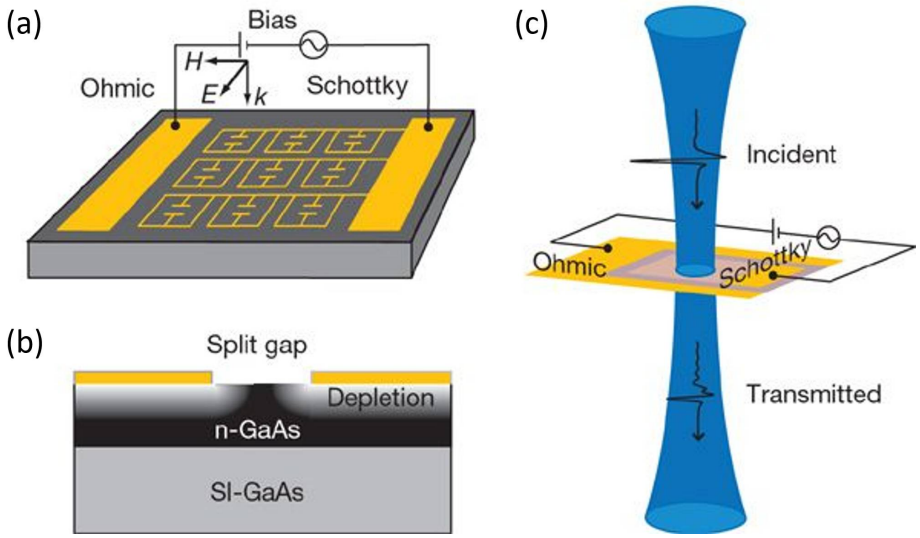

Fig. 1.12 (a) Illustration of device which uses electrical modulation of a Schottky barrier to tune the charge carrier concentration in the local substrate around a resonator array. (b) Side view of substrate and metamaterial. (c) Illustration of THz optical response modulation. Taken from Ref. [147].

The metamaterial structure in a device can also be modulated by varying the conductivity of the surrounding substrate, for example, by making use of the tunable Schottky barrier created between the metal resonators and a doped device substrate [147–151]. The device illustrated in figure (1.12) modulates the size of the depletion region formed due to the Schottky barrier, reducing in size when a forward bias is applied. This increases the charge concentration of the n doped substrate in close proximity to the metamaterial and results in an increased damping of the resonator structure [147]. Conversely, under reverse bias, the depletion region increases and hence the damping is reduced. This Schottky barrier tuning provides a method of electrically tuning the THz optical response of the metamaterial array. Reasonable modulation depths, in the region of 50 % can be achieved [147], however the modulation speed is limited by the RC constant of the Schottky contact with modulation speeds typically limited to a few MHz. A high electron mobility transistor (HEMT) utilizing a tunable two dimensional electron gas (2DEG) can also be used to build electrically tunable THz modulators [152]. In Ref. [1] an amplitude modulation depth of around 33 % was achieved using this technique, and higher modulation speeds are achievable due to the improved mobility of the two dimension electron gas region [153, 154]. However, one

disadvantage of this modulation method is the high fabrication complexity required to build these devices.

In this thesis, Graphene is used as the active tuning element in metamaterial structures. The electrical tuning characteristics of graphene have been discussed, however, graphene is also very easy to integrate with the metamaterial fabrication process, making this material ideal for the electrical tuning of metamaterial structures. There are many demonstrated graphene/metamaterial devices [155–160], with amplitude modulation depths of 60 % achieved [157], and modulation speeds of up to 100 MHz demonstrated [156]. This thesis will look to design novel graphene/metamaterial device architectures using different metamaterial approaches to demonstrate comprehensive electrical control over the amplitude, frequency, phase and polarization of THz radiation.

Chapter 2

Amplitude modulation devices

2.1 Terahertz amplitude modulation overview

Active control over the amplitude of THz radiation is a crucial requirement for any THz device technology, hence the motivation for this chapter is to demonstrate how to design and build a standard high speed graphene/metamaterial amplitude modulator device, whilst laying the groundwork for the more complex devices discussed in later chapters. For THz communication purposes, narrow bandwidth sources are used, and hence the sharp resonant features typical to metamaterial arrays are suitable for engineering a strong tunable THz optical response. Various methods for actively modulating the optical response of metamaterials were discussed in the previous chapter including photoactive semiconductor materials, MEMS systems, and also Schottky and HEMT electrical techniques. Graphene was described as an ideal metamaterial modulation material, as it can be used effectively at room temperature, and due to its large charge carrier concentration tuning range which can be modulated via electrostatic back gating.

There have been a range of graphene integrated metamaterial modulators designed to operate in the far infrared regime [161–163] as well as in the THz region [155, 156, 158, 157, 159, 160]. Modulation speeds in the region of 100 MHz were demonstrated by Jessop et al. in Ref. [156]. The device reported in this reference works by electrically shunting metal dipole antennas in a resonator array using electrically tunable rectangular graphene patches as shown in figure (2.1 (a)). The graphene is electrically contacted through the sharp metal bow tie resonators, which are connected to a source and drain through horizontal biasing lines. Figure (2.1 (b)) illustrates the device performance, which achieves a modulation of the reflected THz power at the metamaterial resonance frequency by applying an electrical modulation across the backgate of the device.

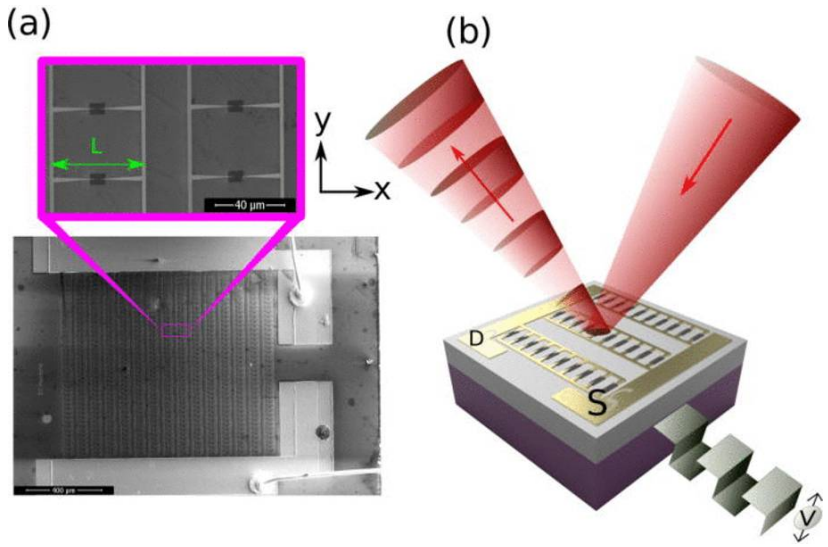

Fig. 2.1 (a) SEM image of full amplitude modulator device and close up of individual graphene loaded bow ties. (b) Illustration of device working principle. Figures taken from Ref. [156]

The work described in this thesis looks to build on this device demonstration by using more complex metamaterial architectures to achieve not only modulation of the THz power, but also modulation of the transmitted polarization and phase, as well as active control of the metamaterial resonance frequency. This chapter will look to outline and describe the method used for designing, fabricating and testing such metamaterial and graphene modulators. An amplitude modulator device will be realized which successfully achieves electrical modulation of the THz transmission amplitude by around 20 %.

2.2 Dipole resonator Array

To introduce the concept of a metamaterial array as well as the Comsol simulation method for designing these structures, a simple metal dipole resonator array is first considered. When excited with incident radiation normal to the surface, which has an electric field polarized along the individual dipole lengths, free charges in the metal will be accelerated in the direction of the incident electric field, leading to an induced current in the antenna. With the resonator length being shorter than the wavelength of incident radiation, a restoring force is created due to the build up of charges at either end of the resonator. This electrostatic restoring force is analogous to the mechanical restoring force on a mass attached to a spring, and hence the oscillation of charges in each dipole antenna can be mathematical described using a simple Lorentz oscillator model [164].

2.2.1 Lorentz oscillator

When the resonators are excited on resonance by the electric field of incident THz radiation, free charge carriers are accelerated in the field. The resultant charge carrier concentration at the ends of each resonator gives an induced electric dipole moment which leads to the metamaterial structure displaying abnormally high polarizability values. This can be mathematically described using the polarization vector, $\vec{P}$ which is dependant on the incident electric field $\vec{E}$, and the electrical susceptibility of the resonator array, $\tilde{\chi}$ according to the following equation.

$$\vec{P} = \varepsilon_0 \tilde{\chi} \vec{E} \tag{2.1}$$

The susceptibility, $\tilde{\chi}$, and resultant induced polarization in the resonator, $\vec{P}$ will be strongly frequency dependant, and can be derived from the time dependant polarizability described in the following Lorentz oscillator equation.

$$\frac{d^2 P_y(\omega)}{d^2 t} + \gamma \frac{dP_y(\omega)}{dt} + \omega_0^2 P_y(\omega) = \frac{Nq^2}{m} E_y \tag{2.2}$$

The driving force comes from the incident electric field polarized in the y direction, E_y, for the example resonator in figure (2.2). A damping term γ describes the ohmic and radiative loss of the metal resonator. ω_0 is the resonance frequency of the dipole antennas, and N describes the free charge carrier density in the metal, with m and q describing the mass and charge of an electron. This equation can be solved for a sinusoidally varying excitation source to determine the complex polarization amplitude as a function of frequency, $\tilde{P}_y(\omega)$, with the result given in equation (2.3).

$$\tilde{P}_y(\omega) \;=\; \frac{Nq^2/m}{(\omega_0^2 - \omega^2) + j\gamma\omega} E_{0y} \tag{2.3}$$

When the angular frequency of the driving electric field matches the resonance frequency of the resonator, ω_0, the induced polarization in the antenna is at a maximum, and completely imaginary, with the amplitude dependant on the damping term. This corresponds to the current in the antenna being completely in phase with the incident driving force, leading to these oscillating dipoles re-radiating electromagnetic waves which destructively interfere with the incident driving THz field, thus resulting in a minimum in transmission and a maximum in reflection. These extreme susceptibility characteristics can be used to build dipole metamaterial arrays, as described in (2.2 (a)), which possess exotic optical properties which can be lithographically tailored to resonate at essentially any required frequency.

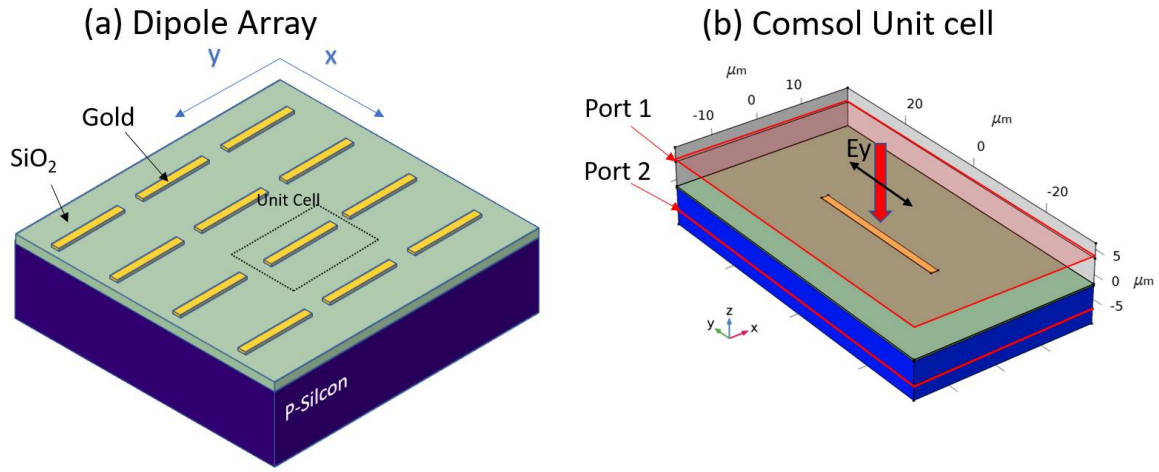

Fig. 2.2 (a) Illustration of dipole resonator metamaterial array on a p-doped silicon substrate with a 300 nm SiO_2 spacer layer. (b) Unit cell used to simulate the dipole resonator array, showing the two ports and different material regions.

2.2.2 Comsol simulation

To simulate the optical properties of the array such as the one illustrated in figure (2.2), a FEM Comsol simulation can be performed, using the base unit cell shown in figure (2.2 (b)). This simulation is identical to the Silicon/SiO_2 substrate simulation shown in chapter 1, however, now there is a gold dipole on top of the SiO_2. The gold thickness is 100 nm, its width is 1.5 μm, and four different dipole lengths, L_{Dipole}, are simulated between 23 and 32 μm. By using repeating boundaries in the x and y dimensions, a quasi-infinite metamaterial array can be simulated from the base unit cell. To ensure there is minimal electromagnetic coupling between the dipoles in the array, a large surrounding area of substrate is used, with a total width of $1.2 \times L_{Dipole}$, and a length of $2.2 \times L_{Dipole}$. To describe the electromagnetic material properties of the gold, the permittivity and permeability material parameters are set to 1. The frequency dependent conductivity $\sigma_{Au,AC}$ is described using a similar Drude model expression as is used for the p-doped silicon, discussed in chapter 1.

$$\tilde{\sigma}_{Au,AC}(f) = \frac{\sigma_{Au,DC}}{1 + j2\pi f \tau_{Au}} \tag{2.4}$$

A gold scattering time, τ_{Au}, of $200fs$ is used [165] and the DC conductivity, $\sigma_{Au,DC}$, of $4.4 \times 10^7 S/m$ is used [166]. Incident radiation is defined at port 1 with a nominal power of 1 W, travelling towards the sample with the electric field polarized in the y direction. The charge carrier concentration induced in the resonators ($L_{Dipole} = 32\mu m$), when excited on resonance ($f = 1.85$ THz), is shown in figure (2.3 (a)). To probe the induced charge carrier polarity and concentration on the surface of the metal, the electric field in the z direction 20 nm above the gold is probed. The electric field at resonance is plotted at the phase where the dipole polarization is maximal, and hence is $\pi/2$ out of phase with the driving electric field.

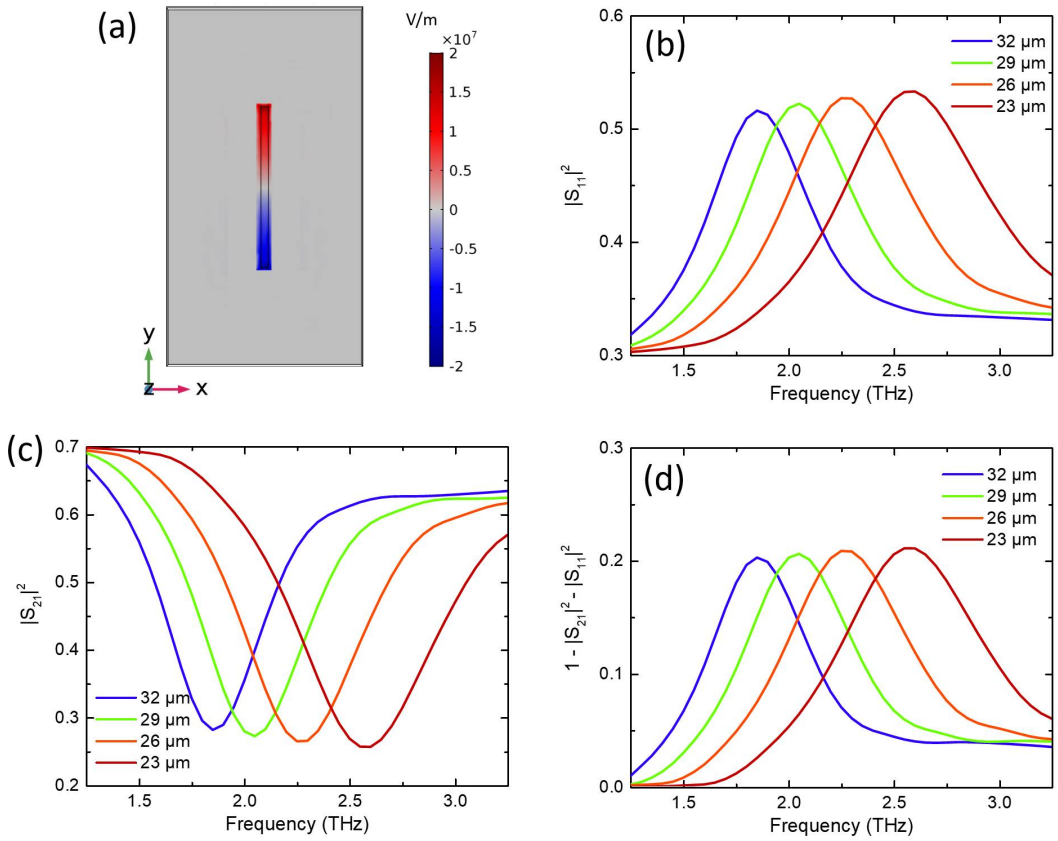

Fig. 2.3 (a) Charge carrier concentration in the dipole resonators probed by measuring the electric field in the z direction 20 nm above the metal. (b) Reflected power, (c) Transmitted power and (d) power loss as a function of frequency for the four different dipole resonator lengths, normalised to the incident power.

The resultant steady state electric field amplitude in the y direction is probed at port 1 and port 2, and compared with the incident electric field to determine the S-parameters for the sample. The reflection from the sample can be probed by measuring the total electric field at port 1, and removing the excitation electric field term. The S-parameter for reflection,

S_{11}, can now be determined by comparing the ratio between the excitation electric field and the reflected electric field. A plot of the reflected power ratio, $|S_{11}|^2$, is shown in figure (2.3 (b)) for 4 different values of L_{Dipole}, and for excitation frequencies between 1.25 and 3.25 THz. At 1.25 THz, none of these resonators are strongly excited, and the reflection is similar to the background substrate reflection ratio of 0.3 in figure (1.8), shown in chapter 1. As the frequency of excitation is increased towards the resonance frequency of the dipole resonators, the induced current and resultant polarizability of the resonator array increases. The metal dipoles in the array act as a radiating dipole antennas, and hence, a larger power is re-radiated in the backwards direction, increasing the $|S_{11}|^2$ term. For the $L_{Dipole} = 32\ \mu$m, the resonance frequency is at around 1.85 THz, corresponding to a reflectivity peak of 0.52. As the excitation frequency is shifted above or below this point, the reflection decreases due to the dipole radiation from the resonator array decreasing in intensity. Crucially, this resonance frequency can be controlled by tuning the length of the dipole antennas, as illustrated by the different dipole lengths in figure (2.3 (b)) . As the dipole length is decreased, the resonance frequency increases, and the resonance wavelength scales essentially linearly with the length of the dipoles.

The transmission power through the sample $|S_{21}|^2$ is probed by measuring the electric field at port 2. At low frequencies, the transmission is close to the value of 0.7 predicted for the substrate in figure (1.8). As the frequency is increased towards the resonance frequency, the transmission decreases, with a minimum value of 0.3 measured at 1.85 THz for $L_{Dipole} = 32\ \mu m$ as shown in figure ((2.3 (c)). The dip in transmission is due to the radiating electric field from the dipole array being π out of phase with the transmitted component of the incident radiation. As a result, these two terms destructively interfere with each other causing a transmission dip at the same frequency as the reflection peak. The proportional loss due to the resonator array can be determined by measuring $1 - |S_{21}|^2 - |S_{11}|^2$, and the result is shown in figure (2.3 (d)). The loss is primarily due to ohmic loss in the gold resonator which is proportional to the induced current in the resonator squared, starting at zero away from resonance at 1.25 THz, and increasing to a peak of around 0.2 at the resonance frequency. The radiation efficiency of the antenna can be determined from the proportion between the power lost due to re-radiation and the power dissipated due to ohmic loss in the metal. This efficiency, as well as resonance amplitude and Q factor, can be controlled by changing the resonator shape, and this will be discussed in more detail later on.

2.2.3 Equivalent circuit model

To describe the dipole resonance condition, it is convenient to build an equivalent LCR circuit model [164, 167] as shown in figure (2.4(a)). The dipole has a self capacitance, C, due to

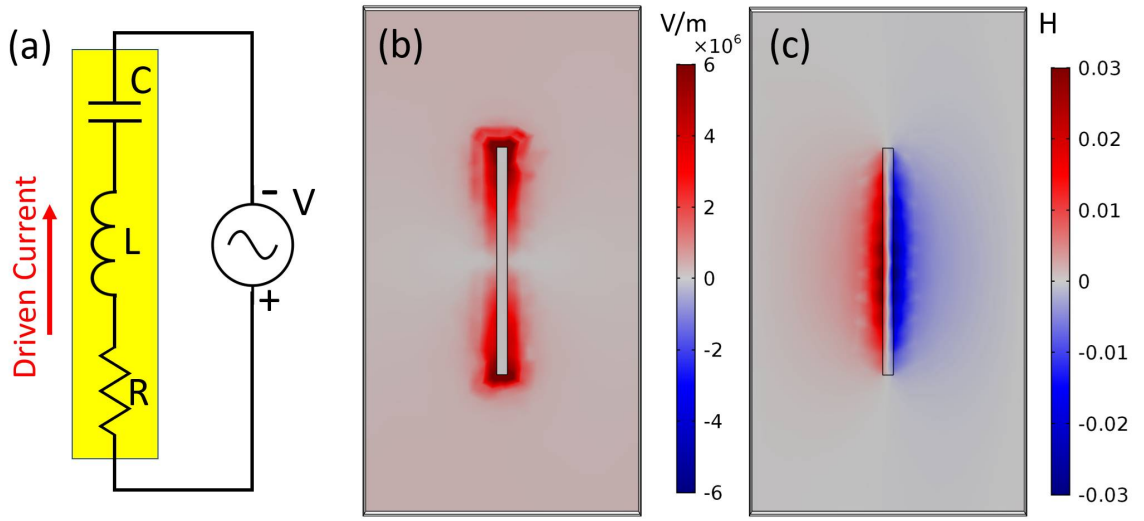

Fig. 2.4 (a) Illustration of equivalent circuit model for the dipole resonator array. (b) Absolute value of the electric field around the dipole antenna at resonance. (c) Magnetic field strength around the dipole antenna at resonance.

the build up of charges at either end of the resonator, with energy stored in the electric field around the dipole as shown in figure (2.4 (b)). The self inductance, L, is due to the magnetic field around the resonator, which stores energy as the current flows, shown in figure (2.4 (c)). The resonator periodically cycles energy stored between the electric field and the magnetic field, with the resistor value R describing the energy lost per cycle from emitting radiation and from ohmic losses in the metal. The voltage source in figure (2.4 (a)) describes the electromotive force of the incident electric field on the electrons, with the induced current, $I = \frac{V}{Z}$ from this driving voltage determined by considering the overall impedance of the circuit as given by the following equation.

$$Z = j\omega L + \frac{j}{\omega C} + R \tag{2.5}$$

For the given circuit model, the resonance condition is met at the angular frequency, ω, where the impedance of the inductor and capacitor cancel out, leading to the complex circuit impedance having a completely real value. The resonant frequency, ω_0, can be determined from the inductance and capacitance values as follows.

$$\omega_0 = \frac{1}{\sqrt{LC}} \tag{2.6}$$

The Q factor of this resonance is defined as the ratio between the energy stored in the reactive components in the circuit and the energy dissipated by the resistive components. This can be determined using the following equation.

$$Q = \frac{1}{R}\sqrt{\frac{L}{C}} \tag{2.7}$$

The Q factor determines sharpness of the resonance in the frequency domain, and can also be determined by dividing the resonant angular frequency ω_0 with the width at half maximum $\Delta\omega$ of the current squared .

$$Q = \frac{\omega_0}{\Delta\omega} \tag{2.8}$$

To determine the self capacitance value, C, for the dipole antennas, the charges collected in the upper half of the resonator, q, is probed in the Comsol simulation shown in figure (2.3(a)), and compared to the voltage between each end of the resonator, with the capacitance estimated using the equation $C = \frac{q}{V}$. To determine the self inductance, the average current distribution in the antenna, I is probed in the Comsol simulation, and the magnetic flux, Φ is measured by integrating the magnetic field in the z direction across the right half of the unit cell. The resultant inductance is estimated using the following equation, $L = \frac{\Phi}{I}$. To determine the resistive loss for the circuit model, the Q factor of the circuit is first determined, by probing the current squared in the resonator as function of frequency in the Comsol simulation. The Q factor value is first determined using equation (2.8), with resistance estimated using equation (2.7), including the predetermined inductance and capacitance values. To compare the circuit model with the simulated results, the complex impedance as a function of frequency, Z, is determined using equation (2.6), to describe the induced current as a function of voltage. The time averaged power drawn from the voltage source, P_{Drawn} can then be determined using equation (2.9).

$$P_{Drawn} = 1/2\ \mathbf{Re}(VI^*) \tag{2.9}$$

This quantity is important, as the ratio of the power drawn and the incident power, $\frac{P_{Drawn}}{P_{Inc}}$, is equal to $|1-|S_{21}|^2|$ [168]. This assumes that when no power is drawn, the transmission power ratio $|S_{21}|^2$ is equal to 1, however, due to the inclusion of a substrate we know that this term should be relatively flat at $|S_{21}|^2_{Sub} = 0.7$, according to figure (1.8) in chapter 1, and therefore the equation is modified as follows.

$$\frac{P_{Drawn}}{P_{Inc}} = |S_{21}|^2_{Sub} - |S_{21}|^2 \tag{2.10}$$

To determine the ratio of the power drawn compared to the incident power, the driving voltage across the dipole resonator is adjusted so the peak current drawn in the circuit matches the Comsol simulation value. This voltage is used to scale the power drawn in equation (2.9) according to the nominal 1 W excitation power used in the Comsol simulation. To convert the power drawn value into a ratio, it is therefore divided by 1 W, and the transmitted power through the sample, $|S_{21}|^2$, can now be determined by rearranging equation (2.10) as follows.

$$|S_{21}|^2 = |S_{21}|^2_{Sub} - \frac{P_{Drawn}}{P_{Inc}} \tag{2.11}$$

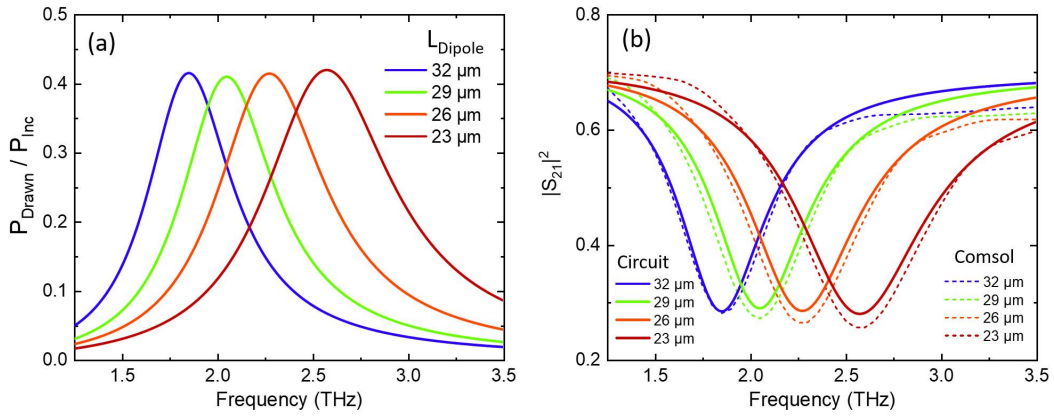

Fig. 2.5 (a) Equivalent circuit simulation results for ratio for power drawn vs incident power. (b) Comparison of equivalent circuit model simulated transmission vs Comsol results.

$\mathbf{L_{Dipole}}$ (μm)	L $\times 10^{-11}$ (H)	C $\times 10^{-16}$ (F)	R (Ω)
32	2.24	3.30	77
29	2.08	2.90	78
26	1.85	2.65	81
23	1.56	2.45	80

Table 2.1 Derived equivalent circuit model values for four different dipole lengths.

This equation is now used to plot the transmission through the sample predicted from this circuit model representation. Table (2.1) shows the derived circuit parameters for 4 different dipole lengths, with the capacitance and inductance increasing with length due to the greater number of charges which can be held for a given voltage, and the larger total magnetic field produced for a given current. Figure (2.5 (a)) shows the circuit model derived value for $\frac{P_{Drawn}}{P_{Inc}}$ as a function of frequency using the derived circuit parameters for the 4 different dipole lengths. The transmission determined from the circuit model is now compared with the

simulated S parameters from the Comsol equation in figure (2.5 (b)). The capacitance values have been adjusted by a few percent compared to the initial estimated values to match the resonance frequency position with the Comsol simulation data. The main difference between the Comsol and circuit model simulations is that when the frequency is increased above the resonant frequency, the Comsol simulation does not increase back to 0.7 and the circuit model simulation does. This is most probably due to high order resonance modes which are not considered in the simple circuit model simulation.

2.3 Split ring resonator

To alter optical properties such as the Q factor of the metamaterial resonance condition, an endless range of resonator types can be used in the metamaterial unit cell. A popular resonator design is the electrically excited split ring resonator, e-SRR. Typical split ring resonators consist of circular of metal resonator with a gap in the middle, and are excited by the magnetic field of incident radiation. The electrically excited SRR is a modified version of this with two SRRs connected back to back, allowing for the resonators to be excited via the electric field in the E_y direction, and can therefore be excited by radiation propagating parallel to the substrate norm.

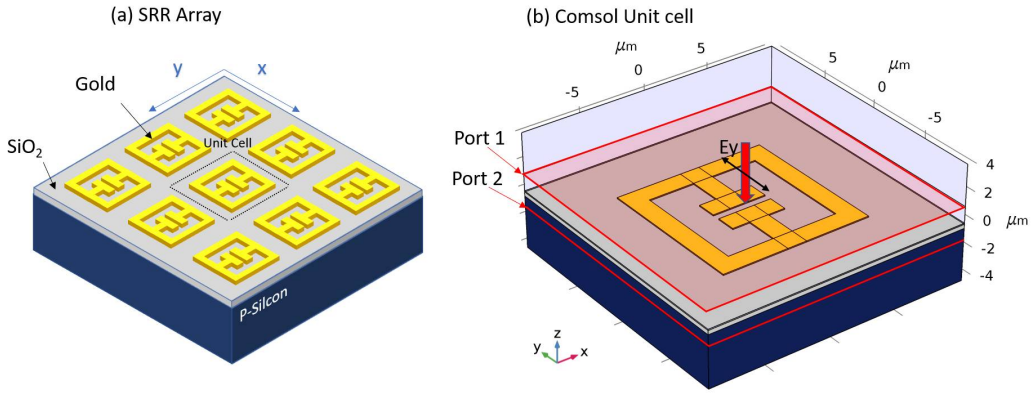

Fig. 2.6 (a) Illustration of SRR metamaterial array. (b) Comsol unit cell for SRR array excited by radiation propagating normal to the surface with electric field polarized in the z direction.

2.3.1 Comsol simulation

An example SRR array which is excited by the electric field of incident radiation is illustrated in figure (2.6 (a)), and the equivalent simulation unit cell is shown in figure (2.6 (b)). This simulation is set up in the same way as was done for figure (2.2), with incident radiation propagating normal to the surface and with the electric field polarized in the y direction. The unit cell dimensions used for the simulation are shown in figure (2.7 (a)), initially using a 'Scale' value of 0.72. The resultant charge carrier distribution is shown in figure (2.7 (b)) when excited with a resonant frequency of 2.85 THz. This is an LC resonance, with charges excited in the outside arms and circulating around the resonator before concentrating across the capacitive gap. This resonance frequency is dependent on the capacitive gap size, the width of the metal lines, and the length of the current path from one side of the capacitor to the other.

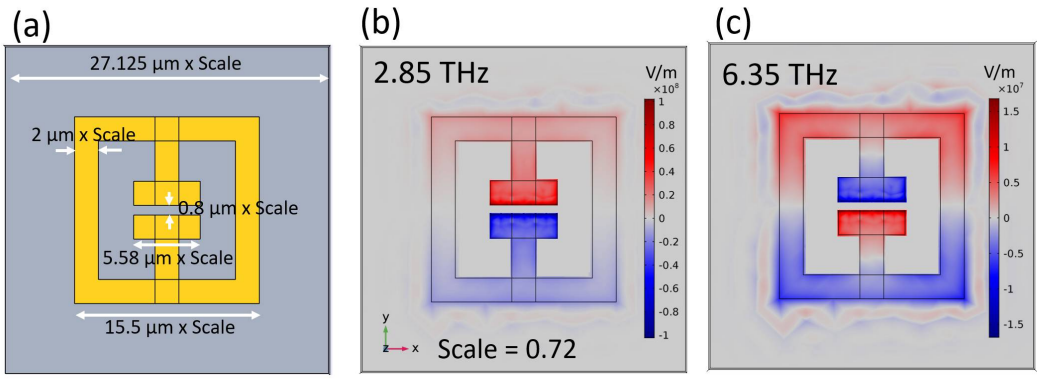

Fig. 2.7 (a) Dimensions of SRR unit cell. Illustration of charge carrier concentration in the SRR when excited at the (b) LC resonance frequency and (c) dipole resonance frequency.

There is a higher order resonance at 6.35 THz, shown in figure (2.7 (c)). This is essentially a dipole resonance, with charges collecting at the top and bottom of the resonator. The dipole resonance wavelength is therefore dependant on the length of the side of the resonator which leads to a resonance frequency which is more than double the LC resonance. The resultant S parameters for 4 different scale sizes are shown in figure (2.8). According to the $|S_{11}|^2$ graph, there is a clear resonance, corresponding to a maximum in reflection at 2.85 THz for a scale value of 0.72. As the scale is reduced to 0.54 the resonance frequency increases to 3.85 THz. This effect is mirrored in the transmission graph in figure (2.8 (b)), with the transmission going to zero at the resonance frequency. There is also a peak in the loss at resonance, shown in figure (2.8 (c)). The dipole resonance is observed in these figures as the much broader peak above 4 THz. The LC resonance is much sharper due to the radiating dipole moment being smaller, leading to a greater Q factor. Due to this higher Q factor

and greater lithographic tuning control, the SRR LC resonance will be considered for the purposes of amplitude modulation.

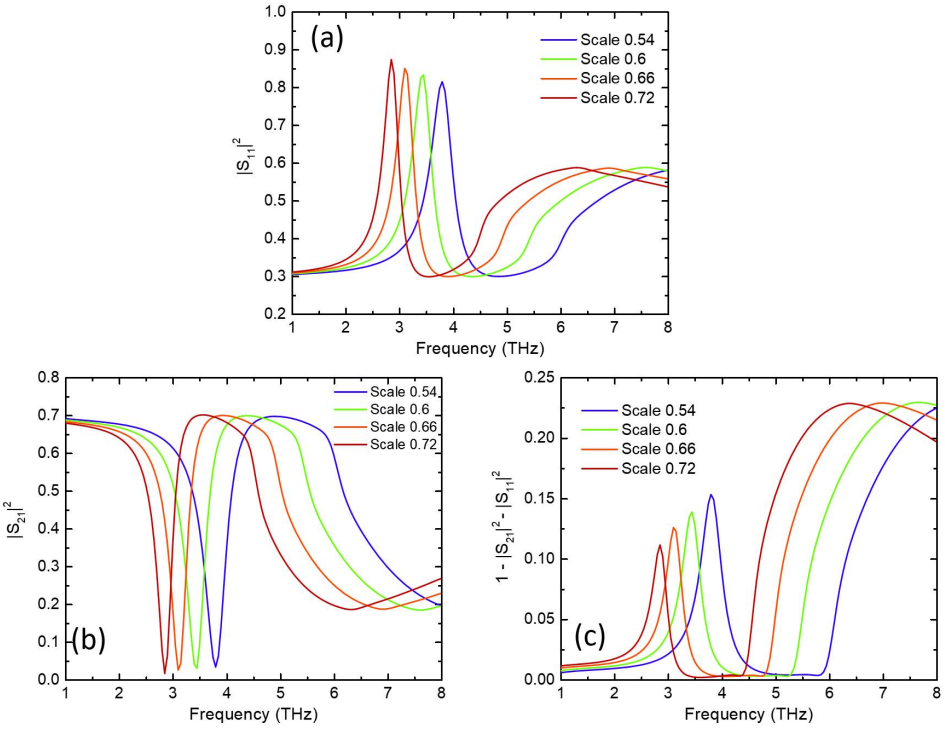

Fig. 2.8 (a) Simulated reflection (b) transmission (c) and loss, from SRR array as a function of frequency for 4 different scale values.

2.3.2 Equivalent circuit model

To understand this resonance condition further, an effective equivalent circuit model can be built as illustrated in figure (2.9 (a)). The impedance of the circuit can be described in a similar way as the case for the dipole resonator, however there are now two inductive paths in parallel.

$$Z = \frac{j\omega L}{2} + \frac{j}{\omega C} + R \tag{2.12}$$

The resonance frequency and the Q factor of the circuit can be determined using the following equations.

$$\omega_0 = \sqrt{\frac{2}{LC}} \tag{2.13}$$

$$Q = \frac{1}{R}\sqrt{\frac{L}{2C}} \tag{2.14}$$

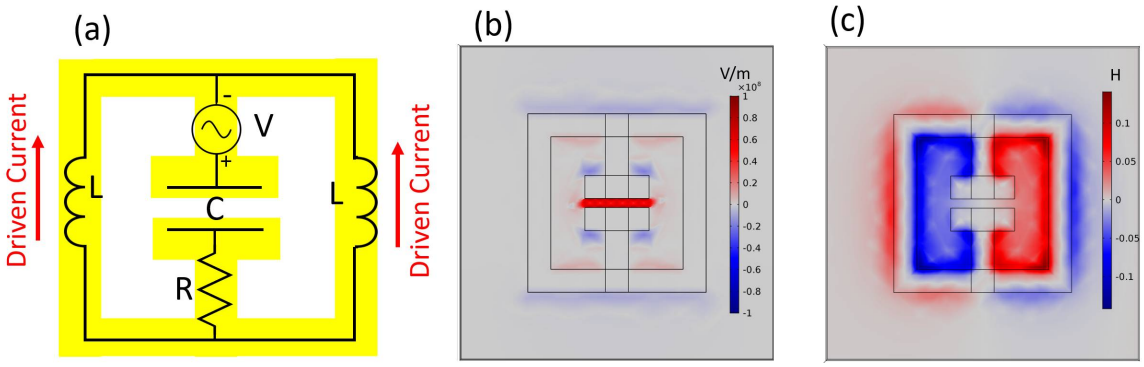

Fig. 2.9 (a) Equivalent circuit model for SRR metamaterial. (b) Comsol simulation of electric field at resonance in the plane of the SRR. (c) Comsol simulation of magnetic field at resonance.

As with the dipole resonator case, the Comsol simulation is used to estimate the self inductance, L, capacitance, C, and resistance, R. The capacitance is estimated by plotting the electric field in the capacitive gap, as shown in figure (2.9 (b)) and comparing this to the charge carrier distribution determined from figure (2.7 (b)). To estimate the inductance, L, the average current flowing in one of the resonator loops is determined and compared to the magnetic flux through as simulated in figure (2.9 (c)). The Q factor can be determined from the power lost as a function of frequency graph shown in figure (2.8 (c)), along with equation (2.8). The value for resistance is then determined from equation (2.14). With the parameters determined for each scale value, the resonance frequency is checked using equation (2.13), and the estimated value for capacitance is adjusted accordingly to ensure the resonant frequency matches. The resultant values are shown in table (2.2). The power drawn from the circuit voltage source as a function of input power is simulated using the same method used for the dipole resonator array. As with the dipole resonator array, this value can then be used to predict the resultant transmission as a function of frequency. The circuit model simulated power drawn and transmission for the SRR array are shown in figures (2.10 (a) and (b)). The Comsol transmission results are included for comparison.

The Comsol and circuit model simulations match up well, as shown in figure (2.10 (b)). The shape of the Comsol simulated transmission for each scale around the resonance peak is slightly different however. This is because the higher order dipole resonance conditions are not contained in the simple circuit model, therefore effecting the circuit model simulated transmission shape, especially at higher frequencies. The low frequency disagreement

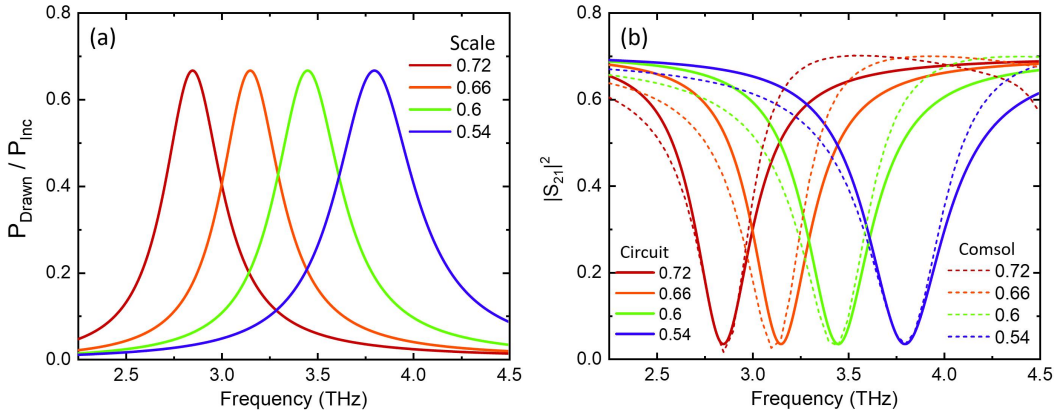

Fig. 2.10 (a) Circuit model simulated power drawn as a function incident power for SRR array. (b) Circuit model simulated and Comsol simulated transmission as a function of frequency and scale.

Scale	L $\times 10^{-12}$ (H)	C $\times$ 10^{-16} (F)	R (Ω)
0.72	6.5	9.60	7.2
0.66	6.3	8.10	7.5
0.6	5.7	7.49	7.2
0.54	4.8	7.31	7.5

Table 2.2 Derived equivalent circuit model values for four different SRR scales.

could be due to the frequency dependent material parameters which are not included in the equivalent circuit model.

2.3.3 Fabrication

With the principles behind the SRR array structure understood, a device is now fabricated using the same lithographic tuning parameters which were simulated using Comsol and the equivalent circuit model. As discussed in the introductory section, 500 μm thick p-doped silicon substrates with an insulating 300 nm SiO_2 layer on top is used to fabricate these devices. The boron doped silicon has a conductivity of 100 Ωm and is cleaved into 2x2 cm areas, and a layer of double layer PMMA e-beam resist is deposited onto the substrate via spin coating. The SRR patterns are designed in a 2D cad file, which is used to write the E-beam pattern. The exposed resist is removed using a developer which consists of MBIK:MEK:IPA with ratios of 1:5:15. The metal resonator structure is then deposited through the resist gaps using a thermal evaporator, with a 10 nm Ti adhesive layer first deposited, and then 80 nm of

Au on top. The sample is then soaked in acetone overnight to remove the resist. This process is illustrated in figure (2.11 (a)), and an SEM of the resultant structure is shown in figure (2.11 (b)).

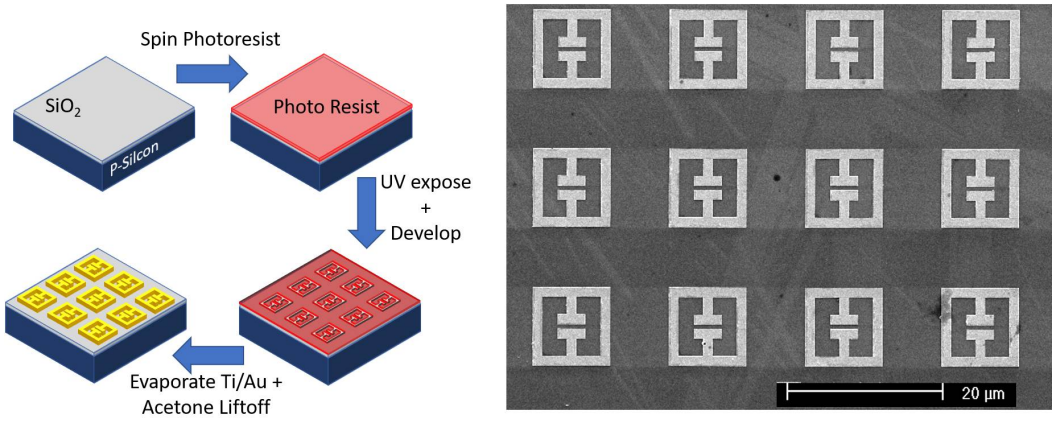

Fig. 2.11 Illustration of Procedure for fabricating metal resonator arrays and SEM of fabricated SRRs.

2.3.4 Time domain spectroscopy results

To test the frequency dependant transmission through the fabricated device the Menlo K15 TDS set-up is used. The operation and working principle for the TDS set-up is described in detail in chapter 1, with the experimental set-up described in figure (1.1). The sample is placed in the beam path at the focus which has a beam width of around 1 mm for low frequencies and a width of around 200 μm for frequencies above 2 THz. An x/y stage is used to scan the sample in the focus using 100 μm steps. The device cad design, showing the four SRR areas is shown in figure (2.12 (a)) and a corresponding TDS image is shown in figure (2.12 (b)). For the TDS plot, the maximum electric field is plotted, after a post processing filter is applied to remove frequency components below 2 THz. This reduces the spot size from 1 mm to 200 μm allowing for the four 1 mm^2 areas to be resolved. The four areas, and the scale associated with each area, are shown. The transmission through the SRR areas are less than the surrounding substrate, and the transmission is minimal over the metal bond pad areas, which are used for when graphene is included in devices such as this.

With the position of the four areas determined in the 2D scan, a long integration time TDS measurement is performed for each of the four areas. An example of the time domain signal measured when passing through a SRR area is shown in figure (2.13 (a)) and is compared with the time domain signal when no device is present. The time domain signal through the sample contains repeat pulses with a detector current peaking at 0.4, 12 ps after the initial

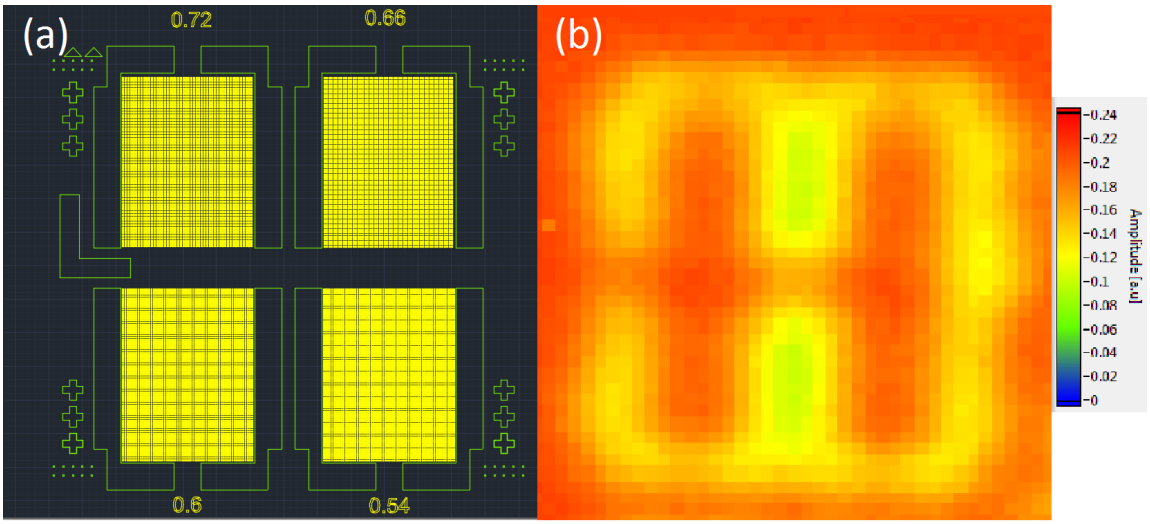

Fig. 2.12 (a) 2D cad of the 4 SRR arrays. (b) TDS x/y scan through the metamaterial array.

pulse. A further repeat pulse, with a detector current peak of 0.1, is present 24 ps after the initial pulse. These extra pulses are due to internal reflections in the substrate, which is around 500 μm thick. The increased effective path length through the silicon for the internal reflections leads to the 12 ps and 24 ps time delay for the second and third pulses respectively. If these peaks are contained in the Fourier Transform conversion from the time domain to the frequency domain, the Fabry Perot effect of the substrate will be shown. To isolate the transmissive properties of the metamaterial, and to negate the Fabry Perot effect of the substrate, a cosine filter is multiplied to the signal, as shown in figure (2.13 (a)). The resultant transmitted power as a function of frequency through the four different SRR scale areas is shown in figure (2.13 (b)), and compared with the reference power when no sample is present.

To determine the S-parameters for transmitted power, $|S_{21}|^2$, the power through the SRR areas is divided by the reference power. The resultant transmitted power ratio as a function of frequency for the four scale areas is shown in figure (2.14) and compared with the equivalent Comsol simulations. For all of the areas, the TDS measured transmission ratio is around 0.5 at 2 THz which corresponds well to the simulated transmission through the whole substrate, without including the Fabry Perot effect. As the frequency is increased, the resonance features of the SRRs begin to reduce the transmitted power causing a minimum at the resonance frequency for each area. The resonant frequency for scale 0.72 is 2.95 THz, which is 100 GHz higher than expected in the Comsol simulation. As the scale is decreased to 0.54, the resonant frequency of the TDS results is measured at around 3.95 THz, compared to the simulated resonance frequency of 3.8 THz. This shows that the resonant frequency is

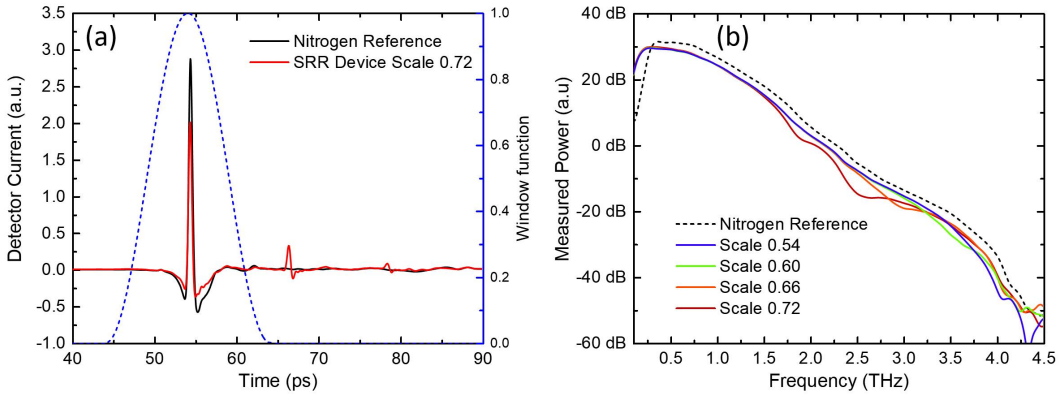

Fig. 2.13 (a) Time domain data of THz pulse passing through the 0.72 scale SRR area compared to passing through nitrogen. The cosine filter is also shown. (b) Frequency domain data for the pulse after passing through 4 different SRR areas, and compared to the data when no sample is present.

consistently off by less than 4 percent, and is most likely due to inconsistencies in substrate permittivity and gold conductivity between the simulation and real sample. The 10 nm titanium layer is not included in the simulation, and therefore this could also explain the frequency offset. A further reason for this discrepancy could be the fact that the simulation uses plane waves, however the TDS uses a focused beam.

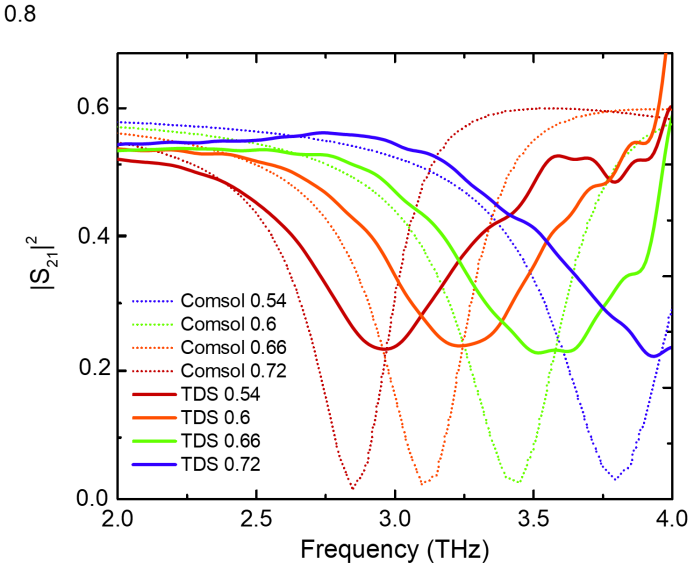

Fig. 2.14 TDS transmission data normalised to transmission through nitrogen for four different scale values. TDS data is compared to Comsol simulation data.

Another difference between the simulation and result is the absolute value of transmission at the resonance frequency. The minimum transmission measured in the TDS data is around 0.2 for all four areas, compared to the simulation which predicts transmission values of less than 0.05 at the resonance frequency. One reason for this could be the spot size in the TDS set-up is larger than expected, allowing power to be transmitted around the $1mm^2$ areas. Although 200 μm features can be defined using the 2D scan, a dummy sample with identically shaped $1mm^2$ areas of thick opaque gold is used to test how much of the incident pulse power leaked around the area. Using this dummy sample, around 10 percent of the incident spot is transmitted when the spot is aligned to the centre of the opaque gold square. This would account for some of the discrepancies between the minimum transmitted power between the simulation and results. An additional reason for this could be that the full sample area is not completely pristine, with some areas not being lifted off correctly, and there could also be discrepancies in the thickness of gold between simulation and result. Apart from these discrepancies, the functional form and trend with changing scale show remarkable agreement between the fabricated sample results and simulation, and the known frequency shift can be accounted for when performing simulations for further devices.

2.4 Electrostatic gating of graphene

The devices discussed thus far have been made up of gold resonator arrays deposited onto a substrate, which display strong lithographically tunable resonance features in the THz region. The next step is to include an electrical tunable material into the device structure to manipulate this resonance condition in a controllable way. For this purpose, graphene is integrated into the resonator array due to its unique, tunable electrical properties which were discussed in chapter 1.

2.4.1 Graphene CVD fabrication

The graphene integrated into the metamaterial devices described in this thesis is grown using chemical vapour deposition (CVD). The graphene is grown by Phillip Braeuninger-Weimer in Stephan Hofmann's group, based in the electrical engineering division at Cambridge, who specializes in this technique [169]. This process uses a methane gas flow which passes by a heated copper catalyst where the graphene flakes self assemble. The copper is then etched away in HCL leaving a graphene film which is transferred onto the Si/SiO_2 substrate used to build the metamaterial array. To convert this static sheet of graphene on the substrate into an electrically tunable medium, the fabrication method described in figure (2.15) is used.

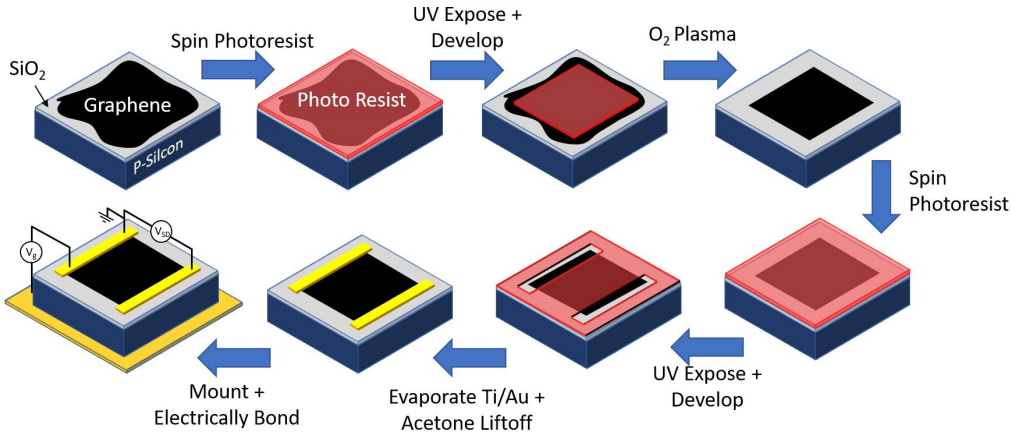

Fig. 2.15 Illustration of fabrication process to create a graphene patch which can be electrostatic backgated.

1813 Shipley Photoresist is first used to define the desired shape for the electrically tunable graphene patch. The resist is spin coated and baked at 120 degrees before a a photomask is used to excite the regions where graphene is not required. After developing using MF-319, the unwanted graphene is left exposed, and is removed using an O2 plasma asher for 1 minute. The rest of the resist is then washed off using acetone, leaving the desired graphene patch. A second photo-resist procedure is performed to define the metal bond pads. This time a photomask is used which exposes the shape for the gold bond pads. After development, the metal pads are formed using the thermal evaporator giving a 10 nm titanium adhesion layer, followed by a 100 nm gold layer. The device is then mounted on a chip carrier with a gold back, using silver paste for physical and electrical contact between the carrier and the p-doped substrate. The gold source and drain bond pads are then independently electrically contacted on different pins of the chip carrier. By mounting the substrate in the chip carrier in this way, it is now possible to apply different electrical biases on the two bond pads as well as to the p-doped substrate.

2.4.2 Electrical properties

The device is now configured to electrically tune the graphene conductivity. This is performed by applying a voltage between the metal bond pads and the back p-doped substrate, as the graphene and p-doped silicon are essentially a capacitor, with the 300 nm SiO_2 layer acting as a dielectric spacer. The induced surface charge carrier concentration in the graphene, n, from an applied backgate voltage, V_g, can be estimated using the standard parallel plate capacitor equation.

$$n = \frac{\varepsilon_0 \varepsilon_r V_g}{te} = \alpha V_g \tag{2.15}$$

ε_0, $\varepsilon_r V_g$, t, and e represent the permittivity of free space, the relative permittivity of the SiO_2 (3.9), the thickness of the SiO_2 layer (300 nm) and the fundamental charge of an electron respectively. This shows that the extra surface charge induced in the graphene layer is proportional to the backgate voltage, with a proportionality constant defined as α. If the graphene is initially doped however, there will be an excess of free charge carries already present in the graphene sheet before backgate biasing, and therefore the free charge carrier concentration equation can be adjusted using an offset voltage term, V_{Dirac}.

$$n = \alpha(V_g - V_{Dirac}) \tag{2.16}$$

V_{Dirac} is the voltage where the doping charge carriers are cancelled out by the induced charge carriers from V_g, and hence indicate the voltage where the free charge carrier concentration, and hence conductivity of the graphene sheet is minimal. The Drude model can be used to describe the sheet conductivity of the graphene as a function of free charge carrier concentration using the following equation.

$$\sigma(V_g) = n(V_g) e \mu \tag{2.17}$$

μ is the mobility of the charges which can be determined from the average scattering time, τ, Fermi velocity, v_F and the Fermi energy, E_F using the following equation.

$$\mu = \frac{e\tau(E_F){v_F}^2}{E_F} \tag{2.18}$$

E_F and v_F are used instead of the effective mass, as this value is poorly defined near the Dirac point given the linear dispersion relation for graphene, as described in the following equation.

$$E(k) = \pm \hbar v_f \sqrt{{K_x}^2 + {K_y}^2} \tag{2.19}$$

Due to the typical graphene Dirac cone dispersion relation, the Fermi velocity of the carriers is relatively constant for energies close to the Dirac Fermi energy. If the scattering time remains constant as the Fermi energy increases, the mobility will reduce according to equation 2.18. However, depending on the dominant scattering effect, τ can also be strongly dependent on E_F. If the main scattering mechanism is from stationary charged impurities, as the number of free charge carriers increases there will more effectively screening from these impurities, causing an increase in τ with respect to E_F. In this case, the mobility can remain

relatively constant as the Fermi energy is increased, leading to a linear increase in graphene conductivity with backgate voltage. Conversely, scattering from non-charged impurities should not be dependent on E_F, and this scattering effect would become more dominant for large E_F values. This can lead to the increase in conductivity becoming non-linear and leveling off as the backgate voltage is increased far away from the Dirac point.

To test the conductivity of a graphene sheet as a function of backgate voltage, the resistance between the source and drain is determined by measuring the voltage required to maintain a 5 mA current across the graphene patch. This resistance is measured as a function of DC voltage across the backgate, applied between the p-doped silicon substrate and the drain, with the drain connected to ground. The sheet conductivity is then inferred from this value, taking into account the dimensions of the graphene patch. The resultant DC sheet conductivity as a function of backgate voltage for a standard graphene sample is shown in figure (2.16).

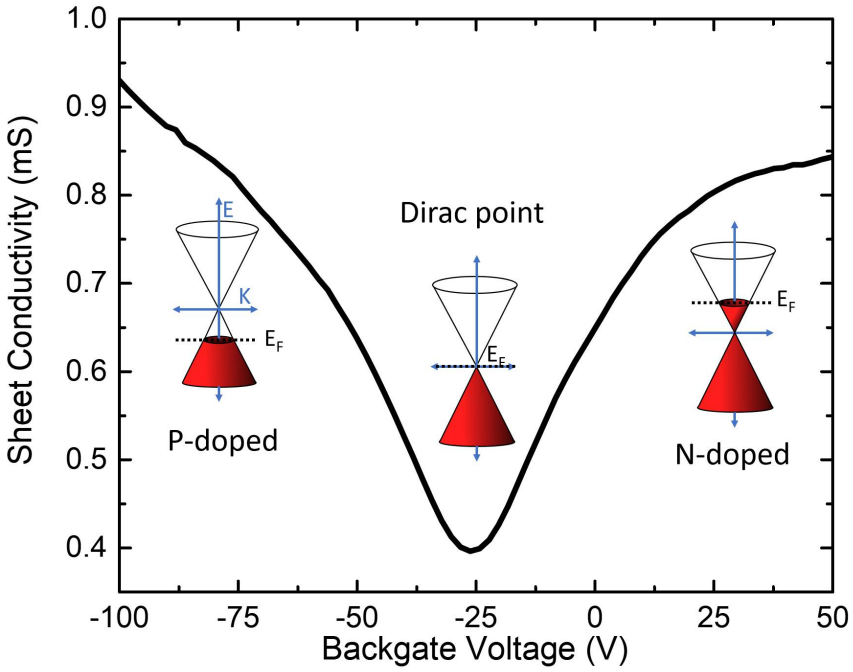

Fig. 2.16 Graphene sheet conductivity measurement as a function of backgate voltage.

The graphene used in this experiment appears to be n-doped, as the Dirac point is at -25 V. At this voltage the excess negative charge carriers doping the graphene have been removed, leaving the sheet positively charged but with minimal free charge carriers. As the voltage is

decreased below -25 V, further electrons are removed from the graphene leaving positively charged holes. In the Dirac cone illustration, the Fermi energy reduced from the Dirac point making room for free holes in the valence band. This causes the conductivity to increase towards 0.9 mS, with the gradient of this increase reducing further from the Dirac point, due to a reduction in mobility as the Fermi energy moves further from the Dirac point. There is also an increase in conductivity as the backgate voltage is increased from -25 V to +50 V with free electrons being drawn into the graphene as Fermi energy increasing above the Dirac point. The gradient near the of the conductivity increase is similar when compared to the p-doping regime near the Dirac point, indicating a similar mobility for the electron and hole carriers. As the voltage is increased towards +50 V, the mobility reduces more dramatically than for the hole case however, with a maximum sheet conductivity of 0.8 mS measured at +50 V.

2.4.3 Comsol simulation

Now that a successful demonstration of electrical tuning of graphene has been established, the Comsol simulation is modified to include graphene in the model. A single layer of graphene would be too thin to include in the FEM simulation, therefore a layer with nominal thickness of 14 nm is used, and the bulk conductivity is scaled appropriately to give the same value for sheet conductivity. This layer is still optically thin, and therefore, despite being several orders of magnitude thicker than the single layer of graphene, the effect on the incident electromagnetic radiation should be the same. The standard Drude model is used to describe the AC conductivity of the graphene as a function of the measured DC conductivity value. The Drude approximation breaks down in the infrared where interband absorption is observed, however, it is only intraband absorption which needs to be considered in the THz region, and hence a Drude approximation based on free charge carriers in the valence or conduction band is valid. The frequency dependant bulk complex conductivity for graphene, $\sigma_{(Bulk,\ AC)}$ is described in equation (2.20).

$$\sigma_{(Bulk,\ AC)} = \frac{\sigma_{(sheet,\ DC)}}{t_{Grap}} \frac{1}{1 + i2\pi f\tau} \tag{2.20}$$

The DC sheet conductivity, $\sigma_{(Sheet,\ DC)}$, is described using equation (2.17), with the conductivity range experimentally measured as shown in figure (2.16). t_{Grap} is the nominal thickness of the graphene layer used in the simulation, with a value of 14 nm typically chosen. f is the frequency of the THz radiation, and τ is the scattering time for the graphene, which is assumed to be constant for all conductivity values for simplicity. The graphene layer is included in the simulation as shown in figure (2.17 (a)).

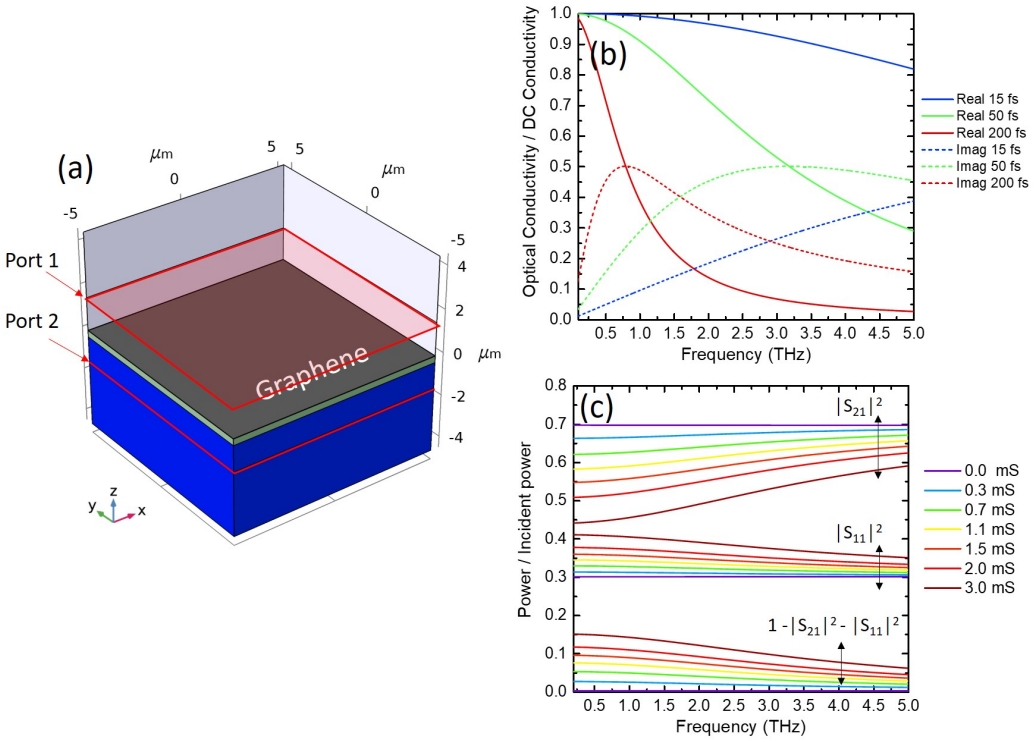

Fig. 2.17 (a) Unit cell of substrate for Comsol simulation including graphene layer. (b) Optical conductivity divided by DC conductivity as a function of frequency for three different scattering times for graphene using equation (2.20). (c) Comsol simulation of transmitted power, reflected power and power lost as a function of frequency and graphene DC conductivity using a graphene scattering time of 50 fs.

The real and imaginary parts of the bulk conductivity as a function of frequency, taken from equation (2.20), are shown in figure (2.17 (b)). Three different scattering times are shown to illustrate the effect the scattering time has on the conductivity. Very high mobility graphene will have high scattering times, illustrated by the $\tau = 200\ fs$ trace, leading to a dominant imaginary conductivity above 1.5 THz. Very low mobility graphene will have a mainly real conductivity term, as shown by the trace for $\tau = 15\ fs$. The graphene used in this thesis, has been shown to have a scattering time values of up to 50 fs, shown by the green trace, resulting in a mainly real conductivity below 3 THz. This graphene can therefore be used to variably damp the metal resonant features, rather than sustain surface plasmons on the graphene itself. The transmission through, and reflection from the graphene sample is simulated for different DC sheet conductivities, using $\tau = 50\ fs$, as shown in figure (2.17 (c)). As the graphene conductivity increases, the transmission reduces, and the reflection increases, as expected. However, the graphene is more metallic at low frequencies,

and therefore, as the frequency increases, the transmission and reflectance parameters will converge to the base substrate values of 0.7 and 0.3. This optical effect, caused by tuning the graphene conductivity, must be taken into account when using large areas of graphene to variably damp the metal resonator structures, as this will add a perturbation to the optical response of the device.

A graphene sample, fabricated according to figure (2.15), is now placed in the TDS set-up to test the transmission as a function of frequency and gating voltage. A 5 mm hole is drilled into the back of the sample holder to allow for transmission measurements, and the p-doped substrate is contacted with silver paste, around the edges of the hole. The TDS transmission results are shown in figure (2.18).

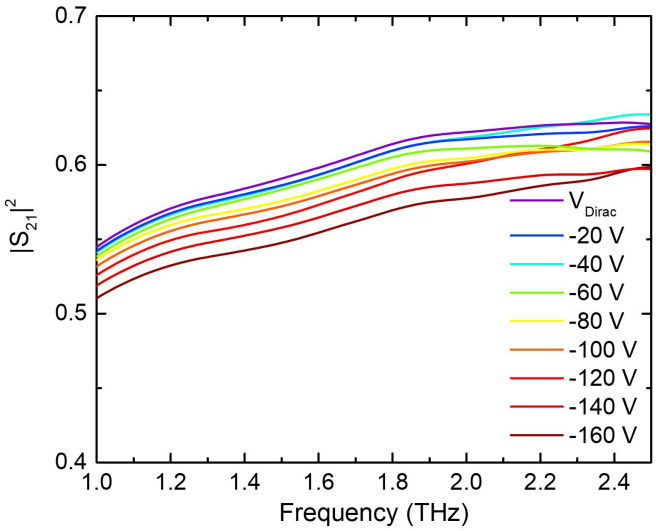

Fig. 2.18 TDS transmission result through graphene patch on p-doped silicon and silicon dioxide substrate as a function of frequency and backgate voltage. Measurement normalised to transmission through nitrogen.

There is a clear increase in transmission as the frequency increases from 1 to 2.5 THz, which we would expect based on the simulation results in figure (2.17 (c)) using a graphene scattering time of 50 fs. There is a clear decrease in the transmission value as the back gate voltage is decreased from the Dirac voltage, modulating the DC sheet conductivity of the graphene from around 0.3 to 1.1 mS. For comparison, at 1.6 THz, the TDS transmission power decreases from 0.59 to 0.55 as the voltage is decreased from V_{Dirac} by -160 V. The transmission simulated values at 1.6 THz change from 0.66 to 0.6 when the graphene DC conductivity is changed from 0.3 mS to 1.1 mS. The proportional difference for the TDS

results matches simulation values, and the DC offset can be due to the difficulties faced when trying to normalise TDS data to gain absolute values of transmitted power.

2.4.4 Graphene encapsulation

One problem with the way the graphene is fabricated in figure (2.15), is that it is left exposed to the atmosphere. Charged impurities can collect on the graphene causing it to become more n or p-doped with time. To compensate for this extra doping, the Dirac point will drift away from 0 V over time. To keep the Dirac point as close to 0 V as possible, and to stabilize it over time, a graphene encapsulation can be performed, acting as a physical barrier against contaminants. A uniform Al_2O_3 layer can be deposited using Atomic layer deposition (ALD) giving thicknesses of up to 100 nm. This deposition is performed over the full graphene device before bonding, and a photo-lithography step is used to open up gaps over the bond pads, using MF319 to etch away the ALD layer. The devices are now bonded and mounted as usual. The encapsulation also reduces the hysteresis in the charge carrier concentration as the voltage is ramped up and down [170]. An example of two graphene device conductivities as a function of backgate voltage are shown in figure (2.19), illustrating the difference in hysteresis between encapsulated and un-encapsulated graphene.

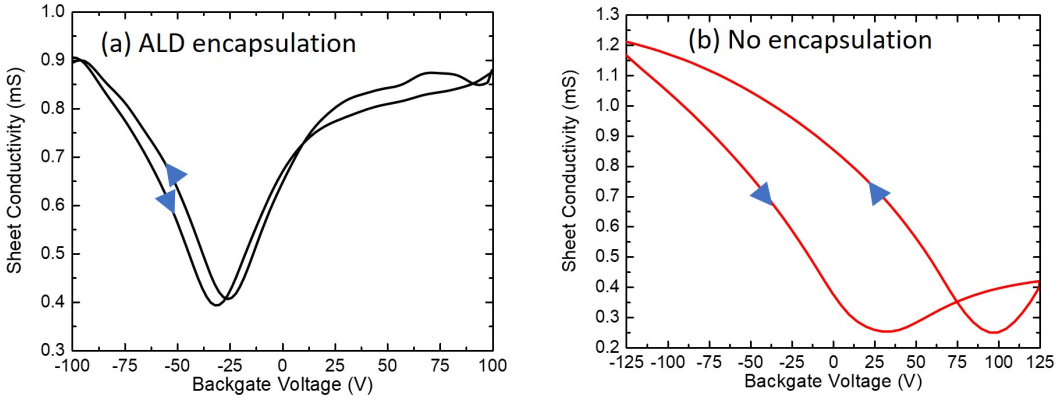

Fig. 2.19 (a) Sheet conductivity of ALD encapsulated graphene as a function of backgate voltage as the voltage is swept from -100 V to 100 V and back again. (b) Sheet conductivity of graphene with no encapsulation as a function of backgate voltage as the voltage is swept from -125 V to 125 V and back again.

Figure (2.19 (a)) shows the sheet conductivity measured for a graphene patch with 100 nm ALD of AL_2O_3 on top as a function of backgate voltage. The voltage starts at -100 V and is increased towards 100 V, showing a Dirac point at -30 V. The voltage is then swept backwards

from 100 V to -100 V, and the resultant conductivity is very similar, showing the Dirac point at - 25 V. The case is somewhat different for the device with no ALD encapsulation shown in figure (2.19 (b)). There is a large difference in the Dirac point when the voltage is swept in both directions. When increasing the voltage, the Dirac point is measured to be at 25 V, showing a n-doped graphene sample which seems to have a higher hole mobility than electron mobility. As the voltage is decreased from 125 V, however, the Dirac point seems to have shifted to 100 V. This is due to charge trapping sites in the graphene, stopping charges from being able to be freely removed from the graphene. The ALD encapsulation reduces the charge trapping problem, whilst also stabilizing the Dirac point over a long period of time.

2.5 Split ring resonators and graphene amplitude modulators

In this chapter thus far, static metal resonator arrays have been shown to exhibit strong interaction with THz radiation at a lithographically tunable resonance frequency. Further to this, electrically tunable graphene devices have been realized which have a conductivity determined by the voltage applied to the backgate voltage. To build devices to modulate the optical properties of THz radiation, these two principles are combined, using the metal resonators to exhibit a strong THz response, whilst using graphene to variably damp the strength of this response.

2.5.1 Fabrication

The fabrication process for such a device involves a combination of the processes shown in figure (2.11 and 2.15). This process is illustrated in figure (2.20). The fabrication starts with the processed graphene, configured for electrical back gating. The next three steps lay out the optional graphene encapsulation using ALD of Al_2O_3 discussed in the previous section. Once step four is completed the resonator structure is added, using the same methods described in figure (2.11), however, instead of depositing the SRRs onto a blank SiO_2 substrate, the SRRs are deposited onto the electrically tunable graphene area. Once the metal SRRs are deposited, the device is bonded and mounted onto a chip holder, in the same way as the graphene device, leaving a hole in the back for transmission TDS characterization.

A device for amplitude modulation is fabricated using this technique, with an SEM image of the fabricated SRR areas shown in figure (2.21 (a)). This contains horizontal SRR electrical biasing lines as well as the SRR array. The dark background is a continuous sheet of graphene with the graphene domain edges are noticeable, and the grey substrate visible in

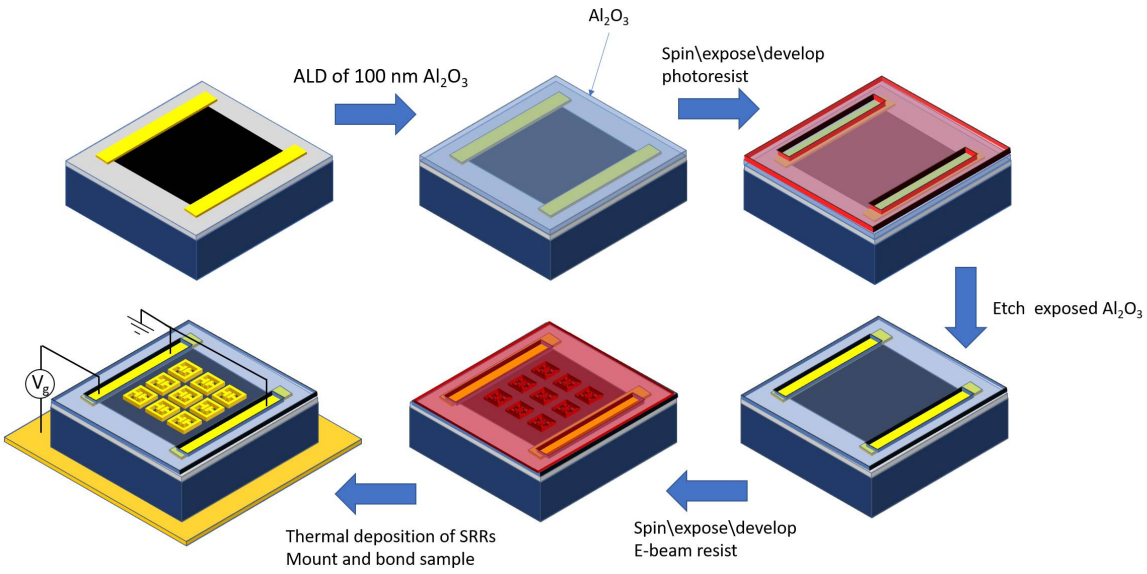

Fig. 2.20 Illustration of Fabrication procedure to build SRR and graphene amplitude modulator device.

places. However, the uniformity of the graphene is sufficient to be used for variable resonator damping purposes. An electrical measurement of the graphene conductivity as a function of backgate is performed using the same source-Drain backgate measurement which was used for figure (2.16) with the result shown in figure (2.21).

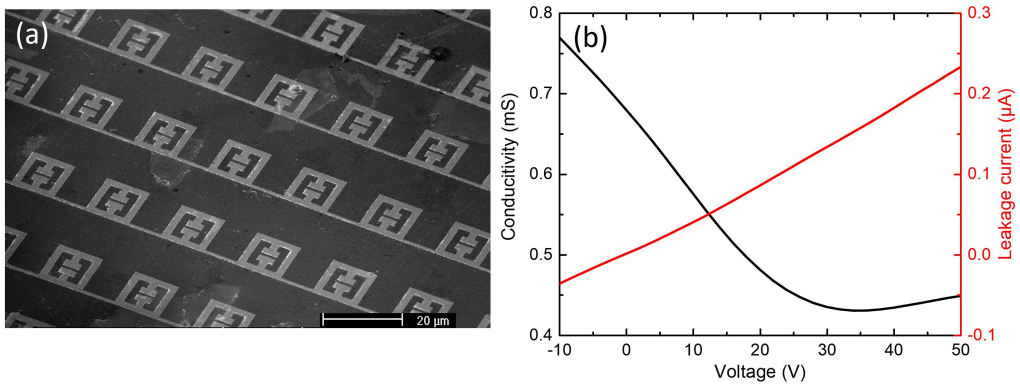

Fig. 2.21 (a) SEM of SRR resonator structure on graphene layer for amplitude modulator device. (b) Electrical measurement of graphene sheet conductivity as a function of backgate voltage as well as leakage current through the backgate.

Ideally we would like the backgate current leakage to be as little as possible as the voltage is swept, and in this case less than 1 μA is leaking as shown in figure (2.21). This leakage is not high enough to affect the device performance, however, if it is > 1 nA, it tends to increase over time as the device is used due to the current irreversibly tunnelling through the dielectric barrier in a concentrated position. In practice, backgate leakage was the main failure mode in this device fabrication process. Two separate substrates producing 4 separate devices each were fabricated, and the gate leakage for 7 out of 8 of those devices was unacceptably high at 100s of μA when 10's of volts were applied. These devices had an asymmetrical Schottky like conduction pattern due to the doped substrate, metal contact. Device performance begins to break down when the leakage is above 1 μA, and hence there was a fabrication yield of 12.5 % for this device design. The reason for this leakage was determined to be primarily due to pin holes in the SiO_2 layer as when the device area was decreased, the yield increased, with the chance of a pinhole being located in a critical area being linked to the area. In future chapters this yield is improved by reducing the device area, whilst also increasing the number of devices per sample.

2.5.2 Comsol simulation

To simulate the damping effect of the graphene on the metal resonator array, a Comsol simulation is performed using the unit cell shown in figure (2.22 (a)). A 14 nm graphene layer is added above the silicon dioxide, with the AC conductivity value governed by equation (2.20). On top of this, the 100 nm Al_2O_3 layer is added which is given a relative permittivity value of 9.1 as taken from literature [171]. The gold features on top of the Al_2O_3 are described using the same method used in figure (2.6). In this case, however, there are horizontal lines added in the SRR structure, which can be used to electrically bias the SRRs themselves if connected to bond pads on the edge of the device. Due to the 100 nm Al_2O_3 layer, the SRRs and graphene layer act as two capacitor plates, providing an alternative 'top' gate to change the conductivity of the graphene. As the extra lines are perpendicular to the incoming radiation electric field polarized in the y direction, their is negligible interaction with the incident radiation. Therefore, the resonant features shown in figure (2.7) should not be perturbed by the presence of these horizontal lines.

The charge carrier concentration in the SRRs is shown at the LC resonant frequency for two different graphene DC conductivities in figure (2.22 (a) and (b)). When the graphene DC sheet conductivity is increased from 0.1 mS to 1.9 mS, the magnitude of the charge build up reduces. This is because the near field coupling between the SRRs and the graphene layer causes current to be driven in the graphene, dissipating power in the process. This effect is shown in figure (2.22 (c)) with the electric field from the SRR shown penetrating

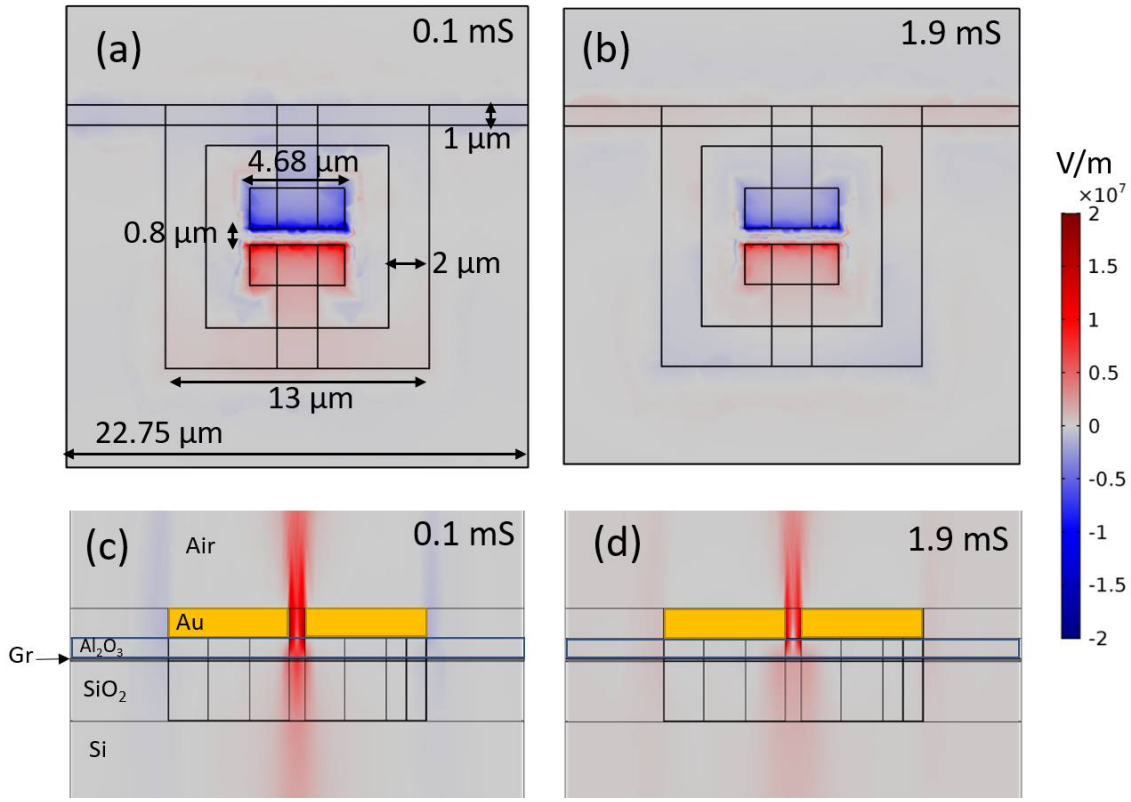

Fig. 2.22 (a) Lithographic tuning parameters for unit cell of SRR device and electric field strength for a graphene DC conductivity value of 0.1 mS (b) Electric field strength for graphene DC conductivity value of 1.9 mS. (c) Side on view of electric field strength penetrating graphene layer for conductivity of (c) 0.1 mS and (d) 1.9 mS.

the graphene layer. The electric field in the capacitive gap has a large component parallel to the graphene plane, and therefore this is where the majority of the energy is dissipated in the graphene. As the graphene conductivity is increased, the dissipation of energy increases, and the electric field strength in the graphene is decreased, as shown in figure (2.22 (d)). As the thickness of the Al_2O_3 is reduced, dissipation in the graphene increases, as the overlap with the SRR electric field increases. The controllable dissipation in graphene will have an effect on the resonance condition, acting as a variable damping. The resultant effect on the S parameters of the devices is shown in figure (2.23).

As the conductivity increases, the energy dissipation in the graphene increases and the Q factor of the SRR resonance decreases. As a result, the reflection magnitude at resonance will reduce as shown in figure (2.23 (a)), and the transmission will increase as shown in figure (2.23 (b)). These devices can therefore be used as amplitude modulators for a radiation source which matches the resonance frequency. Modulation depths in the region of 15%

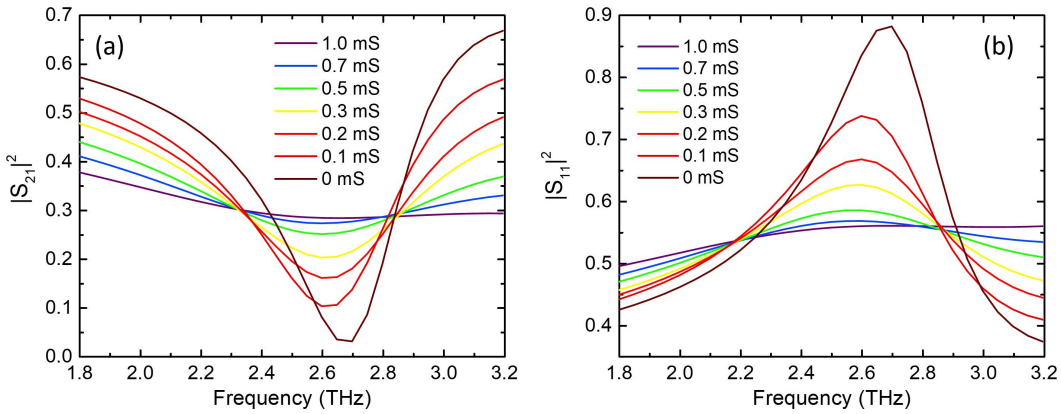

Fig. 2.23 Comsol simulation of (a) transmission and (b) reflection from SRR and graphene modulator device as a function of frequency and graphene DC conductivity.

are predicted to be achievable for graphene conductivities between 0.3 and 1.3 mS when in reflection mode, with modulation depths of 20 % achievable in transmission mode.

2.5.3 Equivalent circuit model

To further understand the graphene damping mechanism, the equivalent circuit shown in figure (2.10) is modified to include a variable resistor in series to compensate for the additional loss introduced by the graphene layer. The resultant equivalent circuit model is shown in figure (2.24 (a)). To describe the power dissipation in the graphene, P_{Diss}, as a function of graphene sheet conductivity σ_{Grap}, and the time averaged electric field in the SRR capacitive gap, $||E_{Gap}||$, the following equation can be used.

$$P_{Diss} \propto \sigma_{Grap}||E_{Gap}||^2 \tag{2.21}$$

For simplicity, only the real component of the graphene conductivity is included, as its inductive component is small in the THz range due to the low 50 fs graphene scattering time. The important point to take from this equation is that the dissipated power scales linearly with the graphene conductivity for a given electric field strength. Also the graphene will have a strong damping effect where there are strongly concentrated electric fields parallel to the graphene surface, and therefore despite having a sheet of graphene over the whole device area, it is the graphene in the capacitive gap which is having the most relevant damping effect. A device with patches of graphene just in the SRR gaps would therefore have a similar damping effect. The Q factor of the resonant structure is defined as the energy stored divided by the

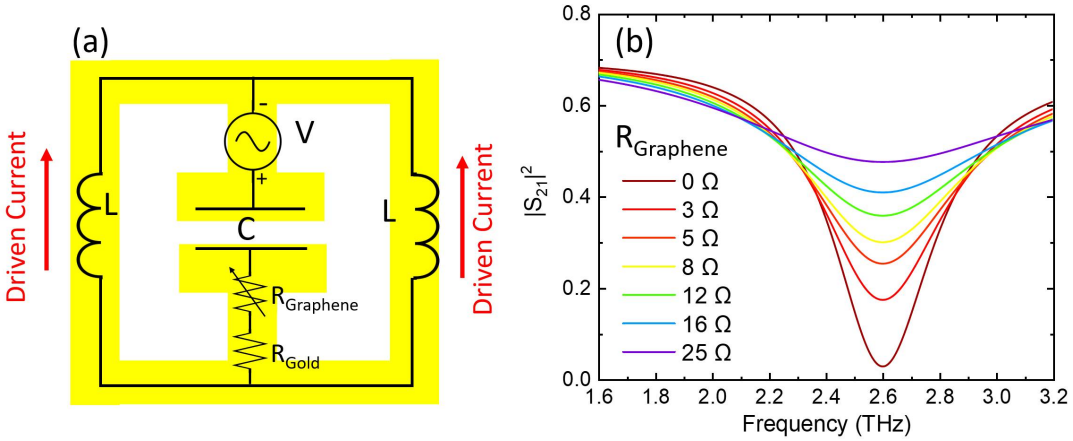

Fig. 2.24 (a) Illustration for equivalent circuit model of SRR resonator array with graphene damping. (b) Equivalent circuit model simulation of transmission through 13 μm SRR array as a function of graphene conductivity using values of $L = 8.75x10^{-12}$ H , $C = 8.56x10^{-16}$ F and $\mathbf{R_{Gold}} = 12\ \Omega$

energy dissipated per cycle, and therefore, as the conductivity of the graphene increases, the Q factor reduces. The equivalent in series resistor, $R_{Graphene}$, used to describe this reduction in Q factor can be determined for various sheet conductivity values by probing the Q factor of the resonance in the Comsol simulation as the graphene conductivity is changed. We first used this method to determine the equivalent resistor describing the total loss in the gold resonators, R_{Gold}, with no graphene present in the simulation. The graphene layer is added, and the change in Q factor is measured for different graphene conductivity values. The following equation can be used to determine the in series graphene resistance, $R_{Graphene}$, for various sheet conductivity values.

$$Q = \frac{1}{R_{Gold} + R_{Graphene}} \sqrt{\frac{L}{2C}} \tag{2.22}$$

The absolute value of this resistor is dependant on geometric factors such as the thickness of the Si_2O_3 layer, and the size of the SRR capacitor cap, and therefore the damping range of the graphene can be lithographically modified. The inductance and capacitor values, L and C, in figure (2.24 (a)) are defined using the Comsol model shown in figure (2.22), using the same technique as described for figure (2.10). The transmission as a function of frequency is then derived from using equation (2.11) with the results shown in figure (2.24 (b)). This device displays a resonance at 2.6 THz causing a transmission dip. The amplitude of this dip can be modified as the effective graphene resistor value is changed. When compared to

the Comsol model, at low frequencies, the graphene reflectivity will start to influence the transmission spectrum, an effect which is not contained in the circuit model. Also at higher frequencies, the higher order resonances will start to influence the transmission, with this effect not included in the equivalent circuit model. However, this circuit model simulation matches the Comsol simulations well particularly around the resonance frequency with the fundamental graphene damping mechanism captured using this simple equivalent circuit model representation.

2.5.4 Time domain spectroscopy results

With the graphene damping mechanism and amplitude modulator operating principle explored, the device described in figure (2.22) is now fabricated. The process described in figure (2.20) is used for this fabrication and the graphene conductivity is first characterized before being placed in the TDS transmission set-up with the transmission spectrum measured for different backgate voltage. The transmission power, normalized to air, is shown in figure (2.25 (a) and (b)) comparing Comsol simulation results with TDS transmission measurements.

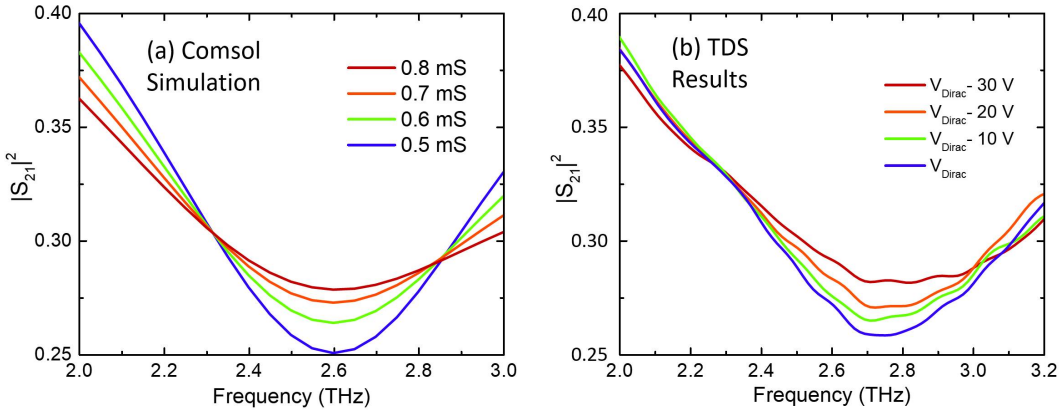

Fig. 2.25 (a) Comsol simulation of transmission through SRR and graphene device as a function of graphene DC sheet conductivity. (b) TDS measured transmission through SRR and graphene device as a function of backgate voltage.

The usual frequency shift of around 3 % between simulation and results is once again observed. The fact that this offset is consistent between different samples shows that this can be accounted for when designing new devices. Crucially, as the backgate voltage is decreased from V_{Dirac} to $V_{Dirac} - 30\ V$, the Q factor of the resonance reduces, causing an increase in transmission at the resonant frequency of around 12 %, and showing strong

correlation between the simulation and results. These devices could therefore be used as electrically controllable amplitude modulators for a THz source operating at around 2.7 THz. The different ways of integrating these devices with THz sources, as well as the potential modulation speed of such a device will be discussed in chapter 5.

2.6 Chapter conclusion

This chapter has described the working process for simulating, fabricating and testing THz optoelectronic modulators by integrating standard metamaterial structures with electrically controllable graphene. A simple amplitude modulator device using graphene to variably damp the metamaterial resonance is demonstrated, giving amplitude modulation depths in the region of 12%, achieved by varying the backgate voltage by 30 V. Further to this device demonstration, this chapter has laid the theoretical and practical groundwork for the more complicated metamaterial and graphene devices which are to be discussed in the following chapters.

Chapter 3

Resonant frequency tuning devices

3.1 Terahertz frequency tuning review

This chapter will look to design and experimentally demonstrate ways of building metamaterial and graphene devices with electrically tunable resonance frequencies. The previous chapter focused on a method for variably damping the Lorentz resonance of a metamaterial array, by using graphene as a variably damping medium. This method produced metamaterial devices displaying resonances with electrically tunable Q factors, which could be implemented as THz amplitude modulators. It is advantageous, however, to be able to change the resonance frequency of the metamaterial, rather than just damping the resonance. This can potentially lead to much higher modulation depths, but can also have dramatic effects on the phase of the transmission and reflected THz components [172], whilst also being applicable as an electrically controllable band pass/reject filter. Large resonance frequency modulation has been achievable using photo active silicon [137, 139–141] and MEMS devices [143], however a purely electrical scheme with no moving parts is ideal.

A range of theoretical and experimental approaches have been explored in order to achieve THz tunability based on purely graphene resonant features without the use of metal metamaterial components [173, 174, 104]. There are huge challenges in realising high Q-factor resonant features in graphene resonators for schemes not based on optical pumping, where very high quality graphene is required to produce significant modulation of the optical response. Graphene resonant features have been hybridized with metallic features in a range of theoretical demonstrations [168], with a few experimental demonstrations such as that described in reference [175], achieving transmission peak tuning from around 6 THz to 4 THz, but with achievable Q factors below 1. Another such design is shown in figure (3.1 (a)), taken from reference [157], which hybridises a graphene localised surface plasmon with an inverted metallic split ring resonator structure achieving a tuning range between 8

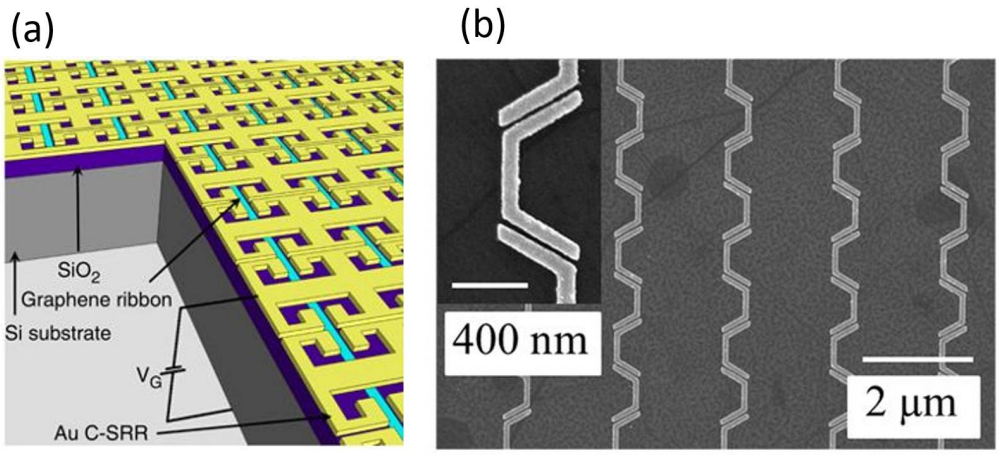

Fig. 3.1 (a) Frequency modulator device based on the hybridisation between a Graphene surface plasmon and SRR plasmonic resonance, modified from reference ([157]) (b) Infrared modulator device which uses the electrically tunable inductance of graphene to modify the resonance frequency of metal resonator elements, modified from reference ([162])

THz and 10 THz, however, with achievable Q factors <2. To sustain a surface plasmon on graphene with a reasonable Q-factor, a very high scattering time and mobility is required, and this is difficult to realise for large area graphene samples. Therefore, based on current graphene fabrication constraints, the frequency tuning capability of this method has limited applicability for real THz devices. In the previous section we have considered only the real part of the graphene conductivity which acts to damp the resonance Q factor. This is because the graphene conductivity is dominated by the real part in the THz region when the graphene scattering time is less than 50 fs. There are graphene modulation schemes working in the infrared region, which are able to utilise the tunable imaginary part of the graphene conductivity, achieving tuning ranges of 46-41 THz and 50-40 THz in references [161] and [162] respectively with Q factors of around 4 achievable. This means the graphene can act as a variable inductor in an equivalent circuit model instead of a variable resistor (ie. lossy element). The device design for reference [162] is illustrated in figure (3.1 (b)), which is able to tune the resonant frequency of the metal resonator elements by altering the effective inductance of the graphene shunting the resonator gaps via electrostatic back gating. Such a scheme would be achievable around 3 THz, however, graphene with much longer scattering times (>ps) would be required to allow the imaginary conductivity part to sufficiently dominate. In this chapter, different methods to produce a frequency controllable resonance device with high Q factor are demonstrated using more complex metallic resonant features, which only rely on variable damping of the graphene layer, and do not require high mobility graphene to operate efficiently.

3.2 Double split ring resonator device

Intuitively, the simplest way of building a metal resonator array with a tunable resonant frequency response is to build two different sized metamaterial arrays contained in the same device which can be independently variably damped using graphene. If these two differently scaled areas are spatially distributed in an arrangement which is much smaller in scale than the incident THz spot size, the net optical response will be a summation of the different resonant areas. If one of these areas, with a lower resonant frequency, is effectively switched off by a large graphene damping, the resultant resonant frequency of the device will be dominated by the higher frequency resonant area. Conversely, if the higher frequency resonant area damping is higher, the lower frequency resonant elements dominate, causing a net reduction in the resonant frequency. To test this theory, the SRR/graphene device described in chapter 2 is modified, with a metamaterial structure built by spatially alternating two differently scaled SRRs. Each of these individual SRRs has a small patch of graphene positioned in the capacitive gap, instead of a large patch of graphene damping the whole array. To variably bias differently sized SRRs, horizontal biasing lines are used as before, however the biasing lines for the larger SRRs (SRR1) are connected to a bond pad on the left of the sample, and the lines for the smaller SRRs (SRR2) are connected to a bond pad on the right side of the sample. This allows for the graphene damping the larger SRRs to be electrically disconnected from the graphene damping the smaller SRRs. This device design is illustrated in figure (3.2) along with the lithographic tuning for each individual resonator element, showing which parameters are included in the linear scaling term, 'Scale'. The double SRR array is built using individual lithographically defined SRRs shown in figure (3.2 (b)), however, two different 'Scale' values are used, stacked in an alternating array according to figure ((3.2 (a)), with each SRR contained within a 22.75 by 26.25 μm area.

3.2.1 Comsol simulation

A Comsol simulation of this device is now performed to determine how the frequency dependant transmission changes as the graphene conductivity in the SRR1 and SRR2 areas is varied independently. The simulation process is identical to the one for the single SRR device used in chapter 2, however two independent graphene patches with different conductivities are used to variably damp the two SRR areas. The lithographic scaling parameter 'scale' for the SRR1 resonators and the SRR2 resonators is 1.15 and 0.98 respectively with the simulation unit cell shown in figure (3.3 (a)). These scale values are chosen so the two resonators will exhibit resonances at different frequencies, however, these resonances will not be so far away as to be completely distinct. We would like to simulate the interplay between

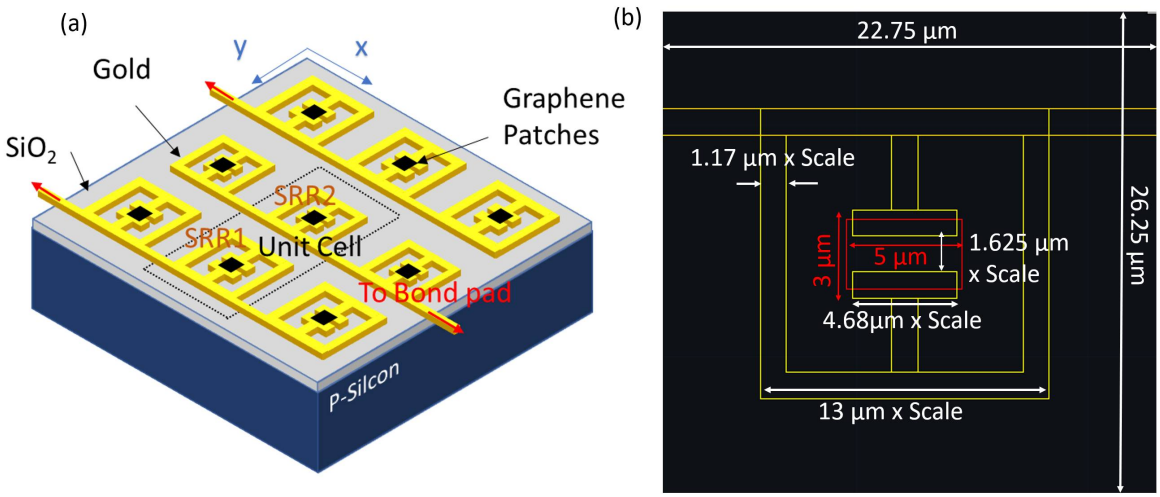

Fig. 3.2 (a)Illustration of 2 SRR metamaterial structure with two alternating SRR sizes connected to different bond pads. (b) Dimensions for individual SRRs in double SRR array, with parameters scaled using the value 'Scale'.

these two resonances conditions as they are independently damped, and to determine if such a device configuration can produce continuous resonance frequency tuning of the net device response.

The simulated transmission through the metamaterial array as a function of frequency for various graphene conductivities, is plotted in figure (3.3 (b)). This figure shows an effective switching between the 2.35 THz low frequency SRR1 resonance and the 2.85 THz high frequency SRR2 resonance when each resonator is progressively damped independently. When both resonators have graphene conductivity values of 0.3 mS, the resonance condition is not well defined, due to the linear superposition of the individual Lorentz resonances. Hence, this device is not predicted to produce a continuous resonance frequency peak tuning between 2.35 THz and 2.85 THz, but more of a binary tuning between the two Lorentz resonance conditions.

To further understand this resonance tuning, the resultant simulated electric field distribution in the resonators at both resonance frequencies for different graphene conductivity configurations is shown in figure (3.4). When the SRR2 resonators are heavily damped by the graphene square with a conductivity of 1 mS, and the SRR1 resonators graphene conduc-

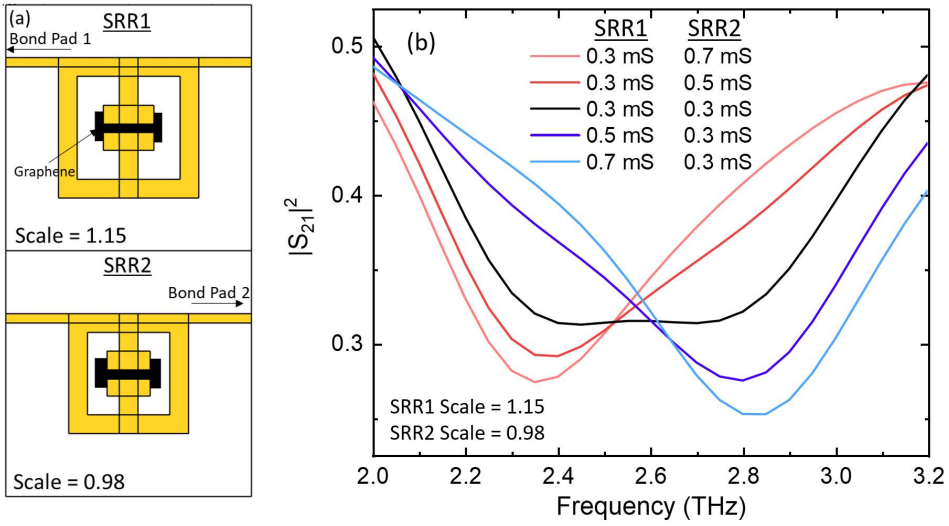

Fig. 3.3 (a) Double SRR unit cell using scale values of 1.15 and 0.98 for SRR1 and SRR2. (b) Corresponding Comsol transmission simulation for different graphene conductivities.

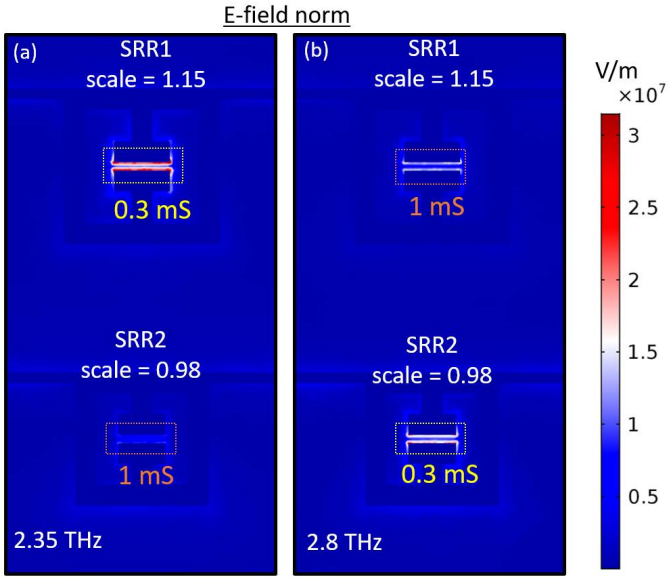

Fig. 3.4 Electric field concentration in double SRR resonator gap when graphene conductivity is (a) 0.3 mS / 1 mS (f=2.35 THz) and (b) 1.0 ms / 0.3 mS (f=2.8 THz) for SRR1 and SRR2 respectively

tivity is kept at 0.3 mS, the resonance of the SRR2 resonator at 2.35 THz dominates. This corresponds to a strong SRR1 electric field concentration observed in figure (3.4 (a)) when

compared to the SRR2 resonator leading to the transmission dip simulated in figure (3.3). Figure (3.4 (b)) illustrates the opposite effect, with the SRR1 resonator being damped heavily by graphene, with the SRR1 resonator graphene conductivity set to 0.3 mS. The smaller resonator now dominates with a resonance frequency of 2.8 THz, once again illustrating why there is a transmission dip at this frequency in figure (3.3).

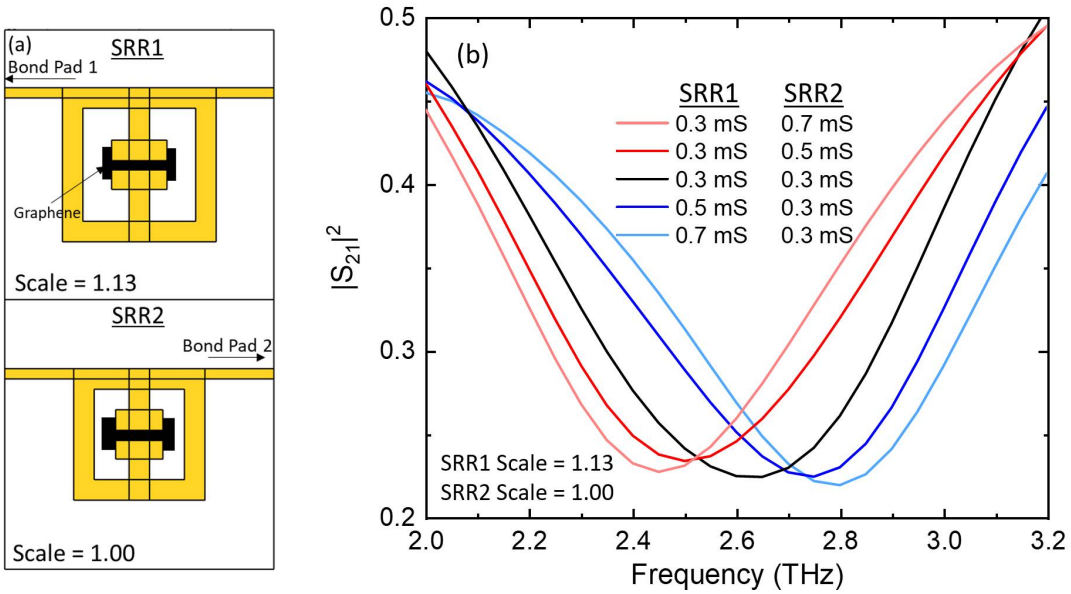

Fig. 3.5 (a) Double SRR unit cell using scale values of 1.13 and 1.0 for SRR1 and SRR2. (b) Corresponding Comsol transmission simulation for different graphene conductivities.

For a more continuous resonance frequency tuning, the linear superposition when both resonators are on must have a clear defined transmission dip. To achieve this, the resonators need to be more closely matched in size and to test this theory a simulation is performed, as shown in figure (3.5), using scale values of 1.13 and 1 for SRR1 and SRR2 respectively. When the graphene conductivity is set to 0.3 mS for both the larger and smaller SRR, there is a clear minimum transmission frequency at 2.65 THz. As the resonators are more closely matched, the resultant transmission peak is much sharper than the equivalent black curve in figure (3.3 (b)). As the SRR1 resonators are progressively damped by increasing the graphene conductivity, the resonance frequency of the metamaterial array is continually shifted towards the 2.45 THz SRR1 resonator resonance, with the Q factor of the resonance condition increasing. The same effect, in the opposite direction happens when the SRR1 resonators are progressively damped instead. The maximum net continuous resonance frequency modulation range of 2.45 to 2.8 THz is achieved in this simulation. A larger tuning

range was achieved for the device simulated in figure (3.3), from 2.35 THz to 2.85 THz, however, a continuous tuning of the transmission peak was not achieved in this case, and therefore there is a trade-off between the total tuning range and how continuous the tuning is. Both of these lithographic tuning conditions will now be fabricated into devices to test the simulated designs in practice.

3.2.2 Fabrication

As these devices require two independently addressable SRR areas, the fabrication is somewhat more complicated than the single SRR device. The single SRR design used a sheet of graphene which was etched into a large square using photolithography, and an oxygen plasma ash, before being electrically contacted on either side by thermal evaporation of source and drain contacts. For the double SRR devices, the graphene needs to be etched into squares which have a side length of 3.5 μm which required e-beam lithography. The new graphene etching process is illustrated in figure (3.6)

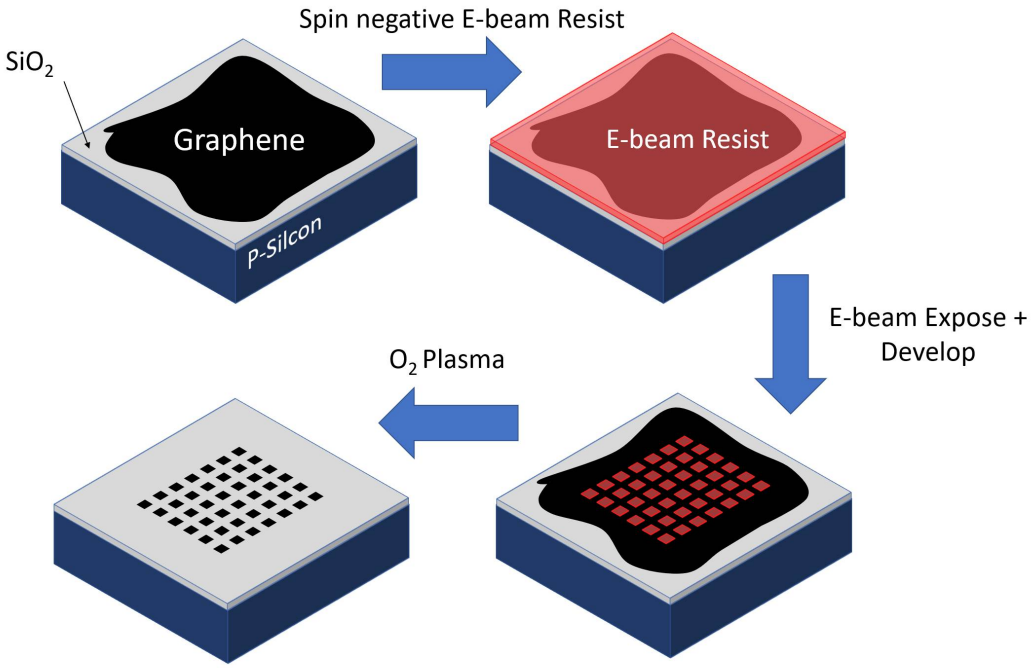

Fig. 3.6 Illustration of graphene etching process for double SRR device.

For this process a negative e-beam resist, MaN-2410 is used, which gives a 1μm thick layer when spun on at a rate of 7000 RPM. It is possible to use photolithography for feature sizes down to a few microns, however this becomes increasingly difficult due to the fringing fields around the optical mask. The alignment of the graphene squares with SRR features is also critical, and therefore e-beam lithography was used instead. The negative e-beam resist is exposed over the required graphene patches, and then it is developed for around 1 minute in MaN developer, leaving the required patch areas covered with resit and the rest of the graphene sheet exposed. The plasma asher is used to remove the unwanted graphene areas, and acetone is used to wash away the resist leaving the required graphene squares. With graphene patches defined, the e-beam step for the SRR arrays is then performed with the graphene electrically contacted to the left or right bond pad through the individual Ti/Au SRR structure. Sometimes all the graphene can be removed during the graphene etching process due to the resit not sufficiently protecting the required areas, particularly when the e-beam layer is too thin. To counter this the MaN-2410 resist was used instead of the 10 times thinner MaN-2401 variant. During the first processing batch, graphene was lost during the SRR metallization fabrication stage, particularly during the metal liftoff process. An alternative approach is to define the SRR array first before the CVD grown graphene layer is deposited on top. The procedure laid out in figure (3.6) can then be performed as normal, resulting in the graphene squares sitting on top of the SRR metal features instead of being sandwiched between the substrate and SRRs. This technique actually has some advantages, as the metal liftoff process can be more thoroughly performed when there is no chance of accidentally removing the graphene.

An SEM image of an example SRR structure which has had liftoff problems is shown in figure (3.7). When doing an electrical test of the fabricated 2 SRR devices, it was found that the SRR1 and SRR2 areas were shorted for all 8 fabricated devices so could not be measured. Each device area is around 2 mm by 2 mm, and it is essential that there is no stray metal area which has not lifted off properly electrically contacting the different SRR areas. Each device is made up of around 80 distinct SRR rows, and if any of the consecutive rows of SRRs are electrically connected, the full area will be shorted. Unfortunately, the central part of the SRR structure is difficult to lift-off as demonstrated in figure (3.7 (a)), and there are a few areas where this residual gold ends up shorting consecutive SRRs. Further to this, figure (3.7 (b)) shows an example stray graphene area which has not been correctly etched away. If the graphene patches have not been etched completely, stray graphene could provide a current path between the two SRR arrays. Over such a large sample area, it is statistically difficult to ensure that there is not one stray graphene strand, or failed metal liftoff area shorting the arrays of small and large SRRs.

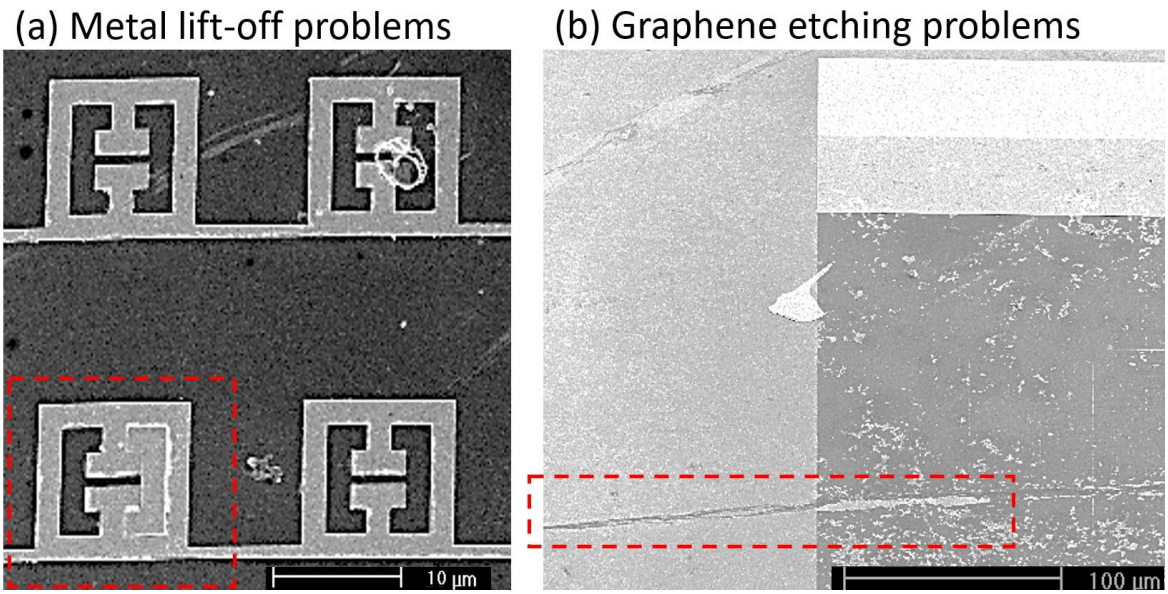

Fig. 3.7 (a) Image showing metal liftoff problems leaving loose metal which could short the arrays. (b) SEM showing graphene etching failure. (Highlighting failure areas in red box)

To solve this fabrication issue, the double SRR metamaterial design is adjusted with a new fabricated design shown in figure (3.8 (a)). The overall sample size has reduced from 2 mm $\times$ 2 mm to 1 mm $\times$ 1.2 mm, hence reducing the area to nearly a quarter of its original size. This reduces the chance of stray un-etched graphene path or a metal liftoff strand shorting the two electrically distinct arrays. This also reduces the chance of shorting through the backgate due to the SiO_2 pinhole problem discussed in chapter 2. In this new, more robust design, the two SRR arrays are grouped together in sets of 4 rows (41 SRRs in each row), with a 26.25 μm gap separating these areas. As illustrated in figure (3.8 (a)), this means that there is now only 8 gaps which must have no electrical short across the whole sample for the two arrays to be electrically isolated, greatly enhancing the yield. A few devices areas were electrically shorted through graphene with leakage currents in the order of 100s of μA when 10 V was applied, however, after a large voltage in excess of 50 V was applied between the two SRR areas, the leakage current suddenly dropped to 100s of nA. It seems that the short was coming from a thin un-etched graphene line, which after a large amount of current was applied, was etched away. This is an effective last resort to save devices which are initially electrically shorted.

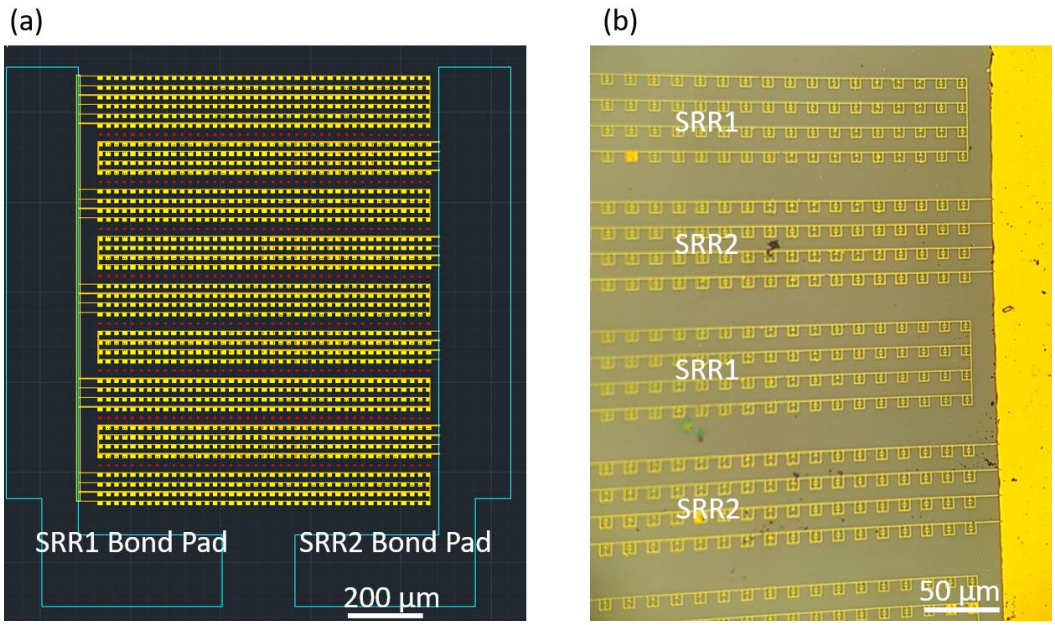

Fig. 3.8 (a) Layout of 2 SRR design for greater robustness. (b) Image of resulting 2 SRR device section.

3.2.3 TDS results

Two different SRR1 and SRR2 designs are now fabricated using the more robust fabrication process outlined. The first device, labelled Device A, is designed with SRR1 and SRR2 scales of 0.93 and 0.77 respectively. This device was designed to produce a similar binary frequency tuning response as the simulated device in (3.3). The scale for these devices was adjusted to produce a resonance tuning range around 2.9 THz to match the output frequency of a QCL, whilst also being measurable by the TDS system. This device was now tested in the transmission TDS system for different backgate voltages applied to the SRR1 and SRR2 areas. For this device design, it is not possible to do a direct electrical measurement of the graphene in the metamaterial array to determine the Dirac point voltage which was around + 30 V for this device. Therefore, a 1 mm $\times$ 1 mm graphene patch is etched and connected with a source and drain as described in chapter 2, on the same substrate as the device. This etched area comes from the same original CVD grown graphene layer, and is processed in parallel with the device. The electrical characteristics of this patch should therefore be representative of the graphene in the SRR area. The only difference could come from the metal doping from the Ti/Au playing a more significant role, however, the base Dirac point characteristics should be preserved [176]. For Device A, the SRR2 section has a minor short through the backgate and therefore couldn't be biased too far from the Dirac point at 30 V. Therefore, the voltage across the SRR2 section was kept at V_{Dirac} and the

voltage across the SRR1 section was progressively reduced away from the Dirac point, with the resultant transmission change shown in figure (3.8 (a)). A binary shift in the resonance frequency from 2.75 THz to over 3.5 THz is observed as the SRR1 voltage is changed. The TDS results above 3.5 THz are close to the noise floor of the TDS measurement, however, so there is some doubt in the transmission shape at these frequencies. The corresponding Comsol simulation shown in figure (3.8 (b)) a similar tuning response, shifted to a lower frequency due to the difference in material properties between simulation and results.

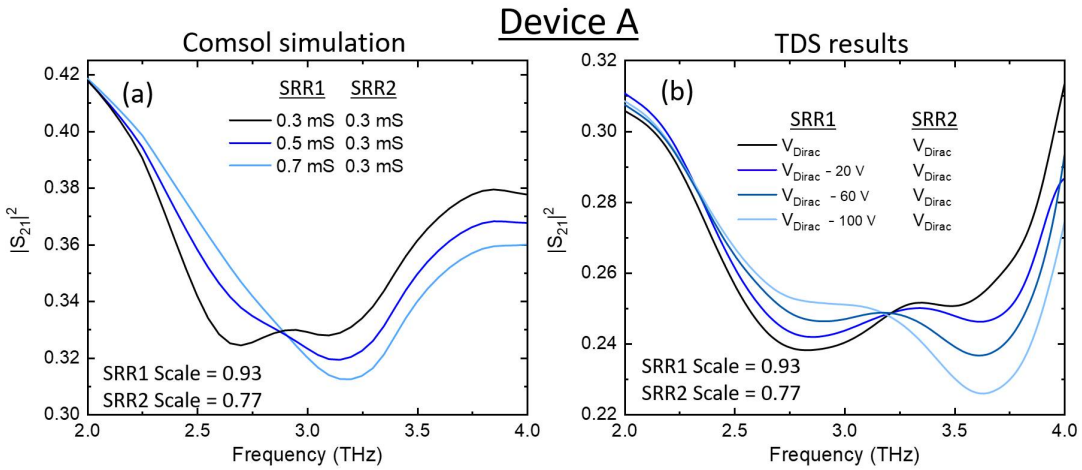

Fig. 3.9 (a) Comsol simulation of transmission for Device A as the conductivity for the SRR1 graphene is changed. (b) Corresponding TDS measured transmission for Device A as the backgate voltage for SRR1 graphene is moved away from V_{Dirac} (30 V).

Another device area, labelled Device B, is now tested which has scale values of 0.96 and 0.88 for SRR1 and SRR2 respectively. This device was fabricated on the same substrate as Device A, and hence uses the same Dirac point approximation at 30 V. This device was also designed to operate around 2.9 THz, however, unlike Device A, a continuous resonance frequency should be possible due to the more similar scale values, as demonstrated in figure (3.5). The transmission through Device B is shown in figure (3.10 (b)) and compared to the equivalent simulation results in (3.10 (a)). This result shows more of a continuous frequency tuning as the damping is switched between SRR1 and SRR2. When both graphene regions are biased at the Dirac point, there is a resonance visible at 2.62 THz. When the SRR1 section is increasingly damped, applying V_{Dirac} - 100 V across the backgate, the resonance frequency increases to around 2.7 THz. If the SRR2 section is damped instead, the resonance frequency is reduced to 2.58 THz.

When comparing the simulation for closely packed, consecutive large and small resonators, shown in figure (3.4) and the more robust, double SRR design with 26.25 μm gaps

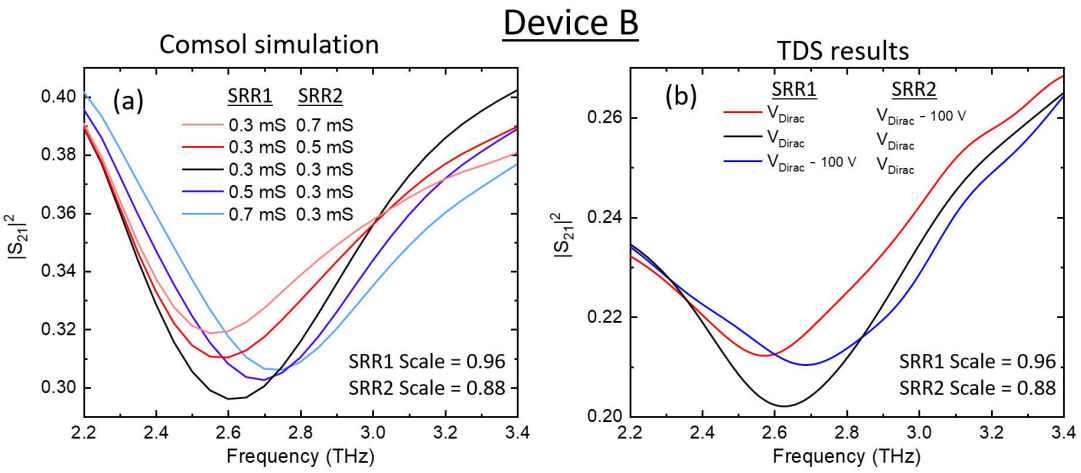

Fig. 3.10 (a) Comsol simulation of transmission for Device B as the conductivity of both SRR1 and SRR2 graphene is changed. (b) Corresponding TDS measured transmission for Device B as the backgate voltage for SRR1 and SRR2 graphene is moved away from V_{Dirac} (30 V).

between grouped SRR1 and SRR2 sections, shown in figure (3.9 (a) and 3.10 (a)), there is a trade off between the Q factor of the tunable resonance, and fabrication yield. The TDS measurements for the device shown in figure (3.9) displays a continuous tuning range of the resonance frequency from around 2.58 THz to 2.7 THz, however, the Q factor is very poor, and hence it is not easy to conclusively quantify the resonance frequency. The Comsol simulation results are sharper, which may be due to the TDS spot not equally being effected by both areas, or due to liftoff problems with many of the SRR arrays not being correctly formed. The fabrication yield of 2 substrates containing 4 devices areas was 1 fully working device, and 1 device with 1 SRR area shorted with the other operating normally. This fabrication yield of less then 25 % is still more favourable than the 0 % fabrication yield achieved for 8 areas of the original 2 mm x 2 mm double SRR design. Despite the weak Q factor of these devices, this is a successful experimental demonstration of the capability to build a spatially addressable graphene/metamaterial array. Such an architecture could have applications for THz wavefront engineering, including applications such as electrically tunable THz flat lenses [177].

3.3 Coupled resonators

To build a metamaterial and graphene frequency tunable device with an improved Q factor, a different method is attempted which involves using two resonators in the unit cell which

are capacitively coupled together, leading to resonances with much higher Q factors. The working principle of this device involves bringing two resonators, which individually possess Lorentz resonance peaks at similar frequencies, into close proximity. These two resonators will destructively interfere at their original resonance frequency, causing a splitting of the single Lorentz resonance into two different resonances, a lower frequency resonance named the out-of-phase bonding resonance, and a higher resonance resonance named the in-phase anti-bonding resonance. The region in between these two resonances has a transmission maximum due to this destructive interference. For active modulation of the resonance condition, graphene is then used to variably damp one of these resonators. When the resonator is strongly damped, the destructive interference effect will be reduced, and the coupled resonator system can be modified into a single resonator system. The two splitting resonances will convert into a single resonance at the original Lorentz resonance frequency as one of the resonators is progressively damped. This will lead to a dramatic change in the resonance frequency condition, and if tuned correctly, should lead to a continuous tuning of the resonance frequency of the metamaterial.

3.3.1 Overview

The transmission peak created via the destructive interference between two resonators which would normally have a transmission dip at this frequency, can be described as an electromagnetically induced transparency (EIT) analogue. EIT traditionally refers to quantum destructive interference between excitation states in atomic systems, leading to a narrow transmission window, however, classical analogs of this effect have been demonstrated using coupled bright and dark plasmonic resonators [178–184]. Other than for resonant frequency tuning, these metamaterial structures are of interest as EIT produces an extreme modification of the dispersion properties of the metamaterial, and this has many interesting applications for slow light, [185–188] enhanced nonlinear effects, [189, 190] and ultra-sensitive biosensing [191, 192]. The coupled resonator device described in this chapter uses a modification of a basic coupled resonator shape which has previously been reported in reference [182]. The static coupled resonator unit cell described in this paper is shown in figure (3.11). This unit cell comprises a radiant C-shaped resonator which couples strongly with incident radiation, and a sub-radiant O shaped resonator which does not couple as strongly with the incident radiation, but is more strongly excited via capacitive coupling with the C-shaped radiant resonator. This unit cell is pictorially described in figure (3.11 (a)), and the resultant simulated transmission as a function of frequency for the metamaterial array built from this unit cell is shown in figure (3.11 (b)). Two transmission dips are visible, labelled the bonding and

anti-bonding mode, and the induced current for these two resonance conditions are shown in figure (3.11 (c) and (d)).

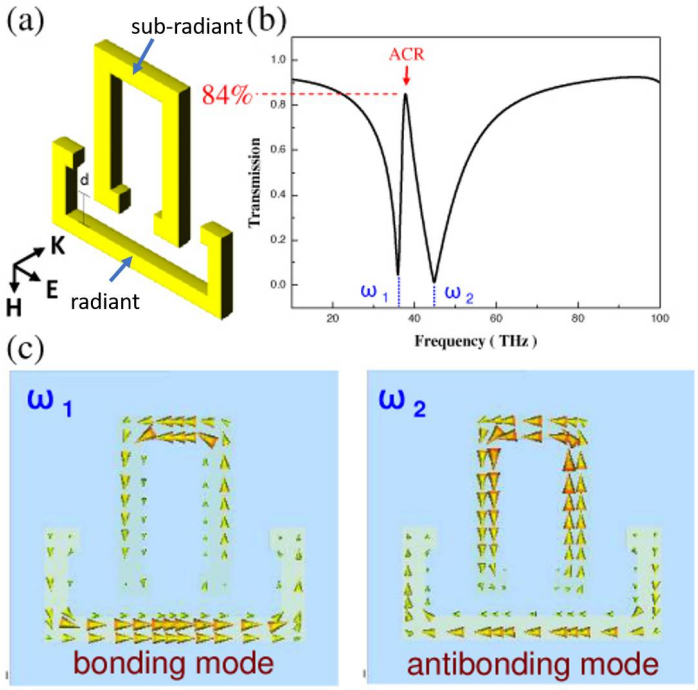

Fig. 3.11 (a) Pictorial representation of static coupled resonator array unit cell. (b) Transmission spectrum of metamaterial array built from coupled resonators. Current in resonators for the (c) bonding mode and (d) anti-bonding mode. Adapted from reference ([182])

It is clear that this coupled resonator design provides very sharp resonance features, making this a promising starting point for building a frequency tunable modulator device. To convert a static coupled resonator array such as the one described in figure (3.11) into an active, electrically tunable device, chemical vapor deposition (CVD) grown graphene is implemented into the structure to variably damp one of the resonators. An advantage of this technique is that it does not require high graphene mobilities to be effective as it is only using graphene to damp metal resonances, unlike the other metal/graphene hybrid designs already discussed, [175, 193] which sustain plasmons on the graphene itself. Similar coupled resonator techniques have been used in the gigahertz region (5 GHz), where one of the coupled resonators exhibiting an EIT analog is electrically modified, resulting in a tuning of the resonance frequency of the coupled resonators [194, 195]. In the THz region, there is demonstrated tunable EIT device employing photoactive silicon with impressive modulation effects [141], however, as already discussed, an all electrical tuning method is desirable. This device also does not allow for continuous tuning of the resonance frequency, with a binary tuning of the resonance condition demonstrated. This section will look to demonstrate

a lithographic tuning method for designing coupled resonators which display continuous resonance frequency tuning by integrating with electrically tunable graphene.

3.3.2 Comsol simulation design

Before building a full device containing graphene, simulations and TDS measurements for static coupled resonator designs are first performed, to build up an understanding of the underlying coupled resonator principle. The basic coupled resonator array design is shown in figure (3.12 (a)) and the basic unit cell for the Comsol simulation is shown in figure (3.12 (b)). The lithographic tuning parameters of the unit cell are shown in figure (3.12 (b)). There are 3 variable parameters in this unit cell, 'L', the length of the sub-radiant resonator, 'G', the gap between the the resonators, and 'scale', which applies a linear scaling factor to all parameters.

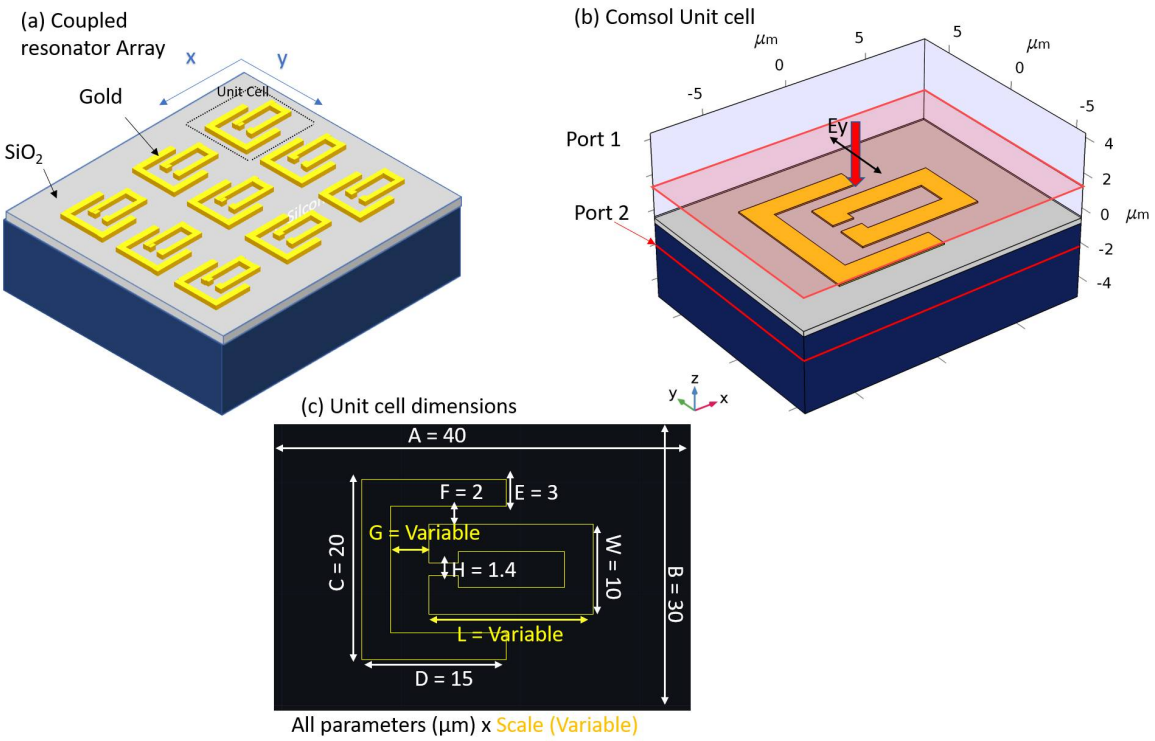

Fig. 3.12 (a) Illustration of static coupled resonator array. (b) Comsol simulation unit cell of static coupled resonator. (c) Unit cell lithographic tuning showing key parameters to be varied (G, L, Scale).

Before simulating the coupled resonators together, it is important to first simulate the two resonators in the unit cell in isolation, to build up an understanding of the resonance coupling.

For the resonators to destructively interfere with each other, they must have an overlapping Lorentz resonance. These resonators cannot be identical in shape however, otherwise they will both be driven equally by the incident electric field, and hence due to symmetry it would be impossible to have current flowing parallel to the incident electric field in one resonator, and anti-parallel in the other. One of the resonators is designed to strongly couple to the external field and is shaped like a large C which has a large parallel metal component in the y direction. An O shaped resonator is used which has a much smaller component parallel to the incident electric field, and hence will be excited less strongly. This means that for the bonding mode resonance, the O shaped resonator can have a dipole configuration which is oppositely polarized to the incident driving electric field, as it is strongly excited via capacitive coupling with the C shaped resonator. These resonators are labelled radiant and sub-radiant respectively, as the C shaped resonator will re-emit radiation more efficiently at resonance, acting as a much larger oscillating dipole antenna than the O shaped, sub-radiant resonator. Both of these resonators are initially simulated independently to lithographically tune the sizes to match up the resonant frequency. This simulation is shown in figure (3.13), using Scale = 1 and varying the parameter L.

Figure (3.13 (a)) shows the charge carrier distribution in the radiant resonator at its individual dipole resonance frequency of 1.55 THz, by probing the electric field in the z direction 20 nm above the resonator. Figure (3.13 (b)) shows the charge carrier distribution in the sub-radiant resonator at resonance using a resonator side length of 19.5 μm. The induced z dipole moment is much smaller when compared to the radiant resonator, thus illustrating why it does not re-radiate as strongly. The S-parameters for the radiant resonator are shown in figure (3.13 (c)), with a broad resonance shown at 1.55 THz, possessing a Q factor of around 5. Figure (3.13 (d)) shows the frequency dependent transmission for the sub-radiant resonator of different side lengths, 'L', keeping all other parameters constant. This figure illustrates how to lithographically tune the resonant elements so they strongly interfere, with side lengths, L, of 17, 19.5 and 22 μm showing standard Lorentz resonance peaks around the resonance frequency of the radiant resonator. These resonances are weaker than the radiant resonator, with the transmission only being reduced to a minimum value of 0.1 at resonance compared to 0. The Q factor of these resonances is much higher, with a value of around 15 measured. Both resonators can be described in a circuit model with an in series ohmic loss and radiation loss resistor, defining the achievable Q factor along with the inductive and capacitive components. The sub-radiant resonators re-emit much less energy than the radiant resonators, and therefore the overall loss is lower, resulting in the measured higher Q factor. This highlights one of the fundamental strengths of coupled resonator designs, providing the opportunity to use highly radiant resonators to strongly couple with incoming radiation, while

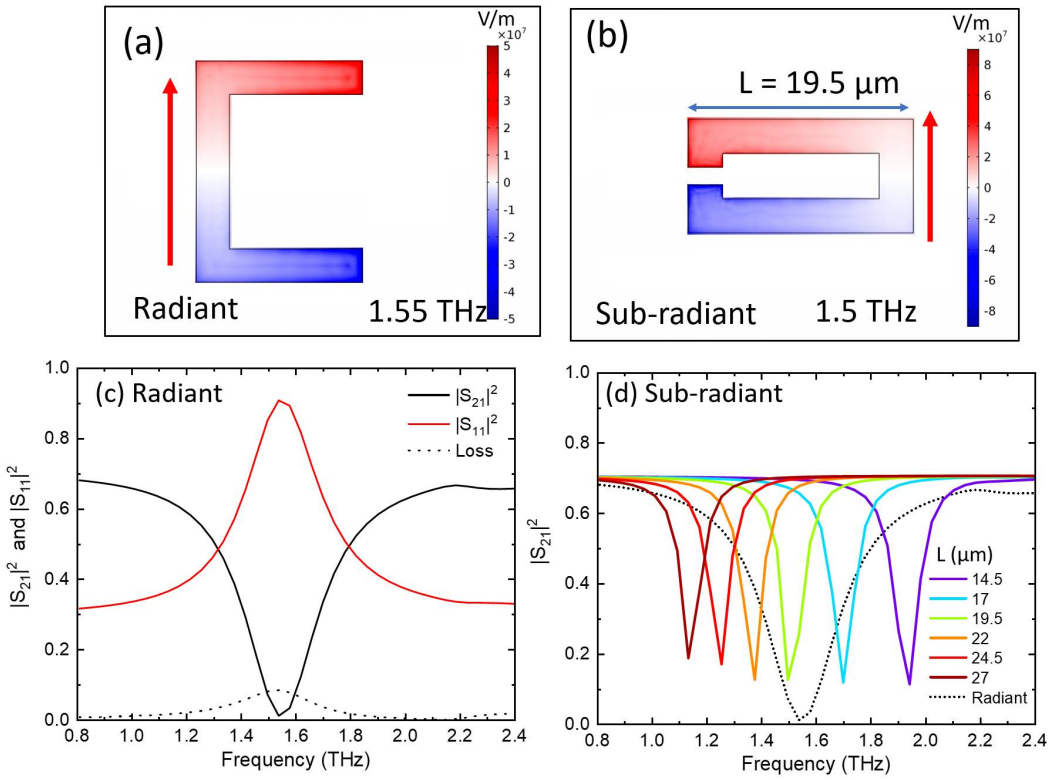

Fig. 3.13 (a) Comsol simulation of charge distribution in radiant resonator at individual resonance. (b) Comsol simulation of charge distribution in sub-radiant resonator at resonance. S parameters Comsol simulation for (c) radiant resonator and (d) different sub-radiant resonator lithographic tuning sizes. (Scale=1)

creating sharp resonance features by coupling this resonator with a high Q-factor sub-radiant resonator. Better still, a completely dark resonance condition, which does not re-radiate, could also be used to couple with the radiant, for example, a quadruple resonance condition [196]. The two resonators are now simulated together setting the variable parameters as Scale = 1, G = 4 μm, and the the sub-radiant resonator length L = 19.5 μm (1.5 THz), with the results shown in figure (3.14).

Two resonances are now observed, on either side of where the single radiant resonator resonance of 1.55 THz was. The 1.35 THz bonding resonance charge carrier distribution is shown in figure (3.14 (a)), showing induced currents in each resonator rotating around their centre with the same handedness. This causes an opposite polarity build-up of charges across the capacitive gap between the C shaped and O shaped resonators, effectively reducing the electron restoring force in each of the resonators, and hence resulting in a lower frequency resonance condition. The higher frequency 1.7 THz anti-bonding resonance charge distribution is shown in figure (3.14 (b)), with current now oscillating with different handedness in both

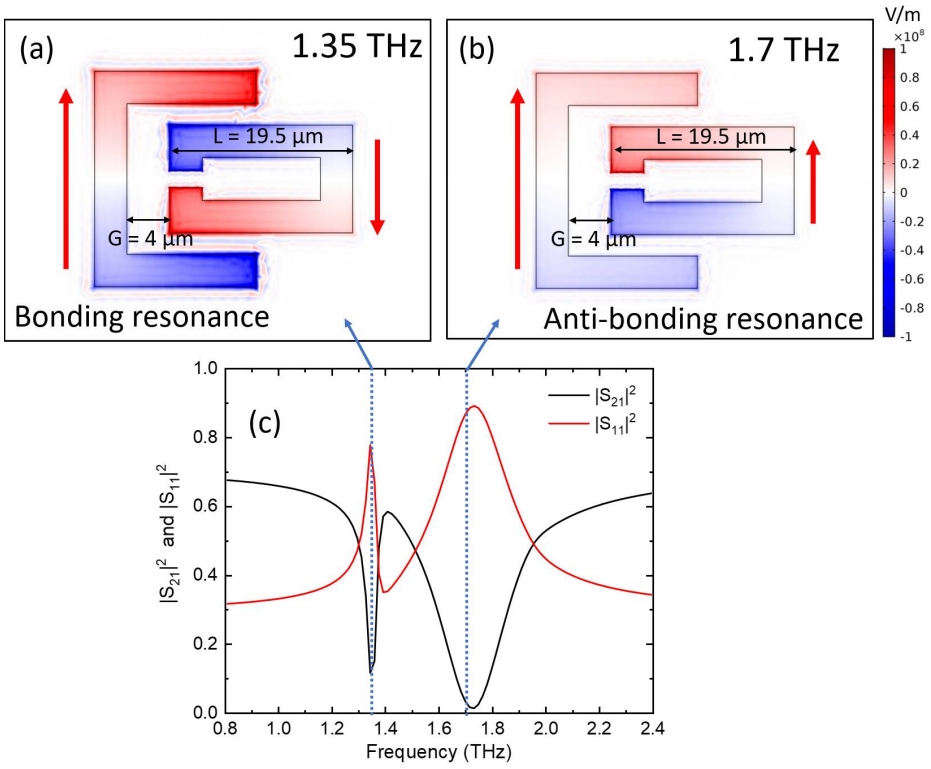

Fig. 3.14 Charge carrier distribution for (a) Bonding resonance and (b) anti-bonding resonance. (c) Simulated S parameters as a function of frequency showing the two resonance peaks. (Scale=1, G=4 μm, L=19.5 μm)

resonators. There is now an electrostatic repulsion caused by the capacitive gap between the resonators, effectively increasing the restoring force in each resonator, resulting in a higher resonance frequency than the original 1.55 THz individual resonator Lorentz resonance. The Comsol simulated frequency dependent S-parameters are shown in figure (3.14 (c)), with a very sharp bonding resonance peak observed at 1.35 THz which has a Q factor greater than 20. A broader resonance peak is observed at 1.7 THz due to the anti-bonding resonance. This peak has a similar shape to the individual radiant resonator response, shifted by 200 GHz, and with a slight Q factor improvement. The metamaterial now displays a transparency around 1.4 THz due to the EIT effect, caused by the destructive interference between the coupled resonators around their original resonance frequencies. From this graph, the interesting region for designing a frequency tunable filter for example, is the incredibly sharp bonding resonance peak at 1.35 THz. To understand how detuning the individual Lorentz resonance frequency of the radiant and sub-radiant resonators effects the resultant bonding resonance condition, a Comsol sweep using different sub-radiant resonator lengths (17, 19.5 and 22

μm), keeping all other parameters constant, with G = 4 μm and Scale = 1, was performed and the results are shown in figure (3.15).

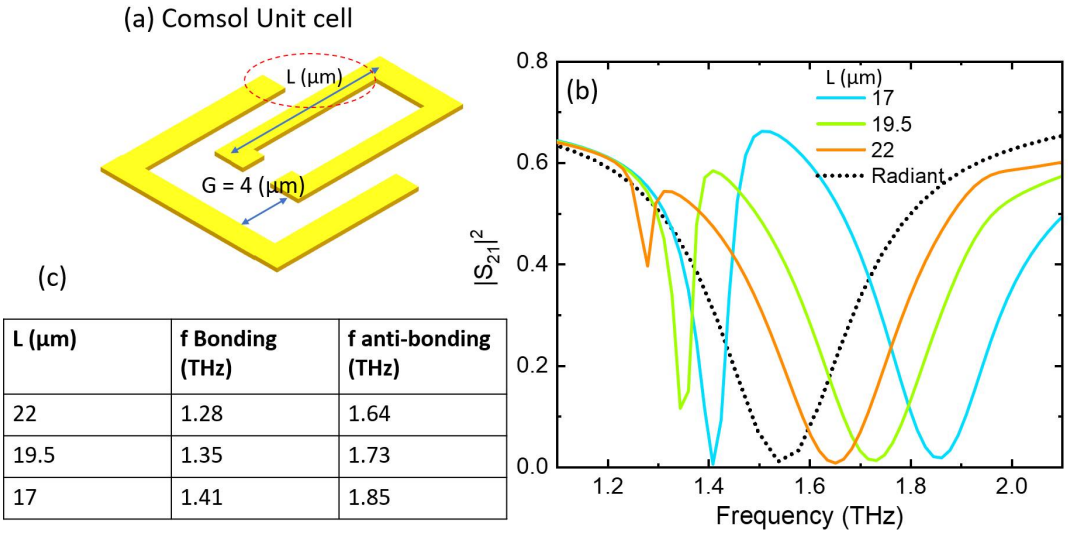

(c)

L (μm)	f Bonding (THz)	f anti-bonding (THz)
22	1.28	1.64
19.5	1.35	1.73
17	1.41	1.85

Fig. 3.15 (a) Illustration of the Comsol unit cell for the coupled resonator metamaterial array, highlighting the tuning parameter, L. (b) Transmission through coupled metamaterial array for different sub-radiant lengths, shown alongside the transmission when only the radiant resonator is present in the unit cell. (c) Table of resonance frequency positions. (Scale=1)

From these simulation results, it is clear that the position of the bonding and anti-bonding resonances in frequency can be lithographically tuned around the radiant Lorentz resonance frequency as the resonator detuning is varied. When the length of THz sub-radiant resonator is 19.5 μm, its own Lorentz resonance frequency of 1.5 THz closely matches the radiant resonance frequency of 1.55 THz. This causes the splitting resonance frequencies to be reasonably symmetrical around the radiant resonance. The bonding resonance frequency is lower by around 180 GHz, and the anti-bonding resonance is greater by around 180 GHz. When the length of the sub-radiant resonator is increased to 22 μm, its own Lorentz resonance frequency is decreased to 1.38 THz, and as a result, the resonance splitting is red shifted accordingly. The bonding resonance is now at the lower frequency of 1.28 THz, and the anti-bonding resonance peak is now at 1.64 THz and very close to the original radiant Lorentz resonator resonance (1.55 THz). If the length of the sub-radiant resonator was increased further, the anti-bonding resonance would continue to be red shifted until it transformed into the original radiant Lorentz. The amplitude of the bonding peak would continue to decrease to zero as the length is increased before a new Lorentz peak would start to appear with coupling breaking down. This bonding peak will first disappear completely at a specific length, before it reappears with increasing amplitude as the length is increased further with

the two resonators not interacting with each other, and the overall response given by a simple sum of the two Lorentz resonance conditions. The opposite effect is observed as the length of the sub-radiant resonator is decreased to 17 μm. The Lorentz resonance of the sub-radiant resonator is blue shifted to 1.7 THz causing the bonding resonance to blue shift towards the radiant Lorentz resonance frequency (1.41 THz), and the anti-bonding resonance to blue shift away (1.85 THz). If the resonator was decreased in length further, the bonding resonance would transform into the radiant resonance, with the anti-bonding resonance transforming in to the higher frequency Lorentz resonance of the short sub-radiant resonator. There is no decrease in the amplitude during this process, however as the two effects require the same current circulation direction in the sub-radiant resonator, they therefore do not counter act each other.

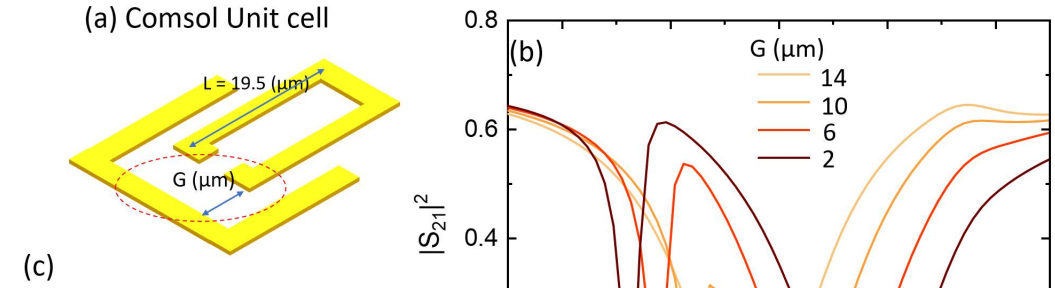

(c)

G (μm)	f Bonding (THz)	f anti-bonding (THz)
14	1.55	1.55
10	1.44	1.62
6	1.38	1.69
2	1.32	1.77

Fig. 3.16 (a) Illustration of the Comsol unit cell for the coupled resonator highlighting tuning of coupling distance. (b) Transmission through coupled metamaterial array for different coupling strengths. (c) Table of resonance frequency positions. Scale=1

The strength of the splitting can also be tuned by varying the proximity of the two resonators using the variable, G. This is illustrated in figure (3.16 (a)), varying G, whilst keeping all other parameters constant, with L = 19.5 μm and Scale = 1, with the resultant transmission spectrum shown in figure (3.16 (b)). In this figure, the length of the sub-radiant resonator was chosen to be 16 μm as it matches up well with the radiant resonant frequency. When the two resonators are separated from each other with a value of 14 μm for G, only a single resonance peak is observed. This is essentially the summation of the two resonator peaks, however, as they are both at the same frequency, this is very similar to the standard

Lorentz resonance of the radiant resonator. As the resonators are brought closer together, with G being 10 μm, the standard resonance starts to split. This initially looks like the standard radiant resonance, with a sharp transmission peak in the centre which looks like an inversion of the sub-radiant resonance. This effect can be roughly described as the radiant resonator acting normally, until the frequency approaches the resonant frequency of the sub-radiant resonator, at which point it strongly destructively interferes with the radiant resonator, leading to a transmission peak, described as an EIT analogue. As the distance between the resonators is increased, this transmission peak increases in amplitude, and the radiant resonance properly splits into two distinct coupled resonance conditions. The splitting distance in frequency increases progressively as the capacitive coupling is increased as shown in figure (3.16 (b)) with the peak frequencies tabulated in figure (3.16 (c)). When G = 10 μm, the difference between the bonding and anti-bonding resonances is 0.18 THz with this progressively increasing to 0.45 THz when G = 2 μm.

(a) Comsol Unit cell

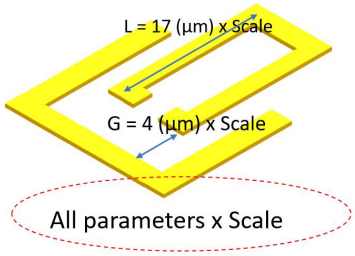

(c)

Scale	f Bonding (THz)	f anti-bonding (THz)
0.81	1.78	2.35
0.78	1.87	2.45
0.74	1.95	2.55
0.71	2.04	2.68

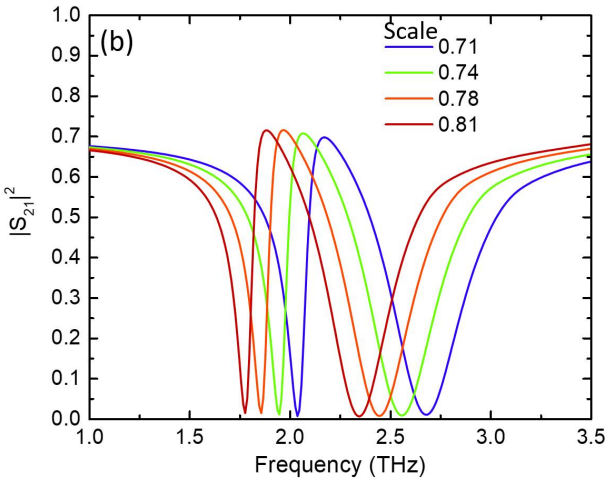

Fig. 3.17 (a) Illustration of the Comsol unit cell for the coupled resonator highlighting tuning of Scale value. (b) Transmission through coupled metamaterial array for different values of Scale. (c) Table of resonance frequency positions. G=4 μm and L=17 μm

The final parameter to test in simulation is the overall linear tuning factor, Scale. As was shown in chapter 2, linearly increasing all the lithographic tuning dimensions of a device should decrease the resonance frequency of the device with a roughly inverse correlation. With the coupling regime determined by tuning G and L, the absolute value of the bonding and anti-bonding peaks can be shifted by tuning the value 'scale'. This is illustrated in figure (3.17 (a)) with the transmission TDS result shown in figure (3.17 (b)) for 4 different 'Scale'

values. The resonance features are shown to red shift as the Scale value is increased from 0.71 to 0.81. According to the table of resonance values shown in figure (3.17 (c)), the percentage difference in frequency between the bonding and anti-bonding resonance remains constant for each scale value, and hence the coupling condition has not been altered by tuning the 'Scale' value. This tuning parameter can therefore be used to precisely choose the resonance frequencies of the device to match a required QCL for example.

3.3.3 Time domain spectroscopy results

With various coupling regimes, and lithographic tuning methods simulated using Comsol, before going any further with the integration of graphene into these designs, a static resonator device is now fabricated using a standard e-beam lithography mask and thermal evaporation of Ti/Au as described in chapter 2. Four different 1 mm $\times$ 1 mm static metamaterial areas with identical lithographic parameters to the devices simulated in figure (3.17), are fabricated on a single silicon substrate, with an SEM image of the device shown in figure (3.18).

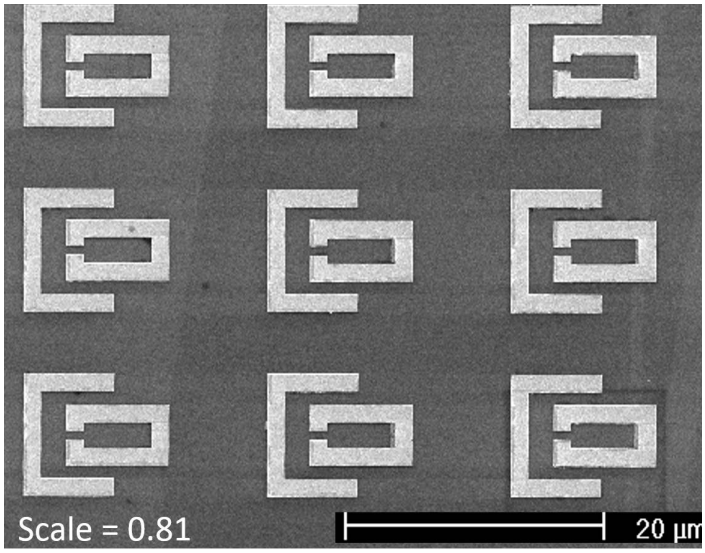

Fig. 3.18 SEM image of static coupled resonator array.

The four different areas, using scale values of 0.71, 0.74, 0.78 and 0.81, are now tested in the transmission TDS system using the same method described in chapter 2. Figure (3.19 (a)) shows the time domain transmitted pulses for four different scaling factors, and the frequency dependant transmission coefficients normalized to transmission through nitrogen are shown in figure (3.19 (b)). For comparison, the equivalent Comsol simulation is shown in figure (3.17 (b)). The TDS results show two resonant peaks per sample area, and there is a predicable blue shift in the resonance condition as the scaling factor is decreased from

0.81 to 0.71 which is shown by the tabulated resonance frequency in figure (3.19 (c)). When comparing the TDS results to the equivalent Comsol simulation, there is once again a blue shift of around 100 GHz at around 2.5 THz for the anti-bonding peak, however the bonding resonance peak is not shifted by the same percentage. This may be because any offset in the refractive index of the surrounding medium will effect the two resonance conditions differently, as the electric field of the resonant modes will have a different spatial distribution, and hence a different mode overlap with the substrate. The largest difference is the high Q factors for the bonding resonance peak shown in the Comsol simulation which are not replicated in the TDS results. This is most likely due to the limited frequency resolution of the TDS procedure, which used a Hann window function with a width of around 15 ps, as described in chapter 2. This results in a convolution of the window function in the frequency domain with the real data, which causes an artificial broadening of spectral features. The anti-bonding peaks are captured more accurately in the TDS measurement when compared to the Comsol simulation as the Q factor is now sufficiently low meaning the broadening of the window function convolution has less effect. The transmission does not go to zero, as predicted by the simulation, which was also observed for the static SRR devices in chapter 2. These areas are reasonably small, (1 mm $\times$ 1 mm) and therefore a portion of the incident spot which may not be perfectly aligned to the active area can leak around the resonator structure. This effect is more pronounced for the lower frequency bonding resonance, which could be due to the spot size increasing as the frequency decreases, as well as due to the frequency broadening already discussed.

3.4 Coupled resonator with graphene

With the static coupled resonator array investigated, the Comsol simulation is now modified to include a graphene square across the sub-radiant resonator capacitive gap. Figure (3.16) showed that the destructive interference effect of the sub-radiant resonator on the radiant resonator could be tuned by physically tuning the displacement of the two resonators. By varying the interaction strength between the resonators, the metamaterial array could be tuned between a coupled resonator regime and a single resonator regime, resulting in a dramatic, and continuous tuning of the resonant frequencies of the metamaterial array. The next step is to try and demonstrate a similar resonance tuning effect using graphene to variably damp the sub-radiant resonator. The goal is to effectively turn the frequency splitting effect on and off by varying the graphene conductivity, and as a result, demonstrating a continuous electrical tuning of the resonance frequency of the metamaterial.

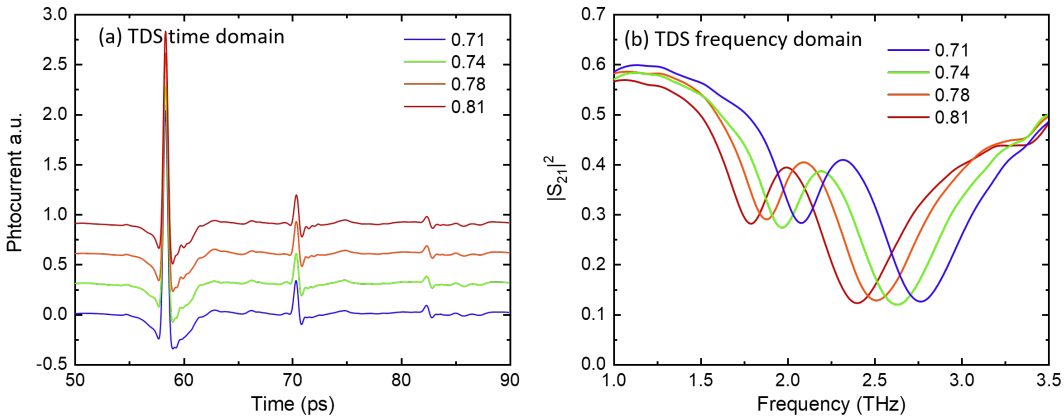

Scale (c)	f Bonding (THz)	f anti-bonding (THz)
0.81	1.78	2.4
0.78	1.88	2.5
0.74	1.98	2.62
0.71	2.08	2.76

Fig. 3.19 (a)TDS transmission result, time domain for coupled resonator arrays with 4 different scaling factors. Results have DC offset for clarity. (b) TDS transmission results, frequency domain, normalized to air. (c) Table of resonance frequency positions for the different 'Scale' values.

3.4.1 Comsol simulation design

The Comsol simulations previously discussed are now modified to include a square of graphene shunting the capacitive gap of the sub-radiant resonator. To actively tune the graphene via electrical backgating, there must be a way of electrically contacting the graphene so charges can be added and removed by the application of a backgate voltage. Metal biasing lines are therefore introduced into the resonator structure, somewhat like the ones included in the 2 SRR device, shown at the start of this chapter. The design to include electrical biasing of graphene is shown in figure (3.20). The biasing scheme uses standard 1 μm thick biasing lines which are connected to bond pads at either side of the array. There is a short line parallel to the y direction which is used to connect just the sub-radiant resonators with the horizontal biasing lines. The graphene, which was directly transferred on top of the metamaterial structure, and then etched using the method described in figure (3.6), is then electrically contacted throughout the sub-radiant resonator. The backgating method described in figure (3.20 (b)) is then used, with the device fabricated on the usual p-doped silicon substrate with a 300 nm SiO_2 insulating layer. Due to the added complexity of these devices, the graphene encapsulation process was not included, to simplify the fabrication process.

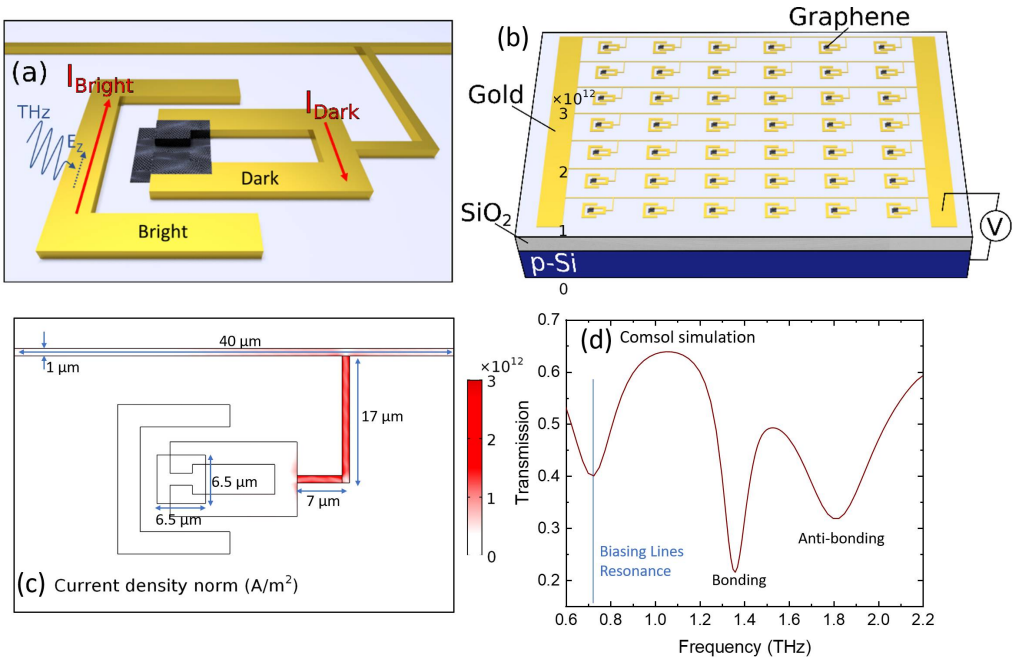

Fig. 3.20 (a) Illustration of coupled resonator unit cell integrated with graphene. (b) Illustration of full metamaterial device with electrostatic backgating. (c) Lithographic unit cell parameters and current density when excited at 0.75 THz. (d) Simulated transmission through metamaterial array with graphene conductivity set to 0 mS.

The lithographic design of the unit cell is the same as shown in figure (3.12 (c)) using G = 4 μm, L=17 μm and Scale = 1, with the biasing lines and graphene patch sizes shown in figure (3.20 (c)). This design is essentially a scaled up version of the previous measured static devices with results shown in 3.19, allowing for it to be easily measured using the TDS system (both resonances below 2 THz). It is important that the extra parallel biasing line section connected with the sub-radiant resonator does not have any resonance features in the frequency region of interest, and also that it does not change the coupling condition between the radiant and sub-radiant resonators. Figure (3.20 (c)) shows the current density in the biasing lines when the metamaterial is excited at 0.75 THz, leading to a strong dipole like resonance. The full frequency dependant S-parameter simulation in figure (3.20 (d)) shows the bonding and anti-bonding resonances are present around 1.4 and 1.85 THz, and hence very weakly interact with the added resonance from the biasing lines at 0.75 THz. Also, the biasing lines are carefully positioned to contact the sub-radiant resonator where there is no expected charge carrier build up for the coupling resonance, to not disrupt the bonding and anti-bonding resonances.

The simulation is now modified by varying the graphene DC sheet conductivity value between 0.3 and 1.6 mS, with the resulting transmission simulation shown in figure (3.21).

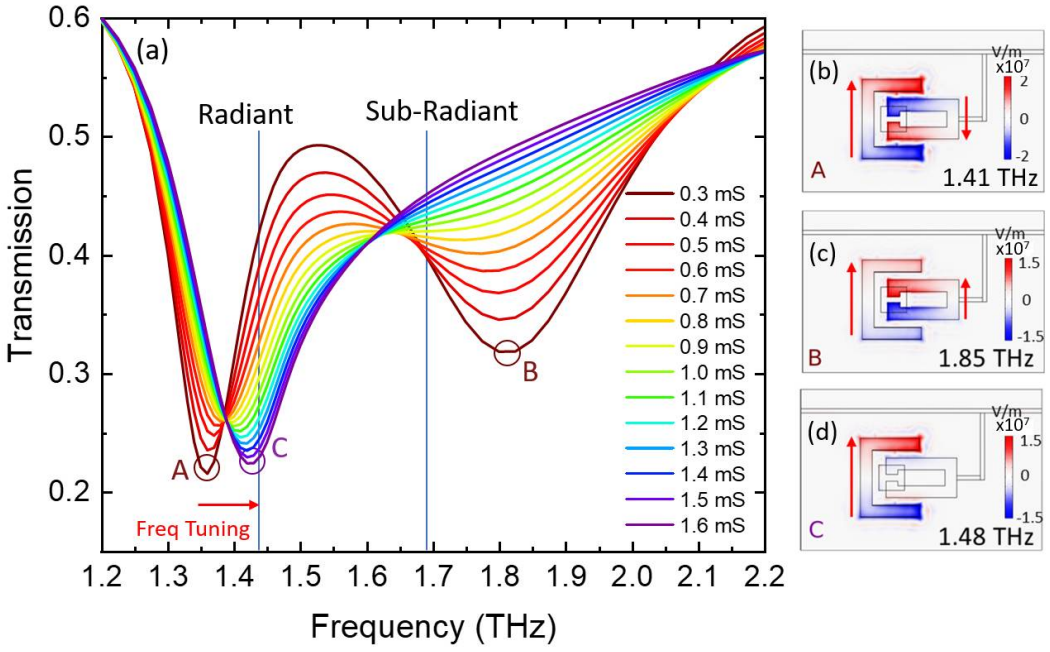

Fig. 3.21 (a) Comsol simulation of transmission through graphene integrated coupled resonator device as a function of frequency with different graphene conductivities. Charge carrier concentration in resonators at (b) bonding resonance (0.3 mS) (c) anti-bonding resonance (0.3 mS) and (d) Lorentz resonance under strong graphene damping (1.6 mS).

In this figure, the standard Lorentz resonance frequencies for the radiant and sub-radiant resonators are indicated, with values of 1.44 THz and 1.68 THz respectively. The charge carrier concentrations at the bonding resonance and anti-bonding resonance conditions with the graphene conductivity set to 0.3 mS are shown in figures (3.21 (b) and (c)) respectively. From these figures it is clear that there is no charge carrier accumulation in the biasing lines, and hence the coupled resonances appear unaffected by its necessary inclusion. Figure (3.21 (d)) shows the charge carrier distribution at 1.44 THz when the graphene conductivity is set to 1.6 mS. There is very little charge carrier accumulation in the sub-radiant resonator, and hence this confirms that the radiant resonator is acting as a single Lorentz oscillator with little influence from the sub-radiant resonator. This confirms that the metamaterial array can be successfully converted from a coupled resonator regime to a single resonator regime by variably damping the sub-radiant resonators with electrostatically tunable graphene. The resonance frequencies are plotted as a function of graphene conductivity in figure (3.22). As the graphene conductivity increases and the coupling regime shifts to a single resonator regime, the anti-bonding resonance Q-factor is reduced, while the bonding resonance is blue shifted towards the radiant resonator Lorentz resonance frequency resulting in a continuous

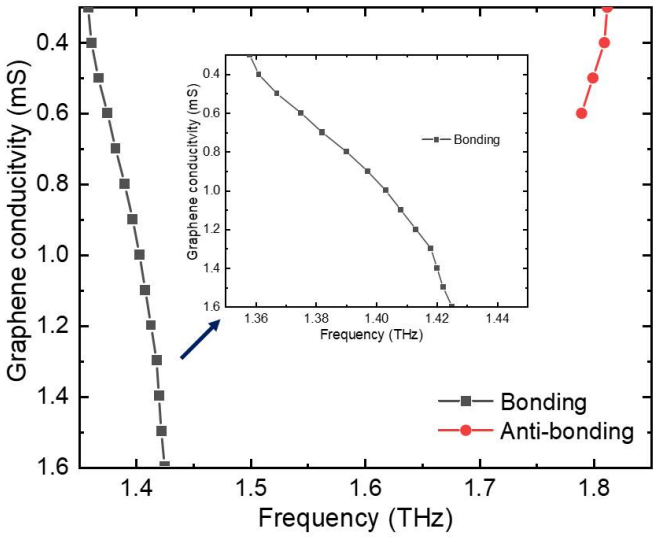

Fig. 3.22 Bonding and anti-bonding resonance frequency for device simulated in figure (3.21). The bonding resonance tuning is highlighted in the inset.

frequency tuning of 70 GHz. In this tuning process the Q factor of the bonding resonance remains around 10, demonstrating effective continuous tuning.

3.4.2 Equivalent circuit model

To further investigate the resonance condition of the coupled resonators as a function of frequency and graphene damping, an equivalent lumped element circuit model is used. As with the resonator array described in chapter 2, the individual resonators in isolation can be described as antennas which have a frequency-dependent impedance described by a LCR electrical circuit. The difference is that these individual LCR circuits are now coupled together via a parallel coupling capacitor. The full, modified circuit is shown in figure (3.23). The AC voltage sources labelled V_1 and V_2 describe the electromotive force from the incident THz radiation driving current in the radiant and sub-radiant resonators, respectively. To account for the smaller coupling with the incident field for the sub-radiant resonator, V_2 is scaled to be 3 times smaller than V_1. The induced current in the Comsol simulations was extracted at resonance frequency when in isolation to determine this voltage ratio.

The individual capacitance values, C_1 and C_2, inductance values, L_1 and L_2, and resistive values, R_1 and R_2, are determined using the same method described in chapter 2, using Comsol simulations containing the isolated individual components. To account for the known 50 GHz offset around 1.5 THz between Comsol simulation and TDS results, the capacitance

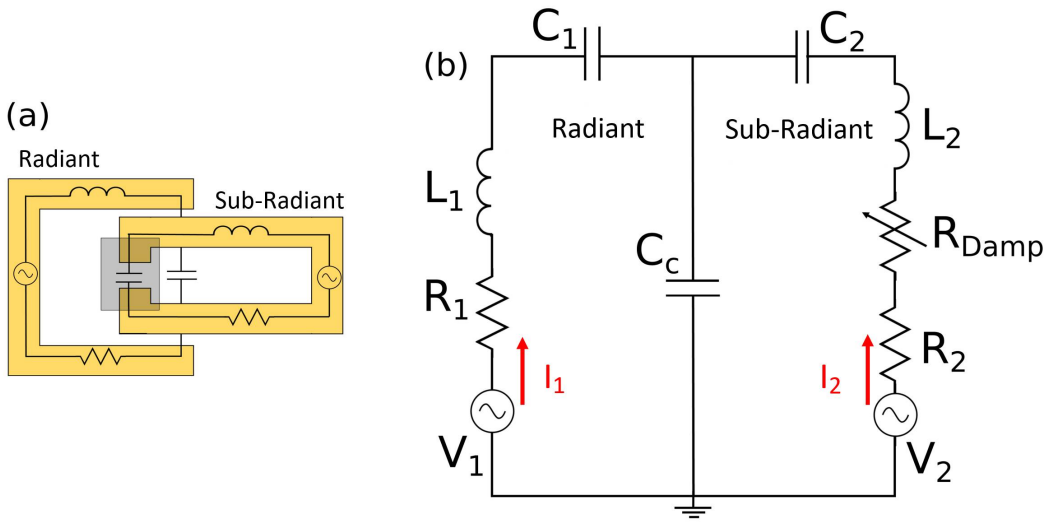

Fig. 3.23 (a) Circuit model illustration for the radiant and sub-radiant resonators. (b) Equivalent circuit model including the capacitive coupling between resonators.

value is scaled accordingly to compensate for this. The extra induced loss by the graphene patch in the dark resonator is once again described by an added variable resistor in series, R_{Damp}. The graphene patch will dissipate power and hence damp the dark resonator as shown in chapter 2. As previously discussed, the inductive qualities of graphene are negligible around 1.5 THz compared to the resonator inductance values and therefore it is sufficient to only consider the resistive loss of the graphene in the circuit model.

With both the individual resonator equivalent circuits determined, the electrostatic, capacitive coupling between the resonators when in close proximity is described as a parallel capacitive coupling, C_C. This capacitor term is used as a free fitting parameter, and is determined using the Comsol simulation when both resonators are included. The power drawn from the two voltage sources can be described according to voltage and corresponding current drawn described in equation (2.9) in chapter 2. With the total power drawn from both sources, P_{Drawn}, is determined as follows.

$$P_{Drawn} = \frac{1}{2} Re(V_1 {i_1}^* + V_2 {i_2}^*) \tag{3.1}$$

In this equation, ${i_1}^*$ and ${i_2}^*$ describe the complex conjugate of the current induced in the radiant and sub-radiant resonators, respectively. Equation (2.11) in chapter 2 can then be used to determine the transmission through the device based on the power drawn, compared to the power incident on the sample. To calculate the current drawn from each current source, a more complex impedance array is required as described in the following equations.

$$\begin{pmatrix} i_1 \\ i_2 \end{pmatrix} = Z^{-1} \begin{pmatrix} V_1 \\ V_2 \end{pmatrix} \tag{3.2}$$

$$Z = \begin{pmatrix} R_1 + jL_1\omega + \frac{C_1+C_c}{j\omega C_1 C_c} & \frac{1}{j\omega C_c} \\ \frac{1}{j\omega C_c} & R_2 + R_{Damp} + jL_2\omega + \frac{C_2+C_c}{j\omega C_2 C_c} \end{pmatrix} \tag{3.3}$$

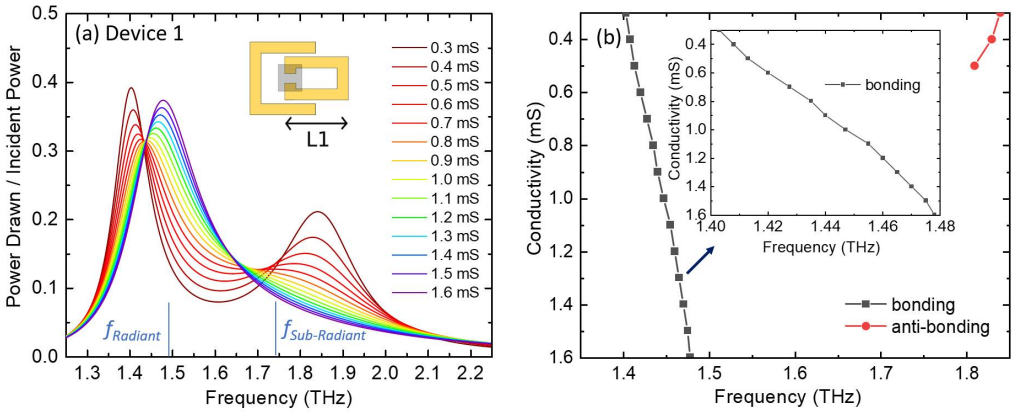

Fig. 3.24 (a) Circuit model simulation of power drawn as a function of frequency and graphene conductivity compared to incident power for Device 1, L2 = 17 μm. (b) Corresponding resonance frequency as a function of graphene conductivity.

This circuit model analysis is performed using the lithographic design scheme simulated in figure (3.21), with this device labelled Device 1. Circuit model analysis for Device 1 is performed with the resultant power drawn from the circuit as a function of frequency and graphene conductivity shown in figure (3.24 (a)). The circuit model values used in this equivalent circuit simulation are listed in table (3.1). The conversion from a coupled regime to a single resonator regime is clearly captured using this simple circuit analysis. Looking at figure (3.24 (b)), which shows the bonding and anti-bonding resonance frequencies as a function of graphene conductivity, a continuous tuning range of around 80 GHz is achieved. This continuous tuning is achieved due to the detuning of the sub-radiant and radiant Lorentz resonance frequencies by 250 GHz, as illustrated in figure (3.24 (a)). To achieve a greater tuning range, a second device labelled Device 2 is designed which uses the same lithographic parameters as Device 1 apart from the sub-radiant resonator length, L, which is increased from 17 μm to 18 μm. Device 1 was lithographically designed to ensure the bonding resonance was close enough to the radiant Lorentz resonance to allow for a continuous tuning as the coupled resonance condition turns into a single resonator condition. With Device 2, we

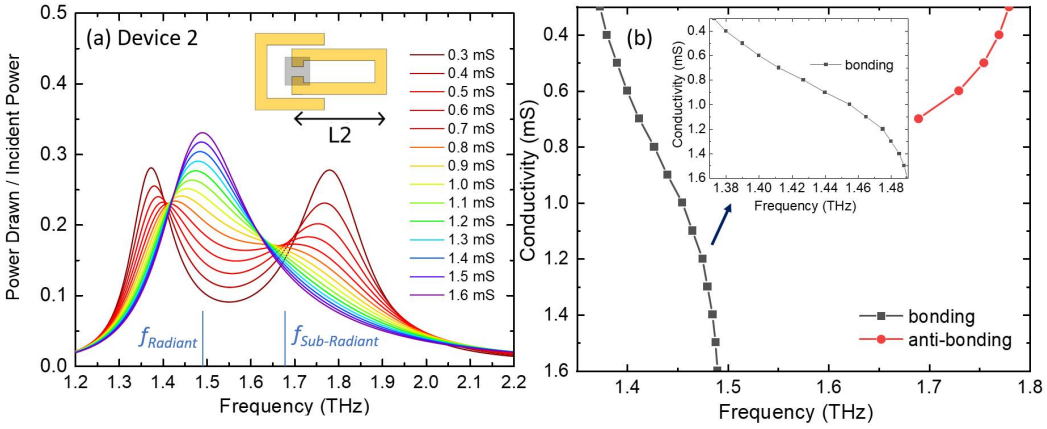

Fig. 3.25 (a) Circuit model simulation of power drawn as a function of frequency and graphene conductivity compared to incident power for Device 2 L2 = 18 μm. (b) Corresponding resonance frequency as a function of graphene conductivity.

Circuit Parameters	Device 1	Device 2
C_1	$5.73\times10^{-16}F$	$5.73\times10^{-16}F$
C_2	$6.48\times10^{-16}F$	$7.09\times10^{-16}F$
L_1	$2.5\times10^{-11}H$	$2.5\times10^{-11}H$
L_2	$1.625\times10^{-11}H$	$1.69\times10^{-11}H$
C_c	$21\times10^{-16}F$	$20\times10^{-16}F$
R_1	10 Ω	10 Ω
R_2	5 Ω	5 Ω

Table 3.1 Derived circuit model parameters for Device 1 and Device 2

are looking to test the limit of this continuous tuning by increasing the frequency difference between these resonances. According to figure (3.15), increasing the length of the sub-radiant resonator will decrease the bonding resonance frequency, and hence the tuning range should be increased when this value is increased between Device 1 and Device 2.

The circuit model simulation result for Device 2 is shown in figure (3.25 (a)). This figure shows that by reducing the detuning of the individual resonator sizes, the coupling regime is more symmetrical around the radiant resonance peak. In this case, the individual resonator Lorentz resonances are only detuned by 175 GHz, resulting in a 120 GHz tuning of the bonding peak towards the radiant peak as shown in figure (3.25 (b)). The amplitude of the peak is reduced more in the intermediate damping case, leading to more of a binary tuning. This shows that there is a trade off between the total tuning range of the metamaterial device, and the conservation of the resonance Q factor.

3.4.3 Time domain spectroscopy results

Device 1 and Device 2 are now fabricated using the lithographic parameters discussed in the previous section. The same fabrication method was used as described for the double SRR device, with graphene transferred on top of device after the metal resonator arrays were first deposited. An SEM image of one of these devices is shown in figure (3.26 (a)). The zoomed in image of the capacitive gap of the sub-radiant resonator is shown clearly showing the etched graphene patch on top of the metal. Like with the double SRR device, the small graphene patches in the device cannot be directly electrically tested, therefore a 1 mm $\times$ 1.2 mm patch of graphene is etched on the same substrate, and electrically connect with a source and drain as discussed in chapter 2. An electrical resistance measurement is performed on this large patch as the backgate voltage is swept to inform the conductivity of the graphene in the device, with the resultant values for Device 1 and Device 2 shown in figure (3.26 (b)). The Dirac point for Device 1 and Device 2 were determined to be around +60 and +100 V respectively. The graphene is not encapsulated, hence this level of p-doping and variation between samples is to be expected. The measured DC sheet conductivity ranges are 1.5 to 0.6 mS and 1.4 to 0.4 mS for Device 1 and Device 2, respectively. This difference in available graphene conductivities is expected due to the difficulty in predicting precisely a priori the tuning range for the graphene due to small inconsistencies in preparation and fabrication.

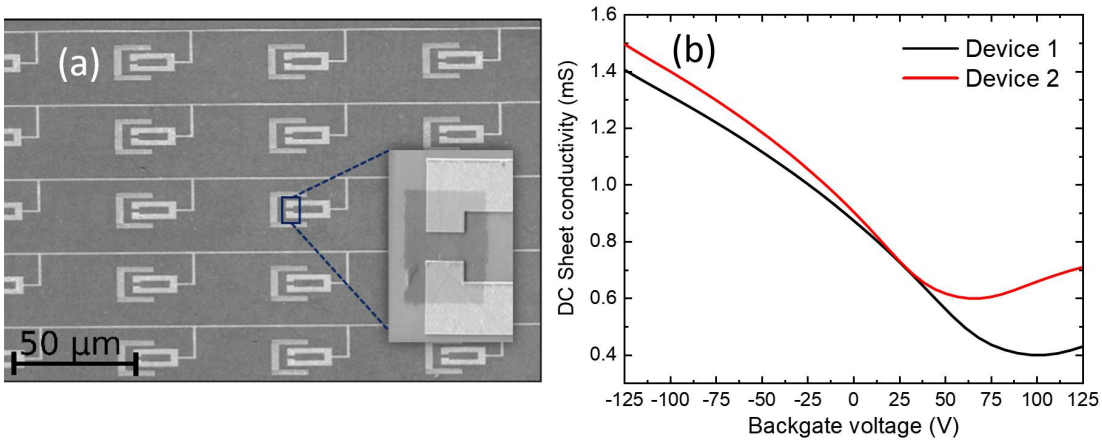

Fig. 3.26 (a) SEM image of Device 2 showing graphene patch shorting sub-radiant resonator capacitive gap. (b) Electrical measurement of graphene conductivity as a function of backgate voltage.

With the graphene conductivity characterised, the frequency-dependent transmission through both devices is now measured using the TDS Menlo K15 system using the methods described in chapter 1. The whole setup is nitrogen purged to remove potential losses due

to water absorption and is normalized with respect to transmission through free space. A 20 ps wide Hann window is applied to select the first transmitted peak and to remove the Fabry–Perot effect arising from multiple reflections from the substrate. Figure (3.27 (a)) shows the measured transmission curves through Device 1 for different backgate voltages. When the graphene is the most conductive, strongly damping the sub-radiant resonator, the radiant Lorentz resonance frequency at 1.48 THz dominates. As the backgate voltage is increased towards the Dirac point, the conductivity reduces and the bonding resonance now becomes more pronounced, shifting the peak resonance frequency to around 1.42 THz. Throughout this transition, the Q-factor remains above 7 with a total continuous frequency shift of around 60 GHz. This experimental data is in good agreement with the Comsol simulation data shown in figure (3.21) which uses the same lithographic tuning parameters. A 50 GHz blue shift is once again observed when comparing the simulation to TDS data due to imperfect material parameters. The Q factor of the Comsol simulation peaks are also higher, which is to be expected due to the frequency resolution constraints of the TDS system, as well as some of the spot power potentially leaking around the active area of the sample.

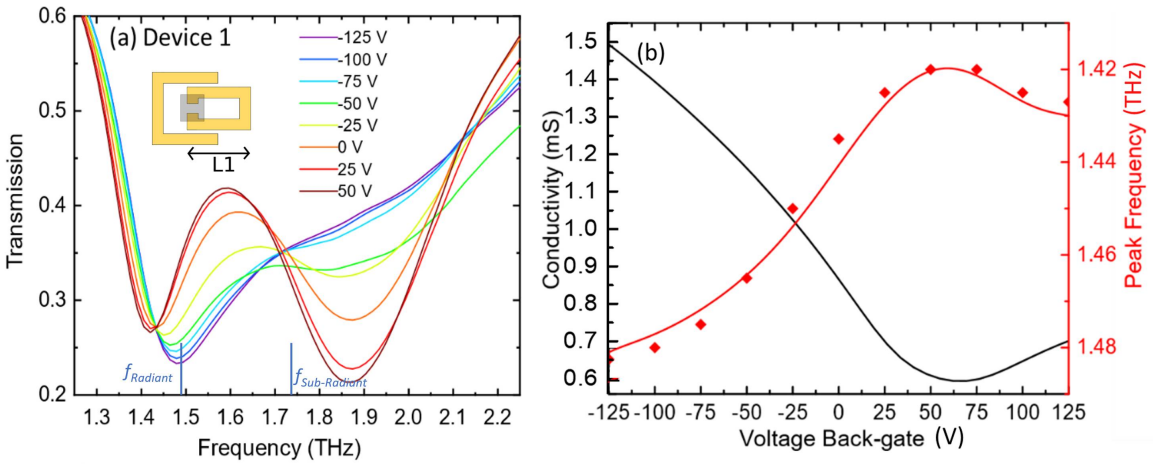

Fig. 3.27 (a) Device 1 TDS transmission as a function of frequency and backgate voltage for L1=17 μm. (b) Predicted bonding resonance frequency from the equivalent circuit model as a function of backgate voltage compared to TDS results.

The TDS measured bonding resonance frequency as a function of backgate voltage, is plotted in figure (3.27 (b)), alongside the predicted values from the corresponding circuit models shown in figure (3.24). The electrical conductivity measurements are also shown for comparison. Despite the simplicity of the circuit model, the TDS data lines up very well.

The TDS transmission measurement is now performed on Device 2 with the result shown in figure (3.28). The longer sub-radiant resonator supports a lower Lorentz resonance than

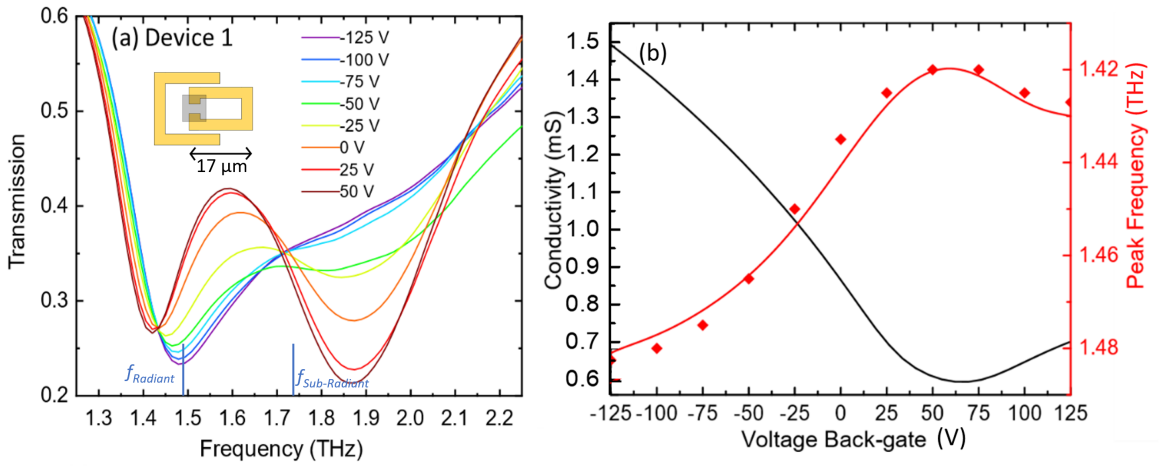

Fig. 3.28 (a)Device 2 TDS transmission as a function of frequency and backgate voltage for L2=18 μm. (b) Predicted bonding resonance frequency from the equivalent circuit model as a function of backgate voltage compared to TDS results.

the sub-radiant resonator in device 1, 1.675 THz instead of 1.74 THz, according to simulation. As discussed in the previous section, this leads to a more symmetric coupling between the radiant and sub-radiant resonators, leading to a greater tuning range of the bonding resonance frequency. The resonance frequency tuning range for Device 2 is around 120 GHz, double the tuning range of Device 1. The transmission through the device shows the resonance peak shifting from around 1.38 to 1.5 THz as the voltage is swept from +100 to -125 V. This greater tuning range does not translate into a continuous frequency shift of the resonance, with the Q-factor changing much more than for Device 1. The bonding resonance dip becomes very poorly defined when the backgate voltage is -25 V, and the tuning range is therefore more of a binary tuning between the coupled resonances and the single radiant Lorentz resonance. The frequency tuning as a function of backgate voltage is once again plotted alongside the circuit model predicted values in figure (3.28 (b)) giving reasonable correlation, despite the poorly defined resonance peak.

3.4.4 Phase modulation

The coupled resonator modulation technique appears to be much more versatile than the single SRR resonator design, whilst also achieving a much more dramatic resonance modulation. These devices would work very well as amplitude modulators, with the transmitted power dropped by over 50 % at 1.8 THz for Device 2 as the backgate voltage is modulated. The EIT phenomena for these coupled resonator designs is accompanied by an extreme modification of

the dispersion properties which could be utilised for a range of applications. The modulation of the resonance frequency has already been discussed in detail, however, the modulation in the transmitted phase through the device can also be dramatically modified, making these devices ideal for use as phase modulators. The TDS measured phase of the transmitted radiation through Device 1 is shown in figure(3.29 (a)), and compared to simulated values determined by the Comsol simulation in figure (3.29 (b)). Sharp modifications of the phase are present in the TDS measurement in the region between 1.4 and 1.5 THz, as well as the region between 1.6 and 1.9 THz. The phase at the resonance should be zero, according to basic Lorentz oscillator, and radiating dipole treatment. There is a sharp change in transmitted phase on either side of this resonance peak with the phase increasing in a positive direction for frequencies greater than the resonance frequency, and in a negative direction for frequencies below the resonance frequency. As the phase changes dramatically around the resonance, a large phase shift can therefore be engineered at 1.45 THz for example, as this frequency is on the right of the bonding resonance peak for low graphene conductivities, and it is on the left of the radiant Lorentz resonance when the graphene damping is increased. This is also the case for the region between 1.6 and 1.9 THz, with a large modulation in the phase observed due to switching from being on the low frequency side of the anti-bonding peak, to the high frequency side of the radiant Lorentz peak. Modulation depths of around 0.15 radians are demonstrated in the TDS results, which is similar to the simulated modulation depth of around 0.2 radians, when considering the available graphene tuning range. Any incident radiation leaking around the active area will wash out the phase modulation, and hence this could be why the TDS measurement modulation depth is slightly less than predicted by the Comsol simulation.

As well as a simple modulation in the transmitted phase, the tunable dispersion properties of the coupled resonator device can also have applications involving the slow light effect [187, 188]. This is achieved by causing an alteration in the group velocity of radiation transmitted through the device. The ability to actively control slow light through a device could have implications for fundamental scientific research as well as the implementation of optical techniques such as slow light buffers [197]. To quantify this phenomenon, the group delay time, Δt_g, described as the time delay of a THz wave packet through the metamaterial region in comparison to air, can be determined by using the following differential equation [198].

$$\Delta t_g = -\frac{\mathrm{d}\Phi}{\mathrm{d}\omega} \tag{3.4}$$

The phase of the transmission through the device is given by Φ, and ω is the angular frequency of the transmitted radiation. To determine the group delay time, the TDS measured

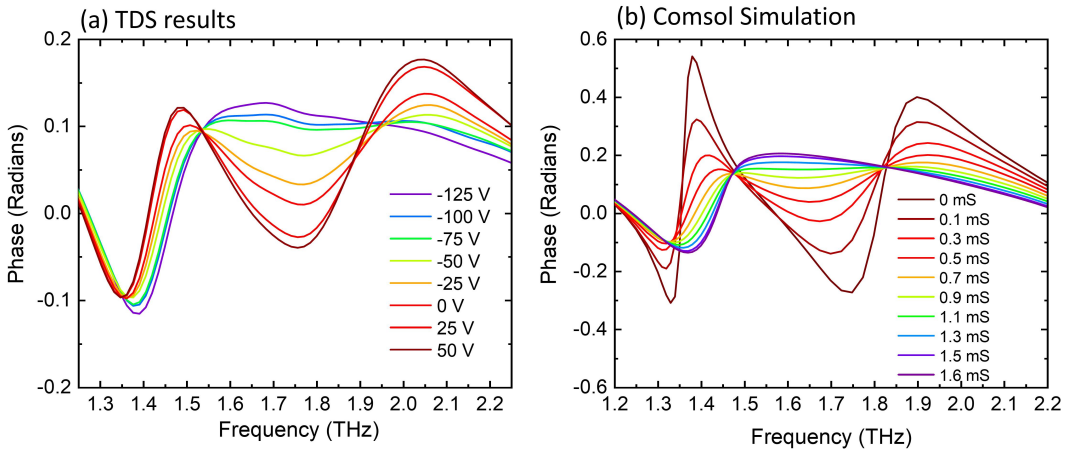

Fig. 3.29 (a) TDS measurement of phase transmitted through Device 1 as a function of frequency and backgate voltage. (b) Corresponding Comsol simulation of transmitted phase as a function of graphene conductivity.

and Comsol simulated transmitted phase is differentiated with respect to the angular frequency for the different backgate and graphene conductivity values. The results are shown in figure (3.30)

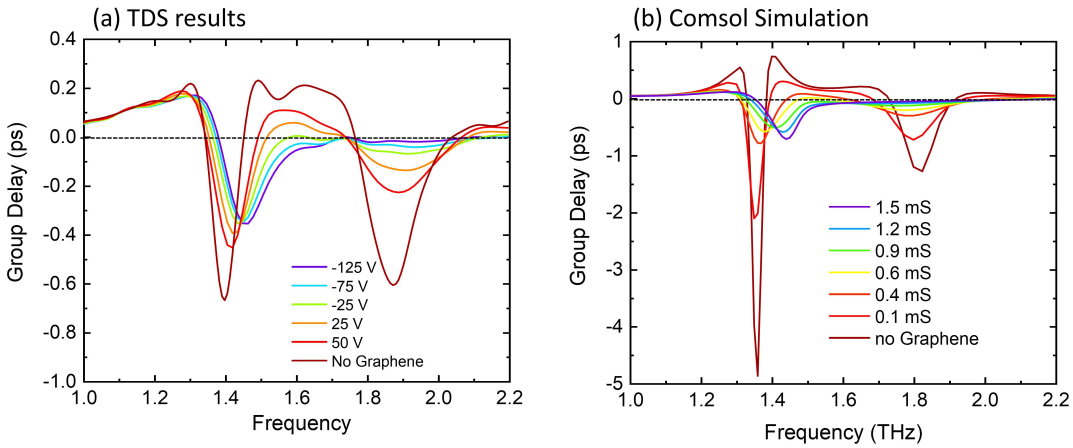

Fig. 3.30 (a) TDS measurement of group delay time as a function of frequency and backgate voltage for Device 1. (b) Simulation of group delay time as a function of frequency and graphene conductivity.

The experimental data using device 1 is accompanied by data using an identical device with no graphene present to determine the group delay when there is no graphene damping. When compared with the Comsol simulated group delay time, there are consistent features with a maximum negative group delay at around 1.4 and 1.85 THz, corresponding to values

of 1.35 and 1.8 THz in the Comsol data. The region of interest for slow light is in between these frequencies when the group delay is positive, corresponding to a positive delay of the transmitted pulse, characterised by the slow light effect. The maximum positive group delay when no graphene damping is present is 0.7 ps at 1.45 THz according to simulation. The TDS measurement gives a maximum value of 0.2 ps, with this discrepancy due, in part, to the limited frequency resolution (50 GHz) of the TDS phase measurement when the TDS time window is only 20 ps. As a result, the phase features measured are artificially broadened and hence the group delay values are underestimated. The overall shape, however, of the group delay is consistent between experiment and simulation with the positive group delay reducing as the graphene damping increases. Despite this device being configured for resonance frequency tuning, it is also effective as a slow light modulator, and could be lithographically optimized to increase the group delay modulation range.

3.5 Chapter conclusion

In this chapter, more sophisticated graphene integrated metamaterial devices have been demonstrated involving lithographically selecting which parts of the metamaterial structure are to be damped. More interesting modulation effects, such as resonant frequency tuning have been demonstrated when compared to devices employing a homogeneous sheet of graphene. The double SRR device demonstrated the ability to address different metamaterial areas independently, leading to a frequency tunable device. The Q factor of the device resonance was very weak, however, this proof of principle could be a precursor to an addressable graphene/metamaterial array device, analogous to a liquid crystal array for example, leading to potential applications such as THz wavefront engineering. To build a high Q factor frequency tunable device, radiant and sub-radiant coupled resonators were investigated. By only damping one of the resonators in the unit cell with graphene, devices were demonstrated which can continuously tune the resonant frequency over 60 GHz with high Q factors, whilst also producing interesting phase and group delay modulation effects.

Chapter 4

Polarisation modulation devices

4.1 Terahertz polarisation overview

In this chapter, electrical polarisation modulation of THz radiation will be investigated. The motivation for this lies in the myriad of current and potential applications where active polarisation control of THz radiation is essential. As discussed in chapter 1, THz communications is one of the more exciting applications for THz science, with polarisation shift keying [199] and polarisation division multiplexing [200] an important part of this picture. The speed of modulation is key for these applications, so fast electrical control over the polarisation condition of the THz radiation is critical. There are also many THz applications in material characterisation where control over the polarisation is required. One pure physics application involves probing and characterizing the surface states of topological insulators such as Bi_2Se_3 by varying the polarisation condition of incident THz radiation [201, 202]. There are many material science and pharmaceutical applications involving probing the birefringence of materials [203] such as pharmaceutical tablets to gain insight into the pill compression process [10, 11]. Also, due to the inherently chiral nature of biological materials, being able to control the ellipticity and handedness of THz radiation could be instrumental in characterizing materials such as DNA and amino acids with THz polarisation spectroscopy [204, 205].Despite these motivations, there is a distinct shortage of available modular devices to control THz polarisation electrically.

There has been work focused on producing unique THz and sub-THz sources which have the ability to emit with different polarisation conditions, for example, polarization tunable photo-conductive antennas [206]. However, due to the technological challenges with building THz sources, integrating an external polarisation modulator with a standardized THz source, such as a QCL or a standard TDS photo-conductive antenna, would arguably have more technological relevance. Static polarisation components such as waveplates and grid

polarisers are available to purchase in the THz range, however the goal of this project is to advance the technology of electrically tunable polarisation devices analogous to the Pockels cell and liquid crystal devices which are so vital for photonics technologies. This chapter will look to demonstrate how to combine chiral metamaterials, which act on the polarisation of transmitted radiation, with the electrical modulation of graphene to build modular devices for all electrical polarisation control of THz radiation.

4.2 Chiral metamaterials

In this chapter, devices which look to act on the angle and ellipticity of transmitted THz radiation are described. For this purpose a new type of metamaterial resonator structure is introduced. The designs discussed in the previous chapters all have mirror symmetry along the y and/or the x axis (excluding any electrical biasing lines) and therefore, when excited by THz radiation polarised in the y direction, E_y, the resonating dipoles induced in the resonators will have no net component in the x direction and hence no E_x radiation is emitted. To act on the polarisation of the incident radiation, a chiral/bianisotropic resonator array which contains no lines of mirror symmetry can be employed.

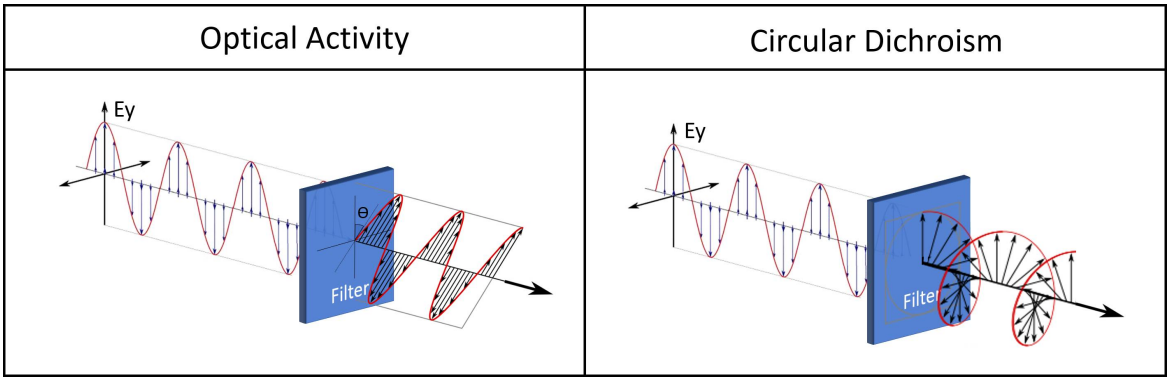

Fig. 4.1 Left side shows a filter displaying optical activity, rotating the angle of transmitted radiation by θ. Right side shows a filter displaying circular dichroism, converting linear radiation to circular polarised radiation.

4.2.1 Chirality and polarisation overview

Chiral metamaterials are of interest in science and technology as they can be used to exhibit exotic optical properties such as optical activity and circular dichroism, as well as being exploitable for producing negative refractive index materials [207]. Optical activity simply refers to a material which rotates the angle of plane polarised radiation as it passes through.

A material exhibiting circular dichroism has a different absorption for left handed circular polarised radiation (*Lhd*) and right handed circular polarised radiation (*Rhd*), and hence the transmission of these components is non equal. These mechanisms are described pictorially in figure (4.1)

To describe the electric field vector, $\vec{E}$, of any given polarisation condition, the electric field is broken down into two orthogonally polarised components, for example E_y and E_x. In this chapter these components are described as traveling plane waves propagating in the z direction, shown in their complex form in the following equations.

$$\vec{E} = E_x \hat{\mathbf{i}} + E_y \hat{\mathbf{j}} \tag{4.1}$$

$$E_x = E_{x0} e^{j(\omega t - k_x z + \phi_x)} \tag{4.2}$$

$$E_y = E_{y0} e^{j(\omega t - k_y z + \phi_y)} \tag{4.3}$$

E_{y0} and E_{x0} describe the electric field amplitude of both components. The angular frequency, ω, is the same for both components and the wavenumber for the x and y polarisations, $k_{x,y}$, is dependent on the effective refractive index of the medium for each component. Any DC offset in the phase between the two propagating components is contained in the $\phi_{x,y}$ terms. For a given position in z, as time t passes through a full period, the real part of $\vec{E}$ will trace out an elliptical path on a polar plot as shown in figure (4.2).

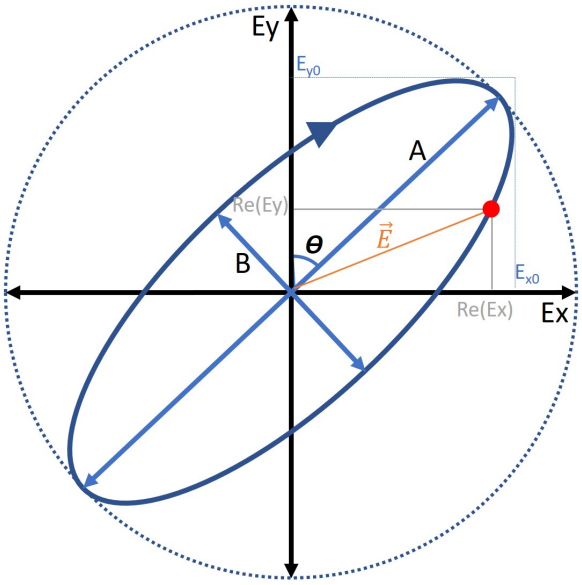

Fig. 4.2 Polar plot representation of an ellipse traced by the real part of the electric field vector at a fixed z point for general elliptical polarisation. The propagation direction of the radiation is in the z direction.

The polarisation can be described generally as elliptical polarisation with a degree of ellipticity, ε, given by the ratio between the semi-major axis, A, and the semi-minor axis, B, as shown in the following equation.

$$\varepsilon = \frac{B}{A} \tag{4.4}$$

The cases of perfectly linearly and circular polarised radiation are characterised by the extremes of ellipticity corresponding to values of 0 and 1 respectively. The angle of the semi-major axis, θ, is particularly relevant for optical activity devices as this describes the polarisation angle, and becomes more relevant the closer to linear polarisation the radiation becomes. To complete the picture, we must determine with which handedness the electric field is tracing the ellipse in the polar plot with time. For this, the linear polarisation basis containing E_x and E_y can be replaced instead with a circular polarisation basis with eigenvalues, *Rhd* and *Lhd*.

$$\vec{E} = Lhd\,\frac{1}{2}(\hat{\mathbf{j}} + j\,\hat{\mathbf{i}}) + Rhd\,\frac{1}{2}(\hat{\mathbf{j}} - j\,\hat{\mathbf{i}}) \tag{4.5}$$

The time and spatial varying eignevalues for the circular polarisation basis can be derived from the previous eigenvalues, E_y and E_x as follows.

$$Rhd = (E_y + jE_x) \tag{4.6}$$

$$Lhd = (E_y - jE_x) \tag{4.7}$$

If we wish to transfer back to the Cartesian basis from the circular polarisation basis, E_y and E_x are found as follows.

$$E_y = 1/2(Lhd + Rhd) \tag{4.8}$$

$$E_x = i/2(Lhd - Rhd) \tag{4.9}$$

From equations 4.8 and 4.9 it is clear that an incident plane polarised wave is equivalent to an equal combination of left handed and right handed circular polarised radiation. It is convenient to use this circular polarisation basis when dealing with chiral materials with ε and θ easily determined from the transmitted *Lhd* and *Rhd* components.

$$\theta = 1/2(arg(Rhd) - arg(Lhd)) \tag{4.10}$$

$$\varepsilon = \frac{abs(Rhd) - abs(Lhd)}{abs(Rhd) + abs(Lhd)} \tag{4.11}$$

θ describes the angle between the semi-major axis and the E_y axis, with positive and negative values corresponding to clockwise and anti-clockwise rotated angles respectively. According to equation 4.11, the value of ε is positive if $abs(Rhd) > abs(Lhd)$ and negative if $abs(Lhd) > abs(Rhd)$. For any given elliptical polarisation, the magnitude of ε describes the shape of the ellipse and the sign of ε determines the handedness with which $\vec{E}$ traces out the ellipse. If ε is positive, the angle of $\vec{E}$ will be rotating in a clockwise direction with time, as is the case in figure (4.2), and alternatively if ε is negative, the angle will rotate in a counter clockwise direction.

Describing elliptical polarisation in a circular polarisation basis, rather than in a linear basis, is convenient when dealing with chiral structures which display an inherent handedness in their physical structure. Therefore, the transmission coefficient through these materials will be strongly dependent on the handedness of incident radiation. For a material displaying circular dichroism, the magnitude of the transmitted *Lhd* and *Rhd* components will be different and hence this material will convert linear polarisation to elliptical polarisation, or ideally circular polarisation if one of these components is zero.

For a material displaying optical activity, it is the phase difference between the transmitted *Rhd* and *Lhd* components which causes the polarisation change. In the ideal case, the absolute value of these terms will remain unchanged, resulting in no change to the ellipticity of the transmitted radiation, however the transmitted polarisation angle, θ, will be rotated. For incident E_y radiation, which by definition has a polarisation angle $\theta = 0$, the phase difference between *Rhd* and *Lhd* is zero. After passing through the chiral material, a phase difference is introduced between *Rhd* and *Lhd* which results in a non zero value of θ, and a rotation of the polarisation angle. To rotate the polarisation completely from E_y to E_x, a phase difference of $\pi/2$ is required between the transmitted *Rhd* and *Lhd* components.

4.2.2 Review of metamaterial polarisers

There has been a wealth of static chiral metamaterial structures designed to exhibit the optical properties discussed in the previous section [208–213]. These involve fully 3D spiral structures, as illustrated in (4.3 (a)). However, for the ease of fabrication, 3D chirality can be artificially produced by overlaying rotated metamaterial layers, with the most simple example illustrated in figure (4.3 (b)). It is also possible to manipulate the transmitted polarisation using a 2D bianisotropic layer, using a structure similar to the one shown in figure (4.3 (c)), ensuring there are no lines of mirror symmetry along the surface.

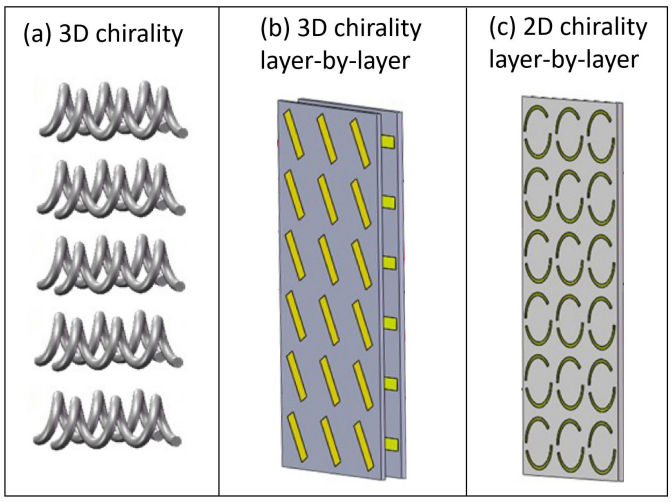

Fig. 4.3 (a) Example of structure which possesses 3D chirality. (b) Example of stacked 2D layers to produce 3D chirality. (c) Example of 2D bianisotropic structure with no lines of mirror symmetry. Figure adapted from reference [213]

For this chapter however, it is the active control of the polarisation condition of THz radiation which is of interest. One way of actively controlling the optical response of these chiral/bianisotropic resonator structures is to integrate photo-active materials such as silicon within the metal resonator structures. As discussed in Chapter 1, silicon can be converted from a dielectric to a conductor when excited with a near-infrared pump beam, creating new conductive channels within the resonator structure or damping the structure as a whole. Zhang *et al*. [139] demonstrated a 3D chiral pillar structure with silicon integrated within the metal structure acting as conductive channels which can short sections of the metamaterial circuit when photo-excited. This structure is shown in figure (4.4).

When the silicon is resistive, the 3D structure displays chiral dichroism, leading to incident linear polarisation being converted into highly elliptical polarisation. When the silicon is photo-excited, the handedness of the resonator structure flips, and therefore the handedness of the transmitted radiation can be modulated. Also, as reported in figure (4.4 (e)) the polarisation angle of the transmitted radiation is shown to be modulated by around 10 degrees at 1 THz, and up to 20 degrees at 1.1 THz. Photo-active silicon has also been used in double layer, 3D chiral devices achieving polarisation angle rotation of up to 45 degrees [140], as well as in single layer, 2D bianisotropic devices [138], achieving successful tuning of the polarisation handedness.

As discussed in Chapter 1, MEMS is another powerful tool to manipulate metamaterial properties. Kan *et al*. [145] demonstrated a tuning method which involves the enantiomeric switching of MEMS spirals to rotate the polarisation of incident radiation. The device

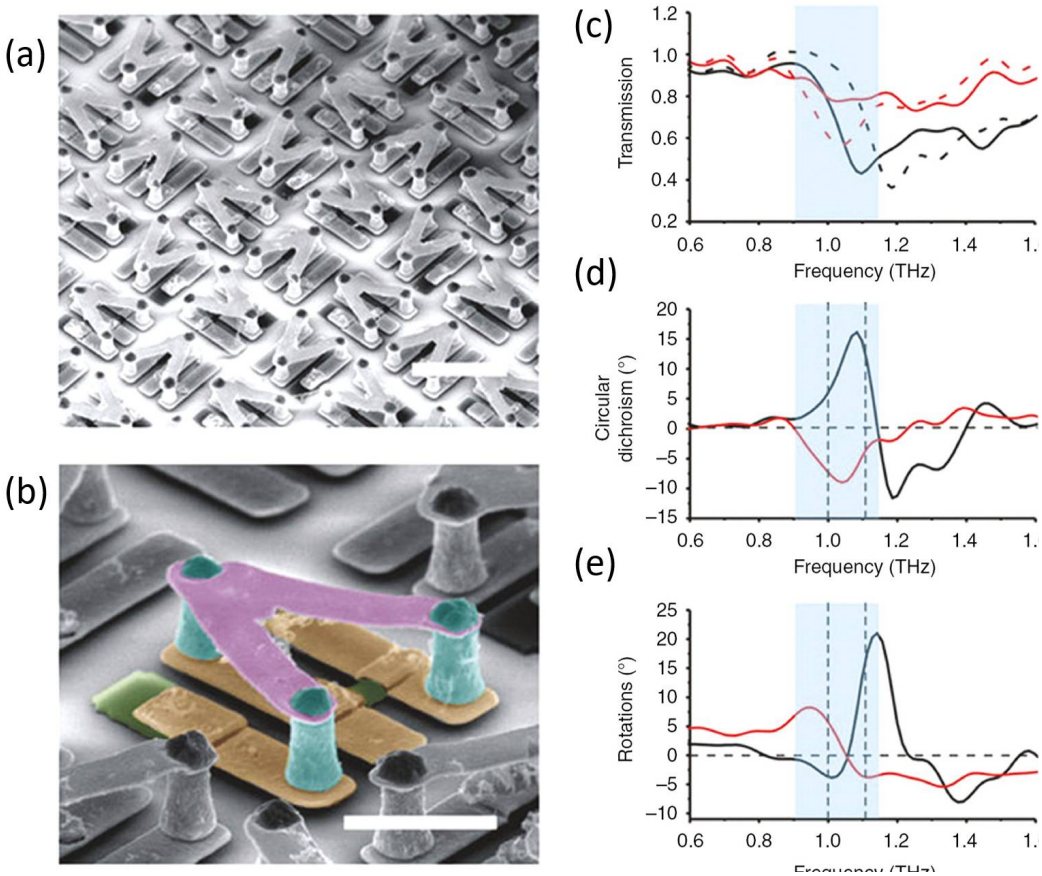

Fig. 4.4 (a) and (b) SEM images of 3D pillar structure device taken from reference [139]. The green sections in (b) are the photoactive silicon sections. (c) The measured transmission spectra of LHD (solid) and RHD (dashed) circular polarisations, without (black) and with (red) photo excitation. (d) Circular dichroism and (e) polarisation angle without (black) and with (red) photo excitation.

structure is illustrated in figure (4.5). The deformable MEMS spirals can be pushed inwards or outwards by applying a pressure differential between the two sides of the film. Spirals have an inherent 3D chirality due to the fundamental handedness of the structure, and by inverting the spiral in the MEMS device, the handedness of the spiral can be flipped. As shown in figure (4.5 (c)), this device displays smooth plane polarisation angle tuning from +30 degrees to -30 degrees as the displacement of the spiral from the surface is controlled.

The active metamaterial devices discussed thus far either use photoactive silicon or incorporate a MEMS scheme to tune the polarisation of transmitted radiation. These modulation techniques have the capacity for large modulation depths, however, an electronic modulation scheme is preferable for many reasons, not least due to the ease of implementation out of the lab, as well as the potential high modulation speeds. The novel devices, presented in this

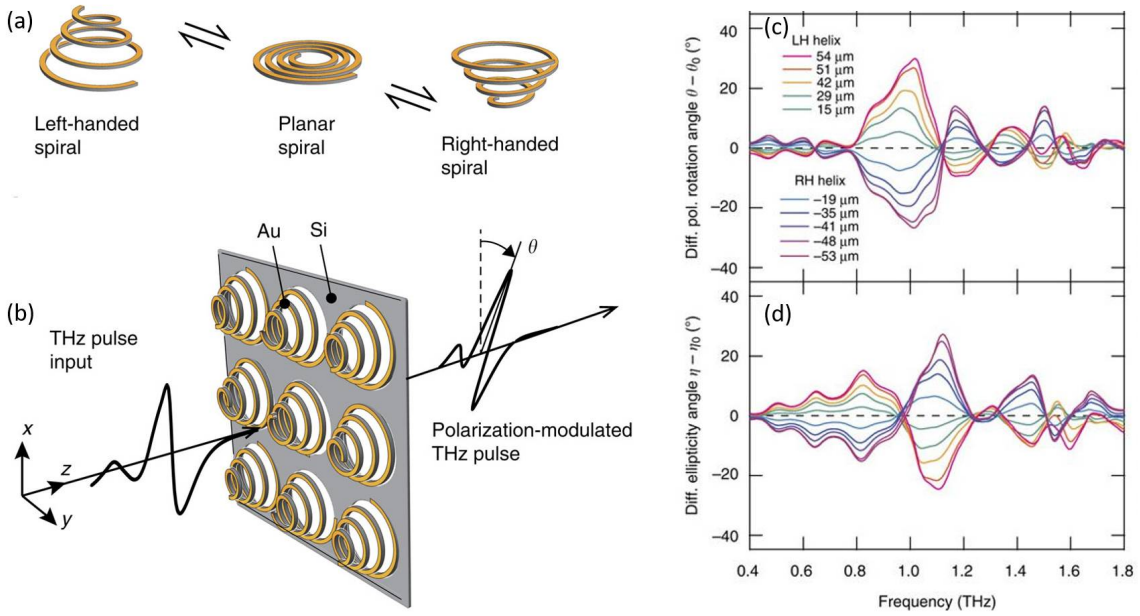

Fig. 4.5 (a) and (b) illustrations of spiral MEMS device operation, taken from reference [145]. Modulation of result for the (c) polarisation angle and (d) polarisation ellipticity.

chapter, will therefore look to incorporate static chiral/bianisotropic metamaterial designs with electrically biasable graphene for active tuning. The goal is to produce devices which display electrically tunable optical activity and circular dichroism for polarisation control of THz radiation.

4.3 Polarisation time domain spectroscopy set-up

To analyze the frequency dependent polarisation properties of transmitted radiation through a polarisation modulation device, the TDS set-up described in Chapter 1 is modified to be capable of detecting relative transmission powers for orthogonal polarisations. The emitter and detector are typically designed to emit maximum power and have maximum detection efficiency respectively along their defined polarisation axis. However, the transmitted radiation from the emitter antenna is not purely linear and therefore a grid polariser is first used to clean up the E_y linear polarisation impinging on the device. These grid polarisers are purchased from 'Purewave' and are made up 5 μm thick tungsten wire, spaced apart by 12.5 μm, and are designed to maximally transmit along their polarisation axis, with ideally zero transmission orthogonal to this axis. To use this set-up to characterise the polarisation conversion effect a given device has on incident E_y radiation, at least two measurements

are required to determine the relative amplitude and phase of E_y and E_x for the transmitted radiation through the device. The alignment of the emitter and detector is very important for relative amplitudes, and hence rotating the detector mid measurement was found to add a large degree of variability, with the detector becoming misaligned as it was rotated. To solve this problem, the detector was aligned and kept fixed at 45 degrees where it has equal sensitivity for the transmitted E_y and E_x components. An identical polariser was then placed between the device and the detector, and rotated to selectively transmit either the E_y or E_x component. This was done using a motorized stage to have as little effect on the alignment as possible whilst allowing the measurement to be performed in a nitrogen purged environment. The new polarisation sensitive TDS set-up is illustrated in figure (4.6).

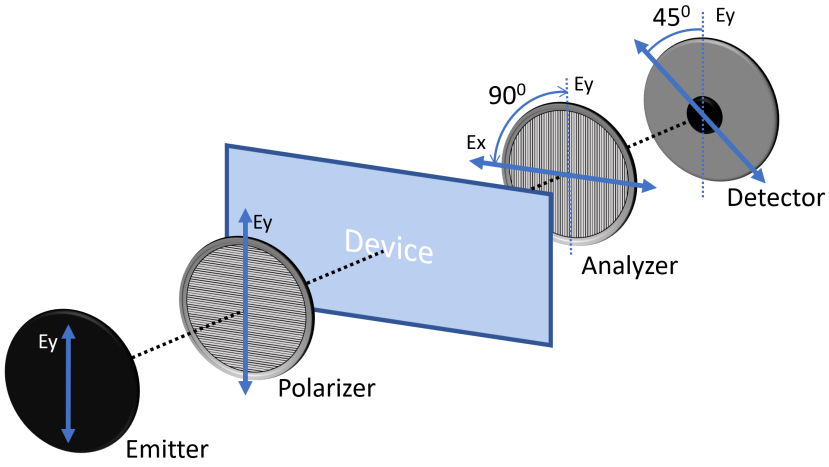

Fig. 4.6 set-up for polarisation sensitive TDS measurement with added grid polariser before and after the device.

To understand the electric field measured by the detector as a function of the relative angles of all the TDS components, a matrix multiplication method was performed. Firstly, to describe the polarisers transmission, including the unwanted orthogonal transmission component due to imperfect isolation, the following matrix was used.

$$Pol_{1,2} = \begin{bmatrix} P_{\parallel}\cos^2(\theta_P) + P_{\perp}\sin^2(\theta_P) & (P_{\parallel} - P_{\perp})(\cos(\theta_P)\sin(\theta_P)) \\ (P_{\parallel} - P_{\perp})(\cos(\theta_P)\sin(\theta_P)) & P_{\parallel}\sin^2(\theta_P) + P_{\perp}\cos^2(\theta_P) \end{bmatrix} \tag{4.12}$$

The terms $P_{\parallel}$ and $P_{\perp}$ describe the transmission components parallel to the polariser axis and orthogonal to the polariser axis respectively and for an ideal polariser, $P_{\parallel}$ would be 1 and $P_{\perp}$ would be zero. In reality, these are complex numbers due to the phase difference between

the two transmitted components which comes from the highly birefringent nature of the polarisers. It is assumed that the parameters for both polarisers, with identical specifications and origin, are the same. θ_p is the angle between the polariser transmission axis and the incident electric field polarization, which is in the y direction in this case as illustrated in figure (4.6). The following matrices, *Emit* and *Detect*, describe the polarisation condition of the radiation produced by the emitter and the polarisation sensitivity of the detector respectively.

$$Emit = \begin{bmatrix} E_{\parallel}\cos(\theta_E) + E_{\perp}\sin(\theta_E) \\ E_{\parallel}\sin(\theta_E) - E_{\perp}\cos(\theta_E) \end{bmatrix} \; Detect = \begin{bmatrix} D_{\parallel}\cos(\theta_D) + D_{\perp}\sin(\theta_D) \\ D_{\parallel}\sin(\theta_D) - D_{\perp}\cos(\theta_D) \end{bmatrix} \tag{4.13}$$

$E_{\parallel}$ and $E_{\perp}$ are the complex emitted electric field components along the standard emission axis and orthogonal to this axis respectively, with θ_E describing the angle of the emitter axis relative to y as the emitted is always aligned in this direction. Similarly, for the detector, $D_{\parallel}$ and $D_{\perp}$, describe the sensitivity parallel to and orthogonal to the typical detection axis respectively, with θ_D describing angle between the incident polarization and detector axis. Finally, to determine a value for the electric field detected, the following Jones matrix multiplication is performed, giving a single complex number, $EField$. This describes the amplitude and phase of the transmitted electric field, normalised to the electric field which would be measured using ideal components all aligned to their maximum power transmission axis. When no device is present, the device matrix, *Device*, is represented by a 2x2 identity matrix and therefore has no effect on the result.

$$EField = Detect^{\mathsf{T}} \times Pol_2 \times Device \times Pol_1 \times Emit \tag{4.14}$$

To test this theoretical framework, as well as to derive the relative physical parameters for the components in the set-up, three sets of measurements were completed with no device present. In these experiments, the photo-response of the detector was measured for different analyser angles as it was swept through 180 degrees. Three different sweeps were performed, with the detector fixed at 0 and 90 degrees respectively. The measured amplitude and phase of the transmitted electric field with the detector fixed at 0 degrees is shown in figure (4.7).

These results are normalised with respect to the electric field measured in the standard TDS configuration with no polarisers present. Two different frequencies are shown to highlight the frequency dependent nature of the polarisation efficiency as well as the orthogonal detector and emitter responses. As illustrated in figure (4.7), we can use this measurement

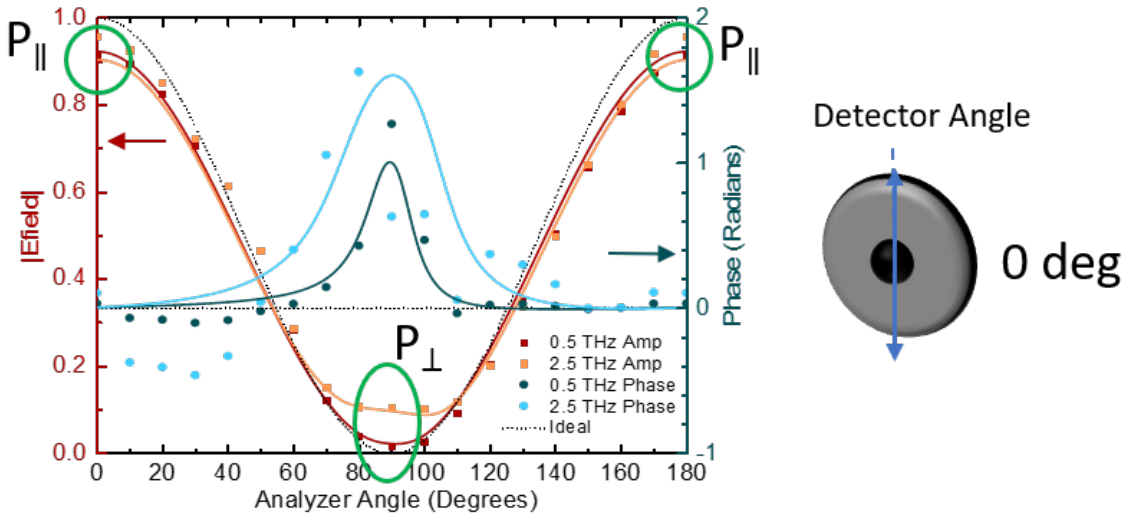

Fig. 4.7 Measured and simulated values for electric field amplitude and phase as the analyser is rotated through 180 degrees with the the detector set to 0 degrees.

to determine values for the transmission through the polariser for radiation polarised on axis ($P_{\parallel}$), and the transmission for orthogonally polarised radiation ($P_{\perp}$), by measuring the amplitude and phase at analyser angles 0 and 90 degrees respectively. To determine the values $E_{\perp}$ and $D_{\perp}$ this experiment was repeated with the detector rotated by 90 degrees with respect to the emitter. This result is shown in figure (4.8). To characterize the detector sensitivity to the orthogonal polarisation axis, $D_{\perp}$, the amplitude and phase of the electric field was probed when the analyser angle was set to 0 degrees. This ensures only E_y polarised radiation is impinging on the detector, which is rotated 90 degrees, and hence the orthogonal sensitivity component can be isolated. To measure the electric field emitted from the emitter in the orthogonal polarisation, $E_{\perp}$, the measurement result with both the analyser and polariser set to 90 degrees is probed. As the detector is orders of magnitude more sensitive on its detection axis, it can be estimated that it is only the E_x polarized component transmitting through the polarizer and analyser which is being detected, allowing for the emitter orthogonal emission term to be characterised.

These scatter graphs describing the measured electric field as a function of analyser angle are accompanied by simulation curves created from equation 4.3. The fitting parameters for these simulations are determined for 0.5 and 2.5 THz using the data as discussed, and shown alongside a simulated curve using ideal parameter values (values of 1 for all on axis terms and values of 0 for all orthogonal terms). The extracted simulation fitting parameters are shown in table (4.1) alongside values extracted in a similar manner for 0.75, 1.5 and 2 THz. $E_{\parallel}$ and $D_{\parallel}$ are normalised to 1 for all frequencies and hence are not shown.

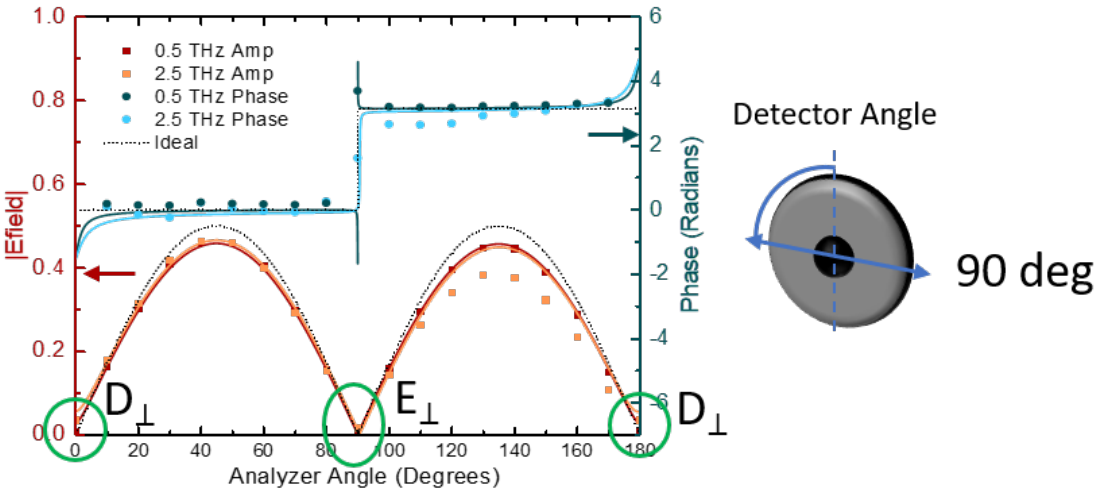

Fig. 4.8 Measured and simulated values for electric field amplitude and phase as the analyser is rotated through 180 degrees with the the detector set to 90 degrees.

Param	0.5 THz	0.75 THz	1.5 THz	2.0 THz	2.5 THz
$P_{\parallel}$	0.96	0.96	0.95	0.95	0.95
$P_{\perp}$	0.011 + 0.018j	0.016 + 0.025j	0.014 + 0.037j	0.012 + 0.069j	0.001 + 0.1j
$E_{\perp}$	+0.03j	+0.01j	+0.04j	+0.06j	0.06j
$D_{\perp}$	-0.03j	-0.03j	-0.03j	-0.04j	-0.06j

Table 4.1 Table of simulation fitting parameters extracted for 5 different frequencies

As the frequency of radiation passing through the polariser increases from 0.5 to 2.5 THz, the parallel transmission decreases slightly from 0.96 to 0.95. However, the orthogonal transmission magnitude increases from 0.02 to 0.1 with the polarisers becoming less effective at isolating linear polarisation. Also the phase difference between the orthogonal polarisations becomes more severe as the frequency increases, which is to be expected from a birefringent material, with the slow axis time delay having a larger effect on the phase as the wavelength decreases. $E_{\perp}$ and $D_{\perp}$ are completely imaginary, which is required by symmetry otherwise the defined polarisation axis for the antennas would change.

As described in figure (4.6), the polarisation set-up to test devices requires the detector to be at a 45 degree angle to the emitter. If all the components were perfect, the measured electric field ratio between the analyser set to 0 degrees and 90 degrees should be equal to the ratio between the emitted E_y and E_x components from the device. Due to the non-zero orthogonal polarisation terms for the components in the set-up, a characterisation of the set-up is performed before each measurement to measure the crosstalk between the E_y and E_x. The crosstalk due to imperfections in components is illustrated well in figure (4.9). When

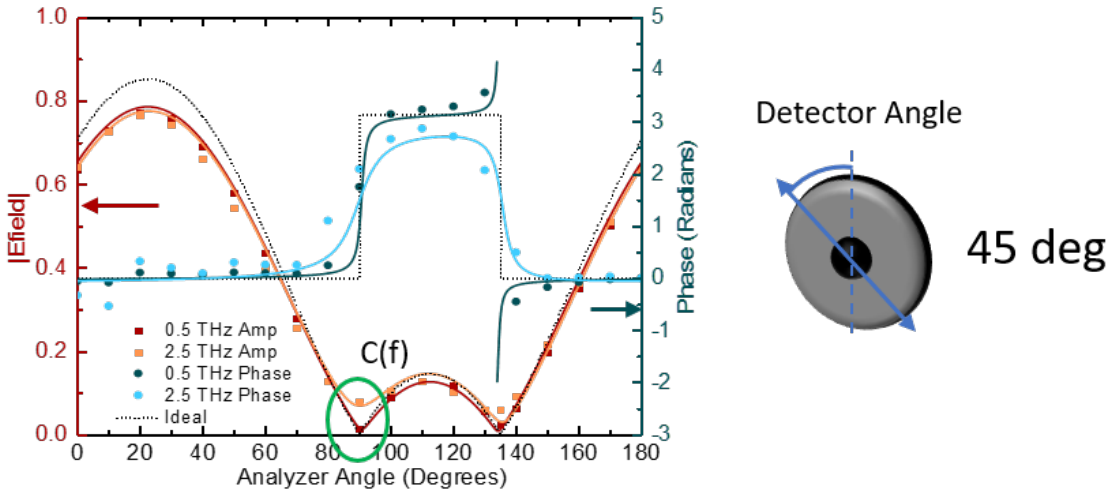

Fig. 4.9 Measured and simulated values for electric field amplitude and phase as the analyser is rotated through 180 degrees with the the detector set to 45 degrees.

the analyser is set to 90 degrees to probe E_x, there should be no signal, as the emitter is set to transmit E_y. There is however a non zero, false positive signal measured and this crosstalk needs to be accounted for in the final measurement. A normalisation measurement is first performed to quantify the amplitude and phase of this crosstalk term as a function of frequency. Two measurements are performed with no device in the beam path. For the first measurement, the analyser is set to 0 degrees to measure the E_y component, E_yMeas, and for the second measurement the analyser is rotated to 90 degrees to measure the transmitted E_x component, E_xMeas . These two terms, containing an amplitude and phase component, are now compared to determine the crosstalk term, $C(f)$, using the following simultaneous equations.

$$E_y(f) = \frac{E_yMeas(f)}{P_{\|}} - E_x(f) \times C(f) \tag{4.15}$$

$$E_x(f) = \frac{E_xMeas(f)}{P_{\|}} - E_y(f) \times C(f) \tag{4.16}$$

$E_x(f)$ and $E_y(f)$ are the actual electric field components impinging on the analyser, which we are trying to determine from the measured values, E_xMeas and E_yMeas. To simplify these equations, E_x is set to zero, resulting in the E_xMeas component coming purely from the crosstalk with the E_y component. This is a reasonable assumption to make as both the emitter and polariser are set to transmit E_y radiation and hence the E_x component will be negligible. $C(f)$ is therefore attributed solely to the imperfect polarisation isolation coming from the analyser. With this simplification in place, $E_yMeas(f)$ is now equal to E_y, and

equation (4.15) and (4.16) can be combined to give the crosstalk term, $C(f) = \frac{E_xMeas(f)}{E_yMeas(f)}$. An example measured crosstalk dependence is shown in figure (4.10).

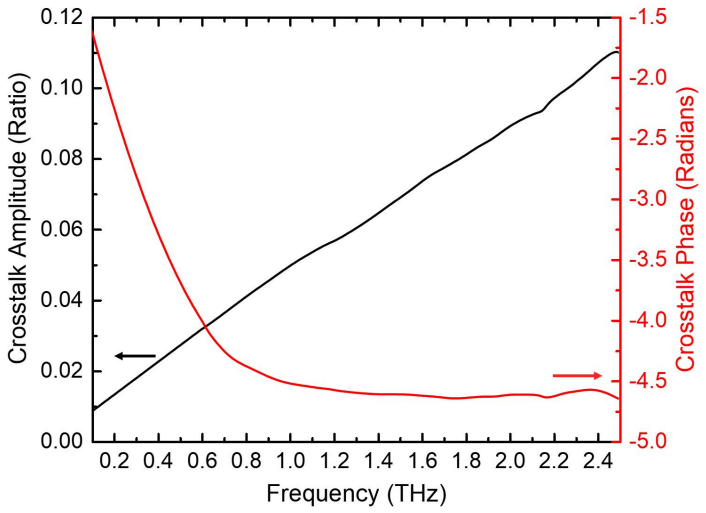

Fig. 4.10 Typical characterisation of the TDS polarisation set-up crosstalk amplitude and phase as a function of frequency

The crosstalk dependence $C(f)$ is first measured before a device is placed in the beam path. Once the device is added, $E_yMeas(f)$ and $E_xMeas(f)$ are measured as before. Now the simultaneous equations, equation (4.15) and (4.16) can be rearranged to determine the actual E_x and E_y signals by including $C(f)$ as shown in equation (4.17) and (4.18).

$$E_x(f) = \frac{E_xMeas(f) - E_yMeas(f) \times C(f)}{P_{\|}(1 - C(f)^2)} \tag{4.17}$$

$$E_y(f) = \frac{E_yMeas(f) - E_xMeas(f) \times C(f)}{P_{\|}(1 - C(f)^2)} \tag{4.18}$$

Using this method, the amplitude and phase of the transmitted E_x and E_y components can be used to fully characterise how a chiral/bianisotropic device changes the polarisation condition of incident E_y radiation.

4.4 Static bianisotropic metamaterial arrays

Before building active metamaterial devices for polarisation modulation, single layer passive metamaterial arrays were fabricated to compare simulation results with TDS measurements from the new polarisation set-up. These static arrays are configured to exhibit 2D anisotropy

and are designed to be excited with E_y plane polarised radiation. Typically, when a metamaterial is excited at the resonance frequency, a resonating dipole is induced in the array with a net component in the y direction. This causes a maximum in reflection and a minimum in transmission due to destructive interference with the incident radiation. Unlike previous devices however, there is no mirror symmetry in these designs, and therefore it is possible for the incident E_y radiation to excite a resonating dipole which has a net non-zero x component. A proportion of the re-emitted power will be polarised in the E_x direction which will be transmitted in the forward and backwards directions as there is no external E_x fields to interfere with. Hence, when excited at resonance with incident E_y radiation, there will be a minimum in transmitted E_y radiation due to destructive interference, and a maximum in emitted E_x radiation in the transmission direction. This causes the polarisation condition of the transmitted radiation through the device to change, and can be determined by the linear combination of the transmitted E_y and E_x terms.

4.4.1 Passive single layer design

Three different single layer designs are fabricated with the array designs shown in figures (4.11, 4.13 and 4.15). The fabrication process for these devices was the same as described in Chapter 2. These devices were fabricated on the same Si/SiO_2 substrate, and photolithography was used for alignment marks before an e-beam lithography step for the metal arrays was performed. As these are static devices with no graphene present, the bond pad and graphene shaping steps are not required. The first device described is a standard L shaped resonator array with figure (4.11 (a) describing the Autocad design used for the e-beam lithography step, and figure (4.11 (b)) showing an SEM image of the resultant resonator arrays for each device, deposited by thermal evaporation of Ti/Au (10/100 nm) through the the e-beam lithography masks.

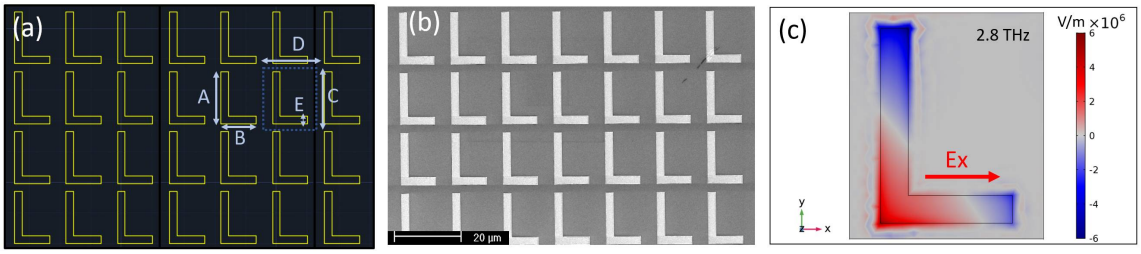

Fig. 4.11 (a) Autocad diagram for the first static 2D bianisotropic resonator array. (b) SEM image of resultant device surface corresponding to Autocad designs after e-beam lithography and Ti/Au deposition. (c) Comsol simulation of E_z 20 nm above the gold indicating the peak charge carrier concentration at different resonance conditions.

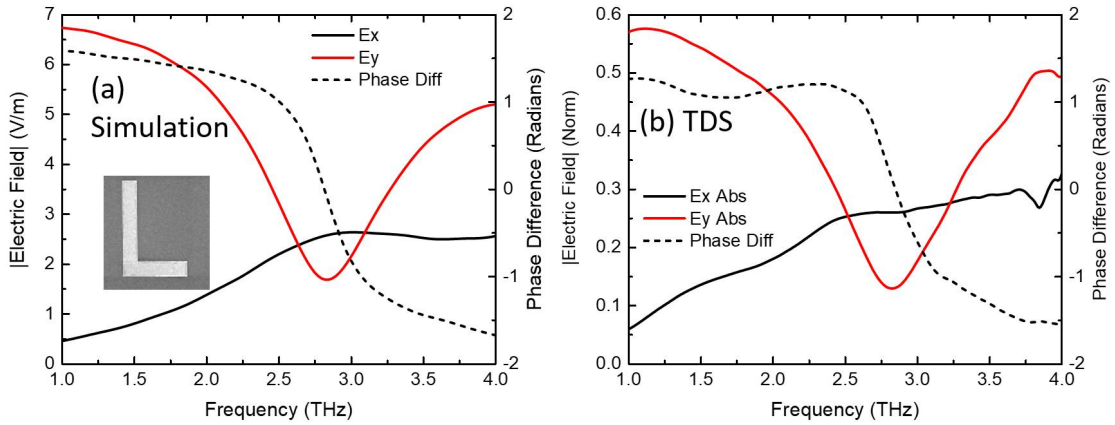

Fig. 4.12 First static bianisotropic device simulation and TDS results for E_y, E_x, and the phase difference between them, as a function of frequency with E_y incident.

A Comsol simulation of the unit cell for this device is shown in figure (4.11 (c)). This figure describes E_z, 20 nm above the resonator at resonance, showing the charge carrier distribution across the resonator when excited by incident E_y radiation at 2.8 THz. This is the second order dipole resonance with a build up of positive charges in the middle of the resonator, and a negative charge build up at the top and right most edge. If this resonator array was symmetrical along the y axis there would be no net electric field induced in the x direction. However, due to the asymmetrical nature of the L shape, when current is induced in the resonator, this includes a net current along the x direction. As a result, there is a net electric dipole moment induced in the x direction due to the build up of charges, despite there being no incident E_x component. This results in an oscillating dipole emitting radiation polarised in the E_x direction which will be in phase with the transmitted E_y component at resonance. The transmitted E_y and re-emitted E_x component as well as the phase difference between them is simulated as a function of frequency in figure (4.12 (a)). A clear resonance frequency is present around 2.7 THz corresponding to a minimum in $|E_y|$ and a maximum in $|E_x|$. The phase difference between E_y and E_x is zero at the resonance corresponding to transmitted linear polarisation. The transmitted polarisation angle is calculated from these electric field values and a polarisation angle of 60 degrees is simulated at the resonance. This device is therefore simulated to rotate the angle of incident E_y radiation by 60 degrees at 2.7 THz.

To test this prediction, this device was now used in the polarisation set-up to determine the proportion of E_y and E_x transmitted when E_y is incident as a function of frequency. The crosstalk for the set-up, $C(f)$, was first characterised using the same method as discussed for figure (4.10). E_xMeas, E_yMeas and $C(f)$ are then used in equations (4.17) and (4.18)

to determine E_y and E_x. These results are presented in figure (4.12 (b)). The TDS result predicts an angle rotation of 64 degrees at 2.7 THz which is within 10 % of the simulation value, showing a good agreement between experiment and theory.

The second device architecture, shown in figure (4.13), consists of two dipole resonators of similar size placed orthogonally to each other. This metamaterial was designed to emit radiation in the E_x direction which was $\pi/2$ out of phase with the transmitted E_y radiation at resonance to produce circular polarisation. When the dipole resonator which is parallel to the y direction is excited by the incident E_y radiation, it drives the resonance in the orthogonal resonator due to the near field coupling in the gap. A Comsol simulation of the charge carrier concentration in the parallel and orthogonal resonators is shown in figure (4.13 (c)). The capacitive coupling is very weak and therefore there is no bonding and anti-bonding resonance, unlike the strongly capacitively coupled devices described in Chapter 3. Instead, at the standard dipole resonance frequency, current is induced in the orthogonal resonator which is in phase with the near field coupling driving force, as it is acting as a Lorentz oscillator. Consequently the currents in the parallel and the orthogonal resonators are $\pi/2$ out of phase at resonance, and therefore the radiated component in the E_x direction will be $\pi/2$ out of phase with the transmitted component in the E_y direction, resulting in highly elliptical polarised radiation.

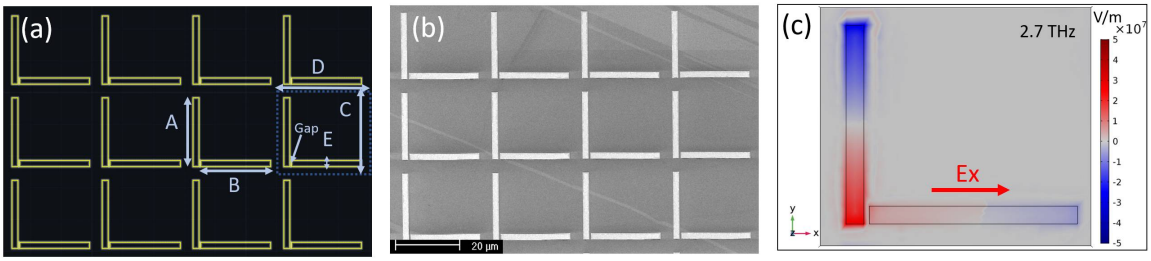

Fig. 4.13 (a) Autocad diagram of second static 2D bianisotropic resonator arrays. (b) SEM image of resultant device surface corresponding to Autocad designs after e-beam lithography and Ti/Au deposition. (c) Comsol simulation of E_z 20 nm above the gold indicating the peak charge carrier concentration at resonance.

The frequency dependent simulation in (4.14 (a)) confirms that there is a clear resonance around 2.7 THz, with the corresponding TDS results in figure (4.14(b)) predicting a resonance at 2.8 THz. This 100 GHz shift is consistent with all the TDS measurements when compared to simulation, throughout Chapter 2 and 3. The phase difference at resonance is -$\pi/2$ leading to nearly circular polarised radiation for both the simulation and the results. The simulated ellipticity at resonance is 0.8 and the corresponding measured ellipticity at resonance is 0.75, once again showing excellent correlation between simulation and results. This device

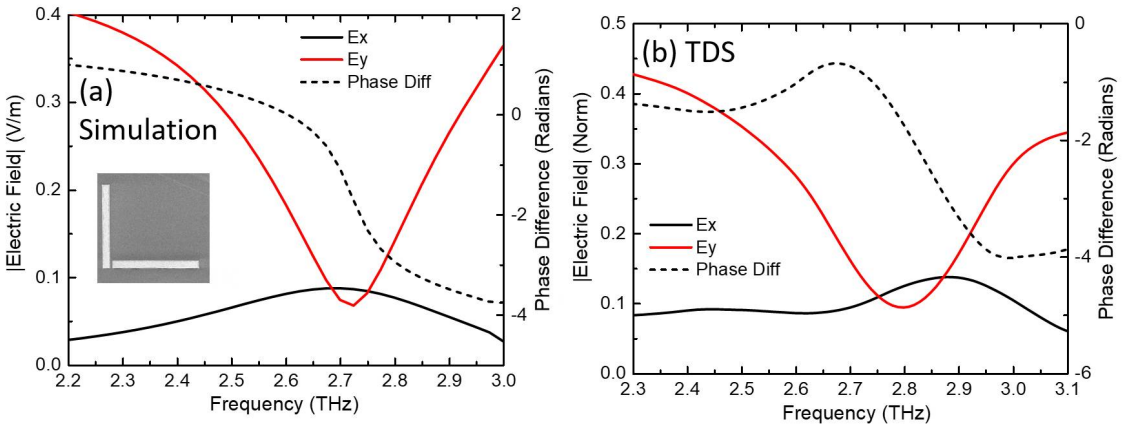

Fig. 4.14 Second static bianisotropic device simulation and TDS results for E_y, E_x, and the phase difference between them, as a function of frequency with E_y incident.

architecture is therefore shown to successfully convert linear E_y radiation into highly elliptical radiation around 2.8 THz.

The third design, shown in figure (4.15), is a more complicated coupled resonator design. This device was designed to take advantage of the sharp coupled resonator features demonstrated in Chapter 3, whilst adding an intrinsic bianisotropy to the design to make it suitable for polarisation modification. The design is very similar to the frequency modulation device presented in Chapter 3, however in this case the bright resonator is the dipole resonator in the middle, which is strongly capacitively coupled with the two dark split ring resonators on either side. The LCR resonance for the split rings is similar in frequency to the dipole resonance of the bright resonator, therefore a splitting of the dipole resonance occurs into a low frequency bonding mode and a high frequency anti-bonding mode. However, unlike the coupled resonator devices presented in chapter 3, due to the added bianisotropy, the dark resonators produce an oscillating electric dipole in the x direction instead of the y direction. Figure (4.15 (c)) shows the simulated charge carrier build up at the bonding resonance (2.65 THz) and anti-bonding resonance (3.5 THz). For the bonding resonance, opposite polarity charges accumulate on either side of the capacitive gap between the bright and dark resonators, leading to both dark resonators exhibiting an electric dipole moment in the x direction. For the anti-bonding mode however, charge carriers with the same polarity accumulate on either side of the capacitive gap, and therefore the induced dipole in the dark resonators is now in the -x direction. The bonding and anti-bonding resonances re-emit E_x components which are either in phase with the transmitted E_y component or 180 degrees out of phase, leading to a clockwise or anti-clockwise rotation of the transmitted plane polarisation angle.

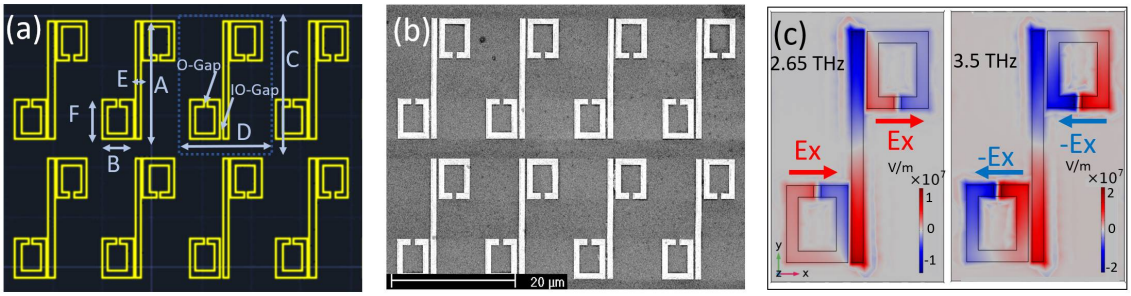

Fig. 4.15 (a) Autocad diagram of the third static 2D bianisotropic resonator arrays. (b) SEM image of resultant device surface corresponding to Autocad designs after e-beam lithography and Ti/Au deposition. (c) Comsol simulation of E_z 20 nm above the gold indicating the peak charge carrier concentration at bonding and anti-bonding resonance conditions.

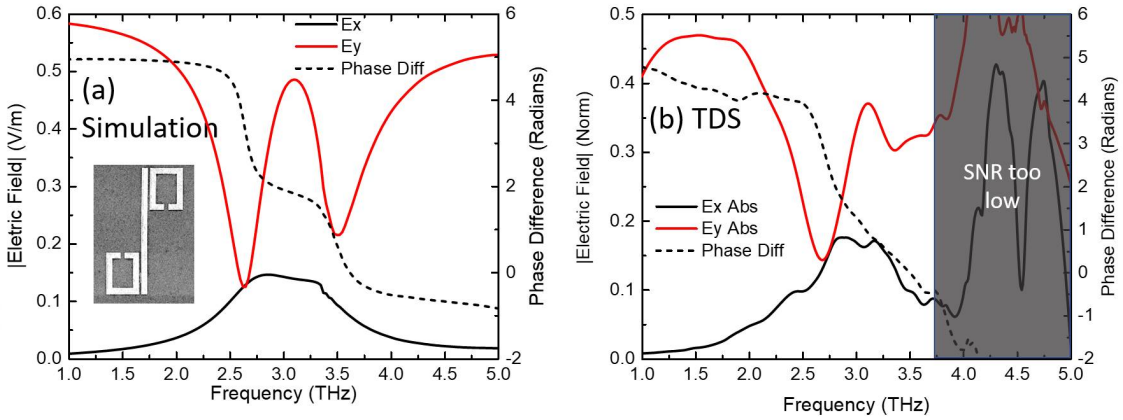

Fig. 4.16 Third static bianisotropic device simulation and TDS results for E_y, E_x, and the phase difference between them, as a function of frequency with E_y incident.

For the third device, the simulated resonance frequencies are 2.6 THz and 3.5 THz, corresponding to $|E_y|$ dips as shown in figure (4.16 (a)). The simulated phase difference at these resonances is π and 0, resulting in transmitted linear polarisation which is rotated in a clockwise and anti-clockwise direction respectively. These opposite rotation directions are predicted by figure (4.15 (c)) which shows the E_x dipole polarity flipping between the bonding and anti-bonding resonances. For the TDS measurement shown in figure (4.16 (b)) the low frequency bonding $|E_y|$ dip at 2.7 THz is well defined, however, as the frequency approaches 3.5 THz, the signal to noise ratio (SNR) of the TDS system becomes too low for reliable measurements, and anything above 3.75 THz is unreliable. A second $|E_y|$ dip is visible around 3.5 THz, as predicted, however it is not properly formed due to the noise levels. The $|E_x|$ term increases in the expected fashion from 1 THz towards the first resonance peak at

2.7 THz, being equal in magnitude to $|E_y|$ at 2.75 THz, with the simulation predicting this to happen at 2.6 THz. At this bonding resonance frequency, the phase difference between E_y and E_x is equal to π for both the simulation and for the TDS results. As a result, the polarisation angle is predicted and measured to be around -45 degrees at this bonding resonance, with an ellipticity close to zero.

From these results, it is clear that the 2D bianisotropic metamaterial designs, with lithographic tunings shown in table (4.2), have a diverse tuning capability, displaying both optical activity and circular dichroism. These results were taken using an integration time of 200 seconds in the TDS system, however, going forward it was decided to increase this integration time to 500 seconds to increase the stability of the measurements, particularly when considering the phase component. Further to this, the phase is very sensitive to the nitrogen purging process, especially at higher frequencies, so instead of waiting for 20 minutes to take measurements after starting nitrogen purging this time was increased to 1 hour to allow the humidity level to drop below 5 % and to stabilize. For the second iteration of devices, it was also decided to lithographically define their resonances to be below 2.5 THz to increase the SNR of the TDS measurement. In the next section, graphene will be introduced into the device design to produce an active metamaterial array, capable of electrically tuning the polarisation of the transmitted THz radiation.

Device	A	B	C	D	E	F	Gap	O-Gap	IO-Gap
First	17.4	11.83	20.184	17.4	2.4	-	-	-	-
Second	21.6	22.68	25.92	29.484	1.944	-	0.6048	-	-
Third	23.4	6.24	27.3	17.55	1.17	7.8	-	0.78	0.39

Table 4.2 Lithographic tuning parameters describing the device designs shown in figure (4.11, 4.13 and 4.15). Sizes in μm.

4.5 Active single layer device

The approach taken in this chapter to create an active polarisation modulator, involved a 2D bianisotropic metamaterial structure incorporated with electrostatically gated graphene to variably damp the resonance condition, and hence modify the transmitted polarisation through the device. Any of the static devices discussed in the previous section could be converted into active devices by the inclusion of graphene. However, as was shown by the frequency modulator device in chapter 3, using a coupled resonator scheme and only variably damping one of the resonators with graphene, instead of damping the whole resonator array, results in much higher Q-factor resonances, and greater modulation depths. Therefore, the

third static resonator device design was chosen to be converted into an active polarisation modulator. The base metamaterial structure for the active device is therefore similar to the third static 2D device shown in figure (4.15), with added biasing lines to electrically contact the dark resonators, which have variable graphene damping included.

4.5.1 Active single layer design

The active device structure is illustrated in figure (4.17 (a)) along with an SEM image in figure (4.17 (b)), showing the bright dipole resonator which is in the middle and two C-shaped dark resonators on either side, with graphene patches covering the capacitive gaps. These dark resonators are connected to bond pads on the right and left side of the device via the thin metal biasing lines. As with the frequency modulator device in Chapter 3, these biasing lines are designed to exhibit optical resonance features at a much lower frequency (< 1THz) than the relevant frequency for the device. Fabrication for this device follows the same process as the frequency modulator device, using a different E-beam mask to define the new metal resonator array. As with the previous devices, a 1.2 mm $\times$ 1 mm graphene patch with a source and drain is fabricated on the same sample for electrical characterisation.

When the graphene conductivity is low, near the Dirac point, the device will act in a similar manner as the static device shown in figure (4.16), causing a rotation in the transmitted polarisation angle at the bonding and anti-bonding resonance frequencies. When the graphene conductivity is increased by inducing carriers via back gating, the dark resonators will essentially be switched off, leaving a standard dipole array, which is not bianisotropic and hence will transmit E_y radiation with little polarisation rotation. This operating principle is diagrammatically illustrated in figure (4.17 (c)). Incident E_y THz radiation is rotated by an angle, θ, after passing through the device which is dependent on the graphene conductivity controlled by the backgate voltage. A Comsol simulation of the transmitted E_y and E_x components when E_y radiation is incident, with very low (0.1 mS) and very high (1.9 mS) graphene conductivities is shown in figure (4.18 (a) and (b)). By observing the transmitted E_y component in these figures, it is clear that the metamaterial array is in a coupled resonator regime when the graphene conductivity is at 0.1 ms, with transmission dips at 1.65 THz (bonding resonance), and 2.07 THz (anti-bonding resonance). When the graphene conductivity is increased to 1.9 mS, the coupled resonator regime is transformed into a single resonator regime with a single Lorentz resonance visible around 1.75 THz. Crucially, for polarization modulation, at the bonding and anti-bonding resonances, the transmitted E_y/E_x ratio is increased as the conductivity is increased from 0.1 mS to 1.9 mS, causing a modification of the transmitted polarisation condition. The corresponding charge

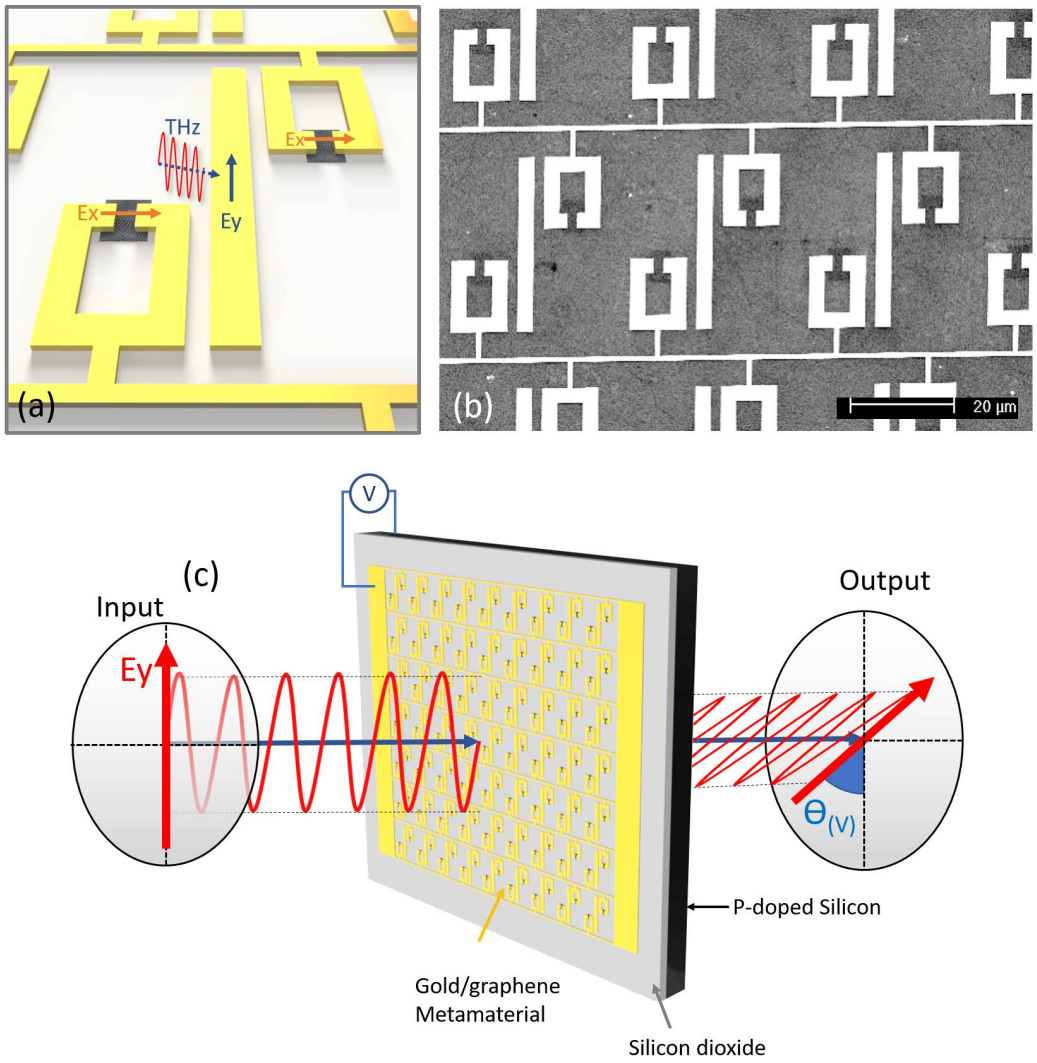

Fig. 4.17 (a) Inventor diagram of single layer polarisation modulator. (b) SEM of device surface, with the white areas indicating gold, and the dark patches showing the graphene in the C-shaped resonator gap. (c) Illustration of device operation.

carrier distribution in the resonators at the anti-bonding and bonding resonances for the two conductivities is shown in figure (4.18 (c)-(f)).

At low graphene conductivity, current in the dark resonators is induced via coupling with the bright dipole resonator when it is excited with E_y radiation at the bonding resonance frequency. The x component of the induced dipole moments in the dark resonators constructively interfere, resulting in a non-zero propagating component polarized in the E_x direction. As the graphene conductivity is increased, loss in the dark resonators is increased, resulting in a damping of the coupling resonance and a smaller charge carrier build up, leading to a reduction in the strength of the net dipole in the E_x direction. As well as this, a reduction in

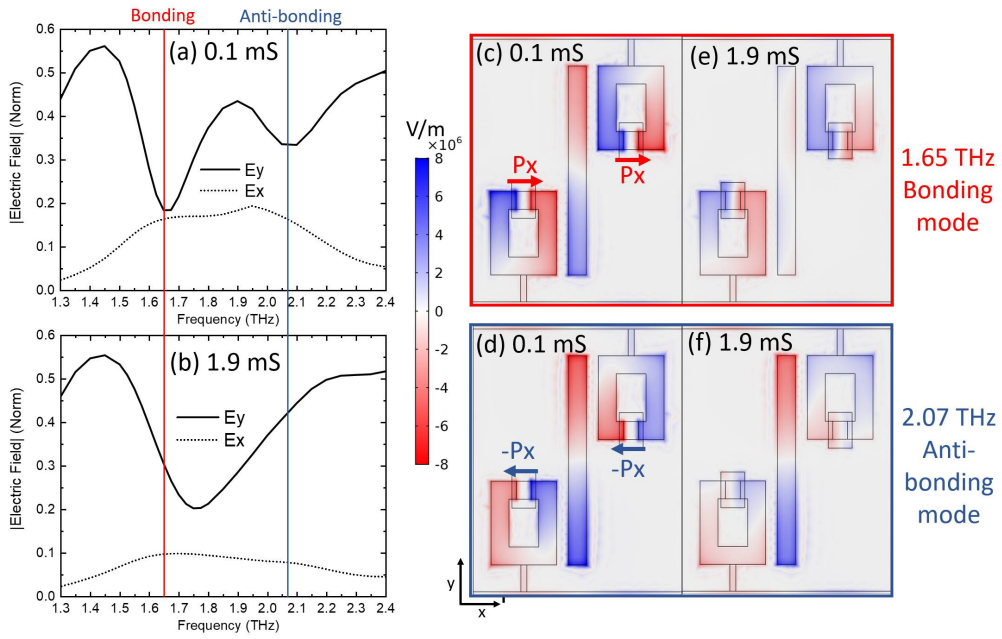

Fig. 4.18 Transmitted E_y and E_x amplitude when E_y is incident for graphene conductivities of (a) 0.1 mS and (b) 1.9 mS. (c)-(f) Simulation of Ez measured 20 nm above the resonators showing charge build up when the graphene conductivity is 0.1 mS and 1.9 mS at the bonding and anti-bonding resonance frequencies. Lithographic tuning parameters shown in figure (4.19)

the bright resonator dipole strength is also observed leading to a larger transmission component of the incident E_y radiation. With the transmitted E_y component increasing, and the re-emitted E_x component decreasing as the graphene conductivity increases, the transmitted polarisation angle is modulated, rotating back towards the incident E_y direction.

4.5.2 Equivalent circuit model

To more easily understand the working principle of this design, an LCR equivalent circuit model, similar to the one shown in the Chapter 3, can be developed. The circuit model considers the coupled resonators as two capacitively coupled LCR circuits. The power drawn by the circuit as a function of incident power, which is proportional to $|1-T|$, is determined to ascertain the change in E_y transmission though the device as a function of frequency and graphene conductivity. In this case however, to determine the re-emitted E_x component, in comparison to E_y, we need to probe the radiation which is radiated in the forward direction from the dark resonators. To do this, the in series resistance must be split into three individual resistors, one which describes ohmic losses in the resonator, R_{Ohmic}, one which describes the

power re-radiated in the reverse direction, R_{Rev}, and one to describe the power re-radiated in the forward direction, R_{Fwd}. As with the circuit model in Chapter 3, the added graphene loss in the dark resonator can be described by an extra variable resistor in series, R_{graph}. The equivalent circuit model is shown in figure (4.19 (b)).

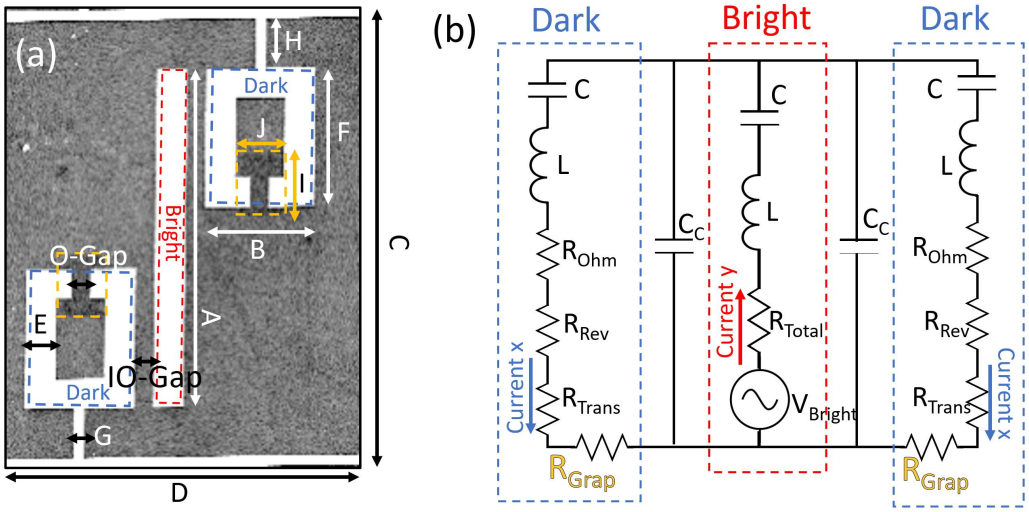

Fig. 4.19 (a) Unit cell SEM image of single layer bianisotropic device. (b) Equivalent Circuit model for single layer bianisotropic device.

Param	A	B	C	D	E	F	G	H	I	J	O-Gap	IO-Gap
Size (μm)	35	11	45	35	3	14	1	4.5	6	4	2	2.5

Table 4.3 Lithographic tuning parameters for active single layer device.

The Comsol simulation using the parameters shown in table (4.3), was first performed for each of the resonators in isolation to determine the individual inductance, capacitance and resistance values. As discussed in Chapter 2, the magnetic field flux as a function of current was used to determine the inductance, and the electric field strength as a function of charge carrier concentration was used to determine the capacitance. Finally, the Q factor of the resonances was used to determine the total in series resistance values. A new process is used to determine the individual resistor ratios in the dark resonators. The ratio between R_{Fwd} and R_{Rev} is identical to the ratio of the power radiated in the forward direction compared to the power radiated in the reverse direction, and from the Comsol simulation, this ratio is determined to be 3.4. This is also given by the ratio between the refractive index of the silicon on the transmission side of the resonator, and the refractive index of the air, on the reverse side of the resonator. The ratio between R_{Ohmic} and R_{Rev} is equal to the ratio of loss given by

$1 - S_{21} - S_{11}$ and the reflection S_{11} found by considering the S-parameters including the dark resonator excited with plane waves polarised in the E_x direction. The value for capacitive coupling was a free fitting parameter which in this case was 1.5×10^{-17} F. The model values determined from the Comsol simulation and used for the graph in figure (4.20 (b)) are given in table (4.4) .

Resonator	R_{Rev}	R_{Fwd}	R_{Ohmic}	R_{Total}	C	L
Dark	12Ω	40Ω	100Ω	152Ω	3.5×10^{-17}F	2.0×10^{-10}H
Bright	-	-	-	100Ω	3.7×10^{-17}F	2.1×10^{-10}H

Table 4.4 Equivalent circuit model values for the design base unit cell shown in figure (4.19 (a))

To determine the graphene conductivity range to be simulated, an electrical measurement was performed on the 1.2 mm × 1.0 mm graphene patch fabricated on the device substrate, using the conductivity measurement technique described in Chapter 2. The measured conductivity as a function of backgate voltage is shown in figure (4.20 (a)) with the Dirac point visible around +30 V and an asymmetric increase in the graphene conductivity on either side of this point, due to the differing carrier effective masses. To convert the sheet conductivity values into R_{graph} values, the Q factor damping of the graphene on the dark resonator as a function of graphene conductivity was simulated in Comsol, when excited in isolation, and converted into the in series damping resistance term. The overall tuning range is from around 0.3 to 1.3 mS and therefore a simulation range was chosen to include these values, with added values at the extremities of this range.

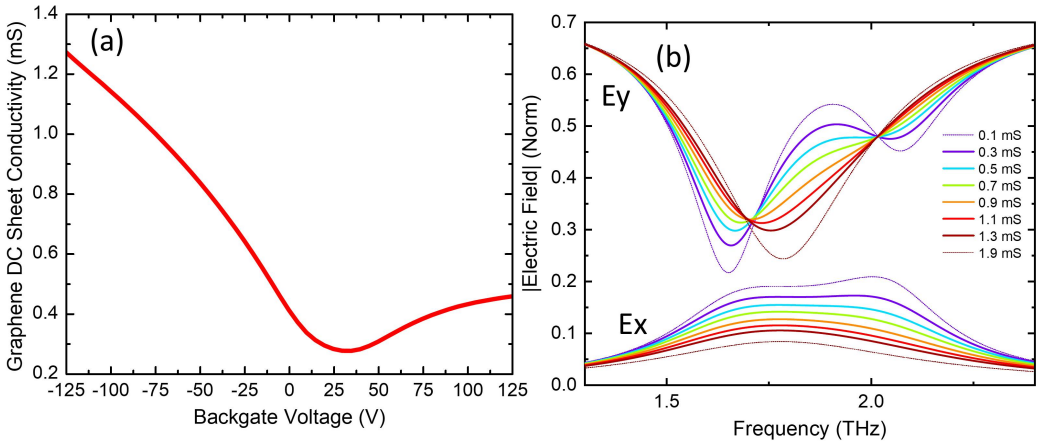

Fig. 4.20 (a) Electrical characterization of graphene DC sheet conductivity as a function of backgate voltage. (b) $|E_y|$ and $|E_x|$ simulated from circuit model.

From figure (4.20 (b)) it is clear that when the graphene conductivity is set to 0.1 mS, the shape of E_y and E_x fit well with the simulation for the third static device in figure (4.16) as well as the Comsol simulation results in figure (4.18 (a)). This device is scaled up in size compared to the static device, resulting in the bonding resonance at 1.65 THz. As the graphene conductivity begins to increase, the bonding and anti-bonding resonances start to disappear. The resonator structure is switching from the coupled resonator regime to a standard dipole resonator regime, with a new resonance at 1.8 THz corresponding to a dip in E_y. This is based on the same mechanism which is discussed in detail for the coupled resonator device in Chapter 3. For this device, however, we are interested in how the proportion between the transmitted E_y and E_x components change as the resonator regime is electrically modified. We are most interested in the bonding resonance at 1.65 THz, where the transmitted E_y component increases with graphene conductivity, and the E_x component decreases. At this operating frequency, the angle of the transmitted radiation is therefore continuously rotated as the graphene conductivity is changed.

4.5.3 Time domain spectroscopy results

With the operating principle of the device understood, it is now tested in the polarisation TDS set-up. Measurements were performed on the device for different backgate voltages, using the same method that was used for the static bianisotropic devices. Once the crosstalk ($C(f)$) for the TDS set-up was determined, the device was placed in the beam path with time domain data $E_yMeas(t)$ and $E_xMeas(t)$ taken for different backgate voltages. When considering the transmission through the device, it may be important, depending on the application, to consider the Fabry-Perot effect caused by the silicon substrate. This will cause a separation of the incident pulse into different path lengths for transmission through the sample, due to a proportion of the pulse being reflected at the silicon/air back facet.

Due to the the multiple reflections in the substrate, the time domain measurements as shown in figure (4.21 (a) and (b)) contain multiple measured pulses with different time delays, reducing in magnitude. Initially, we will just consider the first transmitted pulse, corresponding to the pulse component which passed through the device with no internal reflections. To probe the frequency dependent nature of $E_yMeas(f)$ and $E_xMeas(f)$ from this pulse alone, a cosine filter centered at -25 ps, (E max), with a width of 20 ps is applied, using the technique described in Chapter 1. This measurement has relevance for real world applications for this device as a parylene coating could be implemented to create an anti-reflection coating [214] on the back facet of this device, minimizing the internal reflection peaks. Alternatively, the device could simply be excited at an angle, separating out the transmitted pulses in space.

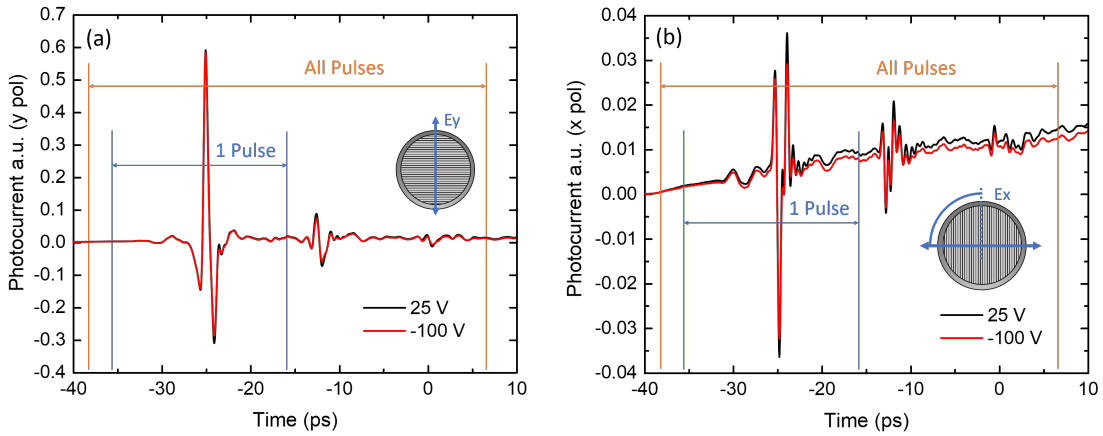

Fig. 4.21 Time domain data passing through single layer device, biased at different backgate voltages for (a)E_yMeas (b)E_xMeas.

Single pulse

$E_y(f)$ and $E_x(f)$ are now determined from the TDS data using equations (4.17) and (4.18) and these values are normalised to $E_y(f)$ when no device is present. These results are compared with Comsol simulation results using the same which is used to probe the predicted transmitted electric field components as a function of frequency and graphene conductivity, negating reflection from the back facet. These measured and simulated $E_y(f)$ and $E_x(f)$ values are shown together in figure (4.22) for comparison.

These values are complex terms and therefore the amplitude and phase components are shown in separate graphs. In figure (4.22 (a)) the measured amplitude of the E_x and E_y components are shown as a function of frequency and backgate voltage. Looking at the amplitude of $E_x(f)$ initially, we can see that across the full frequency range, the amplitude is maximum when the backgate voltage is at the Dirac point, +25 V, with this amplitude reducing as the voltage is decreased towards -100 V. This is due to the level of damping in the dark resonators increasing as the voltage is decreased from the Dirac point, leading to a reduction in the induced charge build up in the dark resonators and a subsequent reduction in the re-emitted radiation amplitude. The amplitude of $E_y(f)$ follows a very similar pattern to the frequency modulator device in Chapter 3. Both of these designs are based on a single bright resonator coupled to either one or two dark resonators. For this design, the coupled resonator bonding and anti-bonding resonances are clearly at +25 V with transmission dips at 1.75 THz and 2.2 THz respectively. For -100 V there is only one visible resonance given by a transmission dip at around 1.85 THz as the metamaterial switches from a coupled resonator to a single resonator regime. The pertinent consequence of this is that the amplitude of E_y at 1.72 THz increases by around 60%. At the same frequency, the amplitude of E_x reduces by

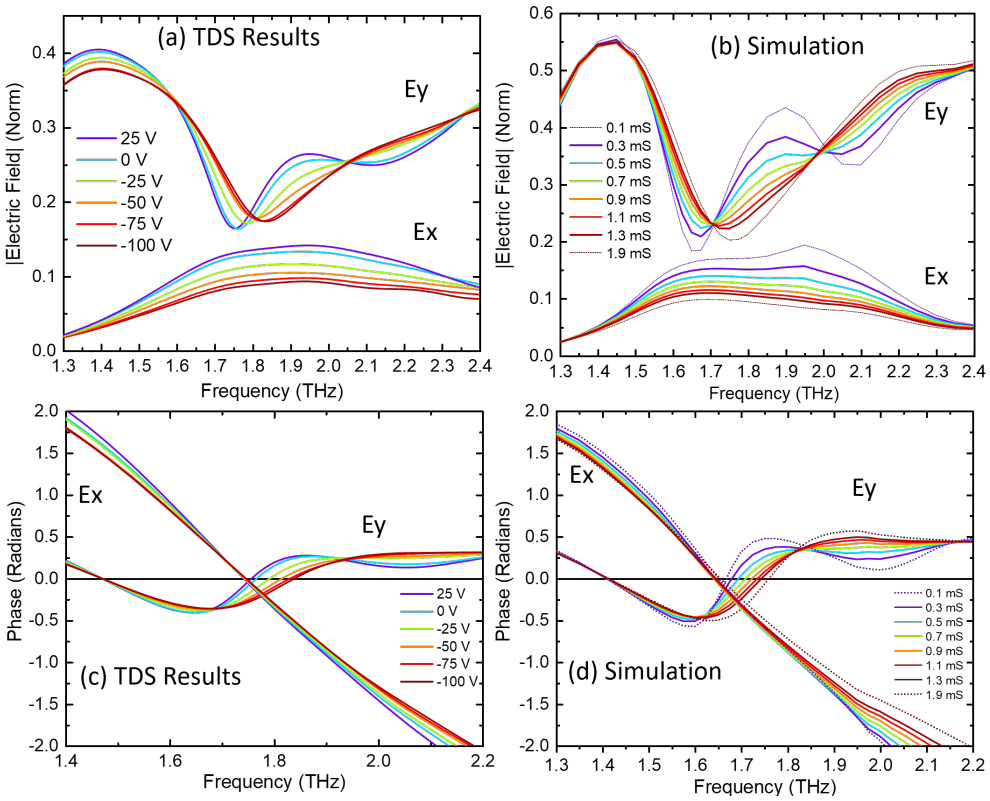

Fig. 4.22 Comparison between TDS measurements and simulation for single layer device with the amplitude and phase plotted for the E_y and E_x components.

around 40 % leading to a change in the ratio of $|E_y|/|E_x|$ from 1.2 to 2.3, and resulting in a modified transmitted polarisation condition. By comparing the TDS results in figure (4.22 (a)) with the simulation results shown in figure (4.22 (b)) there is a very good agreement in terms of the functional form both for the $E_y(f)$ and the $E_x(f)$ components. This is also the case when we compare these results with the circuit model representation shown in figure (4.20). The resonance frequencies of the TDS results are blue shifted by around 75 GHz when compared to simulation, however this is consistent with the results for the other devices shown in Chapter 2 and 3. There is a larger Comsol simulated tuning range for the amplitude of E_y and E_x, with a change of $|E_y|/|E_x|$ from 1.1 to 3. This is due to the fact that a graphene conductivity tuning range from 0.1 to 1.9 mS is used in the simulation compared to a measured device range from 0.3 to 1.1 mS. This larger range was used to gain more insight into the tuning capabilities for the device if graphene with a different conductivity range was used. When the measured device tuning ranges are used in this simulation instead, the ratio $|E_y|/|E_x|$ is shown to change from 1.2 to 2.5, which is within 10 % of the TDS measured values.

To understand the resultant polarisation condition, the phase of the E_y and E_x components has to be taken into account. When the phase difference between the two components is an integer multiple of π, the polarisation is completely linear, corresponding to an ellipticity of 0, described in equation (4.11). For this device to be an effective polarisation rotator, the ellipticity should be as close to zero as possible as the amplitude ratio between E_y and E_x is changed. When looking at the measured phase components in figure (4.22 (c)), the phase of E_x and E_y are equal at a point between 1.7 and 1.8 THz, depending on the backgate voltage. Linear polarisation rotation is also observed at the anti-bonding resonance at around 2.2 THz, with the phase difference approaching π, meaning the angle is rotated in the opposite direction. These two regions would be suitable for polarisation rotation, however, we will focus on the region between 1.7 and 1.8 THz as the $|E_y|/|E_x|$ change is more severe.

In this region, the zero phase difference point increases in frequency as the voltage is decreased from the Dirac point. This frequency is 1.74 THz at +25 V, and increases to 1.79 THz as the voltage is reduced to -100 V. The corresponding simulated cross over frequencies shown in figure (4.22) are 1.67 THz at 0.3 mS and 1.72 THz for 1.1 mS which is commensurate with a frequency shift between the simulated and measured results of 70 GHz. The next step is to plot the polarisation angle and ellipticity as a function of frequency and backgate voltage. To do this, the complex $E_y(f)$ and $E_x(f)$ measured and simulated terms are converted into the *Rhd* and *Lhd* basis using equations (4.6) and (4.7). Then the values of polarisation angle, θ, and ellipticity, ε, are determined from equations (4.10) and (4.11), with the results plotted in figure (4.23).

From figure (4.23 (a)) the angle starts off positive at the lower frequencies, peaking at around 40 degrees at 1.72 THz for the +25 V case. This corresponds to the position in figure (4.22 (c)) where the phase difference between E_y and E_x is zero and the polarisation is completely linear. As the frequency increases, the polarisation angle reduces until it crosses zero at 2.0 THz, which corresponds to a phase difference of $\pi/2$. In this case the polarisation is highly elliptical, with the semi-major axis of the ellipse parallel to the E_y axis. As the frequency increases further, the polarisation angle turns negative, peaking at 2.2 THz corresponding to a phase difference of π, and once again the polarisation is completely linear, and is now flipped to the other side of the E_y axis. From this graph, the frequency where the angle modulation is at its maximum for this device is 1.75 THz. As the backgate voltage is decreased from +25 V to - 125 V, the polarisation angle changes from 39 degrees to 19 degrees. These results are confirmed by the simulation angle results shown in figure (4.23 (b)) showing a remarkably similar functional form with the same frequency offset as discussed for figure (4.22).

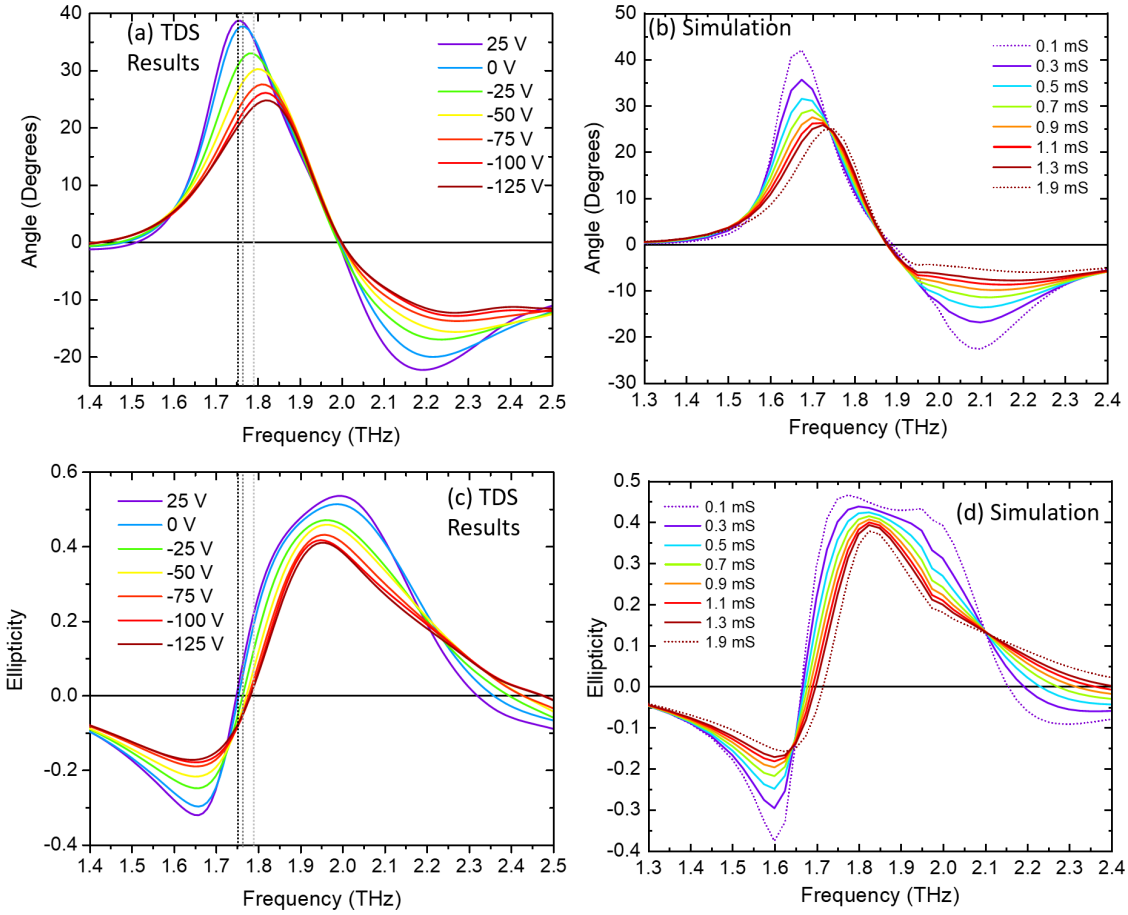

Fig. 4.23 TDS measurement and Comsol simulation of polarisation angle and ellipticity of emitted radiation through single layer device for different backgate voltages, and graphene conductivity values respectively.

The measured and simulated ellipticity values are shown in figures (4.23 (c) and (d)) respectively. At the lower frequencies the ellipticity is negative, corresponding to the polarisation angle rotating in a clockwise direction with time, according to the illustration in figure (4.2). When the ellipticity is zero the polarisation is linear, corresponding to a frequency between 1.7 and 1.8 THz for the TDS results, depending on the backgate voltage. As the conductivity is increased, the frequency for zero ellipticity increases, which is commensurate with the E_y and E_x phase cross over points shown in figure (4.22 (c) and (d)). Beyond this cross over region, the ellipticity is positive, corresponding to elliptically polarised radiation with anti-clockwise procession, peaking at around 0.5 and 0.45 for TDS and simulation respectively. The ellipticity once again becomes zero at the anti-bonding resonance frequency when the phase difference between E_y and E_x, as already discussed, is

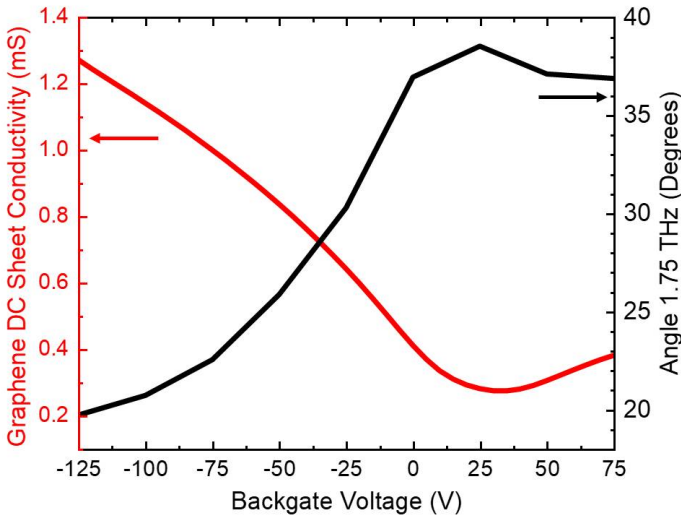

Fig. 4.24 Transmitted radiation angle as a function of backgate voltage at 1.75 THz. Graphene conductivity as a function of backgate voltage is also plotted.

equal to π. The angle as a function of backgate voltage at 1.75 THz is shown in figure (4.24) alongside the graphene conductivity.

When considering the graphs for angle and ellipticity, as the backgate voltage is increased, there are three different frequencies worth highlighting which lead to interesting polarisation modulation effects. These frequencies are 1.75, 1.76, and 1.79 THz, illustrated by the vertical lines in figure (4.23). To visually describe the polarisation condition at these frequencies, the polarisation condition is described by the ellipse traced out over one period by the real value of the electric field, similar to the drawing in figure (4.2). The commensurate polar plots are shown in figure (4.25) for these three frequencies.

These plots are traced out using the real part of the linear combination of E_y and E_x over a time period using a general quadratic equation for an ellipse centered at the origin. The plot can be generated by inserting the absolute values, $|E_y|$ and $|E_x|$ and the phase difference between the E_y and E_x components, $\phi = arg(E_y) - arg(E_x)$, and solving the following quadratic equation for E_y as a function of E_x.

$$\left(\frac{E_x}{|E_x|}\right)^2 - 2\left(\frac{E_x}{|E_x|}\right)\left(\frac{E_y}{|E_y|}\right)\cos(\phi) + \left(\frac{E_y}{|E_y|}\right)^2 = \sin^2(\phi) \tag{4.19}$$

The polarisation condition at 1.75 THz is interesting, as this corresponds to the frequency for maximum polarisation angle change, with the angle rotated by 20 degrees and the ellipticity remaining close to zero. Figure (4.25 (a)) transmitted radiation with a polarisation angle of 39 degrees when the backgate voltage is +25 V with an ellipticity value of zero,

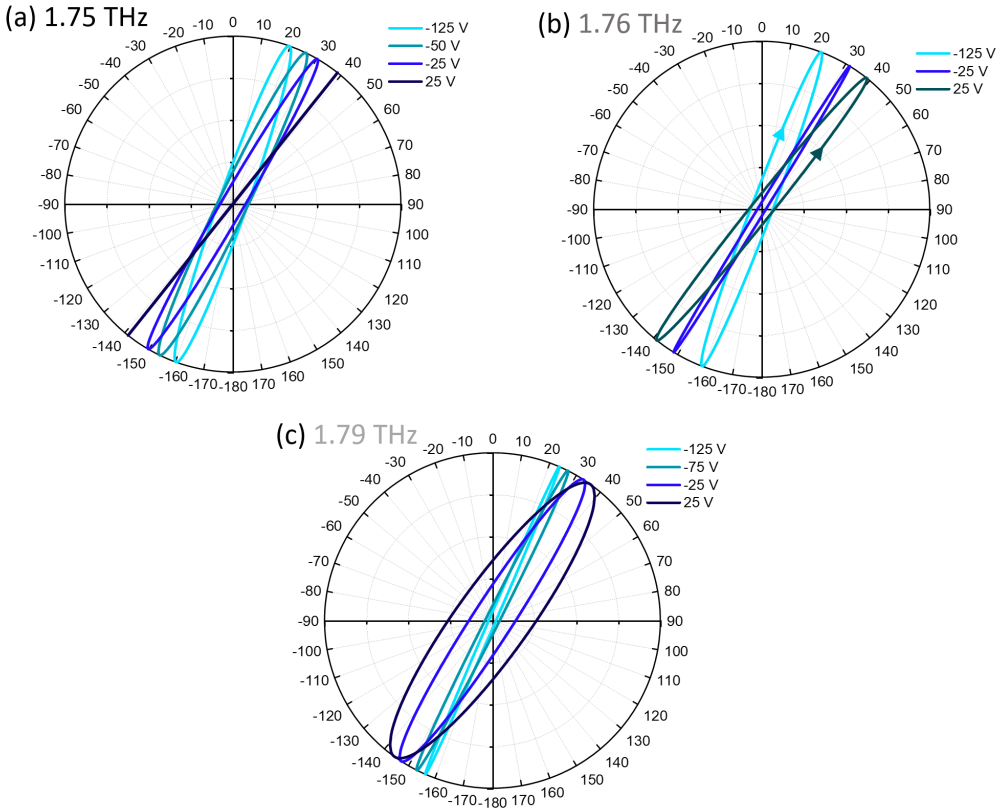

Fig. 4.25 Polar plots to represent measured polarisation condition through single layer devices for different backgate voltages when E_y radiation is incident with a frequency of (a) 1.75 THz, (b) 1.76 THz and (c) 1.79 THz.

corresponding to a straight line in the polar plot. As the voltage is decreased away from the Dirac point, the angle rotates to 19 degrees at -125 V with the ellipticity decreasing from 0 to -0.09. This results in the ellipse width broadening slightly as the angle is rotated.

The ellipse at 1.76 THz, illustrated in figure (4.25 (b)) is interesting as the ellipticity is switched from a positive value to a negative value as the backgate voltage is increased. The ellipticity at +25 V is 0.08 and this value decreases as the voltage is decreased, crossing 0 at around -25 V. As the voltage is decreased further to -125 V the ellipticity decreases to -0.08. The physical manifestation of the change in ellipticity sign, is a switch in the handedness of the elliptical polarisation. The arrows in figure (4.25 (b)) demonstrate the change in direction of the rotating electric field which traces out the ellipse. These values are still very close to zero, however, if these values could be increased towards 1 and -1 respectively, there would be many important applications in chiral THz spectroscopy.

Finally 1.79 THz is an interesting frequency as the ellipticity can be modulated from 0 at -125 V to 0.3 at +25 V. Figure (4.2 (c)) shows the ellipse approaching a straight line at -125

V, and can be continuously broadened as the voltage is increased towards +25 V. For this modulation condition it would be ideal to modulate the ellipticity from 0 to 1. Despite the limited modulation depth of this device, this is a promising first result, showing a diverse range of polarisation modulation effects.

All peaks

The previous results considered the first transmission pulse through the sample only, negating the Fabry-Perot effect of the substrate. If this device is to be used with a CW source, and with no anti-reflection coating on the back, it is necessary to include the Fabry-Perot effect of the substrate when calculating the polarisation rotation of the device. The standard Fabry-Perot effect of a medium, with a refractive index, n, and thickness, t, introduces interference fringes with transmission peaks when the frequency is an integer multiple of c/nt, assuming the surrounding medium has a refractive index of 1 (c is the speed of light in a vacuum). When a metamaterial is deposited onto one of the surfaces of the substrate however, the situation becomes more complicated. As discussed in Chapter 3, the metamaterial adds a highly dispersive component to the transmission and reflection coefficients. The phase modification caused by the metamaterial will change the interference pattern and hence the positions of transmission and reflection peaks. Also, as we have seen in this chapter, the phase components for E_y and E_x are different, which means they will have different interference patterns. It is the case that at certain frequencies, the E_y component can have a Fabry-Perot transmission interference dip while the E_x component has a transmission peak, which would lead to a larger rotation of the transmitted polarisation. This effect is illustrated in figure (4.26).

A Comsol simulation is performed to measure the reflection coefficient from the single layer bianisotropic metamaterial device surface, for radiation originating from the bottom of the unit cell, inside the substrate. The phase of the internal reflected component for incident E_y and E_x is shown in figure (4.26 (a)) with the graphene conductivity set to 0 mS for simplicity. The E_x reflection phase does not change much when compared to reflection inside a standard substrate, this is because the resonators are only weakly excited by incident E_x radiation and therefore the reflection phase is dominated by the Fresnel reflection component from the bare substrate. For the E_y reflection, the case is similar to the phase modulator device described in Chapter 3. At resonance frequency, the phase shift caused by the metamaterial resonance itself is π, however the phase of the Fresnel reflection component from the substrate/Air interface is 0. The phase from the total reflection is therefore dependent on which of these components is larger in amplitude, and in this case the metamaterial reflection for E_y is stronger, causing a phase difference of π between the reflected E_y and E_x components. The

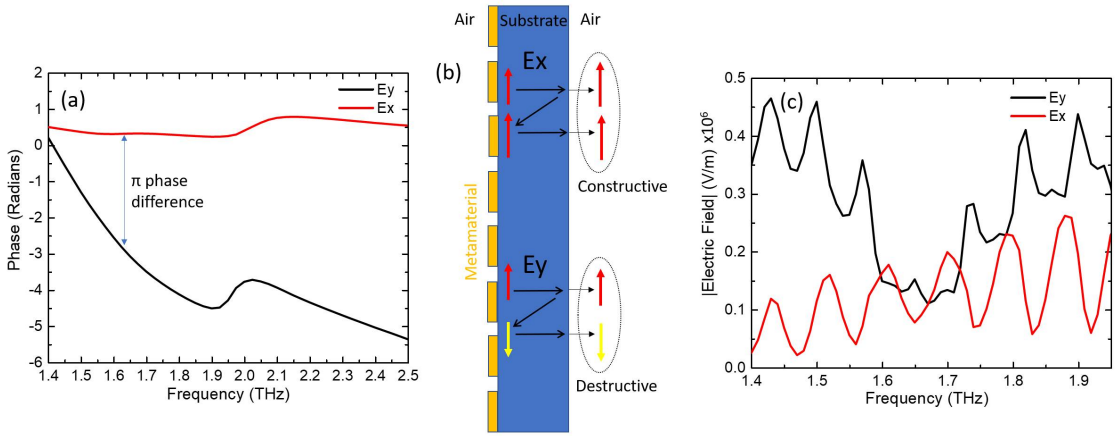

Fig. 4.26 Illustration of Fabry-Perot effect for E_x and E_y components transmitted through sample. (a) Phase of internal reflection from metamaterial surface for E_y and E_x. (b) Illustration of internal reflection phase perturbations at 1.65 THz for E_y and E_x. (c) Comsol simulation of transmitted E_y and E_x components including back facet reflection with incident E_y.

effect on the Fabry-Perot transmission interference for E_x and E_y is illustrated in figure (4.26 (b)). For E_x the effect of the two reflections on the total round trip phase is 0 and therefore a transmission peak will occur when the frequency, f, satisfies the equation $f = \frac{mc}{2nt}$, with m being an integer number greater than zero. For E_y, conversely, the phase shift caused by reflections after one round trip is π, and therefore the transmission peaks for E_x will correspond to transmission dips for E_y. A Comsol simulation of the device transmission components, including the Fabry-Perot effect, caused by incident E_y radiation is shown in figure (4.26 (c)).

The substrate thickness is $500 \pm 50 \mu m$ and therefore it is impossible to predetermine where the Fabry-Perot peaks are going to be. However, it is possible to rotate the sample with respect to the incident radiation, changing the effective substrate thickness, resulting in a change in the Fabry-Perot interference. The resultant interference pattern as a function of angle for a standard silicon/SiO_2 substrate, excited at different angles in the TDS set-up is shown in figure (4.27).

When the silicon substrate is in the normal 0 degrees configuration, constructive interference peaks are shown at 1.50 and 1.58 THz in figure (4.27 (b)). As the angle of the substrate is rotated, these interference peaks start to blue shift. By the time the angle has rotated to 50 degrees, the interference peak has shifted to 1.54 THz, completely inverting the interference fringes. This adds another layer of flexibility to the polarisation control for these devices.

The TDS measurement including all the time domain pulses, as shown in figure (4.21), is performed to determine the amplitude and phase of the transmitted E_y and E_x components as

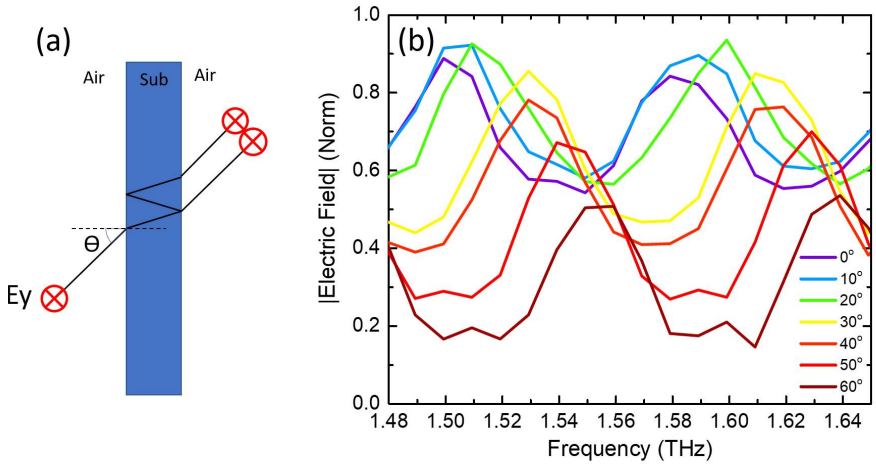

Fig. 4.27 (a) Representation of exciting sample at angle θ. (b) TDS transmission through substrate as a function of angle (degrees) and frequency.

a function of frequency and backgate voltage. These TDS results are plotted alongside the Comsol simulation which includes the Fabry-Perot effect in figure (4.28). These figures are zoomed in to the frequency region between 1.5 and 2.0 THz for more clarity.

These results are determined using the same method that was used for the single pulse case in the previous section. $E_yMeas(f)$ and $E_xMeas(f)$ are determined from the time domain data, now containing all pulses, and the crosstalk value, $C(f)$, which was determined in the previous section, is used in equations (4.17) and (4.18) to determine $E_y(f)$ and $E_x(f)$. The spacing of the E_x interference peaks in figure (4.28 (a)) is 0.085 THz and therefore the substrate thickness is determined to be around 520 μm. This is used to inform the simulation results shown in figure (4.28 (b)) which are determined using an input port above the metamaterial, as with the previous section, however now the silicon substrate is set to be 520 μm thick. An extra air domain containing the second port is placed behind this to include the reflection effect of the second substrate/air interface. The TDS results and simulation share the same functional form, with the peaks being slightly shallower for the TDS results which is most likely due to the substrate back face being unpolished, and therefore reducing the finesse of the Fabry-Perot cavity. The peaks are not perfectly aligned between the TDS and simulation results due to the slight difference in cavity length, which is to be expected as it only takes a small change in cavity length to shift the interference condition dramatically, as shown in figure (4.27).

In figure (4.28 (a)) there is a dip in $|E_y|$ and a corresponding peak in $|E_x|$ at around 1.75 THz, which is similar to the single pulse measurement, however now these components are more pronounced due to the Fabry-Perot effect and the E_x component is now greater than the

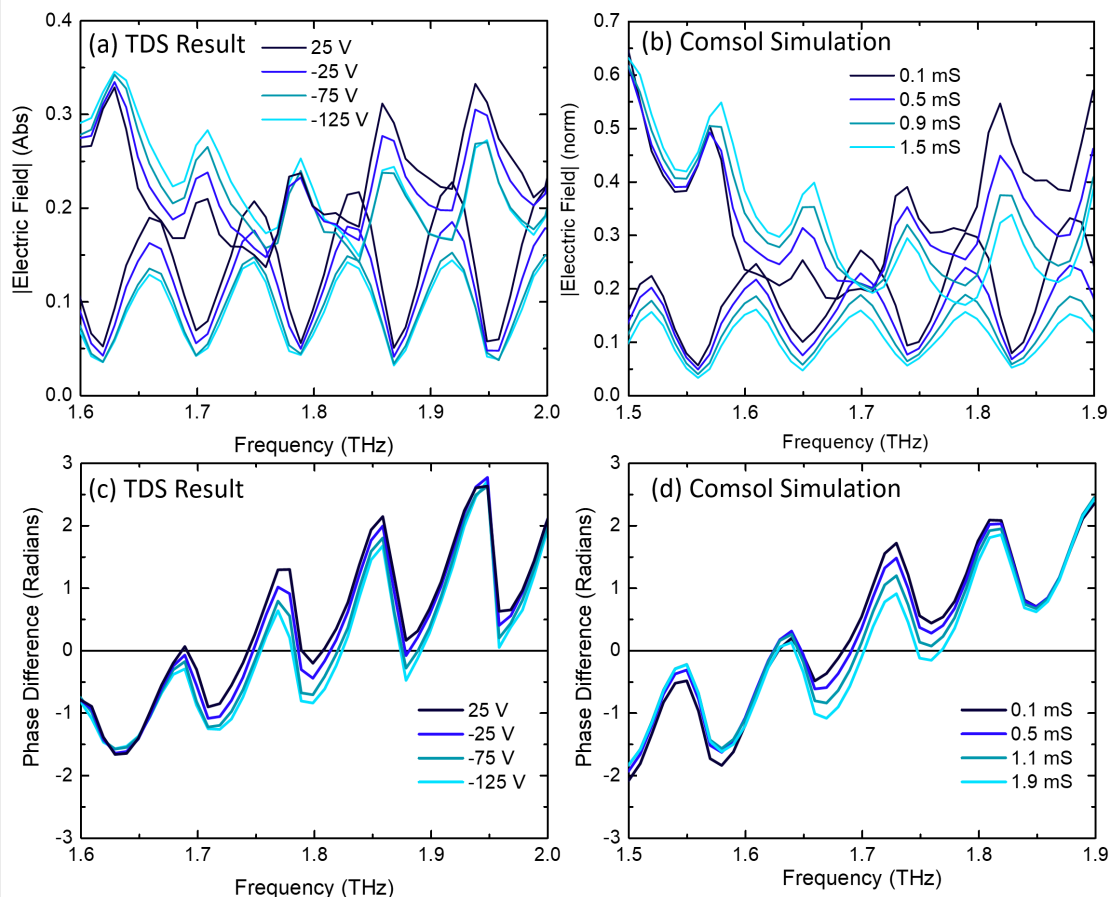

Fig. 4.28 (a) and (c) display the measured $|E_y|$, $|E_x|$ and phase difference between E_y and E_x as a function of frequency and backgate voltage, using all TDS peaks. (b) and (d) shows the equivalent simulated values using a Comsol simulation which includes the reflection from the back of the substrate.

E_y component when the backgate voltage is +25 V. The phase difference between E_y and E_x determined from the TDS experiment and Comsol simulation is shown in figure (4.28 (c) and (d)). The underlying trend for these results is similar to the results for the single pulse measurement, with a high frequency perturbation overlaid on top, caused by the interference fringes. For the TDS measurements, the E_x and E_y phases are once again equal at frequencies roughly between 1.7 and 1.8 THz. The same functional form is shown in the simulation results, with a slightly larger perturbation of 1.5 radians peak-to-peak, compared to the TDS measured perturbation of 1 radians peak-to-peak. This is once again due to the higher finesse of the simulated cavity, assuming a completely flat back facet. Now the polarisation angle and ellipticity for the TDS measurement and simulation are determined using the same method as the previous section using equations (4.10) and (4.11). The results are plotted in figure (4.29)

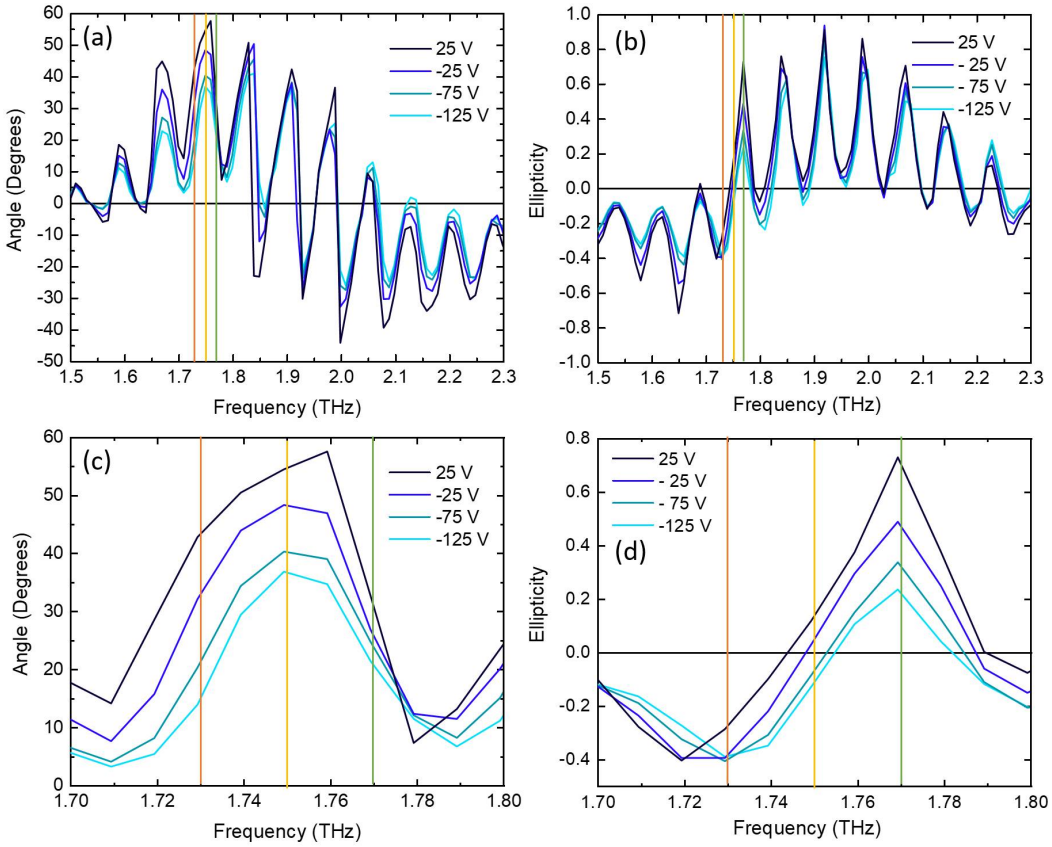

Fig. 4.29 (a) TDS measured transmission polarisation angle as a function of frequency and backgate voltage using all TDS peaks with E_y incident. (b) Corresponding measured ellipticity. (c) and (d) are the same graphs only including the region between 1.7 and 1.8 THz.

The maximum change in angle as the backgate voltage increases is now 32 degrees at 1.73 THz, with the angle changing from 44 degrees to 12 degrees for backgate voltages of +25 V and -125 V respectively. The ellipticity shown in figures (4.29 (b)) has changed dramatically due to the introduction of the Fabry-Perot interference, reflected in the 1 radian ripple in the phase difference results shown in figure (4.28 (c)). The ellipticity follows the same base shape as the single peak example in figure (4.23 (c)), however now there is a dramatic oscillation overlaid on top of this, with the ellipticity changing from around 0 to 1 every 0.04 THz between 1.8 and 2.1 THz. This variation of the angle and ellipticity is not convenient if a uniform broadband polarisation response is required, however these extreme polarisation responses could be useful for modulating a single frequency source such as a quantum cascade laser.

Polar plots for three frequencies, 1.73, 1.75 and 1.77 THz, are shown in figure (4.30). These plots are created using the same method discussed for figure (4.25) and similar frequencies have been chosen to illustrate the effect that including the Fabry-Perot effect has on the polarisation modulation.

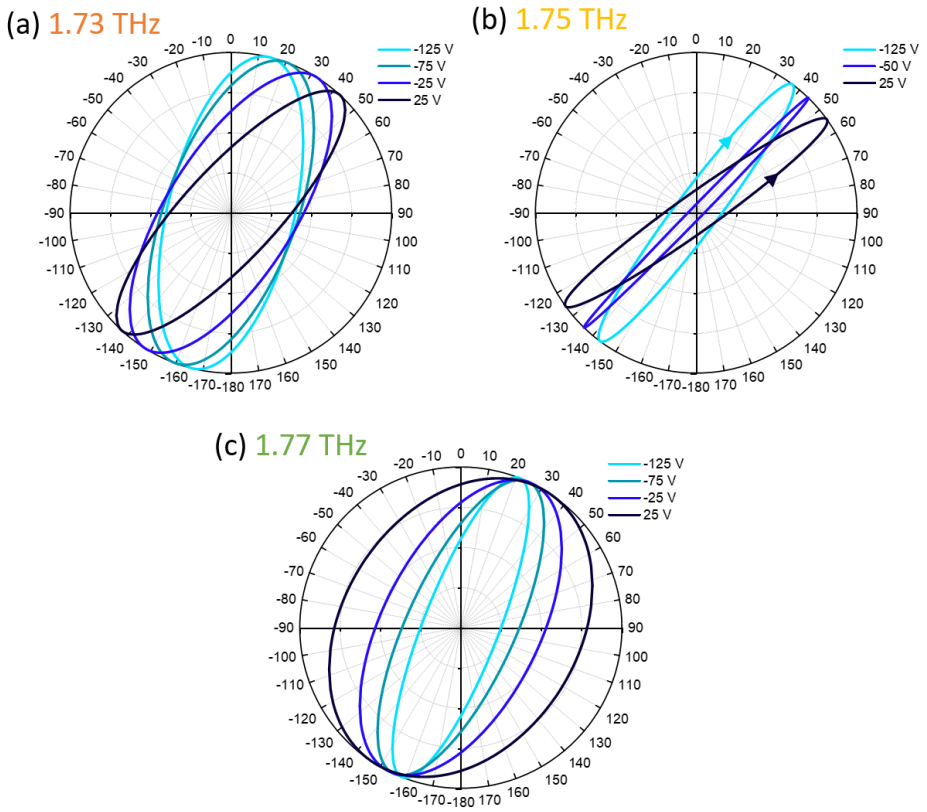

Fig. 4.30 Polar plots of transmission through IO device at different backgate voltages, including all TDS peaks for 3 different frequencies, (a) 1.73 THz, (b) 1.75 THz and (c) 1.77 THz.

The polarisation condition at 1.73 THz was chosen as this frequency corresponds to the maximum change in polarisation angle of 32 degrees. The angle rotates by an extra 12 degrees compared to the equivalent single peak example in figure (4.25 (a)), however the ellipticity is now around 0.4, resulting in thicker ellipses which can be seen in figure (4.30). The ellipse for 1.75 THz, has ellipticity values much closer to 0, as shown in figure (4.30(b)). In this case the angle rotates by 20 degrees, however, the ellipticity handedness also changes as the backgate voltage is changed, in the same way as is observed in figure (4.25 (b)). Now the ellipticity can be modulated from 0.15 to -0.15, which is a larger tuning range than was achievable in the equivalent single peak case, with a tuning range of 0.08 to -0.08 found.

The polar plot at 1.77 THz in figure (4.30 (c)) illustrates how the Fabry-Perot resonance greatly enhances the potential ellipticity tuning, due to the dramatic modification of the phase difference. In this plot, the ellipticity is modified from 0.7 at +25 V to 0.2 at -125 V, providing a much larger tuning range than the single peak equivalent in figure (4.25 (c)), which shows an ellipticity tuning range of 0 to 0.2. It is interesting that such ellipticity modulation is possible for these devices which were initially designed for polarisation rotation. It shows the diverse range of polarisation modulation that these devices are capable of when combining electrically tunable, highly dispersive coupled resonator metamaterials with the Fabry-Perot effect.

4.6 Active double layer device

A new device design for converting linear into circular polarisation is now considered as an alternative to the single layer active device already discussed. This design exploits a two layer 3D chiral array built from a unit cell containing two circular split ring resonators overlaid on top of each other, separated by a 1 μm polyimide spacer layer. The working principle of the device is similar to the static devices described in reference [139], displaying circular dichrosim at certain frequencies, thus converting incident linear polarised radiation into elliptically polarised radiation. To make these devices electrically tunable, graphene is integrated with one of the split ring resonator layers, and the backgate can be variably biased to modulate the ellipticity of the transmitted polarisation, illustrated in (4.31).

4.6.1 Comsol simulation

An illustration of this device architecture is shown in an inventor diagram shown in figure (4.32 (a)). This device consists of a bottom layer of gold split ring resonators, with a similar top layer, rotated by 90 degrees and separated with a polyimide spacer layer. The overlaid split rings are shown in an optical microscope image taken through the developed photoresist for the top layer, shown in figure (4.32 (b)).

Before any fabrication was undertaken, a Comsol simulation was performed using the physical parameters for the unit cell shown in figure (4.32 (c) and (d)) to probe the transmitted E_y and E_x components when E_y radiation is incident. The same material parameters as described in Chapter 2 were used, with the added 1μm polyimide spacer layer described as having a constant effective permittivity of 2.9. To convert linear polarisation into elliptical polarisation, the double layer metamaterial needs to convert a proportion of the incoming E_y radiation into re-emitted E_x polarised radiation, which is $\pi/2$ out of phase with the

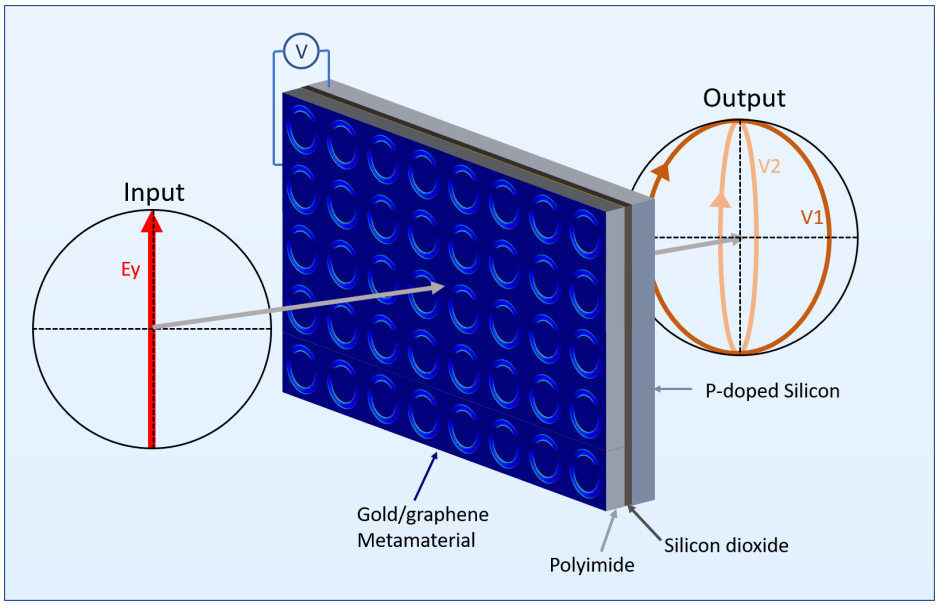

Fig. 4.31 Representation of incident linearly polarised radiation converted to ellipticity polarised radiation, with the ellipticity modulated by varying the backgate voltage.

transmitted E_y component. This is achieved by inducing oppositely circulating currents in the top and bottom resonators when excited at 2 THz.

The split rings are strongly inductively coupled together due to their vertical stacking arrangement. At resonance, the incoming E_y radiation drives a circulating current in the bottom resonator with a net component parallel to the incident electric field. Due to the coupling between the resonators, a circulating current is induced in the top resonator, with the opposite rotation direction. In figure (4.32 (c) and (d)), the induced current at the bottom of each resonator is moving in opposite directions. As the resonators are separated in the z direction, there is a net circulating current, leading to a magnetic dipole moment with a component in the y direction. This oscillating dipole moment will consequently radiate an electric field with non zero E_x component.

For the transmitted polarisation to be elliptical, the resonators are lithographically tuned so that at the required incident frequency the transmitted E_x component is $\pi/2$ out of phase with the E_y component. To modulate the ellipticity of the transmitted polarisation, the bottom resonator array is variably damped by a graphene layer underneath, separated by 100 nm of aluminum oxide. The graphene conductivity can be varied by applying a bias across the backgate between the p-doped silicon and the graphene layer, as illustrated in figure (4.33 (a)). The simulated effect of the graphene conductivity on the induced current is demonstrated in figure (4.33 (b) and (c)), showing the charge carrier concentration for the DC conductivity

extremes of 0.2 and 2.6 mS respectively. The specific device parameters used for this device are contained in table (4.5).

Layer	A	B	C	D	Gap
Top (μm)	11.11	4.04	3.434	40.4	4.04
Bottom (μm)	11.11	4.04	3.434	40.4	4.848

Table 4.5 Lithographic parameters for double layer device

As the conductivity is increased, induced current in the resonators is damped, leading to a lower E_x transmission and a higher E_y transmission amplitude, ultimately resulting in the ellipticity decreasing. The frequency dependent amplitude and phase difference of the transmitted E_y and E_x components are shown in figure (4.34 (a) and (b)) for a range of

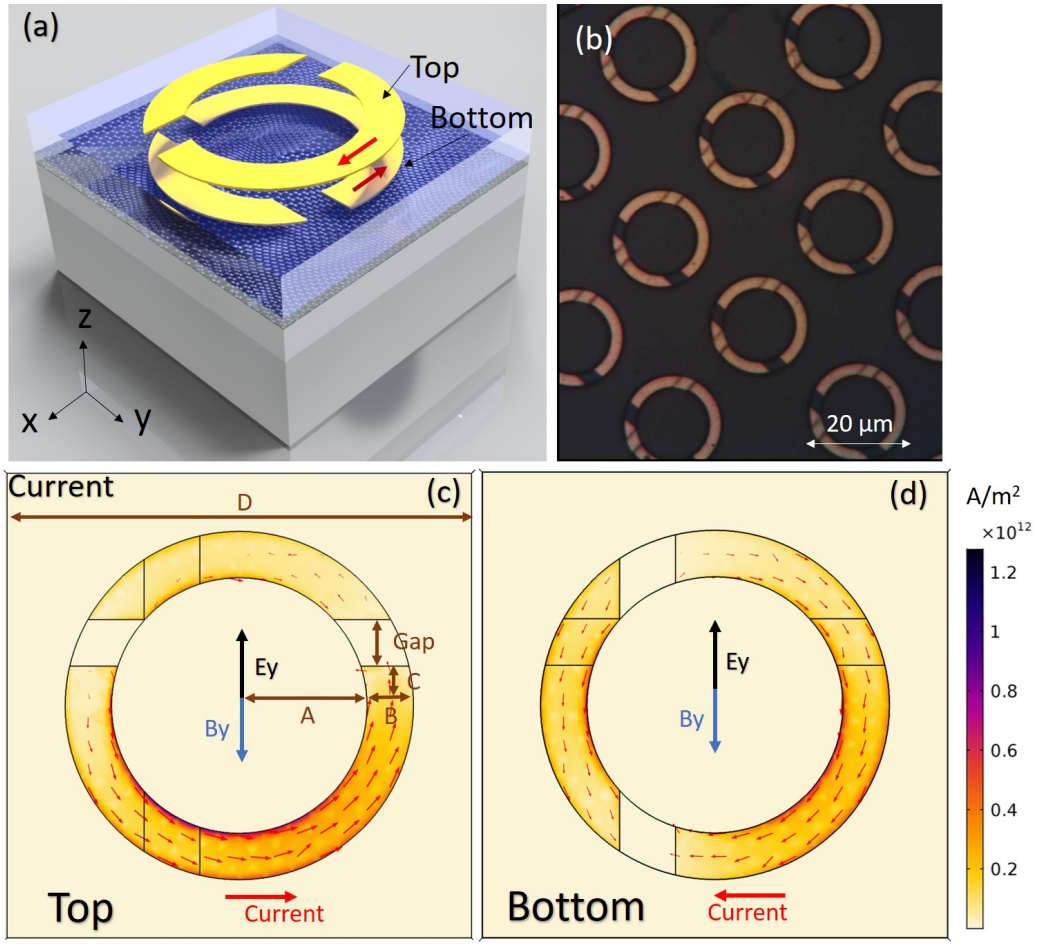

Fig. 4.32 (a) Inventor diagram representing two layer device structure. (b) Optical microscope image of device structure during e-beam lithography step. Comsol simulation of current density in the (c) top and (d) bottom resonators when excited at resonance.

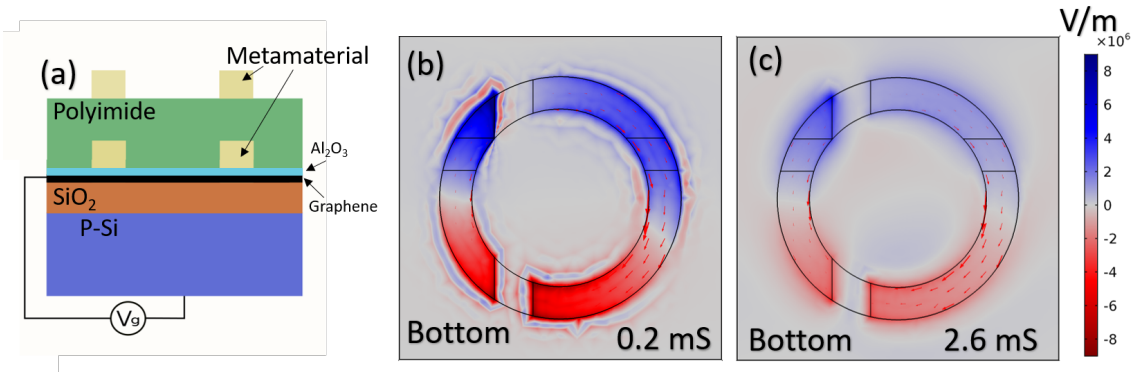

Fig. 4.33 (a) Representation of device cross section and backgate biasing technique. Charge carrier concentration in the bottom resonator for graphene conductivity of (c) 0.2 mS and (d) 2.6 mS determined by probing Ez 20 nm from the metal surface.

graphene conductivities. There is a transmission peak of $|E_x|$ and dip of $|E_y|$ at around 2.05 THz with $|E_x| > |E_y|$ for graphene conductivity of 0 mS. As the conductivity is increase to 0.2 mS, the gap between $|E_x|$ and $|E_y|$ decreases until they are equal. Beyond this conductivity, $|E_y| > |E_x|$, which is to be expected as the induced current is reducing and hence less power is being transferred from the incoming E_y radiation to re-emitted E_x radiation. The phase difference between E_y and E_x, shown in figure (4.34 (b)), is equal to $\pi/2$ radians at 2.05 THz for graphene conductivities of 0 mS, with this frequency staying relatively fixed for all of the conductivities, only moving by a maximum of 0.04 THz as the conductivity is increased to 2.6 mS.

The polarisation angle and ellipticity simulations are shown in figure (4.34 (c) and (d)). At 2.04 THz the angle remains around 0 and the ellipticity is modulated from -1, corresponding to perfect *Rhd* circular polarisation, to -0.2, corresponding to nearly linear polarisation. This device can also work as a linear polarisation rotator, with the angle changing from -30 to -10 degrees at 1.9 THz. However, the ellipticity in this region does not remain constant, changing from 0 to 0.2 as the conductivity is changed.

When $|E_x| = |E_y|$ and the phase difference, $arg(E_y) - arg(E_x)$, is $\pi/2$, the transmitted polarisation condition will be perfectly circular leading to an ellipticity of 1. According to equation (4.6), the output *Lhd* polarisation will be zero, as $E_x = jE_y$. Equation (4.7) shows, however, that the *Rhd* polarisation will be non zero, and hence perfect *Rhd* circular polarisation is transmitted for this condition. The magnitude of the transmitted power components, $|Rhd|^2$ and $|Lhd|^2$, are plotted in figure (4.35 (a)) and the ratio between these two components, $|Rhd|^2/|Lhd|^2$, is shown in figure (4.35 (b)). When this quantity is 1, the transmitted polarisation is perfectly linear. When it is over 1000 or under -1000 the polarisation is effectively circularly polarised in the *Rhd* and *Lhd* directions respectively. The

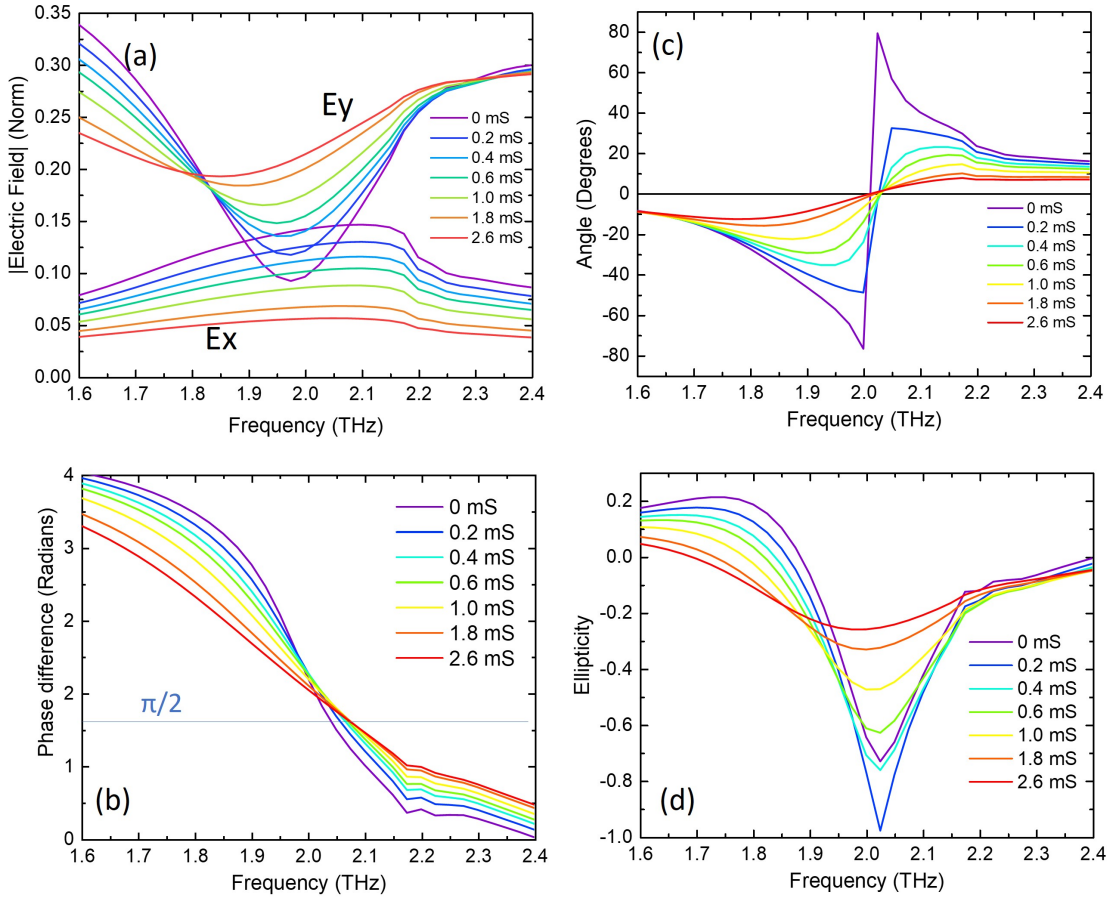

Fig. 4.34 Comsol simulations of double layer device transmission parameters as a function of frequency and DC graphene conductivity. Incoming radiation polarised in E_y direction with nominal power of 1 W.

minimum $|Rhd|^2$ transmission is shown to be at 2.04 THz when the graphene conductivity is at 0.2 mS, corresponding to a power ratio of 10000 illustrated in figure (4.35 (b)). When the graphene conductivity is lower, the magnitude of the E_x increases relative to E_y at 2.04 THz, resulting in $|E_x| > |E_y|$. Conversely, when the graphene conductivity is higher, the magnitude of E_x decreases with respect to E_y resulting in $|E_x| < |E_y|$, also resulting in imperfect circular polarisation. This is a useful device design tool, as the lithography can be modified to change the graphene conductivity where the device transmits perfect circular polarisation, to fit with the conductivity range of the graphene.

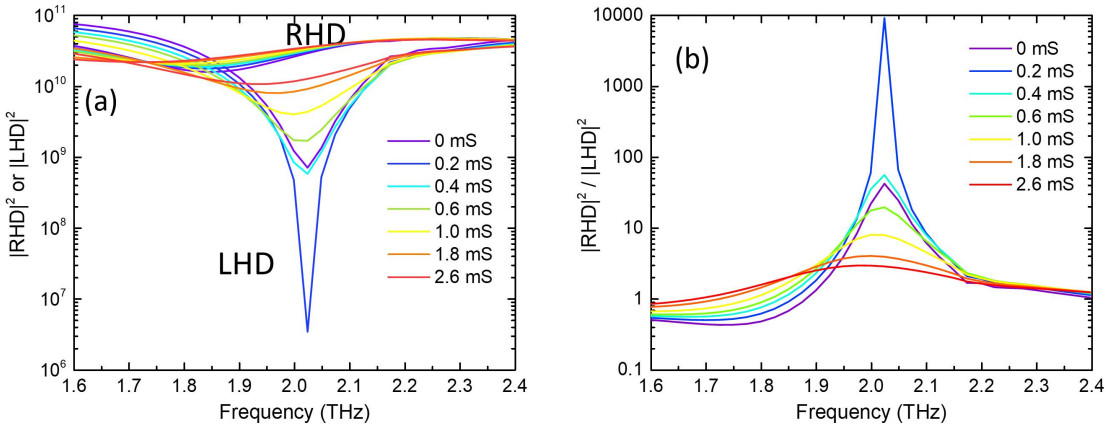

Fig. 4.35 Comsol simulation for double layer device. (a) Transmitted power in the Rhd and Lhd directions (a.u.). (b) Proportion between the transmitted Rhd and Lhd components.

4.6.2 Fabrication

The fabrication of this device follows similar steps to all the other devices, however, as this is a two layer device, a polyimide spacer layer is added into the fabrication process. These steps are illustrated in figure (4.36). The first 4 steps are identical to the process for the SRR device in Chapter 2 with a 3 mm by 3 mm CVD grown graphene patch encapsulated with 100 nm of aluminum oxide, deposited with ALD. E-beam lithography was then used to define the bottom split rings and 10/80 nm of Ti/Au was evaporated through the mask to form the resonators. The next step was to deposit the polyimide layer on top of the bottom resonator array. The polyimide solution consisting of 1 part polyimide, and 3 parts N-Methyl-2-pyrrolidone was mixed for 30 minutes. The solution was then applied using spin coating at 7500 RPM for 60 seconds in a nitrogen purged environment with a humidity RH < 50 % .

In step 7 the polyimide covering the bond pads was removed before curing. The polyimide works as a negative photoresist, and therefore an optical mask was fabricated to cover only the bond pads before illuminating. First the sample was baked at 60 $^{\circ}C$ for 2 minutes and then 90 $^{\circ}C$ for 3 minutes. The sample was then aligned with everything but the bond pads exposed with UV light for 70 seconds. After 5 minutes the sample was again baked at 80 $^{\circ}C$ for 1 minute. The polyimide was then developed for 40 seconds in PA401D and rinsed in PA400R leaving the bond pads uncovered. Finally, the resist was set using a tube furnace, heating the sample to 300 ^{o}C for 1 hour, and ramping down the temperature for a further 6 hours, resulting in a hardened polyimide layer with a thickness of 1 μm.

In step 8, another e-beam lithography process was used to define the split ring resonators for the top layer, and once again 10/80 nm of Ti/Au was deposited using thermal evaporation

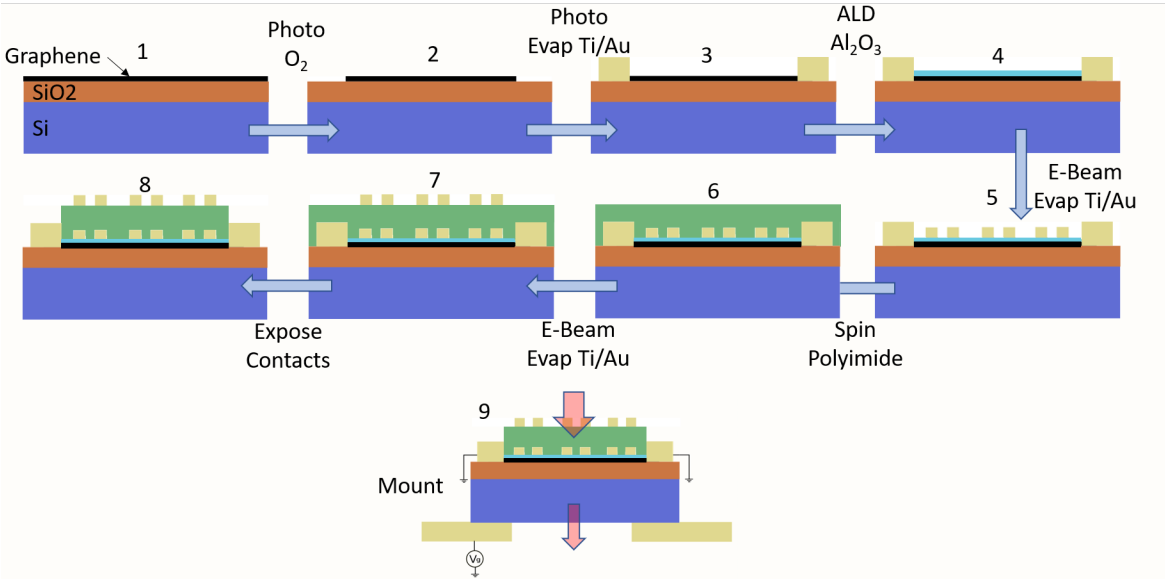

Fig. 4.36 Fabrication process of double layer Chiral resonator device.

to form the resonators. The chip was then mounted and bonded on a sample holder with a 5mm diameter hole in the back for transmission measurements, in the same way as all the previous devices.

4.6.3 Time domain spectroscopy results

Before performing a TDS measurement on the device, an electrical measurement was performed on the sheet of graphene to determine the conductivity as a function of backgate voltage, using the technique described in Chapter 2. The resultant conductivity as a function of backgate voltage is shown in figure (4.37).

As discussed in detail in Chapter 2, ALD of aluminum oxide used to encapsulate the graphene ensures the Dirac point will also remain close to 0 V, in this case around -30 V, and won't drift with time due to exposure with contaminants in the air, or from the polyimide processing. The graphene conductivity can be tuned from 0.4 mS at -30 V to around 0.9 mS for $\pm$100 V. As with the single layer device, the mobility for the holes and electrons is different, leading to an asymmetrical Dirac curve.

The double layer device was placed in the polarisation sensitive TDS set-up described in figure (4.6) using the same procedure as the single layer devices to determine the transmitted E_y and E_x components when E_y is incident. The time domain graphs for $E_y(t)$ and $E_x(t)$ for backgate values of -35 V and +100 V are shown in figure (4.38).

As with the single layer device, there are many pulses separated in time due to internal reflections, as both of these devices are fabricated on 500 μm/300 nm thick Si/SiO_2 substrate.

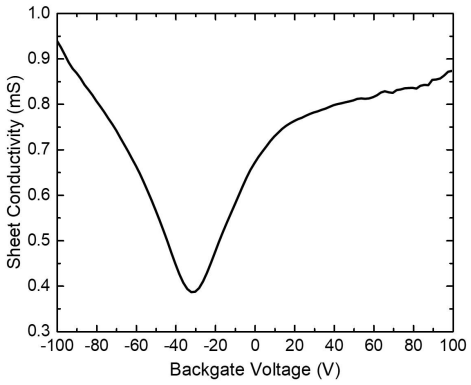

Fig. 4.37 Measurement of the graphene conductivity in the double layer device as a function of backgate voltage.

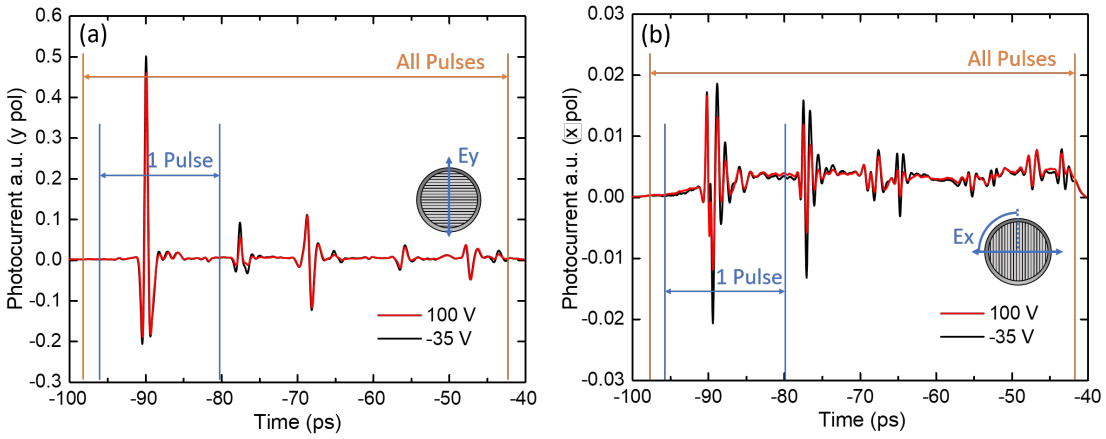

Fig. 4.38 Time domain data through double layer device for E_y and E_x at +100 V and -35 V.

The picture is more complicated in this case however due to the added polyimide layer and the double layer metamaterial. As was done for the single layer device, the primary pulse through the sample is considered first to determine the transmission negating any internal reflection effects. A 15 ps cosine window to select the first pulse was applied and a Fourier transform was performed to determine the frequency dependent components of E_yMeas and E_xMeas.

First pulse

To determine the correct values for $E_x(f)$ and $E_y(f)$, the crosstalk term $C(f)$ was first characterised, using the same method described for the static bianisotropic resonator array, with a similar result as the crosstalk shown in figure (4.10). The measured values, E_xMeas

and E_yMeas, are then used in equations (4.17) and (4.18) along with $C(f)$ to characterise the corrected values for the amplitude and phase of E_x and E_y shown in figure (4.39).

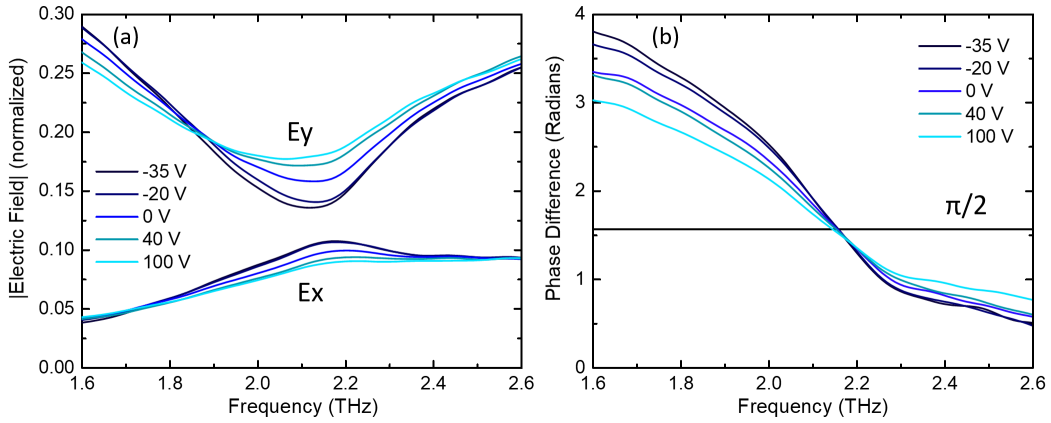

Fig. 4.39 (a) TDS Measurement of $|E_y|$ and $|E_x|$ components transmitted through double layer device for different backgate voltages. (b) Corresponding Phase difference between E_y and E_x.

By comparing the TDS results with the Comsol simulation values in figure (4.34), there is a notable 100 GHz blue shift at 2 THz for the TDS measured values which is consistent with the difference between real and simulated values for all of the other devices. The TDS measured transmitted $|E_y|$ and $|E_x|$ components are shown in figure (4.39 (a)), with a peak in $|E_x|$ and a corresponding dip in $|E_y|$ at around 2.15 THz. The ratio between these values, $|E_y|/|E_x|$, which would ideally be 1 for perfect circular polarisation, is tuned from 1.2 to 2.2 as the backgate voltage is swept from -35 V to 100 V. The equivalent ratio, $|E_y|/|E_x|$, determined from the Comsol simulation in figure (4.34 (a)) at 2.04 THz are 1.2 and 2.5 for graphene conductivities of 0.4 and 1.0 mS respectively. This shows very close agreement between the simulation and results.

The measured phase difference components between E_y and E_x are shown in figure (4.39 (b)). The frequency where the phase difference is $\pi/2$ is 2.15 THz for a backgate voltage of -35 V, with this frequency only moving by 0.01 THz as the backgate voltage is increased towards 100 V. This trend is similar to the simulation results in figure (4.34 (b)), with the phase difference being $\pi/2$ at 2.05 THz. The resulting value for ellipticity and polarisation angle as function of frequency are determined using equations (4.11) and (4.10), inputting E_y and E_x values from the TDS results shown in figures (4.39 (a) and (b)). Graphs for the ellipticity and polarisation angle for different backgate voltages are plotted in figure (4.40 (a) and (b)) respectively. The polarisation condition is described on a polar plot in figure (4.40 (c)), showing the amplitude of the electric field for different angles, using the same method described for the graphs shown in figure (4.25).

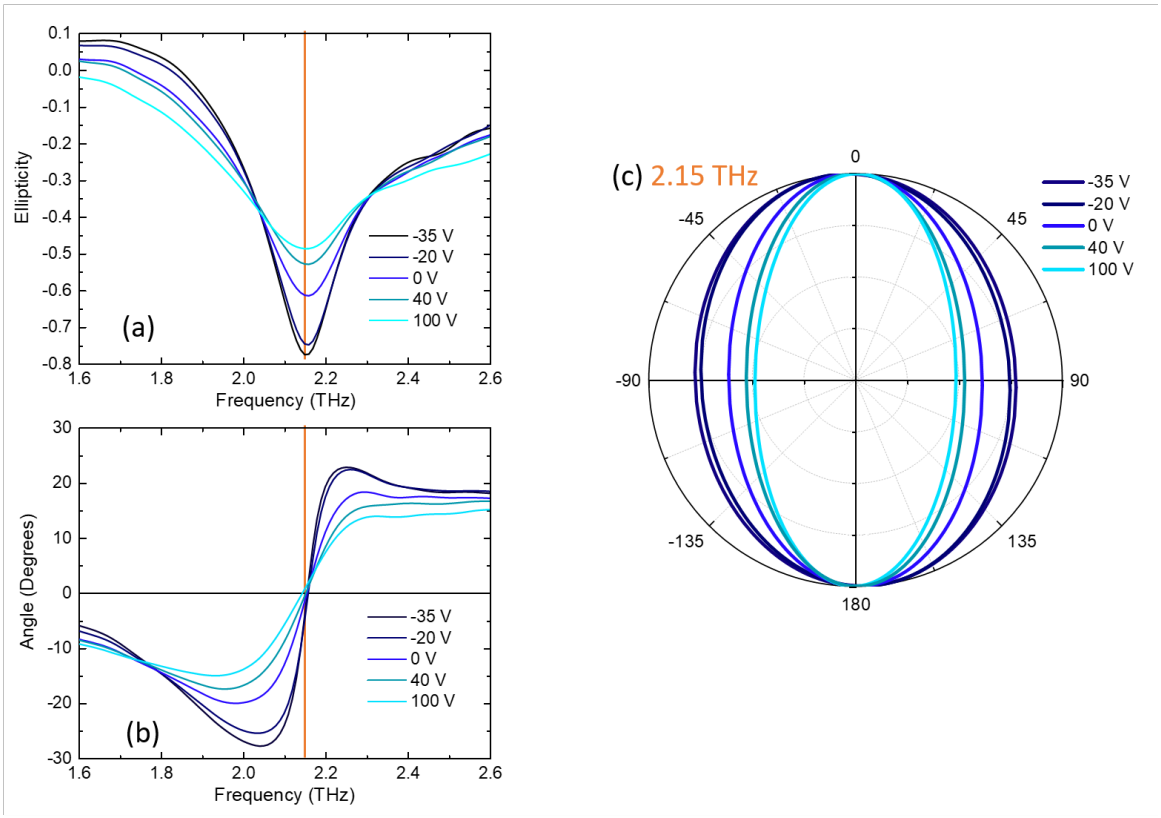

Fig. 4.40 (a) Transmitted ellipticity and (b) angle through double layer device as a function of backgate voltage and frequency. (c) Polar plot representation of transmitted polarisation condition at 2.15 THz for different backgate voltages

The ellipticity of the transmitted radiation at 2.15 THz is modulated from -0.47 to -0.78 as the backgate voltage is increased from -35 to 100 V. At this frequency, the angle is rotated from 0 degrees to -10 degrees. Looking at the polar plot, at -35 V the ellipse is closer to a full circle than is the case for 100 V, with the ellipse closing towards a linear radiation condition. Ideally this device would be able to modulate the radiation from completely linear to circular polarisation, however, due to the limited graphene conductivity range, modulation of the ellipticity is achieved within a reduced range.

All pulses

The next step is to include all the TDS pulses in the device analysis to better understand the transmitted polarisation condition when a CW source is incident. The previous TDS analysis is now repeated including all of the time domain pulses in $E_y(t)$ and $E_x(t)$ instead of just the first one. This includes the Fabry-Perot effect of the 500 μm thick sample causing a similar effect as discussed for the single layer device in figure (4.26). The results for $E_y(f)$ and

$E_x(f)$ are determined by applying a Fourier transform to all of the time domain peaks are shown in figure (4.41), showing the results for different backgate voltages.

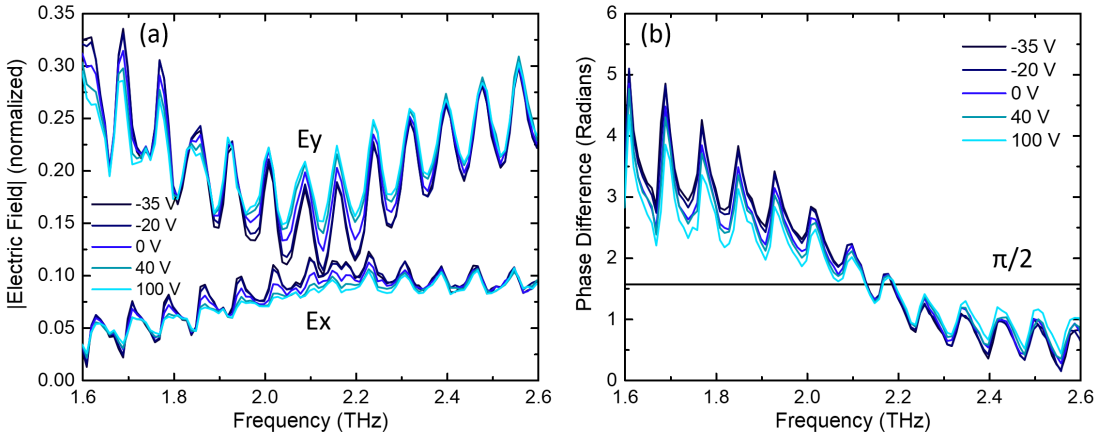

Fig. 4.41 (a) Transmitted $|E_x|$ and $|E_y|$ components when using all time domain peaks. (b) Corresponding phase difference between the E_y and E_x components.

The measured amplitude of E_y and E_x, as well as the phase difference between these values, is shown in figure (4.41 (a) and (b)). The same ripple due to the Fabry-Perot effect of the sample is observed, in a similar fashion to the single layer device. As a result of this, at a backgate voltage of -35 V there is a large decrease in $|E_y|$ from to 0.22 to 0.1 as the frequency is increased from 2.08 to 2.12 THz, with the $|E_x|$ component remaining relatively unchanged at 0.1. This results in a new tuning range of $|E_y|/|E_x|$ from 1 to 1.9 as the voltage is swept from -35 to 100 V. For -35 V, $|E_y|/|E_x|$ is almost exactly 1, and as a result, the output elliptical polarisation is nearly perfectly circular. A similar effect is observed on the measured and simulated E_x and E_y phase graphs as shown in figure (4.41 (c) and (d)). Once again the phase for E_x is shifted by $\pi/2$ so the overlap between E_x and E_y corresponds to the correct condition for circular polarisation. The overlap frequencies are very similar to those determined for the single pulse as shown in figures (4.32 (c) and (d)) however there is an added ripple.

The resultant ellipticity and angle values are determined from the TDS data, using the same method that was used for the single pulse data, and the results are shown in figure (4.42). The frequency of maximum ellipticity change is observed to be at 2.13 THz now, and the ellipticity tuning range is -0.55 to -0.98. The angle changes a significant amount, however when the ellipticity is close to 1, this angle is essentially irrelevant. The ellipse plot in figure (4.42 (c)) demonstrates the improved ellipticity at -35 V with the ellipse nearly filling out the whole circle. As with the single layer device, including the Fabry-Perot effect can actually improve the performance of the device, and can act as an extra tuning tool.

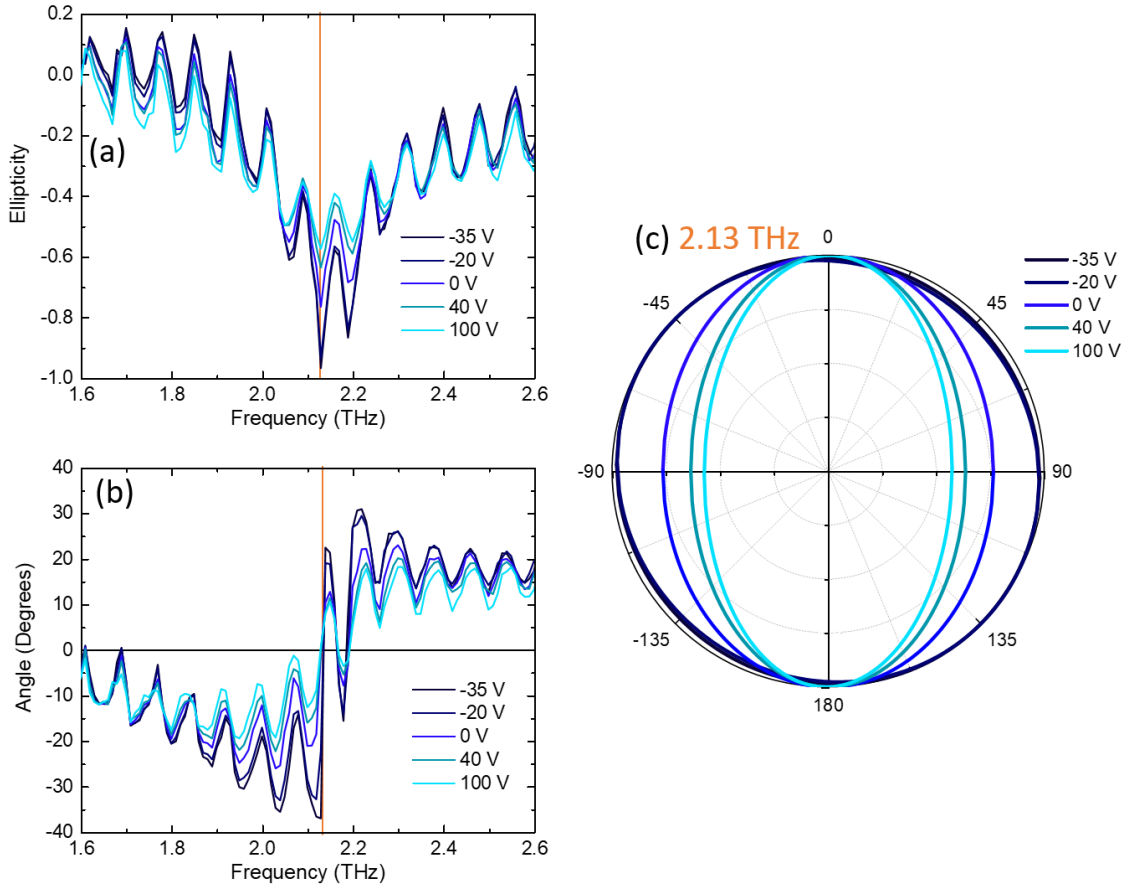

Fig. 4.42 (a) Ellipticity and (b) angle of double layer device using all time domain peaks. (c) Polar plot at 2.13 THz of polarisation condition for different backgate voltages.

4.7 Conclusion

In this chapter a range of metamaterial chiral/bianisotropic device architectures have been explored, demonstrating polarisation control over incident E_y polarized radiation. Three static devices were fabricated, successfully rotating incident radiation by around 60 degrees in one case, and converting linear radiation to highly elliptical ($\varepsilon = 0.8$) radiation in an other, proving the versatility of chiral/bianisotropic metamaterials for polarisation modulator design. Due to the success of the coupled resonator device described in chapter 3, a similar design with bianisotropy built in was employed to build an active polarisation modulator device. This device successfully demonstrated continuous polarisation angle tuning of around 20 degrees when the substrate internal reflections were discounted. When the internal reflections were included in the TDS measurement, the polarisation angle tuning range was increased to around 30 degrees at one frequency whilst successfully tuning the ellipticity from 0.2

to 0.7 at another. A double layer chiral device was also fabricated which converted linear polarisation into nearly perfect circular polarisation, with an ellipticity tuning range from 0.6 to 1.0. Such a device could be used in a myriad of applications, allowing for standard linear polarised sources such as QCLs to be converted into polarisation controllable sources by the inclusion of these modular devices. These devices are limited however, to inherently low insertion losses, therefore a scheme which works in reflection mode could be more suitable for the next iteration of these devices.

Chapter 5

Quantum cascade laser active control

In the previous chapters, we developed devices to actively tune the amplitude, frequency, phase and polarisation of THz radiation. One of the key advantages of these devices is they can be used as modular optoelectronic components to be implemented with any standard THz source or detector. These devices were characterised using a TDS system, however, in this chapter, these devices are implemented with THz QCL sources in various ways to show the flexibility and effectiveness of these THz modulators. THz QCLs have been fabricated in a range of ways to enhance the tunability of the THz system. Two examples are shown in

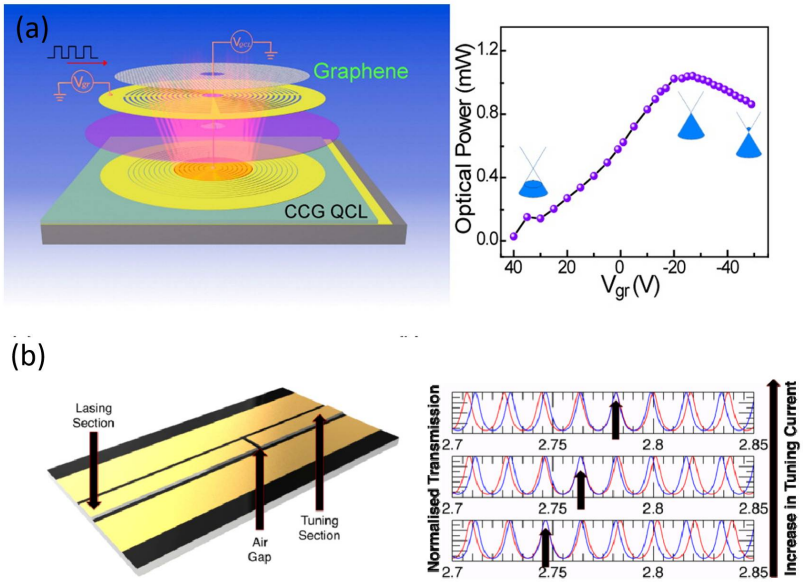

Fig. 5.1 (a) Surface emitting QCL integrated with graphene design and output power as a function of graphene backgate voltage modified from reference [215]. (b) Coupled cavity QCL for frequency tuning and simulation of the vernier tuning effect between the two cavities leading to output frequency tuning, modified from reference [216].

figure (5.26). The design shown in figure (5.26 (a)) is from reference [215] which involves integrating graphene into a surface emitting QCL design. This produces a 100 % amplitude tuning range by varying the backgate voltage of the graphene, without modifying the laser current. The QCL described in figure (5.26) is reported in reference [216] and uses coupled laser cavities to alter the frequency output of the laser utilizing a vernier tuning effect between the two cavities. The output frequency of a laser can be blue shifted or red shifted in the order of 10's of GHz by tuning the current applied to one of the laser ridge sections. Both of these laser designs are highly complex, and we would therefore like to achieve a similar modulation mechanism using a basic QCL which can be externally coupled with the devices described in this thesis, building an easily modifiable modular THz system.

5.1 Polarization control of quantum cascade laser

The simplest way of using these devices for QCL modulation is in transmission mode, effectively replacing the TDS source in previous measurements with a THz QCL, and using a Golay detector to measure the transmitted QCL power through the device as a function of backgate voltage. In this section the polarisation modulators which were presented in Chapter 4 are implemented to show polarisation modulation of two different QCLs. These devices will convert a portion of the incident E_y polarised radiation from the QCL into E_x polarised radiation, causing a modulation of the QCL output polarisation condition. A set-up to control the QCL polarization using these devices, whilst also testing the validity of the TDS characterization is described in figure (5.2)

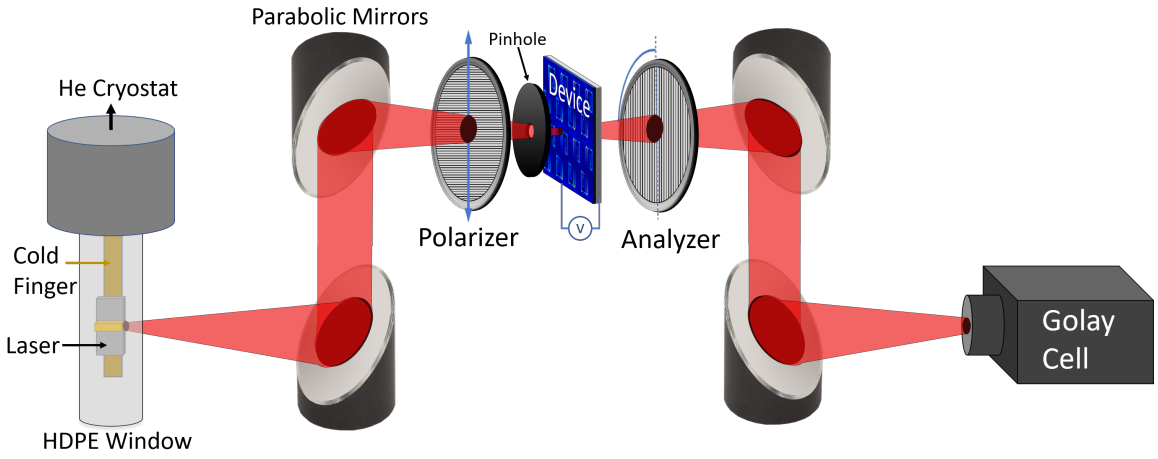

Fig. 5.2 Laser output polarisation tuning set-up.

This experimental set-up takes the output of a QCL, contained in a liquid helium cooled 4K cryostat, through a high density polyethylene window which is then collected by the first parabolic mirror. This mirror has a focal length of 7cm, and is set at this distance from the laser to collimate the beam from the QCL. A second mirror is then used to focus the collimated beam through the polariser and onto the active region of the device, through a 1 mm diameter pinhole. This is used to ensure the incoming polarization is highly linear in the E_y direction. After passing through the sample, the THz radiation passes through the Analyzer, which is again mounted on an active rotation stage, to probe the power transmitted through the device at various polarization angles. The transmitted radiation is then collected by the second set of collimating parabolic mirrors, focusing the beam into a Golay cell which is used to detect the power. A second Golay cell, not shown in the diagram, is used to collect the power from the back facet of the QCL to ensure the power remains normalised throughout the measurement. The laser is run using the method described in Chapter 1, modulated at 10 KHz with a duty cycle of 5 %, and an additional 5 Hz gated square wave used to measure the Golay signal in the lock-in.

5.1.1 Single layer polarisation modulation device

The single layer polarisation device described in section (4.5.1) is first incorporated with a single mode QCL emitting at 2.24 THz. This laser was fabricated in the group using wafer number V208 which is a BTC active region design, fabricated into a single plasmon waveguide as discussed in chapter 1, with a length of 3 mm. This laser was chosen as there are no QCL's operating below 1.94 THz fabricated in the group, and therefore the bonding resonance peak of the device at 1.75 THz could not be tested. The anti-bonding resonance at around 2.15 THz was tested instead, and the laser at 2.24 THz was the closest single mode laser available. A LIV measurement for this QCL was performed using the method described in chapter 1, and a spectrum of the laser output when operating at peak power was measured using the FTIR spectrometer, using the method also described in chapter 1. These measurements are shown in figure (5.3).

Before measuring the polarisation modification of the device, the power from the QCL transmitted through the system with no device present is first measured. The measured electric field passing through the analyzer as a function of angle is determined by taking the square root of the power measured by the Golay. With the laser emitting E_y polarised radiation, if there is no crosstalk term, $C(f)$, the electric field amplitude should be a modular sign wave as a function of analyzer angle. The resultant electric field as a function of the analyzer angle is shown by the normalised black curve in figure (5.4), with the crosstalk term removed using the method discussed in section (4.3). The device was now placed in

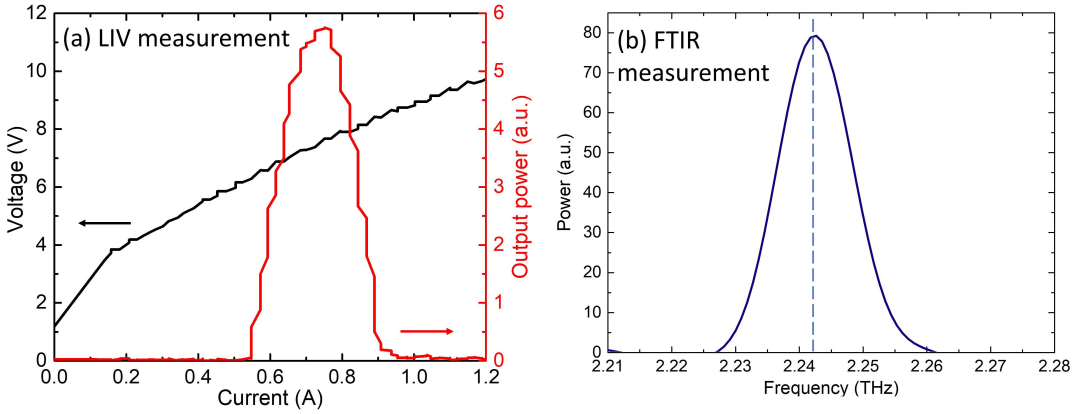

Fig. 5.3 (a) LIV measurement for QCL operating at 2.24 THz (b) FTIR measurement of 2.24 THz QCL with operating current of 0.7 A (J_{Peak}). FTIR resolution is 0.25cm^{-1}

the beam path, with the analyzer rotation measurement taken again with device backgate voltages of 25 V and -100 V, also shown in figure (5.4)

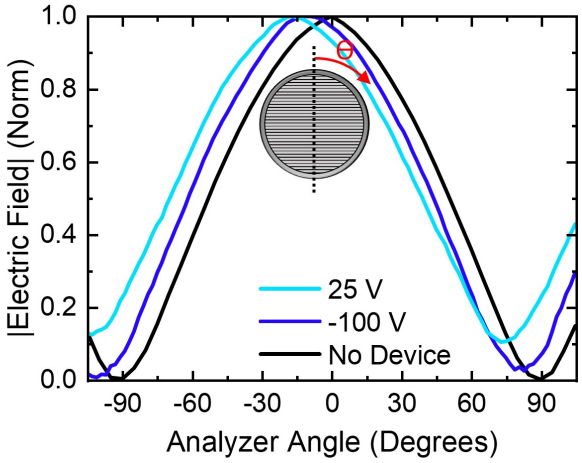

Fig. 5.4 Normalised electric field magnitude transmitted through single layer device as a function of analyzer angle for different backgate voltages, using 2.24 THz laser. Compared to measurement with no device present (Black curve). Crosstalk terms have been removed.

The angle where the electric field amplitude is at a maximum, corresponds to the polarisation angle of the transmitted polarization. With the device backgate at -100 V, the angle rotation is around -9 degrees, with this angle decreasing to around -16 degrees when the backgate voltage is changed to 25 V, corresponding to the Dirac point of the device. The ellipticity of the transmitted radiation increases when the device is placed in the beam, with

the signal only reducing to a minimum value of 0.03 for 25 V and 0.11 for -100 V. These normalized values are equal to the magnitude of the ellipticity of the radiation transmitted through the device. This is commensurate with the TDS measurements at 2.24 THz, with the ellipticity increasing from around 0 to 0.1 in figure (4.29 (b)) as the back gate voltage is changed from 25 V to -100 V.

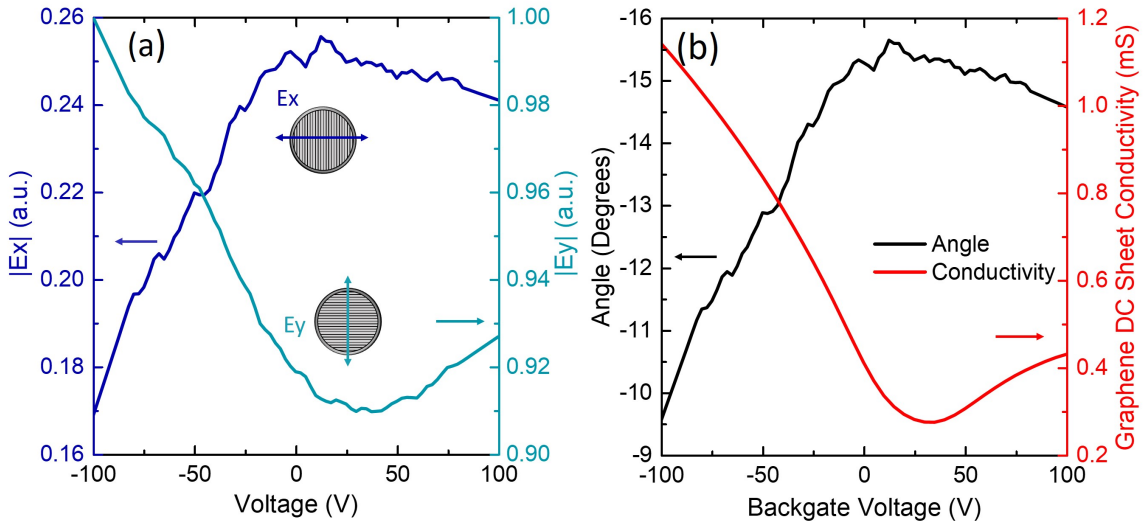

Fig. 5.5 (a) $|E_y|$ and $|E_x|$ transmitted values as a function of backgate voltage, with crosstalk terms removed. (b) Polarization angle as a function of backgate voltage, alongside conductivity measurement.

Now two backgate voltage sweeps are performed, one with the analyzer at 0 degrees to probe $|E_y|$, and one with the analyzer at 90 degrees to probe $|E_x|$. These measurements are shown in figure (5.5 (a)), with the crosstalk terms removed. This graph shows an effective amplitude modulation of the $|E_y|$ and $|E_x|$ transmission terms from 1 to 0.91, and 0.255 to 0.17 respectively. The modulation depth can be defined as the maximum percentage reduction from the peak value, leading to values of 9 % and 25 % for $|E_y|$ and $|Ex|$ respectively. This can be converted into a modulation depth of the transmitted power by taking into account the squared proportionality between electric field and power. The resultant modulation depths for transmitted power polarised in the y and x directions are 18 % and 43 % respectively.

From these values, the polarisation angle of transmitted radiation through the device is determined as a function of backgate voltage, taking into account an estimated ellipticity taken from figure (4.29 (b)). This result is plotted alongside the graphene conductivity measurement in figure (5.5 (b)). When the graphene conductivity is minimum at -30 V, the polarisation angle is maximum to an accuracy of around $\pm 10\,V$, which is a standard Dirac

point variation for graphene. Further to this, the polarisation angle follows the conductivity trend as the voltage is changed, with high graphene conductivities corresponding to low polarisation rotation angles, as predicted in simulations and in the TDS measurements in Chapter 4. The angle is modulated from around -9 degrees at -100 V to just under -16 degrees at 20 V. By comparing this result to the TDS angle plot in figure (4.29 (a)), the rotation angle is less than expected, with a TDS predicted rotation from -20 to -28 degrees as the backgate voltage is increased from -100 V to 25 V. One of the reasons why the polarisation rotation of the QCL output is less than expected could be that the laser is not as well aligned to the sample. This could result in power leaking around the active area, causing a DC reduction in the polarisation rotation. Also, if the spot size is larger than in the TDS set-up, the Fabry-Perot amplitude may be less, as the back surface of the silicon is very rough. The transmitted polarisation was very sensitive to small rotations and translations of the device, and hence varying thicknesses, in the order of 10 μm across the un-polished back facet could be causing these perturbations. In any case, electrical modulation of a QCL polarisation angle has been successfully demonstrated, representing an excellent starting point for further device improvement.

5.1.2 Double layer polarisation modulator device

The double layer device was also tested in the QCL set-up, however this time a single mode laser at 1.94 THz was used. For maximum ellipticity modulation, ideally a laser at 2.13 THz would be used, however there were no single mode laser available at this frequency. Instead, the device should rotate the polarisation angle with the ellipticity remaining near 0.1 at 1.94 THz, and hence this laser was chosen. The QCL was fabricated in the group using the V305 wafer, which is also a BTC design, in a 3 mm single plasmon waveguide. An LIV measurement and a FTIR spectrum at peak power are shown in figure (5.6).

Using the same method used for the single layer device in figure (5.4), the electric field magnitude as a function of analyzer angle is plotted in figure (5.7). The values of $|E_y|$ and $|E_x|$ as a function of backgate voltage are measured once again and plotted in figure (5.8 (a)). The resultant angle and graphene conductivity as a function of backgate voltage, are shown in figure (5.8 (b)).

The ellipticity of the radiation stays very close to zero, as shown in figure (5.7), which is commensurate with the ellipticity TDS measurements shown in figure (4.42 (a)), with the ellipticity amplitude shown to be around 0.1 at 1.94 THz. The value for $|E_y|$ in figure (5.8 (a)) remains relatively unchanged as the backgate voltage is modified, however, $|E_x|$ is modulated between 0.825 to 0.55, corresponding to a 33 % modulation depth. When converted back into power, the modulation depth of transmitted power polarised in the x

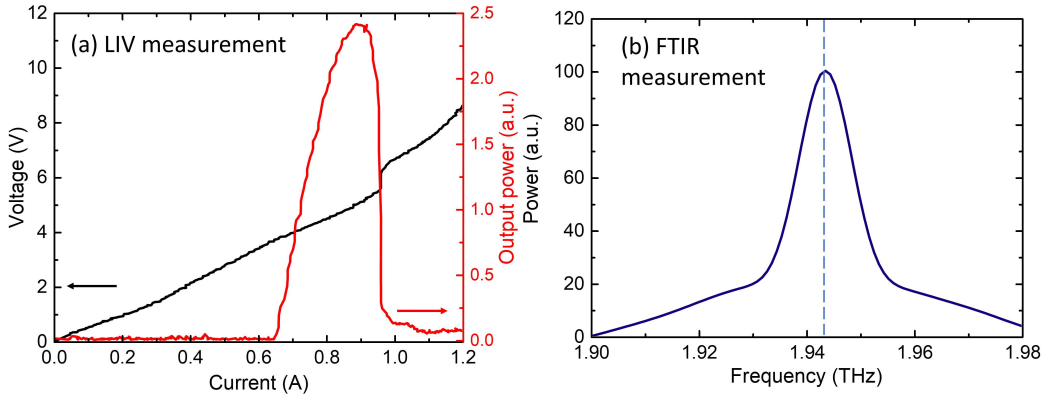

Fig. 5.6 (a) LIV measurement for QCL operating at 1.94 THz (b) FTIR measurement of 1.94 THz QCL with operating current of 0.8 A (J_{Peak}). FTIR resolution is 0.25 cm^{-1}

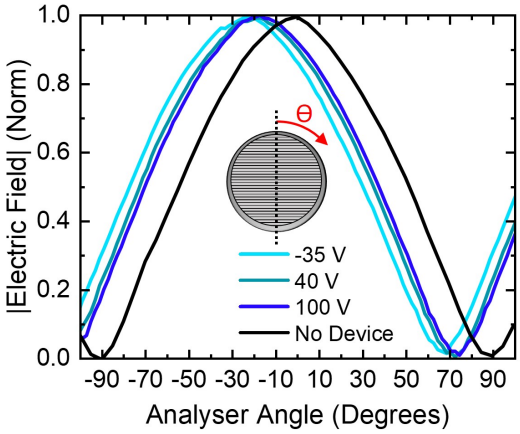

Fig. 5.7 Normalised electric field magnitude transmitted through double layer device as a function of analyzer angle for different backgate voltages, using 1.94 THz laser. Compared to measurement with no device present (Black curve). Crosstalk terms have been removed.

direction is measured to be 56 %. Figure (5.8 (b)) shows that this results in a polarisation angle modulation between -12.5 and -21.5 degrees as the backgate voltage is swept, and as with the single layer device, the polarisation angle follows the graphene conductivity trend well. According to the TDS measurement of the angle, shown in figure (4.42 (a)), the angle is predicted to rotate from around -18 degrees to -28 degrees at 1.94 THz. Once again the QCL result rotation angle is less than the TDS predicted values, due to the same reasons discussed for the single layer device, however the modulation depth and dependence with backgate voltage are commensurate.

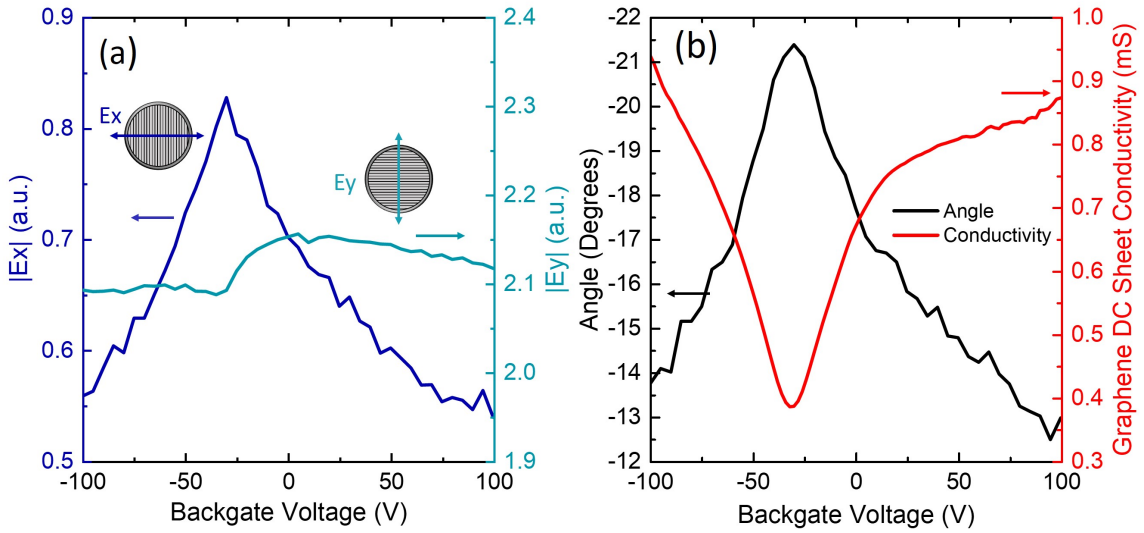

Fig. 5.8 (a) $|E_y|$ and $|E_x|$ transmitted values as a function of backgate voltage through double layer device using 1.94 THz QCL, with crosstalk terms removed. (b) Polarization angle as a function of backgate voltage, alongside conductivity measurement.

5.1.3 Modulation speed measurement

One of the motivations for building polarization modulators based on electrical modulation, was the potentially high modulation (>100 MHz [156]) speeds when compared to mechanically moving devices, and optically excited charge carrier schemes. These devices can essentially be described using an in series RC circuit, with the voltage across the capacitor, and hence the modulation depth, reducing as the AC voltage frequency is increased. This will have a 3 dB roll off at a given frequency determined by the resistor and capacitor values, given by $f_{3dB} = \frac{1}{2\pi RC}$. We require the backgate capacitor to charge as quickly as possible, and therefore it is desirable for the in series resistor value and the total device capacitance to be as small as possible. To estimate the capacitance of the backgate, the parallel plate capacitor model can be used, inputting the surface area of the device, which is around 1 μm^2 for the single layer device, and the thickness and dielectric constant of the silicon dioxide which is 300 nm and 3.9 respectively. The capacitance for the single layer device is therefore estimated to be 110 pF. The p-doped silicon substrate produces the main in series resistance component, and has a bulk resistivity quoted to be 100 Ωm, with a thickness of 500 μm. As there is a 5 mm diameter hole in sample holder for transmission measurements, the total in series resistance from the sample holder to the backgate of the device is difficult to approximate. An LCR meter was therefore used to probe both the capacitance and resistance

values of the effective circuit, giving values of 140 pF and 350 Ω. The capacitance is perhaps larger than expected as the electronics used to bias the device will add some parasitic capacitance, however the measured value is remarkably close to the simple estimated parallel plate capacitor value. The resistance value is indicative of longer current paths through the substrate, which is to be expected due to the hole in sample holder. The order of magnitude, however, is commensurate with the quoted substrate resistivity values.

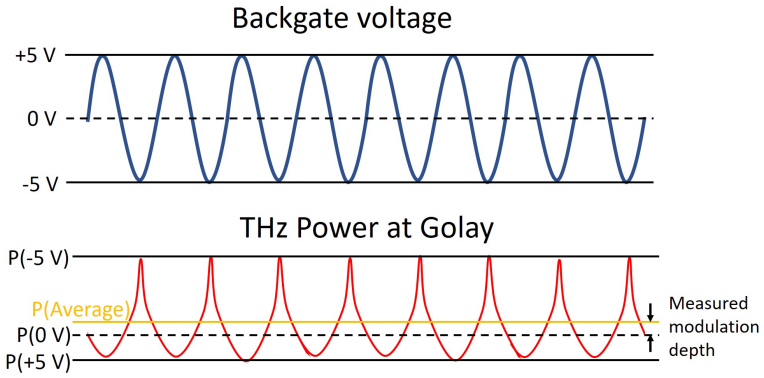

Fig. 5.9 Illustration of modulation depth measurement.

To determine the potential modulation speed of the single layer device, an indirect measurement is performed, which is similar to the method used in reference ([156]). To measure the modulation depth of the device as a function of backgate modulation frequency, a waveform generator is used to modulate the backgate voltage by 10 V peak-to-peak, centered at 0 V, at a range of frequencies up to 30 MHz. The experimental set-up shown in figure (5.2) is used, setting the analyzer to transmit E_y radiation. The laser is now operated in a quasi CW mode, with a speed of 100 Hz, and the 5 Hz gated signal is still used to measure the Golay lock-in signal. The Golay cell can only measure power changes in the order of a few times a second, so it is used to measure the average power transmitted over the device modulation cycle. As the power transmitted through the device does not scale linearly with the change in backgate voltage at 0 V, the DC value measured by the Golay will be different when the backgate voltage is stationary at 0 V and when it is oscillating from -5 to 5 V. This is illustrated pictorially in figure (5.9). The difference in power measured by the Golay when the modulation is 'on' versus when it is 'off' is used to probe the modulation depth for different modulation frequencies, with the results shown in figure (5.10). A standard RC low pass filter simulation is used to accompany the data, using the resistance and capacitance values measured using the LCR monitor.

The modulation depth remains reasonably flat at low frequencies, and it starts to decrease beyond 1 MHz in a similar way as the standard RC low pass filter. The modulation speed is

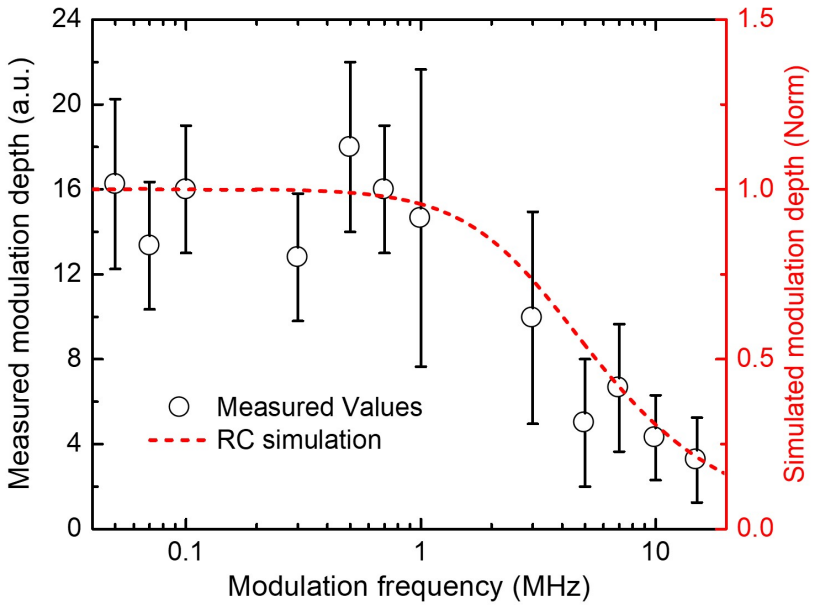

Fig. 5.10 Modulation depth measurement of single layer device. Standard RC simulation is included using values of C=140 pF and R=350 Ω. 10 samples per frequency used to produce error bars.

measured to reduce by half at 5±1 MHz. This lines up well with the RC circuit simulation which shows the voltage across the capacitor reducing to half the DC value at 6 MHz.

To increase the modulation speed, we would want this capacitance and resistance through the p-doped substrate to be as small as possible, taking less time to charge up the graphene. We are limited, however, by the optical alignment with the sample, and is difficult to test these devices if the active surface area is smaller than the single layer device. The spot size at 3 THz can theoretically be reduced below 100 μm, and devices of this size would have a 100 fold reduction in capacitance value. Alternatively, to improve the modulation speed the p-doping in the substrate could be increased, however, this would lead to lower THz transmission through the sample, and hence there is a trade off between speed and optical transmission which needs to be considered. Alternatively, if the device was to work in reflection mode, the large hole in the sample holder would not be necessary which would reduce the resistance to the backgate. Metallic substrates could even be used with resistance values in the order of ohms, increasing the modulation speed by a factor of 100. Reflection mode modulation speeds >100 MHz were demonstrated in reference [156], using a similar graphene/metamaterial device configuration.

5.2 External feedback from mirror

The previous QCL modulation scheme used the laser as a fixed CW source, with the graphene/metamaterial device essentially used as a tunable filter, demonstrating modulation of the amplitude and polarisation of the transmitted THz radiation. The next modulation technique involves influencing the lasing condition of the QCL by using the device to reflect THz radiation back into the laser. This is achieved using an external cavity configuration with one of the metamaterial/graphene devices employed as a tunable external cavity mirror. Before going into the specifics of this modulation scheme, the standard theory behind an external cavity QCL is theoretically discussed and experimentally tested using a standard gold mirror as the external cavity mirror.

5.2.1 Three mirror model theory

A three mirror model theoretical treatment can be used to describe the inclusion of the external cavity mirror feeding back power into the laser cavity. Firstly a two mirror model is used to describe the electric field propagating within the laser cavity. Radiation travelling in the laser cavity can be described using a standard time and spatially dependent plane wave, propagating in the z direction. The time dependant component is not necessary for this consideration however, so for simplicity, only the spatial dependence of the plane wave is considered, as shown in the following equation.

$$E = E_0 e^{(jk+\frac{g}{2}-\frac{\alpha}{2})z} \tag{5.1}$$

This equation includes the loss per meter, α and gain per meter g in the active medium, and the relative phase as a function of wavenumber k and propagation distance z. The electric field amplitude and phase through the cavity is illustrated in figure (5.11).

After one round trip the time independent electric field strength, E, in the cavity can be described using the following equation.

$$E^{1\mathrm{RT}} = E_0 r_1 r_2 e^{(jk+\frac{g}{2}-\frac{\alpha}{2})2L} \tag{5.2}$$

The amplitude is dependent on the portion of radiation reflected from mirror 1 and mirror 2, given by r_1 and r_2 respectively. The phase after one round trip is determined by the wavevector, k, and the length of cavity, L. For constructive laser feedback, and for a standing wave to be produced in the cavity, the phase of E after one round trip must be an integer multiple, m, of 2π. As a result, the round trip electric field can be simplified, with the following conditions met.

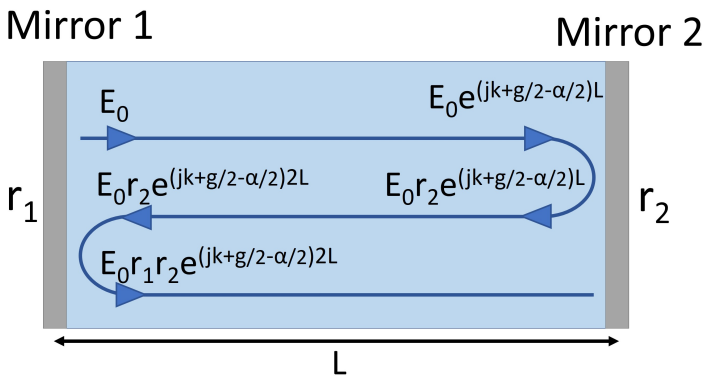

Fig. 5.11 Two mirror model illustration.

$$e^{(j2kL)} = 1 \qquad \text{if} \qquad 2kL = m\pi \tag{5.3}$$

For a laser in steady state operation, the electric field in the cavity must be constant after one round trip with the gain component compensating for the reduction in electric field due to loss, and transmission through the mirrors. Considering equation (5.2), the condition, $E^{1\text{RT}} = E_0$, is satisfied when the other terms are equal to one, giving the following condition for lasing.

$$1 = r_1 r_2 e^{(\frac{g}{2} - \frac{\alpha}{2})2L} \tag{5.4}$$

This can be re-arranged to describe the minimum gain in the active medium for lasing to occur, g_{th}, as a function of α, r_1, and r_2.

$$g_{th} = \alpha + \frac{1}{L}\ln\left(\frac{1}{r_1 r_2}\right) \tag{5.5}$$

This equation is significant, because the gain threshold of the QCL is approximately proportional to the current threshold, $g_{th} \propto J_{th}$, with the population inversion and current being proportional below the laser threshold condition [217]. This equation describes the gain threshold of the laser, based on the the length of the laser, loss in the laser, and crucially the reflectivity of the laser facets. To manipulate the lasing condition of the laser, the effective reflectivity of one of the laser facets can be manipulated by creating an external cavity, and varying the feedback strength into the laser. The threshold gain equation now needs to be re-assessed using a three mirror model as illustrated in figure (5.12). The laser gain, g and loss, α, components are removed in this illustration for simplicity.

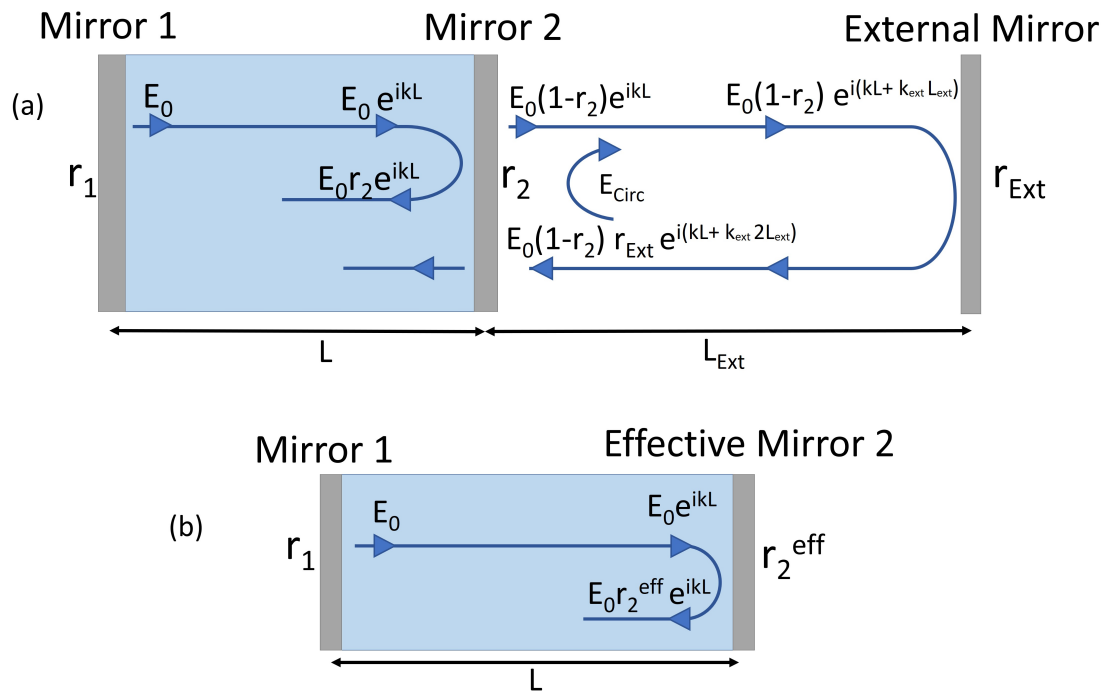

Fig. 5.12 (a) Full three mirror model layout. (b) Equivalent two mirror model with modified effective reflectivity from r_2.

When the propagating radiation in the laser cavity reaches mirror 2, a proportion of the radiation is reflected, given by r_2, and a proportion is transmitted, given by $1-r_2$. The proportion transmitted can then be reflected by the external mirror, and fed back through mirror 2 into the cavity. Any secondary reflections in the external cavity are initially not considered, which is a reasonable approximation assuming the electric field in the external cavity is small compared to the electric field in the laser cavity. The linear combination of these two terms can be used to convert the three mirror model to a two mirror model with the reflectivity from mirror 2 given by r_2^{eff} as shown in figure (5.12 (b)), and in the following equation.

$$r_2^{\text{eff}} = r_2 + (1-r_2)^2 r_{Ext}\, e^{(j2k_{Ext}L_{Ext})} \tag{5.6}$$

This is only valid for when $r_{Ext}r_2 << 1$ with a single round trip in the external cavity being a reasonable approximation. When the feedback is high, multiple round trips in the external cavity must be taken into account. The steady state electric field circulating in the external cavity can then be determined by considering the electric field entering the external cavity through mirror 2, $E_0 e^{jkL}(1-r_2)$ and the electric field after one full round trip in the external cavity, given by the following equation.

$$E_{circ} = \frac{E_0 e^{jkL}(1-r_2)}{1-r_2 r_{Ext} e^{(j2k_{Ext}L_{Ext})}} \tag{5.7}$$

The electric field injected back into the internal cavity is then given by $E_{circ}e^{(j2k_{Ext}L_{Ext})} \times (1-r_2)$ with the new equation for the r_2^{eff} given below.

$$r_2^{\text{eff}} = r_2 + \frac{(1-r_2)^2 r_{Ext}\, e^{(j2k_{Ext}L_{Ext})}}{1-r_2 r_{Ext} e^{(j2k_{Ext}L_{Ext})}} \tag{5.8}$$

In this effective two mirror model consideration, the effective reflectivity of mirror two now has an amplitude, $|r_2^{\text{eff}}|$, and phase change, $\Delta\phi r_2^{\text{eff}}$, associated with it which are both dependent on the magnitude of the reflection from the external mirror, r_{Ext}, and the length of the external cavity, L_{Ext}.

$$r_2^{\text{eff}} = |r_2^{\text{eff}}| e^{(j\Delta\phi r_2^{\text{eff}})} \tag{5.9}$$

The relative amplitude and phase of the electric field after one round trip of the cavity, $E^{1\text{RT}}$, can now be described in a similar way as equation (5.2), however r_2 is replaced with r_2^{eff}.

$$E^{1\text{RT}} = E_0 r_1 r_2^{\text{eff}} e^{(jk+\frac{g}{2}-\frac{\alpha}{2})2L} \tag{5.10}$$

The condition for a standing wave in the cavity has changed as r_2^{eff} has a phase modification term $\Delta\phi r_2^{\text{eff}}$ associated with it due to the coupling with the external cavity. This therefore needs to be added to the standard round trip phase given by $2kL$, giving the modified condition for a standing wave.

$$e^{j(2kL+\Delta\phi r_2^{\text{eff}})} = 1 \qquad \text{if} \qquad 2kl + \Delta\phi r_2^{\text{eff}} = m2\pi \tag{5.11}$$

With this condition met for a given allowed frequency, the threshold gain equation is now modified as follows.

$$g_{th} = \alpha + \frac{1}{L}\ln\left(\frac{1}{r_1 |r_2^{\text{eff}}|}\right) \tag{5.12}$$

This equation shows that the threshold gain for a given permitted frequency can be modified by altering the value of $|r_2^{\text{eff}}|$. This term can be modified by changing the magnitude of the external reflected mirror, r_{Ext}, or by changing the length of the external cavity, L_{Ext}. As $g_{th} \propto J_{th}$, the proportional change in the threshold current when external feedback is included compared to the bare laser case can be shown using the following equation.

$$\frac{J_{th}^{WithFB}}{J_{th}^{NoFB}} = \frac{\alpha + \frac{1}{L}\ln\left(\frac{1}{r_1|r_2^{\text{eff}}|}\right)}{\alpha + \frac{1}{L}\ln\left(\frac{1}{r_1 r_2}\right)} \tag{5.13}$$

This equation illustrates how the laser threshold current can be modified by altering the feedback condition into the laser. If the laser current is below threshold, and the feedback strength from the mirror is increased, the laser can be switched from a non-lasing state to a lasing state essentially giving a 100 % modulation of the output power, thus, illustrating the strength of this modulation method. The threshold current ratio taken from equation (5.13), is plotted in figure (5.13 (a)), as the external feedback mirror strength r_{Ext} is modulated. For this graph, the external cavity is set to an integer wavelength, of a mode allowed in the internal cavity, with the laser frequency nominally set to 2 THz. The internal laser cavity length, L, is 3 mm, with a GaAs refractive index of 3.9. r_1 and r_2 are set to 0.56, simulating the Fresnel reflection from the GaAs/Air interface. As $|r_{Ext}|^2$ is increased from 0 to 1, $|r_2^{\text{eff}}|^2$ is increased from 0.32, with the sole reflection coming from r_2, to 1, with all radiation being fed back into the laser cavity. As the external cavity is an integer number of the lasing wavelength, as r_{Ext} increases, there is no change in the lasing frequency, and the power fed back constructively interferes with the radiation circulating in the laser cavity. As a result, there is a clear reduction in $\frac{J_{th}^{WithFB}}{J_{th}^{NoFB}}$, from 1, with no feedback, to 0.825, with maximum feedback.

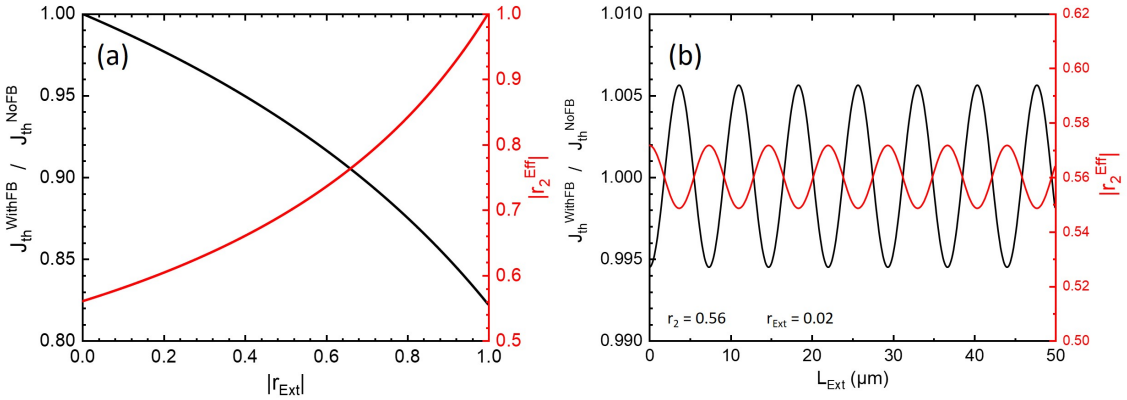

Fig. 5.13 (a) r_2^{eff} and $\frac{J_{th}^{WithFB}}{J_{th}^{NoFB}}$ as a function of external mirror reflectivity. (b) $\frac{J_{th}^{WithFB}}{J_{th}^{NoFB}}$ and r_2^{eff} as a function of external cavity length for $r_{Ext} = 0.14$.

The length of the external cavity L_{Ext} is critical to the feedback condition as this determines the phase of the feedback term. When the feedback destructively interferes with the electric field circulating in the laser cavity, the threshold current condition will actually

increase, with the feedback being detrimental to the lasing condition. To illustrate this, $\frac{J_{th}^{WithFB}}{J_{th}^{NoFB}}$ is plotted as a function of L_{Ext} in figure (5.13 (b)). The same laser parameters are used, with r_{Ext} set to 0.14 to simulate very weak feedback. According to equation (5.6), if $r_2 >> (1-r_2)^2 r_{Ext}$ the phase change, $\Delta\Phi r_2^{\text{eff}}$, caused by changing L_{Ext} is minimal, and hence the magnitude of r_2^{eff} for allowed lasing frequencies varies sinusoidally with L_{Ext}. The resultant value of $\frac{J_{th}^{WithFB}}{J_{th}^{NoFB}}$ will also vary roughly sinusoidally, however, with a peak in r_2^{eff} corresponding to a dip in $\frac{J_{th}^{WithFB}}{J_{th}^{NoFB}}$, as is the case in figure (5.13). If larger values of r_{Ext} are used such that $r_2 >> (1-r_2)^2 r_{Ext}$ no longer holds, the assumption that the phase $\Delta\Phi r_2^{\text{eff}}$ is not changed as the external cavity mirror is moved is no longer valid, leading to a non-sinusoidal response. As a result, the allowed frequencies in the three mirror system will change according to equation (5.11).

To gain insight into the change in lasing frequency due to various feedback conditions, the total round trip phase in the 3 mirror model, given by equation (5.11), is plotted as a function of frequency in figures (5.14 (a) and (b)). These graphs describe the round trip phase for different values of $|r_{Ext}|^2$ and L_{Ext} respectively, and the phase values are wrapped with the integer multiples of 2π removed. The allowed frequencies are given by the intersect points between the round trip phase and the horizontal zero phase line, $\Phi = 0$. When there is no feedback, a linear relationship between round trip phase and frequency is observed, with the allowed frequencies spaced by the free spectral range of the internal cavity which is around 15 GHz. When $|r_{Ext}|^2$ is increased to 0.3, with L_{Ext} set to 30 cm, there is a perturbation on the standard phase lines, with a oscillation frequency given by the free spectral range (FSPR) of the external cavity which is around 5 GHz, causing a shift in the allowed frequencies. As the feedback becomes more severe, the number of allowed frequencies increases, with 8 allowed frequencies when $|r_{Ext}|^2$ is set to 0.6 compared to 4 when no feedback is present.

In figure (5.14 (b)), r_{Ext} is set to 0.4, and the two values for L_{Ext} are used, 30 cm and 30 cm + 30 μm. This causes the perturbation to shift in frequency, allowing the laser output frequency to be continuously tuned.

These graphs, however, only show part of the picture. They determine the frequencies where the round trip phase is an integer multiple of 2π, however, they say nothing about the interference condition between the internal and external cavities, and how the threshold condition will be influenced at these allowed frequencies. To expand on this, the value of $\frac{J_{th}^{WithFB}}{J_{th}^{NoFB}}$ is plotted in figure (5.14 (c) and (d)) with the allowed modes and corresponding threshold values illustrated by the dots. In figure (5.14 (c)) when the feedback is zero, the threshold ratio is 1 for the 4 allowed frequencies, illustrated by the black dots. The frequency dependant gain and loss of the laser will then determine which modes will lase. As the

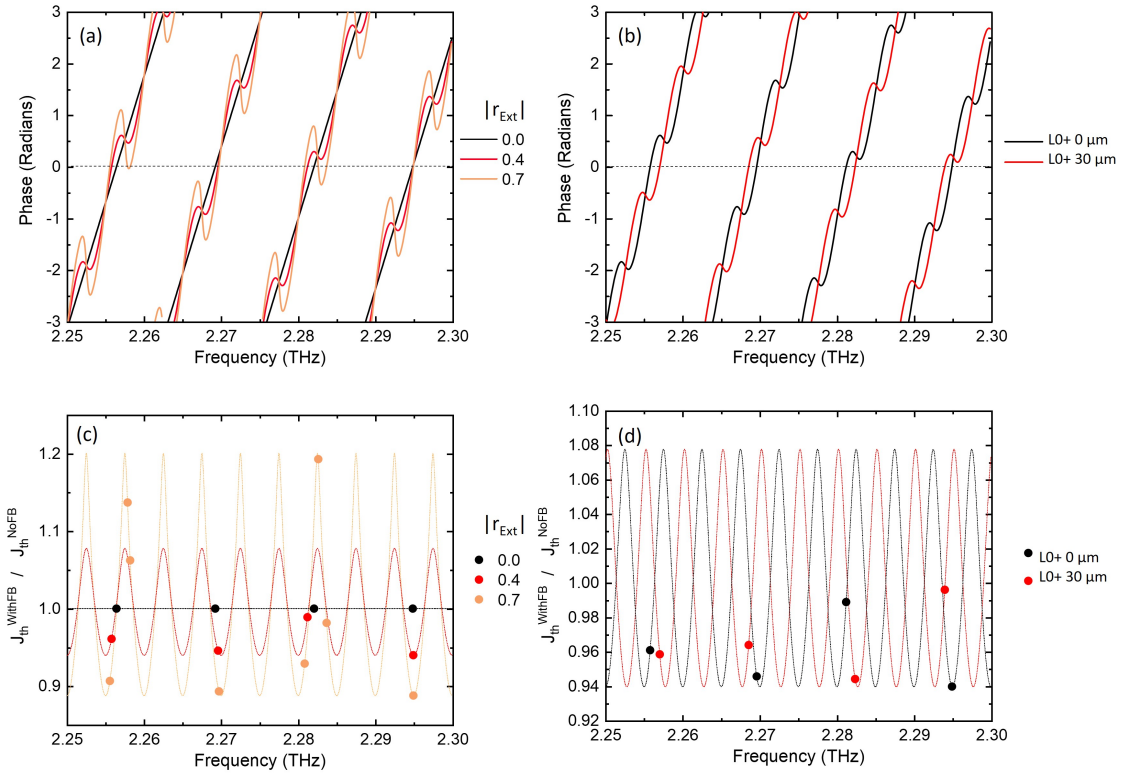

Fig. 5.14 Measuring phase of 1 round trip of 3 mirror cavity by varying (a) r_{Ext} and (b) L_{Ext}. (c) and (d) showing Corresponding values of $\frac{J_{th}^{WithFB}}{J_{th}^{NoFB}}$. 3 mirror model parameters: r_1=0.56, r_2=0.56, L=3 mm, and n=3.9.

feedback strength increases to 0.4, the threshold current drops, however, not at the same rate for each of the allowed frequencies, illustrated by the red dots. There is also a small continuous tuning of the allowed frequency, due to the phase modification, illustrated by the fact the frequency of red dots is shifted slightly compared to the corresponding black dots. The threshold condition for the mode near 2.28 remains reasonably unchanged, however the threshold ratio for the modes near 2.27 THz and 2.295 THz are reduced to below 0.95. In this feedback condition, these modes will preferentially lase, excluding any other factors. As r_{Ext} is increased further to 0.7, the perturbation on the phase causes 8 allowed modes (orange dots), however three of these have a significantly increased threshold current due to the feedback radiation destructively interfering with the circulating radiation in the laser cavity. The modes at 2.27 THz and 2.295 THz are enhanced further, due to constructive interference, with their threshold current ratio reducing to below 0.9. This illustrates how different operating laser modes can be preferentially enhanced or suppressed by applying a varying feedback amplitude.

To actively tune the lasing frequency of the QCL, the length of the external cavity has a strong effect, as illustrated in figure (5.14 (d)). The mode around 2.255 THz is continuously tuned as L_{Ext} is increased by 30 μm, and the threshold current ratio stays relatively constant at 0.96. The two modes around 2.28 and 2.295 THz switch from a constructive interference regime to a destructive interference for the two different external cavity lengths. This has a dramatic effect on the threshold current for these modes, causing the laser to controllably mode hop between these frequencies as the external cavity length is changed.

5.2.2 Experimental set-up

To experimentally verify this theory, an external cavity laser set-up was constructed, using a movable external cavity mirror. As was shown in the previous section, the external cavity has more influence on the laser when r_{Ext} is maximum. Further to this, by looking at equation (5.8), the smaller r_2 is relative to r_{Ext}, the more effect r_{Ext} and L_{Ext} has on the value r_2^{eff}. To enhance the feedback influence on the laser, r_2 is reduced in practice by adding a silicon lens, with an anti-reflection coating. The lens also aids the coupling back into the laser, which increases r_{Ext} as this value in reality has a scaling factor according to coupling loss, and is not purely the reflectivity of the mirror used. The experimental set-up is illustrated in figure (5.15 (a)).

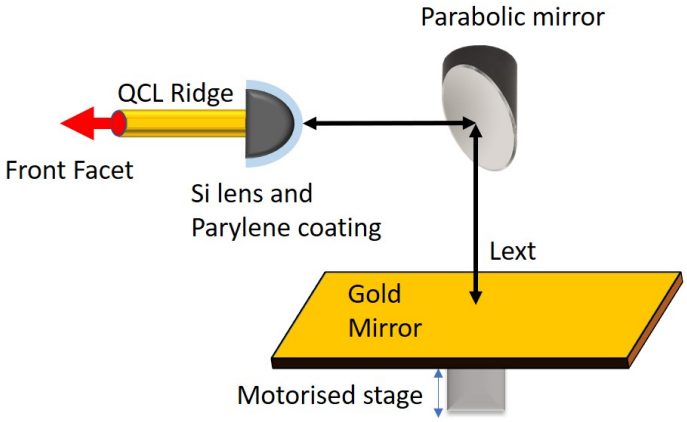

Fig. 5.15 (a) Diagram of external cavity QCL using a gold mirror on a motorized stage with L_{Ext}= 30 cm.

The silicon and GaAs have very similar refractive index value of 3.4 and 3.5 respectively, and hence the reflection from this interface is negated. The refractive index value used for parylene is 1.64, taken from literature [218]. To minimize the the value of the reflection r_2 at 2.9 THz, a parylene coating thickness of 15.5 μm is used. For a perfect anti-reflection coating, the parylene coating refractive index would be 1.84, determined using the following

equation, with n_2, n_0 and n_1 referring to the refractive index of silicon, air and parylene respectively.

$$n_1 = \sqrt{n_0 n_2} \tag{5.14}$$

The parylene coating can therefore not completely cancel the reflection, however, r_2 can still theoretically be reduced to a value of 3 % at 2.9 THz [219]. For this experiment, two different lasers are used with different active regions. These lasers use V557 and V427 wafers, and are both single plasmon wave-guide designs with ridge lengths of 2 and 3 mm respectively. They are both BTC active region designs, and the LIV and spectrum at different current values of these lasers with no lens attached are shown in figure (5.16)

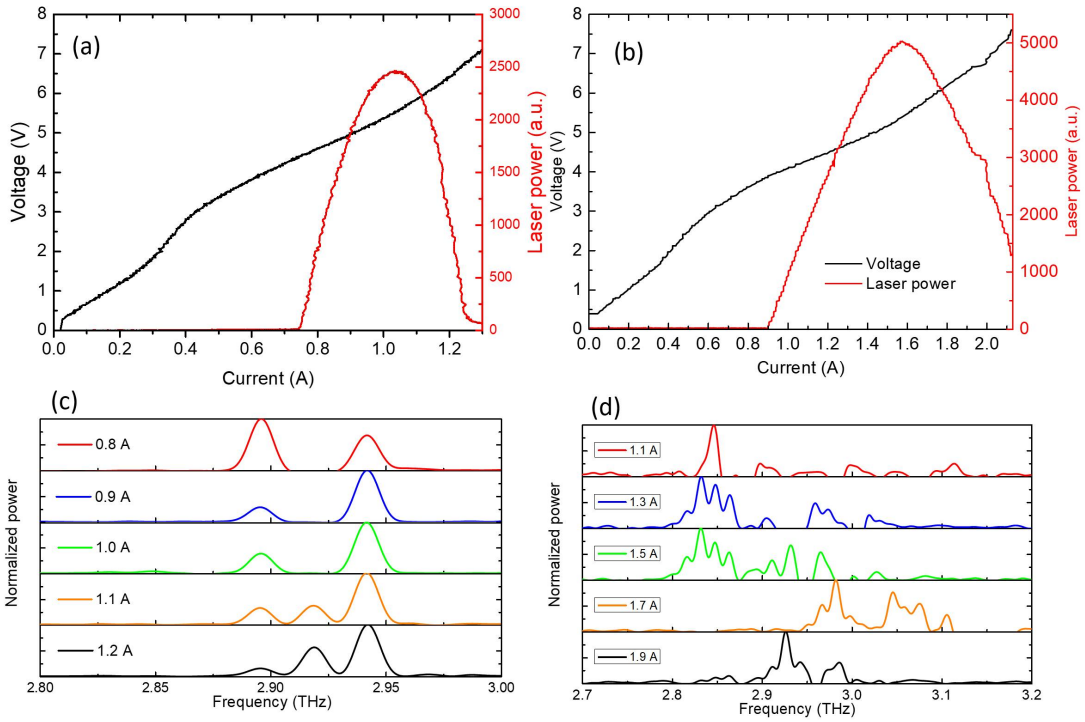

Fig. 5.16 LIV of two pristine QCLs using (a) V427 and (b) V557 wafers. Lasers operated in 10 kHz pulsed mode (5% DC), with 15 Hz gating. (c) and (d) are the corresponding output spectrum measured using an FTIR at different laser current values. FTIR resolution is 7.5 GHz.

These lasers have a silicon lens with an anti-reflection coating attached, and the output power as a function of laser current are shown with and without using a mirror to feedback into the laser cavity, to determine how the dynamic range of the laser changes. The results for V427, shown in figure (5.17 (a)), show that lasing is completely suppressed when no

feedback mirror is used due to the reduction in r_2 leading to the current threshold being too high for lasing to occur. The red, orange and brown curves show the output power as a function of current for three different mirror positions. The red curve indicates the alignment of the mirror such that the threshold current was minimal, giving maximum constructive interference into the laser. The orange and brown curves show intermediate feedback strength mirror positions. It is not possible to measure the absolute distance from the mirror to the QCL with sub micron accuracy, which would be required to predict the feedback regime for different lasing modes. It is possible however, to infer from the power spectrum, and FTIR results, the effect of the external cavity mirror. The orange curve looks to have a much smaller dynamic range than the red one, and the threshold current is increased from 0.7 to 0.75. This is because the mirror was moved to a unfavourable feedback position, leading to a smaller effective r_{Ext}, and smaller resultant value of r_2^{eff}. The brown curve is more complicated to explain, with the threshold current once again increasing, however, the output power is greater beyond 0.85 A. As is shown in figure (5.16), this laser mode hops to a higher frequency around this current. The feedback condition for position 3 may be more favourable to this new frequency. However, it could also be the case that there is a strong water absorption line around this new frequency, and minor changes in the frequency from different feedback conditions could cause drastic changes in power as the frequency scans across the absorption line.

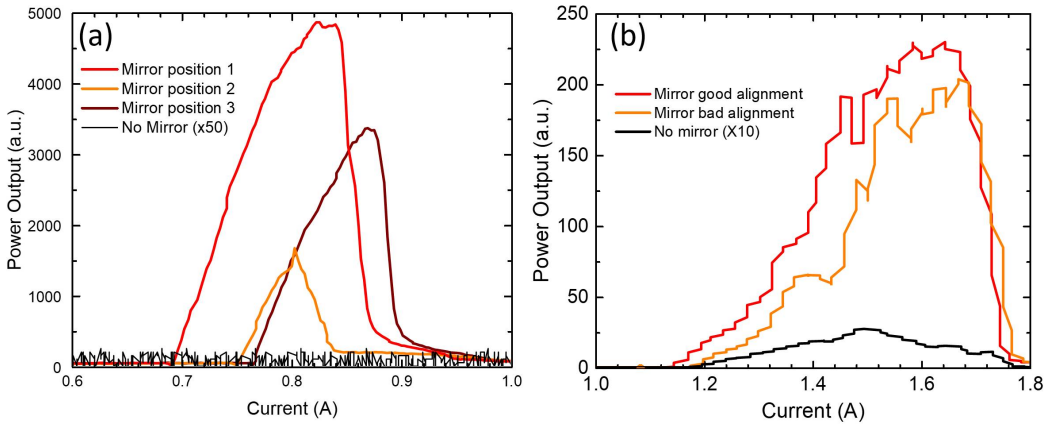

Fig. 5.17 Output power from QCL with anti-reflection coated lens attached as a function of current with and without mirror feedback for (a) V427 laser and (b) V557 laser. Lasers operated in 10 kHz pulsed mode (5% DC), with 15 Hz gating.

Figure (5.17 (b)) shows the output power for the V557 laser, with and without mirror feedback. In this case however, the laser is still lasing when there is no feedback applied. This

highlights the difficulty in aligning the silicon lens to completely suppress lasing. The lens is attached using PMMA to reduce the chance of any air gap between the GaAs waveguide and silicon lens, however, this is not always achieved, and the real value of r_2 can be higher than the theoretically predicted value of around 3%. The lack of full suppression could also be due to the large dynamic range of this laser, and the relatively narrow, ∼100 GHz, suppression range of the anti-reflection coating. When an external cavity mirror is used to feedback into the lens, the power output increases by an order of magnitude, and the threshold current moves, however, by not as much as the other laser. Once again, the dynamic range for a maximally aligned external cavity mirror is compared to an intermediate configuration, where the external cavity mirror position is sub-optimal.

5.2.3 Amplitude modulation results

To measure the effect of L_{Ext} on the output power of the laser, the stage controlling the position of the mirror is now moved in 1μm increments, and the output power of laser measured. Two different starting positions of the mirror are used, one in the focus of the parabolic mirror, for high level of laser feedback, and one far from the focus, for a low level of laser feedback. This was done to test how the laser output power changes when in different feedback strength regimes. The V557 laser was used, operating near I_{Th} with a current of 1.26 A. The results are shown in figure (5.18).

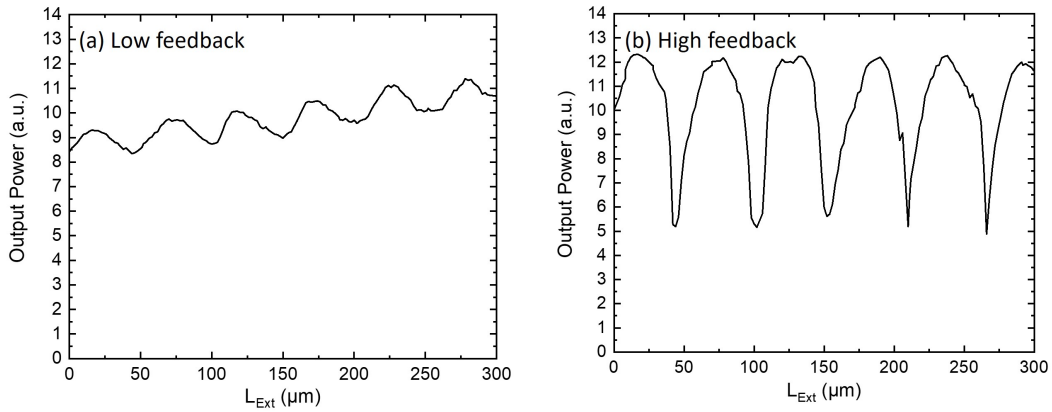

Fig. 5.18 Output power from external cavity V557 laser as a function of external mirror distance for (a) Low feedback and (b) High feedback. Laser operation near threshold (1.26 A), 10 kHz 5% DC, gated at 15 Hz.

For the low feedback strength regime, shown in figure (5.18 (a)), the response with external cavity length is roughly sinusoidal, as the frequency of laser remains unchanged as

the amplitude of r_2^{eff} changes, with the total round-trip phase remaining relative constant. For the stronger feedback regime, the change in output power is no longer sinusoidal due to the increased effect of r_2^{eff} on total round-trip phase, altering the lasing frequency. This feedback modulation scheme, not only provides strong amplitude modulation of the laser, but it can also modify the laser frequency.

5.2.4 Frequency modulation results

To understand the frequency tuning mechanism, FTIR measurements were performed on the external cavity laser for different mirror positions. Firstly, the frequency output of the laser was characterised as a function of current, keeping the external cavity mirror stationary, in the stronger feedback position. Figure (5.19) shows the frequency of the laser, which mode hops between three different modes, as the current is increased from 1.2 to 1.8 A.

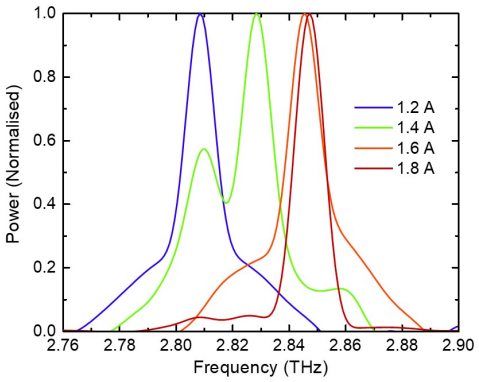

Fig. 5.19 (a) Normalised V557 Laser output spectrum for different operation currents for the external cavity QCL. 10 kHz pulsed (5% DC), gated at 15 Hz.

The transition between the mode at 2.83 THz and 2.85 THz is investigated by biasing the laser with a current of 1.6 A, and changing the length of the external cavity by $1\mu m$ steps, with the forced mode hopping shown in figure (5.20 (a)). As the mirror moves, the phase of the feedback changes, and therefore the mode receiving most constructive feedback is changed, which causes this mode hopping effect. Further to this, the frequency of the laser is also continuously tuned by a very small amount. This was predicted in figure (5.14 (b)), and is due to a sort of vernier tuning effect between the cavities. The switching in power between the two modes is illustrated in figure (5.20 (b)), which plots the peak power of the two modes as the mirror is moved.

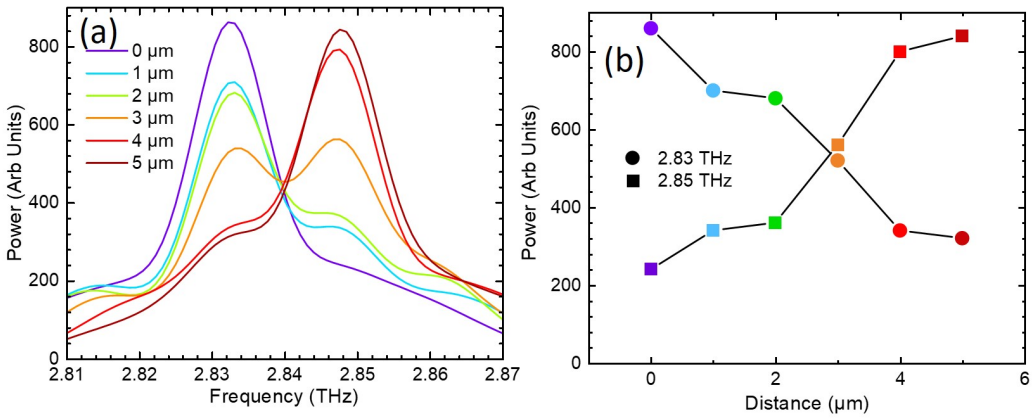

Fig. 5.20 (a) Spectrum of V557 laser output as the external cavity is moved in 1 micron steps with the laser current kept at 1.6 A. 10 kHz pulsed (5% DC), gated at 15 Hz. (b) Relative peak amplitude between two laser modes.

5.3 Active device external cavity feedback

With successful amplitude and frequency control of a QCL demonstrated using a moveable external cavity mirror, the next step is to achieve similar laser modulation using an active device as the feedback element, modifying the laser condition by applying a bias across the devices instead of changing L_{Ext}. This provides the advantage that there are no moving parts required, which is ideal for high speed modulation. Also the distance of mechanical moving parts is difficult to determine with the required nm accuracy, and therefore keeping fixed external cavity components is ideal.

5.3.1 Feedback modulation with split ring resonator device

The SRR/graphene device described in chapter 2 is first used to modulate the V427 laser. The experimental set-up is shown in figure (5.21), which is similar to the moveable mirror set-up shown in (5.15) however no parabolic mirrors are used, to simplify the set-up whilst also allowing for a shorter external cavity of around 1 cm.

Unlike the moving mirror experiment, the SRR/graphene device can change the feedback condition by modifying its reflectivity. The Comsol simulation shown in Chapter 2 is modified to show the reflectivity from the device surface as a function of frequency and graphene conductivity, shown in figure (5.21 (b)). The graphene conductivity as a function of backgate voltage is shown in figure (5.21 (c)), with the Dirac point visible at 25 V. It is

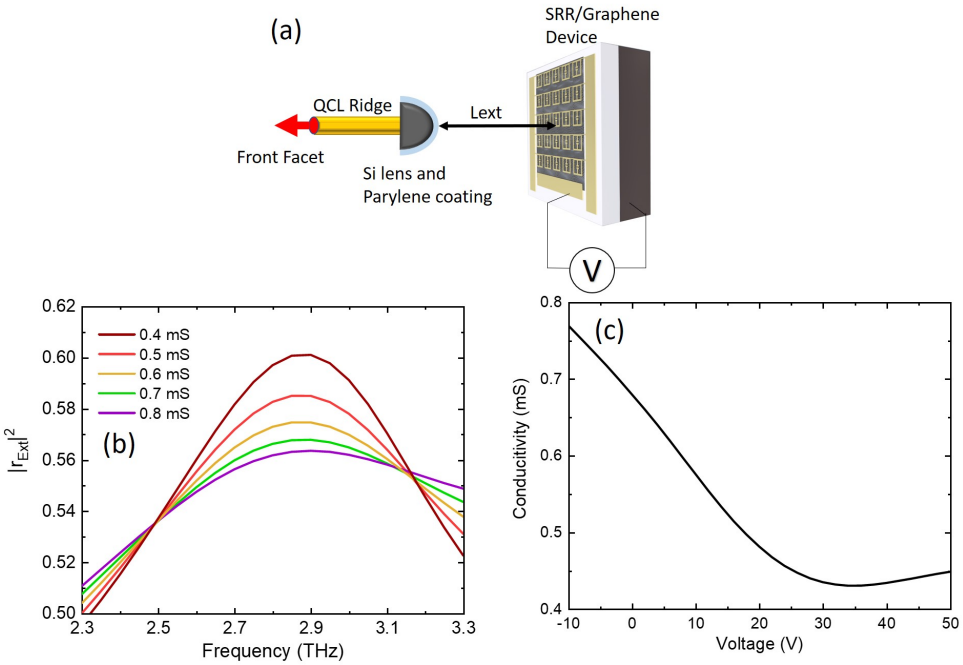

Fig. 5.21 (a) Illustration of external cavity with SRR/graphene device set-up. (b) Comsol simulation of reflectivity from SRR/Graphene device as a function of frequency and graphene conductivity. (c) Backgate graphene conductivity measurement for SRR/Graphene device.

important to note that these simulation results have been shifted by 150 GHz to compensate for the offset between TDS measurement and Comsol simulation observed in chapter 2.

The device is aligned to give a maximum change in output power around the threshold current as the backgate voltage is modulated. To achieve alignment with the active device area, a 5 Hz 10 V peak to peak square wave modulation is applied to the device around 0 V, and the laser is operated with a continuous 10 KHz square wave with 5 % duty cycle, with no gating applied. The signal from the Golay cell is then measured using the lock-in amplifier and the 5 Hz device modulation signal is used as a reference. With the device aligned for a maximum differential signal, a preliminary LIV and FTIR spectrum at different currents is taken with the backgate voltage set to 0 V. These results are shown in figure (5.22).

To determine the proportion of radiation fed back into the QCL, r_{Ext}, from the device, the change in threshold between the bare laser LIV shown in figure (5.16 (a)), and the current threshold shown in figure (5.22 (a)) is used. The threshold condition moves from 0.65 A to 0.77 A, and this proportion is used in equation (5.13) to determine r_2^{eff} compared to r_2 with no lens, which will be 0.56. r_2^{eff} is determined to be around 0.39, giving an r_{Ext} value of 0.37 using equation (5.8), assuming complete constructive interference.

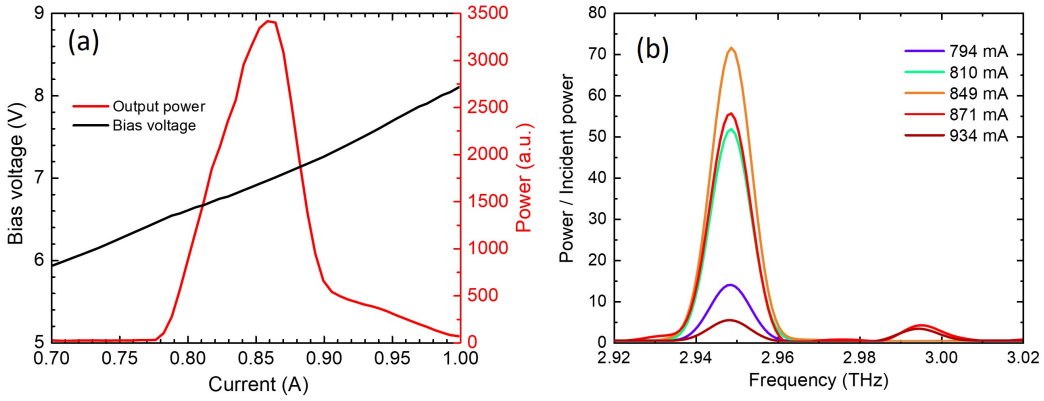

Fig. 5.22 (a) LIV and (b) output spectrum as function of operation current for the V427 external cavity QCL with SRR/graphene device backgate set to 0 V. 10 kHz pulsed (5% DC), gated at 15 Hz.

The backgate of the device is now changed, with separate LIV measurements taken for different values to see how the threshold current and dynamic range changed as the feedback condition is modulated. These results are shown in figure (5.23 (a)). The threshold of the laser is modulated from around 0.785 A when the back gate voltage is 40 V below the Dirac point, to 0.77A at the Dirac point. Using equations (5.13) and (5.8), this change in threshold current corresponds to a 5 % reduction of r_{Ext} as the voltage is decreased by 40 V below the Dirac point, assuming complete constructive interference with the external cavity. This is less than the predicted change in reflectivity shown in figure (5.21 (b)), which is most likely due to the feedback not being completely constructive, and also not all of the feedback power coming from the active device array, hence reducing the modulation depth. The LIV above 0.85 follows an unexpected trend, with the power increasing as the voltage is moved away from the Dirac point. This is most probably due to the laser mode-hopping being influenced by the external cavity feedback, with the feedback condition changing drastically for different modes. This will be investigated in more detail in figure (5.24), where the spectrum of the laser in this region is inspected.

The laser was now operated at three different currents with the output power measured as the backgate voltage was changed. The orange curve in figure (5.23 (b)) shows the normalised output power at 830 mA, as a function of the backgate voltage, and there is a 30 % reduction in output power when the backgate voltage is changed from V_{Dirac} to $V_{Dirac} - 50V$. This is a significant improvement of the modulation depth if the laser was reflected from the device, without being fed back into the cavity, with the simulated change in reflected power reducing by 10 % according to figure (5.21 (b)). This modulation depth is improved further when the

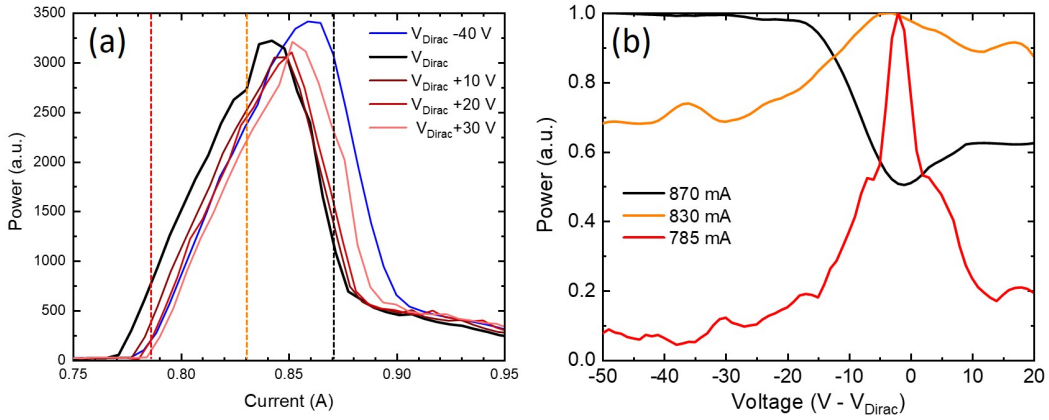

Fig. 5.23 (a) External cavity V427 Laser output power as a function of current for different SRR/graphene backgate values. (b) Output power from laser as a function device backgate for 3 operating currents. 10 kHz pulsed (5% DC), gated at 15 Hz.

laser is operating near threshold, at 785 mA. The red curve in figure (5.23 (b)), shows the laser being completely switched off for voltages below $V_{Dirac} - 40V$ with the laser threshold increase above 785 mA. The laser is switched from a lasing to a non-lasing state by altering the voltage across the device, effectively resulting in a laser power modulation of 100% in this current region. When the current was set to 870 mA, the power reduces by 40 % at V_{Dirac} compared to $V_{Dirac} - 50V$ with the power modulation inverted, most likely due to mode-hopping, as already discussed. To investigate this region, an FTIR measurement is performed with the laser current set to 880 mA, for different backgate voltage values. The results are shown in figure (5.24 (a)).

When the backgate voltage is set to V_{Dirac}-50 V, the mode at 2.95 THz is dominant. As the voltage is increased to V_{Dirac}, the mode at 2.99 THz increases slightly, and the power in the 2.95 THz mode decreases. The increased feedback at the Dirac point essentially causes the laser to mode hop. The power in the 2.99 THz mode is very small compared to the power in the 2.95 THz mode, which could be influenced by an absorption line. The FTIR involves a path length of over 1 m, and there are very strong, and thin, absorption lines around 3 THz. This would explain why the power drops so dramatically in the 880 mA region as the voltage across the backgate is increased towards V_{Dirac}. This mode hopping is very dependant on the length of the external cavity as this determines if the individual modes receive constructive or destructive interference as illustrated in figure (5.14). To demonstrate this experimentally, the external cavity SRR/device was moved a few millimeters further from the lens to 'Position 2', and the FTIR measurement at 880 mA was repeated. The result is shown in figure (5.14 (b)), with the mode hopping still present as the backgate voltage is

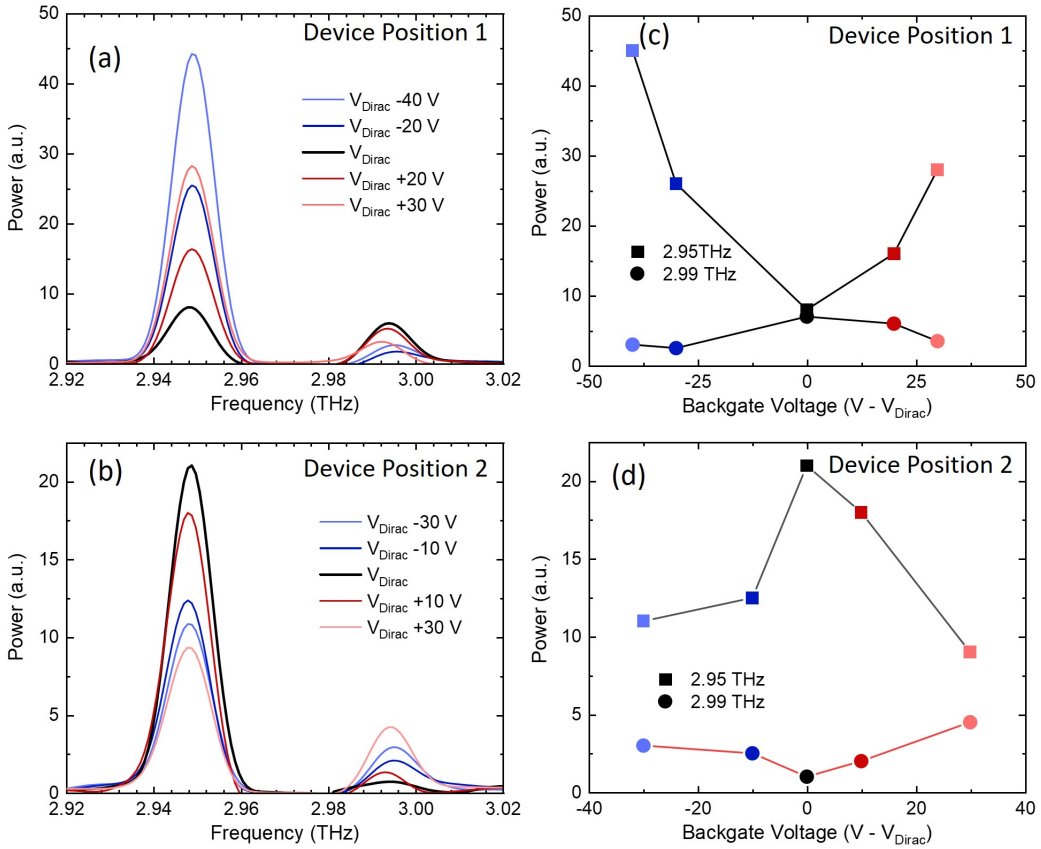

Fig. 5.24 (a) and (b) shown the output spectrum from the V427 laser for different back gate voltages with the laser current set to 880 mA with the device in two different positions. 10 kHz pulsed (5% DC), gated at 15 Hz. (c) and (d) show corresponding peak power values for the two laser modes as a function of backgate voltage.

increase towards V_{Dirac}, however, the mode hopping is now in the opposite direction. The mode at 2.95 THz increases at V_{Dirac}, with the mode at 2.99 THz decreasing. There is also a slight continuous tuning of the 2.99 THz mode, however, the resolution of the FTIR is not sufficient to conclusively determine the frequency shift. This experiment demonstrates how a simple amplitude modulator, with a small modulation depth of around 10 % can be used to modulate a QCL with modulation depths in the region of 100%, whilst also having a degree of control over the spectral mode composition.

5.3.2 Feedback modulation with coupled resonator device

From figure (5.14) we can see that changing the length of the external cavity has more of a drastic change in the lasing frequency than changing the feedback amplitude. Therefore, a

similar QCL tuning effect could be achieved by using a device which modulates the phase of reflection instead of the amplitude. As was shown in chapter 3, the coupled resonator devices have a strong influence on the phase of the transmission around the resonance condition, and this is also true for the reflected component. Tuning the phase fed back into the QCL should have an identical mode hopping effect as mechanically changing L_{Ext} as shown in figure (5.19) as we are modulating the effective external cavity length when we change the phase of reflection. To test this principle, a similar coupled resonator device, lithographically scaled down to operate around 3 THz is now used in an external cavity QCL configuration. The experimental set-up is the same as illustrated in figure (5.21 (a)), however a parabolic mirror was used as the active area for this device is 1 mm $\times$ 1 mm, which is smaller than the SRR/graphene device. The introduction of the parabolic mirrors should also improve the feedback efficiency, and replicates the mirror feedback measurement set-up used to produce figure (5.19 (b)) also using the same V557 laser with the partially suppressed lens.

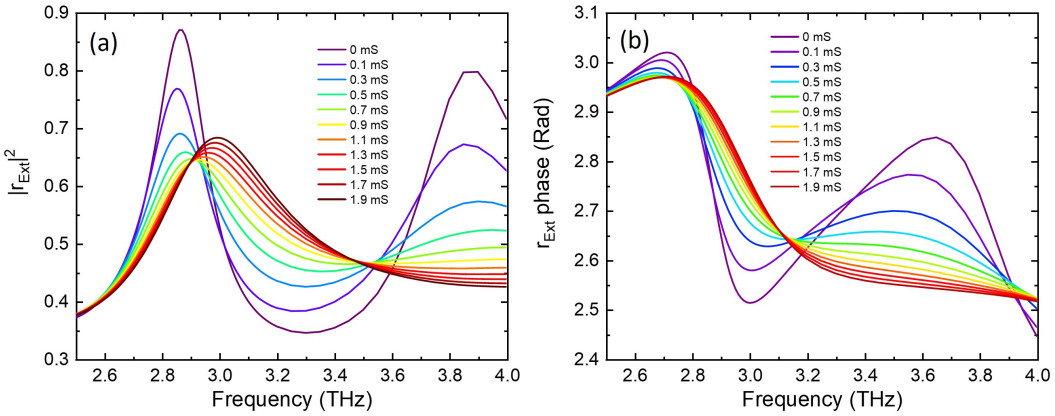

Fig. 5.25 Simulated reflectivity (a) amplitude and (b) phase for couple resonator device used for external cavity QCL feedback.

A Comsol simulation was performed for this device which is identical to device 1 described in chapter 3 with all the parameters scaled to 0.48 of the original size. The simulated reflectivity amplitude and phase are shown in figure (5.15 (a) and (b)) respectively. The mode hopping around 2.85 THz, observed due to the moving mirror in figure (5.19), is now attempted by modulating the backgate voltage across the device instead of moving a mirror distance. According to the Comsol simulation, the reflection amplitude should remain relatively constant around 0.65, and the phase should be modulated by around 0.1 radians for graphene conductivity ranges from 0.3 to 1.3 mS. The free space wavelength of 3 THz is 100 μm, and a change of 0.1 radian corresponds to an effective change in the external

cavity length in the order of 1 μm. According to figure (5.19 (b)), it should be possible to partially hop between modes by modulating the phase to this degree, if L_{Ext} is carefully selected. To this end, the laser is operated around 1.6 A, where this mode hopping occurs, and the external cavity power measurement is performed to find a cavity length where the laser power is changing drastically. With an unstable region found, the backgate voltage is modulated, and the spectrum of the laser measured.

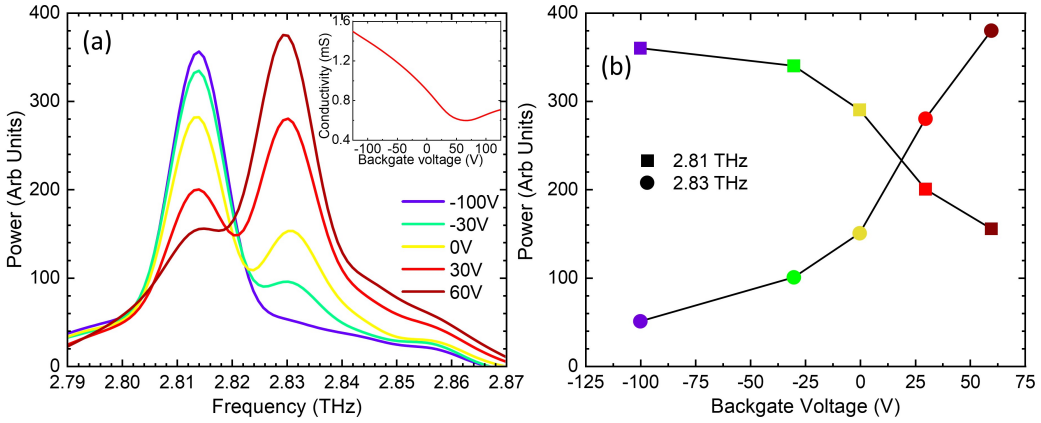

Fig. 5.26 (a) Output spectra of V557 QCL as a function of external cavity device backgate voltage using coupled resonator device with the laser current set to 1.6 A. 10 kHz pulsed (5% DC), gated at 15 Hz. Graphene conductivity measurement contained in the inset. (b) Corresponding mode amplitudes as a function of backgate voltage.

The output spectrum from the QCL as the backgate voltage is changed from - 100 V to 60 V is shown in figure (5.26 (a)) with an electrical characterisation of the graphene conductivity as a function of backgate voltage shown in the inset. In this case, 60 V corresponds to the Dirac point, such that the graphene conductivity can be modulated from 1.3 mS to 0.6 mS by the backgate from -100 V to 60 V. A successful forced mode hopping of the laser from 2.81 THz to 2.83 THz is observed as the backgate voltage, and reflection phase is modulated, further illustrated in figure (5.26 (b)). It is difficult to conclusively say this mode hopping comes from the phase alone, as a change in the amplitude will also have an effect, as determined by the results for the SRR/graphene device. This result does, however, bear a strong resemblance to the results shown in figure (5.20), demonstrating a similar mode hopping which was engineered by moving an external cavity mirror, and hence modulating the phase of the feedback. This therefore supports the case that phase modulation is the dominant tuning mechanism causing the mode hopping in figure (5.26). The external cavity regime is very complicated, as the operating mode of the laser is dependant on many factors, as discussed, as well as many factors beyond the scope of this thesis, including the frequency

dependant gain of the laser, and temperature considerations. These results do however show that by incorporating a metamaterial/graphene device with a THz QCL in an external cavity configuration, we can produce a highly tunable THz source.

5.4 Conclusion

In this section, several tunable THz source configurations have been demonstrated by implementing graphene/metamaterial devices with THz QCLs. MHz polarisation modulation speeds of THz QCLs were demonstrated by passing the laser output through the polarization modulation devices discussed in chapter 4. Being able to electrically tune the polarisation of THz sources could have strong applications for THz communications. Being able to electrically control the polarisation of standard THz sources could also have many potential uses in material characterisation. 100 % amplitude modulation of a QCL was achieved by tuning the feedback into an external cavity QCL. By exploiting this QCL feedback method, the frequency of the output could also be manipulated, providing much greater modulation depths than the devices could achieve in a transmission regime. This incredibly diverse set-up could have applications in gas spectroscopy, with the potential ability to produce a continuously frequency tunable THz QCL. This application was further demonstrated by the large amplitude modulation shown in figure (5.23), which was most likely due to tuning the laser frequency so that it coincided with an absorption line.

Chapter 6

Conclusion and further work

6.1 Conclusion

In this thesis, various graphene integrated metamaterial devices have been demonstrated for the purposes of electrical control of THz radiation. These devices have proven to be highly versatile, demonstrating control of the amplitude, phase, frequency and polarisation. This was achieved by employing an electrostatic graphene modulation scheme capable of high modulation speeds (>100 MHz [156]) due to the lack of mechanical moving parts. These proof of principle devices could therefore be used as modular components in a range of THz systems with potential applications in communications, spectroscopy and imaging.

Chapter 1 discussed the basic theory of THz time-domain spectroscopy (THz-TDS) and THz quantum cascade lasers (THz-QCLs). A range of THz modulator architectures were then discussed which convert passive metamaterial arrays into actively tunable devices, including the implementation of microelectromechanical systems, photoactive semiconductors, and electrostatically tunable graphene.

In chapter 2 the basic theory behind the operation of the devices in this thesis was investigated, based on metamaterial damping using graphene. Both finite element modeling, and equivalent circuit model representation techniques were used to describe the device modulation scheme. The fabrication process required to produce such devices was also laid out. Finally, a functioning THz amplitude modulator was demonstrated and tested in a THz-TDS system, with an amplitude modulation depth of around 12 % achieved for the transmission of 2.7 THz radiation.

Chapter 3 further developed the device design by demonstrating a metamaterial modulation device with two independently tunable resonances. The tuning range was limited for this device, however, this demonstration of a spatially addressable graphene and metamaterial device should open opportunities for applications such as THz wavefront engineering. Next, a

device for demonstrating a much more dramatic tuning range was developed by employing a coupled resonator metamaterial scheme, only variably damping one of the resonant elements in the unit cell. This modulation scheme demonstrated continuous tuning of the resonance frequency over a 60 GHz range [220], whilst also achieving a binary resonance frequency tuning of over 300 GHz. Further to this result, this highly dispersive device was shown to operate as an effective phase modulator, whilst also demonstrating modulation of the slow light effect.

With the coupled resonator modulation scheme demonstrating such versatile tuning, a similar design was developed in Chapter 4 to produce a device capable of actively tuning the polarisation of THz radiation. The coupled metamaterial array was specifically designed with an inbuilt lithographically defined 2D chirality, displaying optical activity and circular dichroism as a result. Polarisation modulation was successfully demonstrated with linear polarisation rotation of up to 20 degrees achieved [221]. A double layer coupled device was then developed, successfully converting incident linear radiation to circular radiation, with an electrically controllable ellipticity.

In chapter 5, the devices discussed in the previous chapters were then integrated with THz QCLs in various configurations, demonstrating how these devices could be externally coupled with a THz source to realise a versatile, tunable THz system. The polarisation modulation devices, working in transmission, are used to successfully rotate the transmitted polarisation from a QCL by up to 9 degrees [221]. To enhance the tuning range of the amplitude modulator device, an external cavity QCL configuration was formed, using the modulator implemented as a variably reflectivity external mirror. Near 100 % amplitude modulation is achieved due to the nonlinear feedback mechanism, drastically enhancing the modulation depth of the device [214]. The external cavity set-up was also used to manipulate the lasing frequency of the laser, with a laser controllably mode hopping between two single mode frequencies achieved by using the coupled resonator device to electrically tune the phase of the radiation in the cavity.

A table of the devices described in this thesis is shown on the following page, with the performance for amplitude modulation, resonant frequency tuning and polarization modulation compared to devices found in literature. The devices described in this thesis are shown in bold.

Type	Scheme	Freq (THz)	Mod depth	Speed	Year	Ref
Amp	Meta/2DEG	0.72	50 %	>kHz	2006	[147]
Amp	Meta/2DEG	0.81	80 %	>2 MHz	2009	[181]
Amp	Graph	Broad	15.2%	20 kHz	2012	[110]
Amp	Graph	0.62	64%	4 kHz	2012	[129]
Amp	Meta/Graph	2	20 %	110 MHz	2016	[156]
Amp	Meta/Graph	Broad	11.5 %	-	2013	[158]
Amp	Meta/Graph	4.7	60 %	40 MHz	2015	[157]
Amp	Meta/Graph	0.8	47 %	12 MHz	2012	[159]
Amp	Optical graph	<1	94 %	200 kHz	2014	[109]
Amp	**Meta/Graph**	**2.7**	**12 %**	**5-100 MHz**		**Page 54**
Amp	**Meta/Graph**	**1.9**	**56 %**	**5-100 MHz**		**Page 152**
Amp	**EC-QCL**	**2.9**	**100 %**	**5-100 MHz**		**Page 170**
Res freq	Meta/Graph	43	5 THz	-	2013	[161]
Res freq	Meta/Graph	55	10 THz	-	2014	[162]
Res freq	Meta/Graph	9	1 THz	-	2015	[157]
Res freq	Meta/Graph	6	2 THz	-	2015	[175]
Res freq	MEMS	0.6	0.3 THz	-	2014	[143]
Res freq	MEMS	0.5	0.1 THz	-	2013	[142]
Res freq	Meta/Silicon	1	0.3 THz	-	2008	[135]
Res freq	**Meta/Graph**	**1.5**	**60 GHz Cont**	**5-100 MHz**		**Page 88**
Res freq	**Meta/Graph**	**1.8**	**300 GHz**	**5-100 MHz**		**Page 89**
Pol	Meta/Silicon	1	θ =30 deg	-	2012	[139]
Pol	Meta/Silicon	1	θ =45 deg	-	2012	[140]
Pol	Meta/Silicon	0.9	ε = 0.2-0.85	1 GHz	2018	[138]
Pol	MEMS	1	θ = 60 deg	-	2015	[145]
Pol	**Meta/Graph**	**1.73**	**θ =30 deg**	**5-100 MHz**		**Page 130**
Pol	**Meta/Graph**	**2.1**	**ε = 0.6-1.0**	**5-100 MHz**		**Page 140**

Table 6.1 Table of devices from literature compared to devices described in this thesis (Bold).

6.2 Further work

6.2.1 Reflection phase modulator device

The coupled resonator devices discussed in chapter 3 showed promise for use as active phase modulators and were used to tune the phase fed back into an external cavity QCL in chapter 5. According to simulation, a maximum reflected phase modulation of around 0.1 radians was achievable in the graphene conductivity tuning range between 0.5 and 1.5 mS. For a more versatile phase modulator device, which could be used in real world applications, we would like to increase the potential tuning range to a value in the order of π radians. The reflection from the air to metamaterial/substrate interface can be described as a linear combination between the metamaterial reflected component and the Fresnel reflection component due to the substrate refractive index. The Fresnel reflection component has a π phase shift as it is going from a low to a high refractive index. The metamaterial reflection also goes through a π phase shift at the resonance frequency with the phase changing away from the resonance in a Lorentz oscillator fashion. The DC offset due to the Fresnel reflection therefore washes out the phase modulation of the metamaterial reflection, reducing the net tuning range of the reflected phase. If the reflection from the other side of this interface, going from Silicon to air is used instead, the Fresnel reflection will no longer have a phase shift, however, the metamaterial resonance will have the same π phase shift as before. In this scenario, the two reflected components are now destructively interfering with each other near resonance, leading to a highly unstable phase regime allowing for much larger tuning ranges. This destructive interference tuning is illustrated in figure (6.1 (a)).

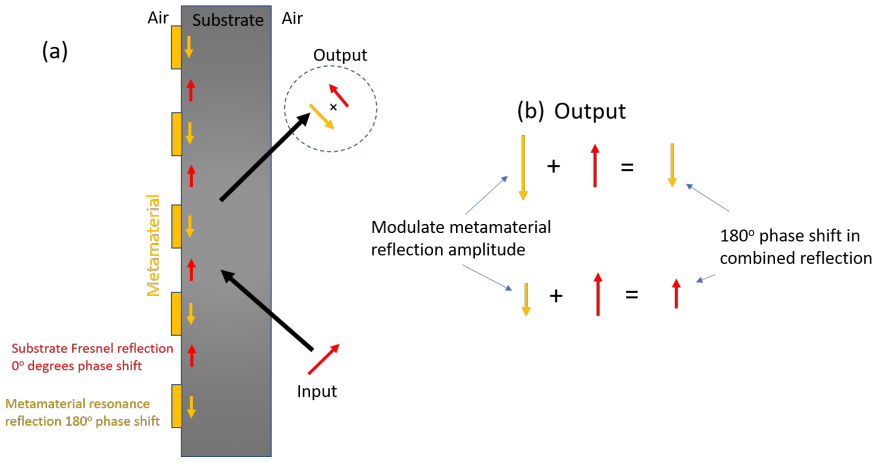

Fig. 6.1 (a) Illustration of phase from Fresnel and metamaterial reflection components at resonance with opposing phase contributions. (b) Illustration of unstable phase tuning regime due to linear combination of phase components.

In this figure the input radiation is impinging on the metamaterial interface from inside the silicon. The reflected component is a linear sum of the metamaterial and Fresnel reflection components which are described by the yellow and red arrows respectively. Figure (6.1 (b)) illustrates the dramatic phase tuning which is achievable by modulating the metamaterial amplitude by only a small amount, if the two reflection components are carefully balanced. A π phase modulation should therefore be achievable for only modest metamaterial amplitude tuning ranges. One can think of this as tuning the effective refractive index of the metamaterial from just below 3.4 (refractive index of silicon) to just above 3.4, flipping the reflection phase from the interface.

To illustrate the greatly increased tuning range achievable by using this interface, the transmission TDS results shown in figure 3 are modified to probe this reflection. Instead of measuring the spectrum of the first transmitted peak, the second internally reflected peak is probed. This measurement is not, however, normalised to the transmission pulse through nitrogen as before, it is now normalised with respect to the first transmission peak. Assuming there is a flat phase reflection from the back silicon/nitrogen interface, any phase perturbation between the first and second peak, other than a basic linear offset, is produced by the reflection from the internal metamaterial interface. The TDS measured results for the transmitted electric field amplitude and phase are shown in figure (6.2 (a) and (b)).

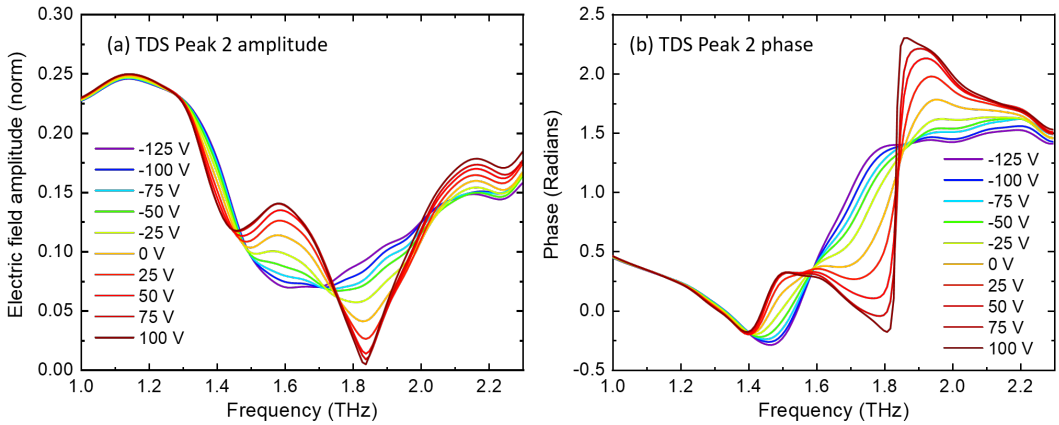

Fig. 6.2 (a) Electric field amplitude determined by gating the second transmitted TDS peak and normalising to the first peak. (b) Phase difference between the first and second peak as a function of frequency and backgate voltage.

The amplitude measurement shows a near 100 % modulation range at the anti-bonding resonance, just over 1.8 THz. This is because the reflection amplitude from the metamaterial component is very close to the component from the Fresnel reflection, and hence, as the metamaterial reflection amplitude is maximal at 100 V (Dirac point), these components

are close to completely destructively interfering, leading to a resultant reflection amplitude close to 0. Due to this unstable phase regime, there is now a maximum phase modulation of >1.5 radians near the resonance, a 15 times improvement compared to reflection from the front facet. If a laser at 1.72 THz is used with this device, the amplitude of reflection remains constant with only a 5 % deviation as the voltage is changed, however, a phase tuning range of 1.2 radians is demonstrated. This device was not designed to work in this refection regime, and therefore, much greater tuning ranges should be achievable by small lithographic alterations to the metamaterial spacing for example. This tuning mechanism also negated any reflection from the back facet, and therefore, the device could be excited at an angle with this component spatially separated, or a parylene anti-reflection coating could be used to negate this reflection. To confirm this result, a reflection TDS measurement should be performed and compared to the indirect transmission first peak normalised to first peak method shown here.

6.2.2 Continuous tuning of terahertz quantum cascade laser improvements

A pertinent application for this phase modulator with an increased tuning range could be in an external cavity feedback configuration similar to the one discussed in chapter 5. However, to be able to tune the frequency of the QCL in a continuous and controllable way, the 3 mirror model could be reduced to a phase tunable 2 mirror model by directly attaching the phase tuning device to the back facet of the QCL in the configuration shown in figure (6.3).

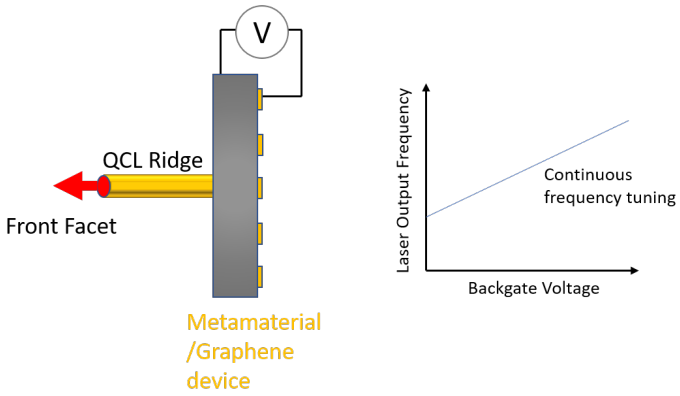

Fig. 6.3 Illustration of continuously tunable THz QCL design.

In this configuration, the total phase of the QCL round trip should be directly tunable by altering the phase of the internal metamaterial interface reflection, and hence the allowed Fabry-Perot lasing frequency should be continuously tunable. This would require the device

to be in the cold finger cryogenic environment along side the QCL, which would require a new electrical biasing scheme. Mechanically fixing the metamaterial/graphene device to the QCL ridge would also be a challenging engineering problem, however silicon lenses have been physically attached (PMMA) successfully before, and therefore, a similar technique could be used for the device. The graphene could have different mobility properties at low temperature, depending on the dominate scattering mechanisms, and therefore would have to be first characterised at a cryogenic temperature. Despite these challenges, such a configuration could achieve continuous electrical single mode tuning of a QCL which would have countless application opportunities in fields such as gas spectroscopy.

6.2.3 Reflection polarisation modulator device

Chapter 4 demonstrated devices which can electrically modulate the polarisation angle of transmitted radiation by up to 30 degrees, and a second device which can modulate the ellipticity of transmitted polarisation from around 0.55 to 1 at a given frequency. These devices have successfully demonstrated polarisation modulation of a THz QCL with potential speeds of 10's of MHz. For the next iteration of these devices, it is necessary to enhance the polarisation modulation depth, getting close to the three ideal scenarios; 90 degree angle modulation, complete linear to circular modulation and complete handedness modulation of circular polarisation.

To achieve this goal using graphene as a tuning mechanism, a different approach is required. As discussed in this chapter it was discovered that the phase of reflection from the metamaterial, when excited from the back, could be drastically changed by tuning the graphene conductivity due to the destructive interference between the Fresnel reflection from the substrate and the metamaterial reflection. As these components are very similar in amplitude, the metamaterial reflected component only needs to be changed by a few percent to cause a complete π phase change in the combined reflected E_y component. If the phase of the E_x component remains unchanged throughout this process, the angle of the polarisation radiation can be dramatically changed.

To test this, a Comsol simulation is performed on the single layer device, exciting with E_y from inside the silicon substrate, and measuring the angle of the reflected component. These simulations are shown in figure (6.4)

Figure (6.4 (a)) shows an example device layout to take advantage of this internal reflection. The reflection from the back air/silicon interface needs to be removed, and therefore an anti-reflection parylene coated lens could be attached to the back of the sample, using the same technique developed for attaching the lenses to QCLs for feedback in chapter 5. The resultant amplitude of E_y and E_x as a function of graphene conductivity is shown in

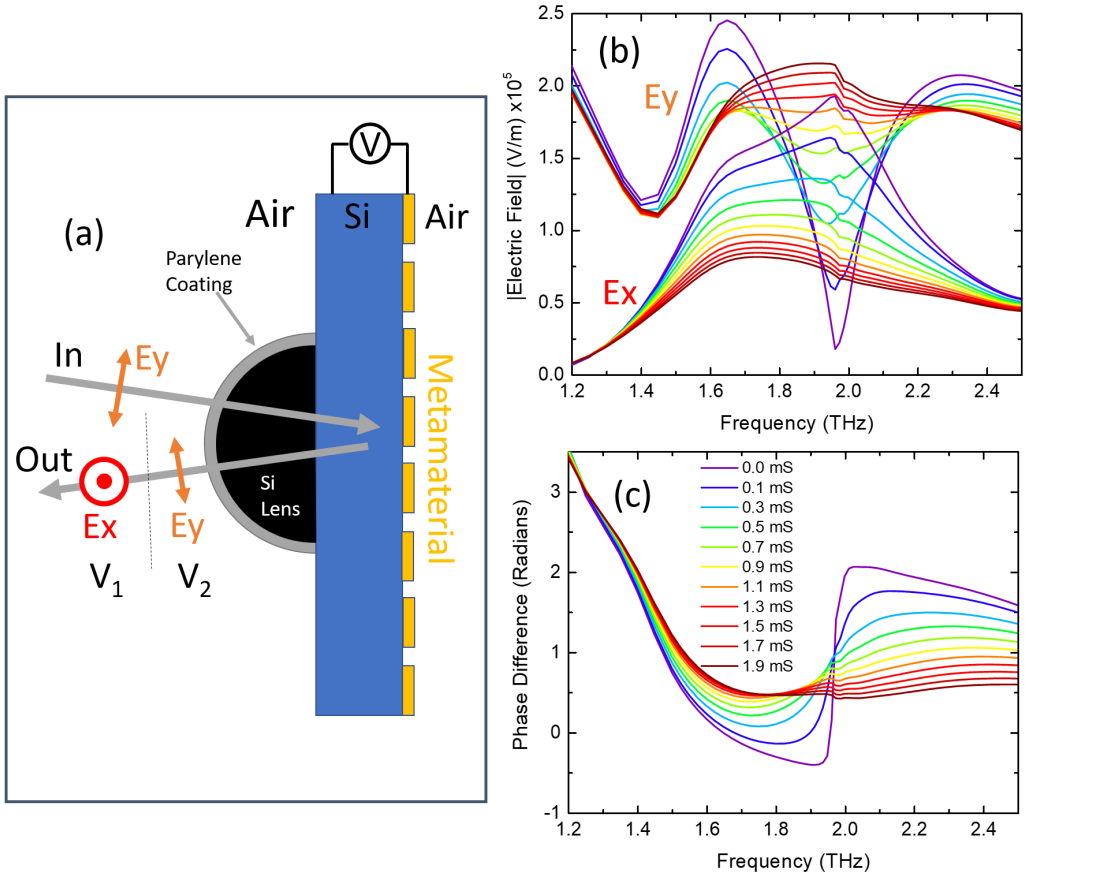

Fig. 6.4 (a) Potential polarisation reflection modulator set-up. (b) Comsol simulation of reflected E_y and E_x amplitude when a nominal power of 1 W is incident, polarised in E_y direction. (c) Simulated phase difference between reflected E_y and E_x.

figure (6.4 (b)) with the phase difference between these components shown in (6.4 (c)). $|E_x|$ follows a similar pattern as was measured in the transmission configuration in (4.22 (b)), however, the $|E_y|$ component changes dramatically at around 1.97 THz due to the destructive interference with the Fresnel reflection component. This results in a near 100 % amplitude modulation of E_y as the graphene conductivity is changed. The phase difference between E_y and E_x is difficult to interpret, however, under 2 THz it is close to 0, which is ideal for linear polarized radiation. Above 2 THz, however, the phase is modulated from 0.5 to 2 as the conductivity is changed, meaning this could cause a powerful ellipticity modulation. The resultant angle and ellipticity results are shown in figure (6.4)

Figure (6.5 (a) and (b)) show the angle and ellipticity as a function of graphene conductivity and frequency. At 1.975 THz the angle is modulated by around 75 degrees with the resultant polar plot extremes shown in figure (6.5 (c)). This is a huge improvement on the

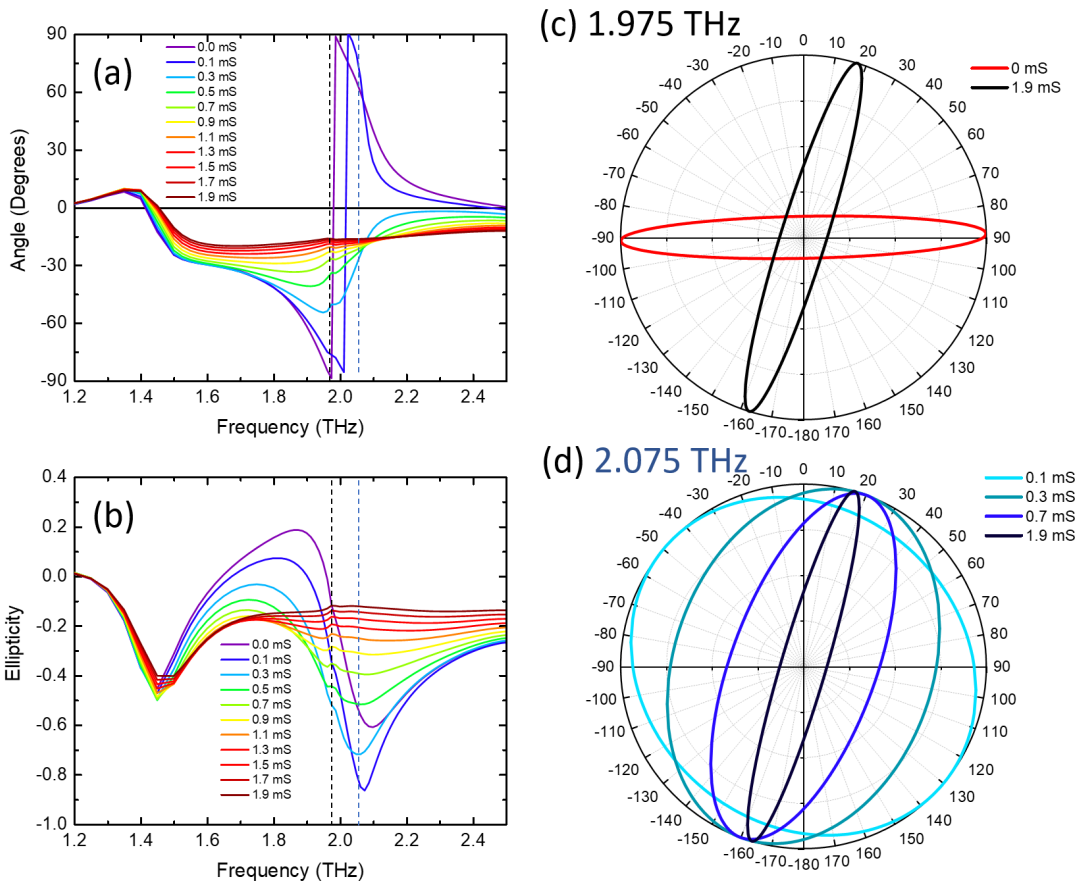

Fig. 6.5 (a)Angle and (b) ellipticity of reflected THz radiation as a function of frequency and for different graphene conductivities. Polar plots illustrating the polarisation condition at (c) 1.975 THz, and (b) 2.075 THz.

polarisation rotation achievable in the transmission configuration, with 30 degrees modulation being the maximum rotation measured. The ellipticity at 2.075 THz is modulated from around -0.1 to -0.9, however the ellipticity of -1 is achievable for a graphene conductivity between 0.1 and 0.3, and just was not contained in this incremental sweep. This ellipticity tuning range of -0.1 to -1 is illustrated in figure (6.5 (d)) showing a much improved ellipticity modulation compared to the tuning range of around 0 to 0.2 demonstrated in transmission mode for the single layer device. This simulation shows a promising way forward for the design of these polarisation modulators, as this device was not optimized for this reflection configuration. There is a large parameter space for potential new designs to improve upon this proof of principle device, and therefore these graphene and metamaterial devices could be

very useful for a multitude of THz applications, requiring high speed, electrical polarisation modulation.

6.2.4 Polarisation sensitive spectroscopy

One of the main applications of TDS systems is material characterisation in fields such as the pharmaceutical industry. There have been a myriad of papers published involving the pill compression process, measured by performing birefringence TDS measurements [10, 11, 51]. Currently, the polarisation of excitation has to be mechanically changed by rotating the sample, which prohibits real time, dynamic compression measurements. The polarisation modulation devices described could be used to actively tune the transmitted polarisation impinging on a sample in a TDS set-up, without requiring mechanical alteration. This would allow for much faster birefringence measurements to be performed enabling transient effects to be captured in such a measurement system. Such a high speed THz room temperature system could enable real time birefringence THz system with countless applications in the characterisation of transient material processes.

References

[1] D. Shrekenhamer, S. Rout, S. Sonkusale, C. Bingham, R. D. Averitt, A. C. Strikwerda, and W. J. Padilla. High speed terahertz modulation from metamaterials with embedded high electron mobility transistors. *Optics Express*, 19(10):9968, 5 2011.

[2] B S. Williams. Terahertz quantum-cascade lasers. *Nature Photonics*, 1(9):517–525, 9 2007.

[3] I. F. Akyildiz, J. M. Jornet, and C. Han. Terahertz band: Next frontier for wireless communications. *Physical Communication*, 12:16–32, 9 2014.

[4] S. S. Dhillon, M. S. Vitiello, E. H. Linfield, A. G. Davies, M. C. Hoffmann, J. Booske, C. Paoloni, M. Gensch, P. Weightman, G. P. Williams, E. Castro-Camus, D. R. S. Cumming, F. Simoens, I. Escorcia-Carranza, J. Grant, S. Lucyszyn, M. Kuwata-Gonokami, K. Konishi, M. Koch, C. A. Schmuttenmaer, T. L. Cocker, R. Huber, A. G. Markelz, Z D Taylor, Vincent P Wallace, J Axel Zeitler, Juraj Sibik, Timothy M Korter, B Ellison, S Rea, P Goldsmith, Ken B Cooper, Roger Appleby, D Pardo, P G Huggard, V Krozer, Haymen Shams, Martyn Fice, Cyril Renaud, Alwyn Seeds, Andreas Stöhr, Mira Naftaly, Nick Ridler, Roland Clarke, John E Cunningham, and Michael B Johnston. The 2017 terahertz science and technology roadmap. *Journal of Physics D: Applied Physics*, 50(4):043001, 2 2017.

[5] S. L. Dexheimer. *Terahertz spectroscopy : principles and applications*. CRC Press/Taylor & Francis, 2008.

[6] H. Richter, S. G. Pavlov, A. D. Semenov, L. Mahler, A. Tredicucci, H. E. Beere, D. A. Ritchie, and H.-W. Hübers. Submegahertz frequency stabilization of a terahertz quantum cascade laser to a molecular absorption line. *Applied Physics Letters*, 96(7):071112, 2 2010.

[7] Y. Ren, J. N. Hovenier, M. Cui, D. J. Hayton, J. R. Gao, T. M. Klapwijk, S. C. Shi, T.-Y. Kao, Q. Hu, and J. L. Reno. Frequency locking of single-mode 3.5-THz quantum cascade lasers using a gas cell. *Applied Physics Letters*, 100(4):041111, 1 2012.

[8] S. Bordács, I. Kézsmárki, D. Szaller, L. Demkó, N. Kida, H. Murakawa, Y. Onose, R. Shimano, T. Rõõm, U. Nagel, S. Miyahara, N. Furukawa, and Y. Tokura. Chirality of matter shows up via spin excitations. *Nature Physics*, 8(10):734–738, 10 2012.

[9] B. C. Park, T. Kim, K. I. Sim, B. Kang, J. W. Kim, B. Cho, K. Jeong, M. Cho, and J. H. Kim. Terahertz single conductance quantum and topological phase transitions in topological insulator Bi2Se3 ultrathin films. *Nature Communications*, 6(1):6552, 12 2015.

[10] D. Markl, A. Strobel, R. Schlossnikl, J. Bøtker, P. Bawuah, C. Ridgway, J. Rantanen, T. Rades, P. Gane, K. Peiponen, and J. A. Zeitler. Characterisation of pore structures of pharmaceutical tablets: A review. *International Journal of Pharmaceutics*, 538(1-2):188–214, 3 2018.

[11] D. Markl, P. Bawuah, C. Ridgway, S. van den Ban, D. J. Goodwin, J. Ketolainen, P. Gane, K. Peiponen, and J. A. Zeitler. Fast and non-destructive pore structure analysis using terahertz time-domain spectroscopy. *International Journal of Pharmaceutics*, 537(1-2):102–110, 2 2018.

[12] T. Yasui, T. Yasuda, K. Sawanaka, and T. Araki. Terahertz paintmeter for noncontact monitoring of thickness and drying progress in paint film. *Applied Optics*, 44(32):6849, 11 2005.

[13] D. D. Arnone, C. M. Ciesla, A. Corchia, S. Egusa, M. Pepper, J. M. Chamberlain, C. Bezant, E. H. Linfield, R. Clothier, and N. Khammo. Applications of terahertz (THz) technology to medical imaging. volume 3828, page 209. International Society for Optics and Photonics, 9 1999.

[14] K. Humphreys, J.P. Loughran, M. Gradziel, W. Lanigan, T. Ward, J. A. Murphy, and C. O'Sullivan. Medical applications of terahertz imaging: a review of current technology and potential applications in biomedical engineering. In *The 26th Annual International Conference of the IEEE Engineering in Medicine and Biology Society*, volume 3, pages 1302–1305. IEEE.

[15] S. Koenig, D. Lopez-Diaz, J. Antes, F. Boes, R. Henneberger, A. Leuther, A. Tessmann, R. Schmogrow, D. Hillerkuss, R. Palmer, T. Zwick, C. Koos, W. Freude, O. Ambacher, J. Leuthold, and I. Kallfass. Wireless sub-THz communication system with high data rate. *Nature Photonics*, 7(12):977–981, 12 2013.

[16] T. Kleine-Ostmann and T. Nagatsuma. A review on terahertz communications research, 2 2011.

[17] J. Y. Suen, M. T. Fang, S. P. Denny, and P. M. Lubin. Modeling of terabit geostationary terahertz satellite links from globally dry locations. *IEEE Transactions on Terahertz Science and Technology*, 5(2):299–313, 3 2015.

[18] B. Choudhury, A. R. Sonde, and R. M. Jha. Terahertz Antenna Technology for Space Applications. pages 1–33. 2016.

[19] G. P. Gallerano and S. Biedron. Overview of terahertz radiation sources. In *Proceedings of the 2004 FEL Conference*, pages 216–221, 2004.

[20] R. A. Lewis. A review of terahertz sources. *Journal of Physics D: Applied Physics*, 47(37):374001, 9 2014.

[21] R. Degl'Innocenti, S. J. Kindness, H. E. Beere, and D. A. Ritchie. All-integrated terahertz modulators. *Nanophotonics*, 7(1):127–144, 1 2018.

[22] C. Sirtori. Applied physics: Bridge for the terahertz gap, 5 2002.

[23] T. W. Crowe, W. L. Bishop, D. W. Porterfield, J. L. Hesler, and R. M. Weikle. Opening the terahertz window with integrated diode circuits. In *IEEE Journal of Solid-State Circuits*, volume 40, pages 2104–2109, 10 2005.

[24] L. A. Samoska. An overview of solid-state integrated circuit amplifiers in the submillimeter-wave and THz regime, 9 2011.

[25] P. Dean, A. Valavanis, J. Keeley, K. Bertling, Y. L. Lim, R. Alhathlool, A. D. Burnett, L. H. Li, S. P. Khanna, D. Indjin, T. Taimre, A. D. Rakić, E. H. Linfield, and A. G. Davies. Terahertz imaging using quantum cascade lasers - A review of systems and applications, 9 2014.

[26] Y. Lee. *Principles of terahertz science and technology*. Springer, 2009.

[27] M. Tonouchi. Cutting-edge terahertz technology, 2 2007.

[28] R. Paiella. *Intersubband transitions in quantum structures*. McGraw-Hill, 2006.

[29] A. Acharyya and J. P. Banerjee. Potentiality of IMPATT Devices as Terahertz Source: An Avalanche Response Time-based Approach to Determine the Upper Cut-off Frequency Limits. *IETE Journal of Research*, 59(2):118, 2013.

[30] T. C. L. G. Sollner, W. D. Goodhue, P. E. Tannenwald, C. D. Parker, and D. D. Peck. Resonant tunneling through quantum wells at frequencies up to 2.5 THz. *Applied Physics Letters*, 43(6):588–590, 9 1983.

[31] A. Khalid, N. J. Pilgrim, G. M. Dunn, M. C. Holland, C. R. Stanley, I. G. Thayne, and D. R. S. Cumming. A planar Gunn diode operating above 100 GHz. *IEEE Electron Device Letters*, 28(10):849–851, 10 2007.

[32] S. M. Sze and K. K. Ng. *Physics of semiconductor devices*. Wiley-Blackwell, 2006.

[33] T. C. Marshall. *Free-electron lasers*. MacMillan, 1985.

[34] M. Mineo and C. Paoloni. Corrugated rectangular waveguide tunable backward wave oscillator for terahertz applications. *IEEE Transactions on Electron Devices*, 57(6):1481–1484, 6 2010.

[35] R. Köhler, A. Tredicucci, F. Beltram, H. E. Beere, E. H. Linfield, A. G. Davies, D. A. Ritchie, R. C. Iotti, and F. Rossi. Terahertz semiconductor-heterostructure laser. *Nature*, 417(6885):156–159, 5 2002.

[36] L. Li, L. Chen, J. Zhu, J. Freeman, P. Dean, A. Valavanis, A. G. Davies, and E. H. Linfield. Terahertz quantum cascade lasers with >1 W output powers. *Electronics Letters*, 50(4):309–311, 2 2014.

[37] M. A. Belkin, F. Capasso, A. Belyanin, D. L. Sivco, A. Y. Cho, D. C. Oakley, C. J. Vineis, and G. W. Turner. Terahertz quantum-cascade-laser source based on intracavity difference-frequency generation. *Nature Photonics*, 1(5):288–292, 5 2007.

[38] R. Sowade, I. Breunig, I. Cámara Mayorga, J. Kiessling, C. Tulea, V. Dierolf, and K. Buse. Continuous-wave optical parametric terahertz source. *Optics Express*, 17(25):22303, 12 2009.

[39] J. Mangeney, A. Merigault, N. Zerounian, P. Crozat, K. Blary, and J. F. Lampin. Continuous wave terahertz generation up to 2THz by photomixing on ion-irradiated In0.53Ga0.47As at 1.55μm wavelengths. *Applied Physics Letters*, 91(24):241102, 12 2007.

[40] N. Kim, S. Han, H. Ko, Y. A. Leem, H. Ryu, C. W. Lee, D. Lee, M. Y. Jeon, S. K. Noh, and K. H. Park. Tunable continuous-wave terahertz generation/detection with compact 155 μm detuned dual-mode laser diode and InGaAs based photomixer. *Optics Express*, 19(16):15397, 8 2011.

[41] I. S. Gregory, C. Baker, W. R. Tribe, I. V. Bradley, M. J. Evans, E. H. Linfield, A. G. Davies, and M. Missous. Optimization of photomixers and antennas for continuous-wave terahertz emission. *IEEE Journal of Quantum Electronics*, 41(5):717–728, 5 2005.

[42] N. M. Burford and M. O. El-Shenawee. Review of terahertz photoconductive antenna technology. *Optical Engineering*, 56(1):010901, 2017.

[43] A. Mussot, A. Kudlinski, R. Habert, I. Dahman, G. Mélin, L. Galkovsky, A. Fleureau, S. Lempereur, L. Lago, D. Bigourd, T. Sylvestre, M. W. Lee, and E. Hugonnot. 20 THz-bandwidth continuous-wave fiber optical parametric amplifier operating at 1 μm using a dispersion-stabilized photonic crystal fiber. *Optics Express*, 20(27):28906, 12 2012.

[44] T. Wang, M. Zalkovskij, K. Iwaszczuk, A. V. Lavrinenko, G. V. Naik, J. Kim, A. Boltasseva, and P. U. Jepsen. Ultrabroadband terahertz conductivity of highly doped ZnO and ITO. *Optical Materials Express*, 5(3):566, 3 2015.

[45] M. Hangyo, M. Tani, and T. Nagashima. Terahertz Time-Domain Spectroscopy of Solids: A Review. *International Journal of Infrared and Millimeter Waves*, 26(12):1661–1690, 12 2005.

[46] R. J. B. Dietz, B. Globisch, M. Gerhard, A. Velauthapillai, D. Stanze, H. Roehle, M. Koch, T. Göbel, and M. Schell. 64 μW pulsed terahertz emission from growth optimized InGaAs/InAlAs heterostructures with separated photoconductive and trapping regions. *Applied Physics Letters*, 103(6):061103, 8 2013.

[47] S. Yassin, K. Su, H. Lin, L. F. Gladden, and J. A. Zeitler. Diffusion and swelling measurements in pharmaceutical powder compacts using terahertz pulsed imaging. *Journal of pharmaceutical sciences*, 104(5):1658–67, 5 2015.

[48] K. Peiponen, P. Bawuah, M. Chakraborty, M. Juuti, J. A. Zeitler, and J. Ketolainen. Estimation of Young's modulus of pharmaceutical tablet obtained by terahertz time-delay measurement. *International Journal of Pharmaceutics*, 489(1-2):100–105, 7 2015.

[49] H. Lin, R. K. May, M. J. Evans, S. Zhong, L. F. Gladden, Y. Shen, J. A. Zeitler, R. K. May, and S. Zhong. Impact of Processing Conditions on Inter-tablet Coating Thickness Variations Measured by Terahertz In-Line Sensing. *Journal of pharmaceutical sciences*, 104(8):2513–22, 8 2015.

[50] V. P. Wallace, D. Ferachou, P. Ke, K. Day, S. Uddin, J. Casas-Finet, C. F. Van Der Walle, R. J. Falconer, and J. A. Zeitler. Modulation of the Hydration Water Around Monoclonal Antibodies on Addition of Excipients Detected by Terahertz Time-Domain Spectroscopy. *Journal of pharmaceutical sciences*, 104(12):4025–4033, 12 2015.

[51] J. Sibik, K. Löbmann, T. Rades, and J. A. Zeitler. Predicting Crystallization of Amorphous Drugs with Terahertz Spectroscopy. *Molecular Pharmaceutics*, 12(8):3062–3068, 8 2015.

[52] N. Y. Tan, R. Li, P. Bräuer, C. D'Agostino, L. F. Gladden, and J. A. Zeitler. Probing hydrogen-bonding in binary liquid mixtures with terahertz time-domain spectroscopy: a comparison of Debye and absorption analysis. *Physical Chemistry Chemical Physics*, 17(8):5999–6008, 2 2015.

[53] P. F. Taday. Applications of terahertz spectroscopy to pharmaceutical sciences. *Philosophical Transactions of the Royal Society of London. Series A: Mathematical, Physical and Engineering Sciences*, 362(1815):351–364, 2 2004.

[54] J. A. Zeitler, P. F. Taday, D. A. Newnham, M. Pepper, K. C. Gordon, and T. Rades. Terahertz pulsed spectroscopy and imaging in the pharmaceutical setting - a review. *Journal of Pharmacy and Pharmacology*, 59(2):209–223, 2 2007.

[55] S. Badhwar, J. Sibik, P. R. Kidambi, H. E. Beere, A. J. Zeitler, S. Hofmann, and D. A. Ritchie. Intrinsic terahertz plasmon signatures in chemical vapour deposited graphene. *Applied Physics Letters*, 103(12):121110, 9 2013.

[56] J. D. Buron, F. Pizzocchero, P. U. Jepsen, D. H. Petersen, J. M. Caridad, B. S. Jessen, T. J. Booth, and P. Bøggild. Graphene mobility mapping. *Scientific Reports*, 5(1):12305, 12 2015.

[57] E. P. Parrott, J. A. Zeitler, and L. F. Gladden. Accurate determination of optical coefficients from chemical samples using terahertz time-domain spectroscopy and effective medium theory. *Optics Letters*, 34(23):3722, 12 2009.

[58] E. P. J. Parrott, J. A. Zeitler, L. F. Gladden, S. N. Taraskin, and S. R. Elliott. Extracting accurate optical parameters from glasses usingterahertz time-domain spectroscopy. *Journal of Non-Crystalline Solids*, 355(37-42):1824–1827, 10 2009.

[59] O. Trushkevych, H. Xu, T. Lu, J. A. Zeitler, R. Rungsawang, F. Gölden, N. Collings, and W. A. Crossland. Broad spectrum measurement of the birefringence of an isothiocyanate based liquid crystal. *Applied Optics*, 49(28):5212, 10 2010.

[60] C. L. K. Dandolo and P. U. Jepsen. THz reflectometric imaging of contemporary panel artwork. In *2013 38th International Conference on Infrared, Millimeter, and Terahertz Waves (IRMMW-THz)*, pages 1–2. IEEE, 9 2013.

[61] M. Naftaly and R. E. Miles. Terahertz Time-Domain Spectroscopy for Material Characterization. *Proceedings of the IEEE*, 95(8):1658–1665, 8 2007.

[62] T. D. Dorney, R. G. Baraniuk, and D. M. Mittleman. Material parameter estimation with terahertz time-domain spectroscopy. *Journal of the Optical Society of America A*, 18(7):1562, 7 2001.

[63] B. Ferguson and X Zhang. Materials for terahertz science and technology. *Nature Materials*, 1(1):26–33, 9 2002.

[64] D. Grischkowsky, S. Keiding, M. van Exter, and C. Fattinger. Far-infrared time-domain spectroscopy with terahertz beams of dielectrics and semiconductors. *Journal of the Optical Society of America B*, 7(10):2006, 10 1990.

[65] S. Krimi, J. Klier, J. Jonuscheit, G. von Freymann, R. Urbansky, and R. Beigang. Highly accurate thickness measurement of multi-layered automotive paints using terahertz technology. *Applied Physics Letters*, 109(2):021105, 7 2016.

[66] S. Krimi, J. Klier, M. Herrmann, J. Jonuscheit, and R. Beigang. Inline multilayer thickness sensing by using terahertz time-domain spectroscopy in reflection geometry. In *2013 38th International Conference on Infrared, Millimeter, and Terahertz Waves (IRMMW-THz)*, pages 1–2. IEEE, 9 2013.

[67] K. Su, Y. Shen, and J. A. Zeitler. Terahertz Sensor for Non-Contact Thickness and Quality Measurement of Automobile Paints of Varying Complexity. *IEEE Transactions on Terahertz Science and Technology*, 4(4):432–439, 7 2014.

[68] V. K. S. Feige, S. Nix, F. Ellrich, J. Jonuscheit, and R. Beigang. Non-contact multilayer thickness measurements with reflection-mode terahertz time-domain spectroscopy. In *2011 Conference on Lasers and Electro-Optics Europe and 12th European Quantum Electronics Conference (CLEO EUROPE/EQEC)*, pages 1–1. IEEE, 5 2011.

[69] F. Sanjuan, A. Bockelt, and B. Vidal. Determination of refractive index and thickness of a multilayer structure with a single terahertz time domain spectroscopy measurement. *Applied Optics*, 53(22):4910, 8 2014.

[70] J. S. Melinger, N. Laman, and D. Grischkowsky. The underlying terahertz vibrational spectrum of explosives solids. *Applied Physics Letters*, 93(1):011102, 7 2008.

[71] A. G. Davies, A. D. Burnett, W. Fan, E. H. Linfield, and J. E. Cunningham. Terahertz spectroscopy of explosives and drugs. *Materials Today*, 11(3):18–26, 3 2008.

[72] H. Liu, Y. Chen, G. J. Bastiaans, and X. C. Zhang. Detection and identification of explosive RDX by THz diffuse reflection spectroscopy. *Optics Express*, 14(1):415, 1 2006.

[73] S. Kong and D. Wu. TeraHertz Time-Domain Spectroscopy for Explosive Trace Detection. In *2006 IEEE International Conference on Computational Intelligence for Homeland Security and Personal Safety*, pages 47–50. IEEE, 10 2006.

[74] Y. C. Shen, T. Lo, P. F. Taday, B. E. Cole, W. R. Tribe, and M. C. Kemp. Detection and identification of explosives using terahertz pulsed spectroscopic imaging. *Applied Physics Letters*, 86(24):241116, 6 2005.

[75] J. F. Federici, B. Schulkin, F. Huang, D. Gary, R. Barat, Fi. Oliveira, and D. Zimdars. THz imaging and sensing for security applications—explosives, weapons and drugs. *Semiconductor Science and Technology*, 20(7):S266–S280, 7 2005.

[76] P. U. Jepsen, R. H. Jacobsen, and S. R. Keiding. Generation and detection of terahertz pulses from biased semiconductor antennas. *Journal of the Optical Society of America B*, 13(11):2424, 11 1996.

[77] P. Gu and M. Tani. Terahertz Radiation from Semiconductor Surfaces. In *Terahertz Optoelectronics*, pages 63–98. Springer-Verlag, Berlin/Heidelberg, 2005.

[78] F. Rossi and T. Kuhn. Theory of ultrafast phenomena in photoexcited semiconductors. *Reviews of Modern Physics*, 74(3):895–950, 8 2002.

[79] B. Globisch, R. J. B. Dietz, R. B. Kohlhaas, T. Göbel, M. Schell, D. Alcer, M. Semtsiv, and W. T. Masselink. Iron doped InGaAs: Competitive THz emitters and detectors fabricated from the same photoconductor. *J. Appl. Phys*, 121:53102, 2017.

[80] S. Rapuano and F. Harris. An introduction to FFT and time domain windows. *IEEE Instrumentation & Measurement Magazine*, 10(6):32–44, 12 2007.

[81] X. Wang, C. Shen, T. Jiang, Z. Zhan, Q. Deng, W. Li, W. Wu, N. Yang, W. Chu, and S. Duan. High-power terahertz quantum cascade lasers with 0.23 W in continuous wave mode. *AIP Advances*, 6(7):075210, 7 2016.

[82] S. Fathololoumi, E. Dupont, C. W. I. Chan, Z. R. Wasilewski, S. R. Laframboise, D. Ban, A. Mátyás, C. Jirauschek, Q. Hu, and H. C. Liu. Terahertz quantum cascade lasers operating up to 200 K with optimized oscillator strength and improved injection tunneling. *Optics Express*, 20(4):3866, 2 2012.

[83] F. Capasso. Band structure engineering of quantum microstructures. *Il Nuovo Cimento B*, 110(5-6):501–507, 5 1995.

[84] B. S. Williams, H. Callebaut, S. Kumar, Q. Hu, and J. L. Reno. 3.4-THz quantum cascade laser based on longitudinal-optical-phonon scattering for depopulation. *Applied Physics Letters*, 82(7):1015–1017, 2 2003.

[85] D. Hofstetter, M. Beck, T. Aellen, J. Faist, U. Oesterle, M. Ilegems, E. Gini, and H. Melchior. Continuous wave operation of a 9.3 μm quantum cascade laser on a Peltier cooler. *Applied Physics Letters*, 78(14):1964–1966, 4 2001.

[86] J. Faist, M. Beck, T. Aellen, and E. Gini. Quantum-cascade lasers based on a bound-to-continuum transition. *Applied Physics Letters*, 78(2):147–149, 1 2001.

[87] G. Scalari, L. Ajili, J. Faist, H. Beere, E. Linfield, D. Ritchie, and G. Davies. Far-infrared (λ87 μm) bound-to-continuum quantum-cascade lasers operating up to 90 K. *Applied Physics Letters*, 82(19):3165–3167, 5 2003.

[88] H. E. Beere, J. C. Fowler, J. Alton, E. H. Linfield, D. A. Ritchie, R. Köhler, A. Tredicucci, G. Scalari, L. Ajili, J. Faist, and S. Barbieri. MBE growth of terahertz quantum cascade lasers. *Journal of Crystal Growth*, 278(1-4):756–764, 5 2005.

[89] J. Faist. *Quantum cascade lasers*. Oxford University Press, 2013.

[90] O. C. Zienkiewicz, R. L. Taylor, P. Nithiarasu, and J. Z. Zhu. *The finite element method*. McGraw-hill, 1977.

[91] O. P. Marshall. *Terahertz quantum cascade lasers : photonic crystal waveguides and high frequency bias modulation*. PhD thesis, 2010.

[92] A. Hangauer, G. Spinner, M. Nikodem, and G. Wysocki. High-speed Modulation Characteristic of a Quantum Cascade Laser. In *CLEO: 2013*, page CM1K.2, Washington, D.C., 2013. OSA.

[93] S. Barbieri, W. Maineult, S. S. Dhillon, C. Sirtori, J. Alton, N. Breuil, H. E. Beere, and D. A. Ritchie. 13GHz direct modulation of terahertz quantum cascade lasers. *Applied Physics Letters*, 91(14):143510, 10 2007.

[94] P. N. Dyachenko, J. J. do Rosário, E. W. Leib, A. Yu. Petrov, M. Störmer, H. Weller, T. Vossmeyer, G. A. Schneider, and M. Eich. Tungsten band edge absorber/emitter based on a monolayer of ceramic microspheres. *Optics Express*, 23(19):A1236, 9 2015.

[95] H. Alius and G. Dodel. Amplitude-, phase-, and frequency modulation of far-infrared radiation by optical excitation of silicon. *Infrared Physics*, 32(C):1–11, 1991.

[96] T. Vogel, G. Dodel, E. Holzhauer, H. Salzmann, and A. Theurer. High-speed switching of far-infrared radiation by photoionization in a semiconductor. *Applied Optics*, 31(3):329, 1 1992.

[97] T. Nozokido, H. Minamide, and K. Mizuno. Modulation of submillimeter wave radiation by laser-produced free carriers in semiconductors. *Electronics and Communications in Japan (Part II: Electronics)*, 80(6):1–9, 6 1997.

[98] S. Busch, B. Scherger, M. Scheller, and M. Koch. Optically controlled terahertz beam steering and imaging. *Optics Letters*, 37(8):1391, 4 2012.

[99] C. Janke, J. G. Rivas, P. H. Bolivar, and H. Kurz. All-optical switching of the transmission of electromagnetic radiation through subwavelength apertures. *Optics Letters*, 30(18):2357, 9 2005.

[100] E. Hendry, M. J. Lockyear, J. Gómez Rivas, L. Kuipers, and M. Bonn. Ultrafast optical switching of the THz transmission through metallic subwavelength hole arrays. *Physical Review B*, 75(23):235305, 6 2007.

[101] T. Okada and K. Tanaka. Photo-designed terahertz devices. *Scientific Reports*, 1(1):121, 12 2011.

[102] S. Gupta, M. Y. Frankel, J. A. Valdmanis, J. F. Whitaker, G. A. Mourou, F. W. Smith, and A. R. Calawa. Subpicosecond carrier lifetime in GaAs grown by molecular beam epitaxy at low temperatures. *Applied Physics Letters*, 59(25):3276–3278, 12 1991.

[103] A. Tredicucci and M. S. Vitiello. Device Concepts for Graphene-Based Terahertz Photonics. *IEEE Journal of Selected Topics in Quantum Electronics*, 20(1):130–138, 1 2014.

[104] Y. Fan, N. Shen, F. Zhang, Q. Zhao, Z. Wei, P. Zhang, J. Dong, Q. Fu, H. Li, and C. M. Soukoulis. Photoexcited Graphene Metasurfaces: Significantly Enhanced and Tunable Magnetic Resonances. *ACS Photonics*, 5(4):1612–1618, 4 2018.

[105] A. A. Dubinov, V. Y. Aleshkin, V. Mitin, T. Otsuji, and V. Ryzhii. Terahertz surface plasmons in optically pumped graphene structures. *Journal of Physics: Condensed Matter*, 23(14):145302, 4 2011.

[106] V. Ryzhii, M. Ryzhii, and T. Otsuji. Negative dynamic conductivity of graphene with optical pumping. *Journal of Applied Physics*, 101(8):083114, 4 2007.

[107] W. Li, B. Chen, C. Meng, W. Fang, Y. Xiao, X. Li, Z. Hu, Y. Xu, L. Tong, H. Wang, W. Liu, J. Bao, and Y. R. Shen. Ultrafast All-Optical Graphene Modulator. *Nano Letters*, 14(2):955–959, 2 2014.

[108] P. Weis, J. L. Garcia-Pomar, M. Höh, B. Reinhard, A. Brodyanski, and M. Rahm. Spectrally Wide-Band Terahertz Wave Modulator Based on Optically Tuned Graphene. *ACS Nano*, 6(10):9118–9124, 10 2012.

[109] Q. Wen, W. Tian, Q. Mao, Z. Chen, W. Liu, Q. Yang, M. Sanderson, and H. Zhang. Graphene based All-Optical Spatial Terahertz Modulator. *Scientific Reports*, 4(1):7409, 5 2015.

[110] B. Sensale-Rodriguez, R. Yan, M. M. Kelly, T. Fang, K. Tahy, W. S. Hwang, D. Jena, L. Liu, and H. G. Xing. Broadband graphene terahertz modulators enabled by intraband transitions. *Nature Communications*, 3(1):780, 1 2012.

[111] J. Ye, M. F. Craciun, M. Koshino, S. Russo, S. Inoue, H. Yuan, H. Shimotani, A. F. Morpurgo, and Y. Iwasa. Accessing the transport properties of graphene and its multilayers at high carrier density. *Proceedings of the National Academy of Sciences of the United States of America*, 108(32):13002–6, 8 2011.

[112] D. K. Efetov and P. Kim. Controlling electron-phonon interactions in graphene at ultrahigh carrier densities. *Physical Review Letters*, 105(25):256805, 12 2010.

[113] S Badhwar. *Laterally confined THz sources and graphene based THz optics*. PhD thesis, University of Cambridge, 2014.

[114] I. Lin, J. Liu, K. Shi, P. Tseng, K. Wu, C. Luo, and L. Li. Terahertz optical properties of multilayer graphene: Experimental observation of strong dependence on stacking arrangements and misorientation angles. *Physical Review B*, 86(23):235446, 12 2012.

[115] J. M. Dawlaty, S. Shivaraman, J. Strait, P. George, M. Chandrashekhar, F. Rana, M. G. Spencer, D. Veksler, and Y. Chen. Measurement of the optical absorption spectra of epitaxial graphene from terahertz to visible. *Applied Physics Letters*, 93(13):131905, 9 2008.

[116] H. Choi, F. Borondics, D. A. Siegel, S. Y. Zhou, M. C. Martin, A. Lanzara, and R. A. Kaindl. Broadband electromagnetic response and ultrafast dynamics of few-layer epitaxial graphene. *Applied Physics Letters*, 94(17):172102, 4 2009.

[117] S. Winnerl, M. Orlita, P. Plochocka, P. Kossacki, M. Potemski, T. Winzer, E. Malic, A. Knorr, M. Sprinkle, C. Berger, W. A. de Heer, H. Schneider, and M. Helm. Carrier Relaxation in Epitaxial Graphene Photoexcited Near the Dirac Point. *Physical Review Letters*, 107(23):237401, 11 2011.

[118] J. D. Buron, F. Pizzocchero, B. S. Jessen, T. J. Booth, P. F. Nielsen, O. Hansen, M. Hilke, E. Whiteway, P. U. Jepsen, P. Bøggild, and D. H. Petersen. Electrically Continuous Graphene from Single Crystal Copper Verified by Terahertz Conductance Spectroscopy and Micro Four-Point Probe. *Nano Letters*, 14(11):6348–6355, 11 2014.

[119] B. Sensale-Rodriguez, R. Yan, L. Liu, D. Jena, and H. G. Xing. Graphene for Reconfigurable Terahertz Optoelectronics. *Proceedings of the IEEE*, 101(7):1705–1716, 7 2013.

[120] B. Sensale-Rodriguez. Graphene-insulator-graphene active plasmonic terahertz devices. *Applied Physics Letters*, 103(12):123109, 9 2013.

[121] B. Sensale-Rodriguez, S. Rafique, R. Yan, M. Zhu, V. Protasenko, D. Jena, L. Liu, and H. G. Xing. Terahertz imaging employing graphene modulator arrays. *Optics Express*, 21(2):2324, 1 2013.

[122] B. Sensale-Rodriguez. Graphene-Based Optoelectronics. *Journal of Lightwave Technology, Vol. 33, Issue 5, pp. 1100-1108*, 33(5):1100–1108, 3 2015.

[123] B. Sensale-Rodriguez, T. Fang, R. Yan, M. M. Kelly, D. Jena, L. Liu, and H. Xing. Unique prospects for graphene-based terahertz modulators. *Applied Physics Letters*, 99(11):113104, 9 2011.

[124] B. Sensale-Rodriguez, R. Yan, S. Rafique, Mingda Z., M. Kelly, V. Protasenko, D. Jena, L. Liu, and H. G. Xing. Exceptional tunability of THz reflectance in graphene structures. In *2012 37th International Conference on Infrared, Millimeter, and Terahertz Waves*, pages 1–3. IEEE, 9 2012.

[125] R. Alaee, M. Farhat, C. Rockstuhl, and F. Lederer. A perfect absorber made of a graphene micro-ribbon metamaterial. *Optics Express*, 20(27):28017, 12 2012.

[126] A. Andryieuski and A. V. Lavrinenko. Graphene metamaterials based tunable terahertz absorber: effective surface conductivity approach. *Optics Express*, 21(7):9144, 4 2013.

[127] N. Kakenov, M. S. Ergoktas, O. Balci, and C. Kocabas. Graphene based terahertz phase modulators. *2D Materials*, 5(3):035018, 5 2018.

[128] Y. Zhang, Y. Feng, B. Zhu, J. Zhao, and T. Jiang. Graphene based tunable metamaterial absorber and polarization modulation in terahertz frequency. *Optics Express*, 22(19):22743, 9 2014.

[129] B. Sensale-Rodriguez, R. Yan, S. Rafique, M. Zhu, W. Li, X. Liang, D. Gundlach, V. Protasenko, M. M. Kelly, D. Jena, L. Liu, and H. G. Xing. Extraordinary Control of Terahertz Beam Reflectance in Graphene Electro-absorption Modulators. *Nano Letters*, 12(9):4518–4522, 9 2012.

[130] Y. Liu and X. Zhang. Metamaterials: a new frontier of science and technology. *Chemical Society Reviews*, 40(5):2494, 4 2011.

[131] D. R. Smith, W. J. Padilla, D. C. Vier, S. C. Nemat-Nasser, and S. Schultz. Composite Medium with Simultaneously Negative Permeability and Permittivity. *Physical Review Letters*, 84(18):4184–4187, 5 2000.

[132] R. A. Shelby, D. R. Smith, and S. Schultz. Experimental verification of a negative index of refraction. *Science (New York, N.Y.)*, 292(5514):77–9, 4 2001.

[133] S. Linden, C. Enkrich, M. Wegener, J. Zhou, T. Koschny, and C. M. Soukoulis. Magnetic Response of Metamaterials at 100 Terahertz. *Science*, 306(5700):1351–1353, 11 2004.

[134] S. P. Burgos, R. de Waele, A. Polman, and H. A. Atwater. A single-layer wide-angle negative-index metamaterial at visible frequencies. *Nature Materials*, 9(5):407–412, 5 2010.

[135] H. T. Chen, J. F. O'Hara, A. K. Azad, A. J. Taylor, R. D. Averitt, D. B. Shrekenhamer, and W. J. Padilla. Experimental demonstration of frequency-agile terahertz metamaterials. *Nature Photonics*, 2(5):295–298, 5 2008.

[136] F. Ma, Y. Qian, Y. Lin, H. Liu, X. Zhang, Z. Liu, J. Ming-Lin Tsai, and C. Lee. Polarization-sensitive microelectromechanical systems based tunable terahertz metamaterials using three dimensional electric split-ring resonator arrays. *Applied Physics Letters*, 102(16):161912, 4 2013.

[137] W. J. Padilla, A. J. Taylor, C. Highstrete, M. Lee, and R. D. Averitt. Dynamical Electric and Magnetic Metamaterial Response at Terahertz Frequencies. *Physical Review Letters*, 96(10):107401, 3 2006.

[138] L. Cong, Y. K. Srivastava, H. Zhang, X. Zhang, J. Han, and R. Singh. All-optical active THz metasurfaces for ultrafast polarization switching and dynamic beam splitting. *Light: Science & Applications*, 7(1):28, 12 2018.

[139] S. Zhang, J. Zhou, Y. Park, J. Rho, R. Singh, S. Nam, A. K. Azad, H. T. Chen, X. Yin, A. J. Taylor, and X. Zhang. Photoinduced handedness switching in terahertz chiral metamolecules. *Nature Communications*, 3(1):942, 1 2012.

[140] J. Zhou, D. R. Chowdhury, R. Zhao, A. K. Azad, H. T. Chen, C. M. Soukoulis, A. J. Taylor, and J. F. O'Hara. Terahertz chiral metamaterials with giant and dynamically tunable optical activity. *Physical Review B - Condensed Matter and Materials Physics*, 86(3):035448, 7 2012.

[141] J. Gu, R. Singh, X. Liu, X. Zhang, Y. Ma, S. Zhang, S. A. Maier, Z. Tian, A. K. Azad, H. T. Chen, A. J. Taylor, J. Han, and W. Zhang. Active control of electromagnetically induced transparency analogue in terahertz metamaterials. *Nature Communications*, 3(1):1151, 1 2012.

[142] Y. Lin, Y. Qian, F. Ma, Z. Liu, and P. Kropelnicki. Development of stress-induced curved actuators for a tunable THz filter based on double split-ring resonators. *Appl. Phys. Lett*, 102:111908, 2013.

[143] Z. Han, K. Kohno, H. Fujita, K. Hirakawa, and H. Toshiyoshi. MEMS reconfigurable metamaterial for terahertz switchable filter and modulator. *Optics Express*, 22(18):21326, 9 2014.

[144] P. Pitchappa, C. P. Ho, L. Dhakar, and C. Lee. Microelectromechanically reconfigurable interpixelated metamaterial for independent tuning of multiple resonances at terahertz spectral region. *Optica*, 2(6):571, 6 2015.

[145] T. Kan, A. Isozaki, N. Kanda, N. Nemoto, K. Konishi, H. Takahashi, M. Kuwata-Gonokami, K. Matsumoto, and I. Shimoyama. Enantiomeric switching of chiral metamaterial for terahertz polarization modulation employing vertically deformable MEMS spirals. *Nature Communications*, 6(1):8422, 12 2015.

[146] Z. Han, K. Kohno, H. Fujita, K. Hirakawa, and H. Toshiyoshi. Tunable Terahertz Filter and Modulator Based on Electrostatic MEMS Reconfigurable SRR Array. *IEEE Journal of Selected Topics in Quantum Electronics*, 21(4):114–122, 7 2015.

[147] H. T. Chen, W. J. Padilla, J. M. O. Zide, A. C. Gossard, A. J. Taylor, and R. D. Averitt. Active terahertz metamaterial devices. *Nature*, 444(7119):597–600, 11 2006.

[148] E. A. Shaner, J. G. Cederberg, and D. Wasserman. Electrically tunable extraordinary optical transmission gratings. *Applied Physics Letters*, 91(18):181110, 10 2007.

[149] O. Paul, C. Imhof, B. Lägel, S. Wolff, J. Heinrich, S. Höfling, A. Forchel, R. Zengerle, R. Beigang, and M. Rahm. Polarization-independent active metamaterial for high-frequency terahertz modulation. *Optics Express*, 17(2):819, 1 2009.

[150] H. Chen, H. Lu, A. K. Azad, R. D. Averitt, A. C. Gossard, S. A. Trugman, J. F. O'Hara, and A. J. Taylor. Electronic control of extraordinary terahertz transmission through subwavelength metal hole arrays. *Optics Express*, 16(11):7641, 5 2008.

[151] H. Chen, S. Palit, T. Tyler, C. M. Bingham, J. M. O. Zide, J. F. O'Hara, D. R. Smith, A. C. Gossard, R. D. Averitt, W. J. Padilla, N. M. Jokerst, and A. J. Taylor. Hybrid metamaterials enable fast electrical modulation of freely propagating terahertz waves. *Applied Physics Letters*, 93(9):091117, 9 2008.

[152] T. Kleine-Ostmann, P. Dawson, K. Pierz, G. Hein, and M. Koch. Room-temperature operation of an electrically driven terahertz modulator. *Applied Physics Letters*, 84(18):3555–3557, 5 2004.

[153] P. K. Singh and S. Sonkusale. High Speed Terahertz Modulator on the Chip Based on Tunable Terahertz Slot Waveguide. *Scientific Reports*, 7(1):40933, 12 2017.

[154] Y. Zhang, S. Qiao, S. Liang, Z. Wu, Z. Yang, Z. Feng, H. Sun, Y. Zhou, L. Sun, Z. Chen, X. Zou, B. Zhang, J. Hu, S. Li, Q. Chen, L. Li, G. Xu, Y. Zhao, and S. Liu. Gbps Terahertz External Modulator Based on a Composite Metamaterial with a Double-Channel Heterostructure. *Nano Letters*, 15(5):3501–3506, 5 2015.

[155] R. Degl'Innocenti, D. S. Jessop, Y. D. Shah, J. Sibik, J. A. Zeitler, P. R. Kidambi, S. Hofmann, H. E. Beere, and D. A. Ritchie. Low-Bias Terahertz Amplitude Modulator Based on Split-Ring Resonators and Graphene. *ACS Nano*, 8(3):2548–2554, 3 2014.

[156] D. S. Jessop, S. J. Kindness, L. Xiao, P. Braeuninger-Weimer, H. Lin, Y. Ren, C. X. Ren, S. Hofmann, J. A. Zeitler, H. E. Beere, D. A. Ritchie, and R. Degl'Innocenti. Graphene based plasmonic terahertz amplitude modulator operating above 100 MHz. *Applied Physics Letters*, 108(17), 2016.

[157] P. Q. Liu, I. J. Luxmoore, S. A. Mikhailov, N. A. Savostianova, F. Valmorra, J. Faist, and G. R. Nash. Highly tunable hybrid metamaterials employing split-ring resonators strongly coupled to graphene surface plasmons. *Nature Communications*, 6(1):8969, 12 2015.

[158] F. Valmorra, G. Scalari, C. Maissen, W. Fu, C. Schönenberger, J. W. Choi, H. G. Park, M. Beck, and J. Faist. Low-Bias Active Control of Terahertz Waves by Coupling Large-Area CVD Graphene to a Terahertz Metamaterial. *Nano Letters*, 13(7):3193–3198, 7 2013.

[159] S. H. Lee, M. Choi, T. Kim, S. Lee, M. Liu, X. Yin, H. K. Choi, S. S. Lee, C. Choi, S. Choi, X. Zhang, and B. Min. Switching terahertz waves with gate-controlled active graphene metamaterials. *Nature Materials*, 11(11):936–941, 11 2012.

[160] R. Degl'innocenti, D S. Jessop, C. W. O. Sol, L. Xiao, S. J. Kindness, H. Lin, J. Axel Zeitler, P. Braeuninger-Weimer, S. Hofmann, Y. Ren, V. S. Kamboj, J. P. Griffiths, H. E. Beere, and D. A. Ritchie. Fast Modulation of Terahertz Quantum Cascade Lasers Using Graphene Loaded Plasmonic Antennas. *ACS Photonics*, 3(3):464–470, 2016.

[161] Y. Yao, M. A. Kats, P. Genevet, N. Yu, Y. Song, J. Kong, and F. Capasso. Broad electrical tuning of graphene-loaded plasmonic antennas. *Nano Letters*, 13(3):1257–1264, 3 2013.

[162] Y. Yao, M. A. Kats, R. Shankar, Y. Song, J. Kong, M. Loncar, and F. Capasso. Wide wavelength tuning of optical antennas on graphene with nanosecond response time. *Nano Letters*, 14(1):214–219, 1 2014.

[163] Y. Yao, R. Shankar, M. A. Kats, Y. Song, J. Kong, M. Loncar, and F. Capasso. Electrically Tunable Metasurface Perfect Absorbers for Ultrathin Mid-Infrared Optical Modulators. *Nano Letters*, 14(11):6526–6532, 11 2014.

[164] T. P. Meyrath, T. Zentgraf, and H. Giessen. Lorentz model for metamaterials: Optical frequency resonance circuits. *Physical Review B*, 75(20):205102, 5 2007.

[165] M. A. Ordal, R. J. Bell, R. W. Alexander, L. L. Long, and M. R. Querry. Optical properties of Au, Ni, and Pb at submillimeter wavelengths. *Applied Optics*, 26(4):744, 2 1987.

[166] M. A. Ordal, R. J. Bell, R. W. Alexander, L. L. Long, and M. R. Querry. Optical properties of fourteen metals in the infrared and far infrared: Al, Co, Cu, Au, Fe, Pb, Mo, Ni, Pd, Pt, Ag, Ti, V, and W. *Applied Optics*, 24(24):4493, 12 1985.

[167] M. Garcia-Vigueras, F. Mesa, F. Medina, R. Rodriguez-Berral, and J. L. Gomez-Tornero. Simplified circuit model for arrays of metallic dipoles sandwiched between dielectric slabs under arbitrary incidence. *IEEE Transactions on Antennas and Propagation*, 60(10):4637–4649, 2012.

[168] M. Amin, M. Farhat, and H. Bağcı. A dynamically reconfigurable Fano metamaterial through graphene tuning for switching and sensing applications. *Scientific Reports*, 3(1):2105, 12 2013.

[169] S. Hofmann, P. Braeuninger-Weimer, and R. S. Weatherup. CVD-enabled graphene manufacture and technology, 7 2015.

[170] J. A. Alexander-Webber, A. A. Sagade, A. I. Aria, Z. A. Van Veldhoven, P. Braeuninger-Weimer, R. Wang, A. Cabrero-Vilatela, M. B. Martin, J. Sui, M. R. Connolly, and S. Hofmann. Encapsulation of graphene transistors and vertical device integration by interface engineering with atomic layer deposited oxide. *2D Materials*, 4(1), 2017.

[171] K. Z. Rajab, M. Naftaly, E. H. Linfield, J. C. Nino, D. Arenas, D. Tanner, R. Mittra, and M. Lanagan. Broadband Dielectric Characterization of Aluminum Oxide (Al 2 O 3). *Journal of Microelectronics and Electronic Packaging*, 5(1):2–7, 2008.

[172] Y. Zhang, Y. Zhao, S. Liang, B. Zhang, L. Wang, T. Zhou, W. Kou, F. Lan, H. Zeng, J. Han, Z. Feng, Q. Chen, P. Mazumder, and Z. Yang. Large phase modulation of THz wave via an enhanced resonant active HEMT metasurface. *Nanophotonics*, 8(1):153–170, 2019.

[173] L. Ju, B. Geng, J. Horng, C. Girit, M. Martin, Z. Hao, H. A. Bechtel, X. Liang, A. Zettl, Y. R. Shen, and F. Wang. Graphene plasmonics for tunable terahertz metamaterials. *Nature Nanotechnology*, 6(10):630–634, 10 2011.

[174] P. A. Huidobro, M. Kraft, S. A. Maier, and J. B. Pendry. Graphene as a Tunable Anisotropic or Isotropic Plasmonic Metasurface. *ACS Nano*, 10(5):5499–5506, 5 2016.

[175] M. M. Jadidi, A. B. Sushkov, R. L. Myers-Ward, A. K. Boyd, K. M. Daniels, D. K. Gaskill, M. S. Fuhrer, H. D. Drew, and T. E. Murphy. Tunable Terahertz Hybrid Metal-Graphene Plasmons. *Nano Letters*, 15(10):7099–7104, 10 2015.

[176] G. Giovannetti, P. A. Khomyakov, G. Brocks, V. M. Karpan, J. Van Den Brink, and P. J. Kelly. Doping Graphene with Metal Contacts. 2008.

[177] N. Yu and F. Capasso. Flat optics with designer metasurfaces, 2014.

[178] S. Zhang, D. A. Genov, Y. Wang, M. Liu, and X. Zhang. Plasmon-Induced Transparency in Metamaterials. *Physical Review Letters*, 101(4):047401, 7 2008.

[179] N. Papasimakis, V. A. Fedotov, N. I. Zheludev, and S. L. Prosvirnin. Metamaterial Analog of Electromagnetically Induced Transparency. *Physical Review Letters*, 101(25):253903, 12 2008.

[180] R. Singh, C. Rockstuhl, F. Lederer, and W. Zhang. Coupling between a dark and a bright eigenmode in a terahertz metamaterial. *Physical Review B*, 79(8):085111, 2 2009.

[181] H. T. Chen, W. J. Padilla, M. J. Cich, A. K. Azad, R. D. Averitt, and A. J. Taylor. A metamaterial solid-state terahertz phase modulator. *Nature Photonics*, 3(3):148–151, 3 2009.

[182] C. Chen, I. Un, N. Tai, and T. Yen. Asymmetric coupling between subradiant and superradiant plasmonic resonances and its enhanced sensing performance. *Optics Express*, 17(17):15372, 8 2009.

[183] Z. Li, Y. Ma, R. Huang, R. Singh, J. Gu, Z. Tian, J. Han, and W. Zhang. Manipulating the plasmon-induced transparency in terahertz metamaterials. *Optics Express*, 19(9):8912, 4 2011.

[184] Y. Ma, Z. Li, Y. Yang, R. Huang, R. Singh, S. Zhang, J. Gu, Z. Tian, J. Han, and W. Zhang. Plasmon-induced transparency in twisted Fano terahertz metamaterials. *Optical Materials Express*, 1(3):391, 7 2011.

[185] Q. Bai, C. Liu, J. Chen, C. Cheng, M. Kang, and H. T. Wang. Tunable slow light in semiconductor metamaterial in a broad terahertz regime. *Journal of Applied Physics*, 107(9), 5 2010.

[186] K. Zhang, C. Wang, L. Qin, R. Peng, D. Xu, X. Xiong, and M. Wang. Dual-mode electromagnetically induced transparency and slow light in a terahertz metamaterial. *Optics Letters*, 39(12):3539, 6 2014.

[187] L. Vestergaard Hau, S. E. Harris, Z. Dutton, and C. H. Behroozi. Light speed reduction to 17 metres per second in an ultracold atomic gas. *Nature*, 397(6720):594–598, 2 1999.

[188] I. Novikova, R. L. Walsworth, and Y. Xiao. Electromagnetically induced transparency-based slow and stored light in warm atoms, 5 2012.

[189] H. Schmidt and A. Imamoglu. Giant Kerr nonlinearities obtained by electromagnetically induced transparency. *Optics Letters*, 21(23):1936, 12 1996.

[190] Y. Wu, J. Saldana, and Y. Zhu. Large enhancement of four-wave mixing by suppression of photon absorption from electromagnetically induced transparency. *Physical Review A - Atomic, Molecular, and Optical Physics*, 67(1):5, 2003.

[191] N. Liu, T. Weiss, M. Mesch, L. Langguth, U. Eigenthaler, M. Hirscher, C. Sönnichsen, and H. Giessen. Planar metamaterial analogue of electromagnetically induced transparency for plasmonic sensing. *Nano Letters*, 10(4):1103–1107, 4 2010.

[192] G. D. Liu, X. Zhai, L. L. Wang, Q. Lin, S. X. Xia, X. Luo, and C. J. Zhao. A High-Performance Refractive Index Sensor Based on Fano Resonance in Si Split-Ring Metasurface. *Plasmonics*, 13(1):15–19, 2 2018.

[193] Z. X. Chen, J. H. Chen, Z. J. Wu, W. Hu, X. J. Zhang, and Y. Q. Lu. Tunable Fano resonance in hybrid graphene-metal gratings. *Applied Physics Letters*, 104(16):161114, 4 2014.

[194] Q. Fu, F. Zhang, Y. Fan, J. Dong, W. Cai, W. Zhu, S. Chen, and R. Yang. Weak coupling between bright and dark resonators with electrical tunability and analysis based on temporal coupled-mode theory. *Applied Physics Letters*, 110(22), 5 2017.

[195] Y. Fan, T. Qiao, F. Zhang, Q. Fu, J. Dong, B. Kong, and H. Li. An electromagnetic modulator based on electrically controllable metamaterial analogue to electromagnetically induced transparency. *Scientific Reports*, 7, 1 2017.

[196] G. Rana, P. Deshmukh, S. Palkhivala, A. Gupta, S. P. Duttagupta, S. S. Prabhu, V. Achanta, and G. S. Agarwal. Quadrupole-Quadrupole Interactions to Control Plasmon-Induced Transparency. *Physical Review Applied*, 9(6), 6 2018.

[197] C. J. Chang-Hasnain, K. U. Pei-Cheng, J. Kim, and S. L. Chuang. Variable optical buffer using slow light in semiconductor nanostructures. In *Proceedings of the IEEE*, volume 91, pages 1884–1896, 11 2003.

[198] S. Xiao, T. Wang, T. Liu, X. Yan, Z. Li, and C. Xu. Active modulation of electromagnetically induced transparency analogue in terahertz hybrid metal-graphene metamaterials. *Carbon*, 126:271–278, 2018.

[199] S. Benedetto and P. Poggiolini. Theory of Polarization Shift Keying Modulation. *IEEE TRANSACTIONS ON COMMUNICATIONS*, 40(4), 1992.

[200] N. Oshima, K. Hashimoto, S. Suzuki, and M. Asada. Terahertz Wireless Data Transmission With Frequency and Polarization Division Multiplexing Using Resonant-Tunneling-Diode Oscillators. *IEEE Transactions on Terahertz Science and Technology*, 7(5):593–598, 9 2017.

[201] G. S. Jenkins, A. B. Sushkov, D. C. Schmadel, N. P. Butch, P. Syers, J. Paglione, and H. D. Drew. Terahertz Kerr and reflectivity measurements on the topological insulator Bi2Se3. *Physical Review B - Condensed Matter and Materials Physics*, 82(12), 2010.

[202] H. Plank and S. D. Ganichev. A review on terahertz photogalvanic spectroscopy of Bi2Te3- and Sb2Te3-based three dimensional topological insulators. *Solid-State Electronics*, 147:44–50, 9 2018.

[203] L. Zhang, H. Zhong, C. Deng, C. Zhang, and Y. Zhao. Characterization of birefringent material using polarization-controlled terahertz spectroscopy. *Optics Express*, 18(19):20491, 9 2010.

[204] J. Xu, G. J. Ramian, and J. F. Galan. Terahertz circular dichroism spectroscopy: A potential approach to the in situ detection of life's metabolic and genetic machinery. *ASTROBIOLOGY*, 3(3):489, 9 2003.

[205] J. Xu, J. Galan, G. Ramian, P. Savvidis, A. Scopatz, R. R. Birge, S. J. Allen, and K. Plaxco. Terahertz circular dichroism spectroscopy of biomolecules. volume 5268, page 19. International Society for Optics and Photonics, 2 2004.

[206] Y. Hirota, R. Hattori, M. Tani, and M. Hangyo. Polarization modulation of terahertz electromagnetic radiation by four-contact photoconductive antenna. 2006.

[207] S. Zhang, Y. Park, J. Li, X. Lu, W. Zhang, and X. Zhang. Negative Refractive Index in Chiral Metamaterials. *Physical Review Letters*, 102(2):023901, 1 2009.

[208] J. M. Woo, S. Hussain, and J. Jang. A terahertz in-line polarization converter based on through-via connected double layer slot structures. *Scientific Reports*, 7(1):42952, 12 2017.

[209] M. Parvinnezhad Hokmabadi, D. S. Wilbert, P. Kung, and S. M. Kim. Polarization-Dependent, Frequency-Selective THz Stereometamaterial Perfect Absorber. *Physical Review Applied*, 1(4):044003, 5 2014.

[210] H. T. Chen, A. J. Taylor, and N. Yu. A review of metasurfaces: Physics and applications. *Reports on Progress in Physics*, 79(7):076401, 7 2016.

[211] N. K. Grady, J. E. Heyes, D. R. Chowdhury, Y. Zeng, M. T. Reiten, A. K. Azad, A. J. Taylor, D. A. R. Dalvit, and H. T. Chen. Terahertz Metamaterials for Linear Polarization Conversion and Anomalous Refraction. *Science*, 340(6138):1304–1307, 2013.

[212] F. Fang, Y. Cheng, and H. Liao. Giant optical activity and circular dichroism in the terahertz region based on bi-layer Y-shaped chiral metamaterial. *Optik*, 125(20):6067–6070, 10 2014.

[213] L. Wu, Z. Yang, Y. Cheng, Z. Lu, P. Zhang, M. Zhao, R. Gong, X. Yuan, Y. Zheng, and J. Duan. Electromagnetic manifestation of chirality in layer-by-layer chiral metamaterials. *Optics Express*, 21(5):5239, 3 2013.

[214] S. J. Kindness, D. S. Jessop, B. Wei, R. Wallis, V. S. Kamboj, L. Xiao, Y. Ren, P. Braeuninger-Weimer, A. I. Aria, S. Hofmann, H. E. Beere, D. A. Ritchie, and R. Degl'Innocenti. External amplitude and frequency modulation of a terahertz quantum cascade laser using metamaterial/graphene devices. *Scientific Reports*, 7(1):1–10, 2017.

[215] G. Liang, X. Hu, X. Yu, Y. Shen, L. H. Li, A. G. Davies, E. H. Linfield, H. K. Liang, Y. Zhang, S. F. Yu, and Q. J. Wang. Integrated Terahertz Graphene Modulator with 100% Modulation Depth. *ACS Photonics*, 2(11):1559–1566, 11 2015.

[216] I. Kundu, P. Dean, A. Valavanis, L. Chen, L. Li, J. E. Cunningham, E. H. Linfield, and A. G. Davies. Discrete Vernier tuning in terahertz quantum cascade lasers using coupled cavities. *Optics Express*, 22(13):16595, 6 2014.

[217] J. Xu, J. M. Hensley, D. B. Fenner, R. P. Green, L. Mahler, A. Tredicucci, M. G. Allen, F. Beltram, H. E. Beere, and D. A. Ritchie. Tunable terahertz quantum cascade lasers with an external cavity. *Applied Physics Letters*, 91(12):121104, 9 2007.

[218] A. J. Gatesman, J. Waldman, M. Ji, C. Musante, and S. Yngvesson. An Anti-Reflection Coating for Silicon Optics at Terahertz Frequencies. *IEEE Microwave and Guided Wave Letters*, 10(7):264–266, 2000.

[219] R. Wallis. *Novel THz technologies: waveguiding, imaging, and near-fi eld microscopy*. PhD thesis, 2017.

[220] S. J. Kindness, N. W. Almond, B. Wei, R. Wallis, W. Michailow, V. S. Kamboj, P. Braeuninger-Weimer, S. Hofmann, H. E. Beere, D. A. Ritchie, and R. Degl'Innocenti. Active Control of Electromagnetically Induced Transparency in a Terahertz Metamaterial Array with Graphene for Continuous Resonance Frequency Tuning, 11 2018.

[221] S. J. Kindness, N. W. Almond, W. Michailow, B. Wei, L. A. Jakob, K. Delfanazari, P. Braeuninger-Weimer, S. Hofmann, H. E. Beere, D. A. Ritchie, and R. Degl'Innocenti. Graphene-Integrated Metamaterial Device for All-Electrical Polarization Control of Terahertz Quantum Cascade LasersKindness, S. J., Almond, N. W., Michailow, W., Wei, B., Jakob, L. A., Delfanazari, K., … Degl'Innocenti, R. (2019). Graphene-Integrated Meta. *ACS Photonics*, 6(6):1547–1555, 6 2019.